

NMR Investigations on Catalysts and Conformations
in Organo- and Photocatalytic Reactions,
and Characterization of Electrolytes and
Supramolecular Switchable Container Molecules



Dissertation

zur Erlangung des Doktorgrades
der Naturwissenschaften (Dr. rer. nat.)
der Fakultät für Chemie und Pharmazie
der Universität Regensburg

vorgelegt von

Matthias Fleischmann

aus Regensburg

2011

Die vorliegende Dissertation beruht auf Arbeiten, die zwischen November 2007 und Juli 2011 im Arbeitskreis von Prof. Dr. Ruth M. Gschwind am Institut für organische Chemie der Universität Regensburg durchgeführt wurden.

Promotionsgesuch eingereicht am: 19.07.2011

Promotionsprüfung am: 19.08.2011

Die Arbeit wurde angeleitet von: Prof. Dr. Ruth M. Gschwind

Prüfungsausschuss:

Vorsitzender: Prof. Dr. Heiner J. Gores

1. Gutachter: Prof. Dr. Ruth M. Gschwind

2. Gutachter: Dr. Kirsten Zeitler

3. Prüfer: Prof. Dr. Manfred Scheer

An dieser Stelle sei allen gedankt, die zum Gelingen dieser Arbeit beigetragen haben. In erster Linie möchte ich mich ganz herzlich bei Prof. Dr. Ruth M. Gschwind für die interessante Themenstellung, die ausgezeichnete Betreuung im Laufe dieser Dissertation und für den großen Freiraum bei der Wahl und Bearbeitung meiner Forschungsinteressen bedanken. Dr. Kirsten Zeitler danke ich vielmals für die Übernahme des Zweitgutachtens und für viele Anregungen in- und außerhalb des Seminars. Prof. Dr. Manfred Scheer danke ich sehr für die Übernahme der Aufgabe des Drittprüfers und für die Kooperation auf dem Gebiet der Supramolekularen Chemie. Prof. Dr. Heiner J. Gores danke ich sehr für die Übernahme des Prüfungsvorsitzes, für sein großes Interesse an unserer Kooperation auf dem Gebiet der Lithium-Ionen-Elektrolyte und für sein Empfehlungsschreiben.

Ich bedanke mich bei Professor Dr. Armin Buschauer als Sprecher des Graduiertenkollegs „Medizinische Chemie“ für die ideelle und finanzielle Unterstützung durch das Stipendium des GRK 760. Ich danke Prof. Dr. Burkhard König für die vielen Anregungen im Seminar und für die Möglichkeit, im Graduiertenkolleg GRK 1626 „Photokatalyse“ auch als Nicht-Mitglied aktiv zu sein.

Ferner möchte ich allen Kooperationspartnern für Ihre Zusammenarbeit danken: Prof. Dr. Wolfram Gronwald (Institut für funktionelle Genomik), Professor Dr. Oliver Reiser und Dr. Valerio D'Elia (Institut für organische Chemie), Prof. Dr. Hans-Robert Kalbitzer, Harald Donaubaue und Konrad Brunner (Institut für Biophysik und physikalische Biochemie) sowie Prof. Dr. Burkhard Luy (Karlsruher Institut für Technologie) für ihre Beiträge zu den Foldamerstudien; Prof. Dr. Magnus Rueping und Dr. Erli Sugiono (Institut für Organische Chemie, RWTH Aachen), Prof. Dr. Sven Rau und Michael Pfeffer (Institut für anorganische Chemie, Universität Ulm), Prof. Dr. Burkhard König (Institut für Organische Chemie) für die Zusammenarbeit in der Organo- und Photokatalyse; Prof. Dr. Heiner J. Gores, Dr. Sandra Zugmann und Hartl Robert (Institut für physikalische Chemie) für die Zusammenarbeit auf dem Gebiet der Lithium-Ionen-Elektrolyte; Prof. Dr. Manfred Scheer und Dr. Fabian Dielmann (Institut für anorganische Chemie) für die Zusammenarbeit auf dem Gebiet der Supramolekularen Chemie.

Besonders herzlich möchte ich allen meinen Kollegen Dr. Guido Federwisch, Dr. Tobias Gärtner, Dr. Roland Kleinmaier, Dr. Katrin Schober, Evelyn Hartmann, Maria Neumeier, Felicitas Von Rekowski, Nils Sorgenfrei, Carina Koch, Michael Hammer und Michael Haindl für die schöne Zeit danken. Dr. Markus Schmid, Diana Drettwan und Christian Feldmeier danke ich zudem für die Zusammenarbeit an einzelnen Teilprojekten dieser Arbeit.

Ich danke den Mitarbeitern der NMR-Abteilung, Dr. Thomas Burgemeister, Fritz Kastner, Annette Schramm und Georgine Stühler, für die Unterstützung auch über die Spektroskopie hinaus, ebenso Nikola Kastner-Pustet und Ulrike Weck.

Danke an alle die hier keinen Platz mehr finden habe!

Danke an alle meine Freunde!

Diese Arbeit wäre ohne den großen Rückhalt meiner Eltern und meiner Familie nicht möglich gewesen. Vielen Dank für die große Unterstützung über eine laaange Zeit!

Am Ende möchte ich einem speziellen Mitglied meiner Familie, meiner Freundin Susanne, danken. Ihr gebührt das größte Dankeschön von allen, da sie mich in allen Lebenslagen unterstützt, motiviert und manchmal auch ausgehalten hat. Danke!

Sensitivity x Resolution x Convenience = constant

Valentin Ananikov

Für Susanne

NMR Investigations on Catalysts and Conformations
in Organo- and Photocatalytic Reactions,
and Characterization of Electrolytes and
Supramolecular Switchable Container Molecules

Contents

1	Introduction and Outline.....	1
2	RDCs in Short Peptidic Foldamers	5
2.1	Abstract	6
2.2	Manuscript.....	7
2.3	Supporting Information	16
2.3.1	Experimental Section	16
2.3.2	Quality check of different <i>cis</i> - β -ACC coordinates with RDC data	19
2.3.3	Structure investigation of 1	21
2.3.4	Structure investigation of 2	25
2.3.5	Statistical information on the calculated structures of 1 and 2	28
2.4	References	29
3	Foldamers with Tunable Orientation of the Steric Shielding.....	31
3.1	Abstract	32
3.2	Manuscript.....	33
3.3	Supporting Information	47
3.3.1	Experimental Section	47
3.3.2	Parametrization of Hyp and Hyp(OBn)	50
3.3.3	Structure investigation of 3 at 273 K	51
3.3.4	Structure investigation of 3 at 240 K	53
3.3.5	Validation of the calculated β angles	54
3.3.6	NMR investigations on the organocatalysts 4 and 5	54
3.3.7	Quantum mechanical calculations for dimeric 4.....	58
3.3.8	Enamine detection for 1	59
3.3.9	Statistical information on the calculated structures of 3	59
3.4	Additional experimental findings.....	60
3.4.1	Preparation of PDMS/CDCl ₃ gels	60
3.4.2	Determination of RDCs.....	61
3.5	References	63

4	Brønsted Acid Catalysis – Hydrogen Bonding vs. Ion Pairing.....	65
4.1	Abstract	66
4.2	Manuscript.....	67
4.3	Supporting Information	77
4.3.1	Experimental Section	77
4.3.2	Temperature dependence of the complexes 1·2, 1·3 and 1·4	78
4.3.3	Evaluation of other potentially existing species.....	80
4.3.4	Concentration dependence of the different complex species	81
4.3.5	DOSY experiments of pure 1-3 and the 1·2 and 1·3 complex species.....	82
4.4	Additional experimental findings.....	85
4.4.1	Influence of the water content.....	85
4.4.2	Investigations of a chiral CF ₃ -substituted binol-phosphate catalyst	89
4.5	References	92
5	NMR Investigations on the Photocatalytic Water Reduction.....	95
5.1	Introduction	96
5.2	Results and Discussion.....	99
5.2.1	NMR investigations on the model compound (tbbpy)PtCl ₂	99
5.2.2	NMR investigations on the photocatalyst [(tbbpy) ₂ Ru(tpphz)PtCl ₂](PF ₆) ₂	105
5.2.3	NMR investigations under catalytic conditions	108
5.3	Conclusion and Outlook.....	111
5.4	Supporting Information	113
5.5	References	116
6	NMR Investigations on Flavin Photocatalysis.....	117
6.1	Introduction	118
6.2	Results and Discussion.....	119
6.3	Conclusion.....	122
6.4	References	123

7	Development of an NMR-Illumination Unit.....	125
7.1	Introduction	126
7.2	Materials and Methods	126
7.3	Results and Discussion.....	128
7.4	Conclusion.....	129
7.5	References	130
8	Measurements of Transference Numbers for Li⁺ Ion Electrolytes	131
8.1	Abstract	132
8.2	Manuscript.....	133
8.3	Additional experimental findings.....	150
8.3.1	Background and aim of the project	150
8.3.2	Optimization of DOSY parameters	151
8.3.3	Investigations on the electrolyte system LiAlCl ₄ in liquid SO ₂	154
8.3.4	Investigations of electrolyte systems with different pulse sequences	157
8.4	References	160
9	Self-assembled Switchable Supramolecular Container Molecules	163
9.1	Introduction	164
9.2	Results and Discussion.....	165
9.3	Conclusion.....	191
9.4	Supporting Information	193
9.4.1	Experimental Section	193
9.4.2	Size estimation from DOSY and X-ray data	194
9.4.3	Experimental spectra	195
9.5	References	199
10	Summary and Outlook	201
11	Appendix	205
11.1	Curriculum Vitae.....	205
11.2	Publikationen.....	206
11.3	Vorträge und Posterpräsentationen	207

1 Introduction and Outline

Over the last decade the field of organocatalysis, *i.e.* the catalysis of chemical reactions by means of small organic molecules, has grown to a thriving area of general concepts, atypical reactivity and widely useful reactions connected with a tremendous increase of the research activities, as stated 2004 by David MacMillan: “Although the modern era of organocatalysis remains in its infancy, the pace of growth in this field of chemistry has been nothing short of breathtaking.” (in A. Berkessel, H. Gröger, *Asymmetric Organocatalysis*, 2005, Wiley VCH). Since then, various generic activation modes, such as H-bond, counterion, enamine, iminium, SOMO or photoredox catalysis, have been identified and successfully applied for a broad variety of asymmetric reactions. Consequently, organocatalysis is now widely accepted as the third main branch of asymmetric catalysis beside enzymatic catalysis and metal catalysis. Furthermore, organocatalysis is in many cases superior to its predecessors, due to its potential in savings in cost, time, energy and chemical waste and easier experimental procedure, non-toxicity and versatility.

Despite the great number of synthetic applications of organo- and photocatalysis, conformational and mechanistic studies for a better understanding of the underlying origin of stereoselectivity, activation modes and mechanisms are rather scarce. But for a further development and improvement of catalysis in general, this knowledge is highly desirable, since it may allow the optimization of existing methodologies as well as the design of new catalytic systems and activation modes for organo- and photocatalysis.

The aim of this thesis was therefore to elucidate several conformational and mechanistic issues of organo- and photocatalysis. For this purpose, several modern NMR spectroscopic methods were applied to elucidate catalyst conformations and H-bond characteristics, to investigate mechanistic issues and to monitor photocatalytic reactions by means of a self-made NMR illumination unit.

In addition, these NMR techniques, applied for mechanistic and conformational studies on organo- and photocatalysts, can be transferred to the research field of supramolecular chemistry and to more application-oriented issues in electrochemical research, as demonstrated in chapter 8 and 9.

In chapter 2, conformational preferences of organocatalytically active tripeptidic foldamers are elucidated in a combined NMR/MD study. Residual dipolar couplings are thereby applied for the validation of structure coordinates for molecular dynamics simulations. Furthermore, the peptide backbone and sidechain conformations are revealed by NOE and/or RDC-based MD simulations.

In chapter 3, the influence of the configuration of (\pm)-*cis*- β -ACC on the conformational preferences of three tripeptidic foldamers is investigated in a combined NMR/MD study. All three peptides show independent of the β -ACC configuration an unexpected high stability of the backbone conformation, induced by a bifurcated H-bond network and allylic strain. The orientation of the cyclopropane ring and its methoxy substituent can be manipulated by the configuration of β -ACC without changing the peptide conformation. This was related to the different selectivities found in the applications of β -ACC in organocatalysis and medicinal chemistry.

In chapter 4, NMR spectroscopy was used to distinguish between the activation modes of hydrogen bonding and ion pairing in Brønsted acid catalysis. It is shown, that for the activation of imines by a phosphate catalyst ion pairing and hydrogen bonding co-exist and that their ratio can be manipulated readily by simply introducing substituents with different electronic properties. Contrary to previous assumptions, the hydrogen bond strength and the amount of the hydrogen bonded species present are found to be decisive for the catalytic reaction. In addition, the influence of the water content on the complex formation is investigated.

In the field of photocatalytic water reduction, in chapter 5 the formation and relevance of Pt-colloids and the supposed cleavage of a chloride from the photocatalyst $[(\text{tbbpy})_2\text{Ru}(\text{tpphz})\text{PtCl}_2](\text{PF}_6)_2$ under irradiation with visible light is investigated by NMR spectroscopy. The detection methods for the $^3J_{\text{H},195\text{Pt}}$ coupling acting as a sensor for a potential Pt-cleavage are optimized by means of a model compound and subsequently applied for the photocatalyst. It is shown that without the sacrificial electron donor triethylamine no cleavage of the $\text{Cl}^-/\text{PtCl}_2$ unit from the photocatalyst or a Cl^-/OH^- exchange upon irradiation in $\text{CD}_3\text{CN}/\text{D}_2\text{O}$ takes place.

The flavin photocatalysis is investigated in chapter 6 by means of DOSY experiments dealing with the self aggregation of riboflavin tetraacetate RFT and a potential association with para-methoxybenzyl alcohol MBA. In pure acetonitrile RFT is a dimer, whereas in water it is a monomer. These aggregation tendencies are correlated with the solvent dependency of the quantum yield of the photooxidation of MBA with RFT. No hints for an association of RFT and MBA are observed by NMR spectroscopy.

In chapter 7 the development of a glass fiber-based NMR-illumination unit designed for the online monitoring of photocatalytic reactions and additionally first test measurements of the photooxidation of MBA with RFT are described.

In the field of electrochemical research, four different methods for the measurement of cationic transference numbers of several non-aqueous lithium ion electrolytes are compared to each other in chapter 8. Whereas the three electrochemical methods yield transference numbers decreasing with concentration, NMR DOSY measurements show increasing transference numbers with increasing concentration. This discrepancy is explained by effects of ion-ion and ion-solvent interaction. Furthermore, two DOSY pulse sequences are compared to each other.

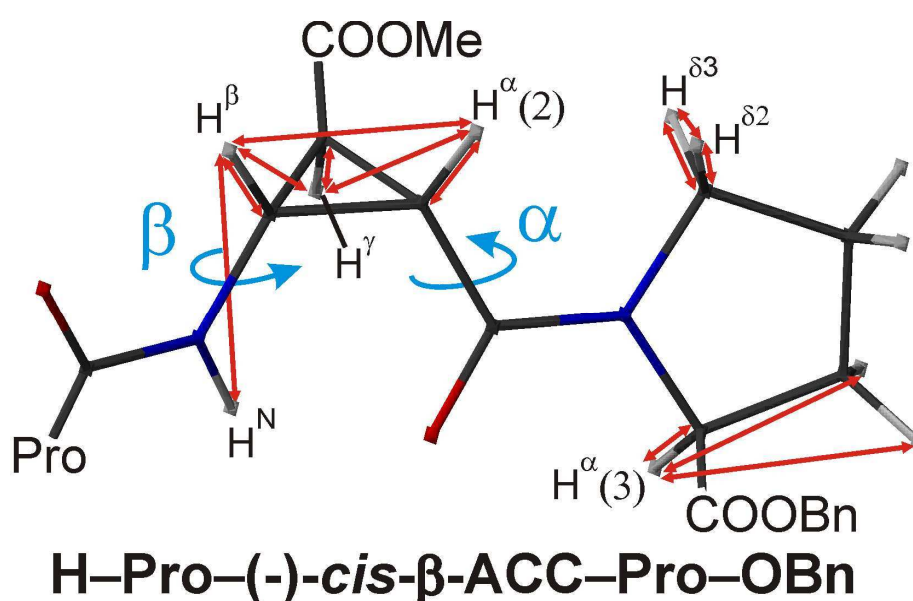
In the field of supramolecular research, a combined solution state NMR and X-ray study about a soluble, self-assembling supramolecular four-state switch with the ability to incorporate guests, composed of $[\text{Cp}^{\text{Bn}}\text{Fe}(\eta^5\text{-P}_5)]$ and CuX ($\text{X} = \text{Cl}, \text{Br}$), is presented in chapter 9. Four different supramolecules are characterized by solution state NMR and three of them by X-ray crystallography. Their solution characteristics, formation pathways, optimal formation conditions and their ability to incorporate guests are described. The manipulation of the solvent mixture delivers a self-assembling reversible supramolecular four-state switch, which even allows the selective incorporation of guests.

2 RDCs in Short Peptidic Foldamers

Communication:

“Residual dipolar couplings in short peptidic Foldamers:

Combined analyses of backbone and side-chain conformations
and evaluation of structure coordinates of rigid unnatural amino acids”



Markus B. Schmid, Matthias Fleischmann, Valerio D’Elia,
Oliver Reiser, Wolfram Gronwald, and Ruth M. Gschwind

ChemBioChem **2009**, *10*, 440–444.

<http://dx.doi.org/10.1002/cbic.200800736>

The syntheses of all peptides studied were performed by Valerio D’Elia. The NMR investigations on **1** and the PRODRG based β -ACC parametrization were accomplished in close collaboration with Markus Schmid, who completed the RDC interpretation and performed the X-Ray based parametrization.

2.1 Abstract

Residual dipolar couplings (RDCs) have been shown to be highly potent structural parameters to determine the configuration of small molecules by NMR, but RDC-supported detailed conformational studies of short open-chain structures have not been reported so far. This study demonstrates that RDCs at natural abundance can provide essential structural information even in the case of short linear peptides with unnatural amino acids. Tripeptidic foldamers, composed of proline and *cis*- β -aminocyclopropanecarboxylic acid (*cis*- β -ACC), which has been successfully incorporated into NPY analogs, integrin ligands, and organocatalysts, are investigated as exemplary systems. An RDC-based approach to select appropriate structures for the force field parametrization of rigid non-standard amino acids is presented. Its relevance is demonstrated by conformational analyses of H-(L)-Pro-(L)-Pro-(-)-*cis*- β -ACC-OBn, for which slight alterations in the proton positions of unnatural amino acids lead to significant deviations in backbone and side-chain conformations. In addition, RDCs in combination with *cis*- β -ACC as a probe for molecular alignment allow to obtain conformational information on the backbone of H-(L)-Pro-(-)-*cis*- β -ACC-(L)-Pro-OBn. In this peptide, RDCs support also the elucidation of preferences of proline side-chain conformations.

2.2 Manuscript

Introduction

Although residual dipolar couplings (RDCs) have been established in the NMR structure determination of biomacromolecules in solution for several years,^[1-2] their potential for the investigation of small molecules has not been fully explored due to difficulties in the evaluation of internal dynamics and conformational averaging. Thus, RDCs have been mostly employed for the determination of configurations in rigid or cyclic compounds^[3-6] or for the structure refinement of cyclic peptides.^[7-8] Only very recently could configurations in more flexible open-chain systems be elucidated.^[9-10] To our knowledge, RDC applications addressing short linear peptides, however, have been restricted to the systematic elucidation of the conformational preferences of individual natural amino acids;^[11-12] neither the conformations of short linear peptides nor the influence or the structure of cyclic unnatural amino acids have been analyzed in detail by RDCs. Since certain unnatural amino acids, for example, β -amino acids, are known to induce strong conformational preferences in peptides, foldamers containing β -amino acids are promising targets for structural investigations supported by RDCs. In particular, the rigid *cis*- β -aminocyclopropanecarboxylic acid^[13] (*cis*- β -ACC) stabilizes even short peptide sequences,^[14] and high activities and selectivities have been found in medicinal chemistry^[15-16] and asymmetric organocatalysis^[17] for *cis*- β -ACC containing peptides. However, the structural analysis of these peptides by NMR and CD methods established for peptides comprised of natural amino acids has been problematic due to difficulties in assigning parameters for the unnatural building blocks and due to a missing body of reference compounds.

To fill this gap, NMR solution studies on tripeptides **1** and **2** (Figure 2.1) are presented here. RDCs were applied as a quality check for the different *cis*- β -ACC parametrizations for molecular dynamics (MD) simulations and to detect preferences in proline side-chain conformations. Furthermore, the use of *cis*- β -ACC as an alignment probe allowed for the analysis of the peptide backbone.

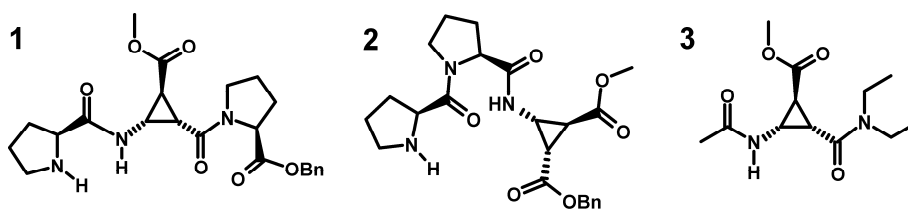


Figure 2.1: H-(L)-Pro- ∇ -(L)-Pro-OBn **1**, H-(L)-Pro-(L)-Pro- ∇ -OBn **2** (for conformational analysis) and Ac- ∇ -NEt₂ **3** (for the parametrization of *cis*- β -ACC); ∇ = (-)-*cis*- β -ACC.

Results and Discussion

RDCs as a quality check for the β -ACC parametrization

In structural studies of small molecules and non-standard amino acids, the appropriate parametrization of these compounds is essential for reliable MD simulations. The hydrogen positions, which are addressed by various NMR-derived restraints, especially influence the results of MD calculations. Since a crystal structure of the enantiomer of **3** (Figure 2.1) was available,^[18] **3** was used as a model compound for **1** and **2** in order to generate a parametrization of *cis*- β -ACC. For this purpose, two sets of coordinates for **3** were prepared, one with the Dundee PRODRG2 server^[19] and the second one from the crystal structure^[18] by a subsequent DFT equilibrium geometry calculation resulting in significantly different hydrogen positions (see the structures in Figure 2.2). As RDCs provide in principle the potential to check the quality of coordinates in rigid molecules, both β -ACC structures were fitted to a set of six experimental RDCs of the rigid β -ACC moiety with the PALES software;^[20-21] these RDCs had been determined from the well-resolved 1D ¹H and ¹H, ¹³C-P.E.HSQC spectra^[22] of samples of **2** in CDCl₃ and in a strained polydimethylsiloxane (PDMS)/CDCl₃ gel.^[23] A comparison of the experimental and the backcalculated RDCs of the two coordinate sets is presented in Figure 2.2.

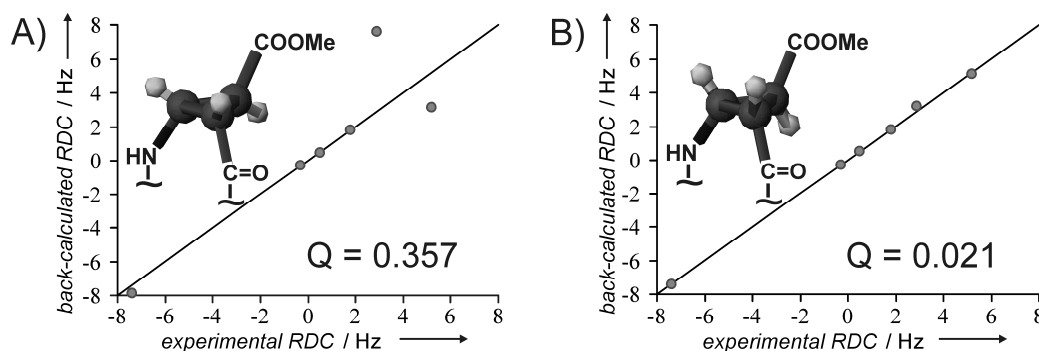


Figure 2.2: Experimental and back-calculated RDCs for *cis*- β -ACC with structure coordinates A) according to the Dundee PRODRG2 server^[19] or B) derived from a crystal structure.^[18] The Q factors allow for the identification of the correct amino acid structure.

Besides demonstrating that the set of experimental data is accurate and the configuration of *cis*- β -ACC is correct, the significantly better Q factor of the X-ray-derived coordinates (Figure 2.2B) indicates their congruence with the actual structure in solution. The coordinate file generated by PRODRG2, on the other hand, can be rejected; in addition to a poor Q factor, a significantly different alignment tensor was calculated, which would lead to the erroneous evaluation of further RDCs. However, the PRODRG2 structure can be improved by an energy minimization calculation, leading to results similar to the crystal structure (see the Supporting Information, chapter 2.3.2).

The impact of such small differences in hydrogen positions on the conformational analyses of short peptides is illustrated by MD calculations on **2** (Figure 2.3). The slightly changed proton coordinates in the two different parametrizations not only lead to an erroneous peptide backbone but also to different proline side-chain conformations. Upon applying the correct parametrization, the most obvious changes occur in the backbone angles Ψ_2 and β (from 57° to 335° and from 243° to 221° , respectively) and in the flip of the side-chain conformation of Pro2 from *down* to *up*. The overall conformational alteration affects significantly the relative position of Pro1 and β -ACC, which is essential for the structural interpretation of the organocatalytic properties of unprotected **2**.^[17] In the structural studies of small molecules such as **2**, it is essential to check whether the experimental NMR parameters originate from one prevalent conformation or are averaged over several coexisting or interconverting conformations. As criteria for the predominant adoption of a well-folded form of short linear peptides, it has been proposed that no NOE restraints are violated and all interproton distances below 3.5 Å that occur in more than half of the calculated structures give rise to observable NOEs.^[14] In addition, the dominant population of a particular conformation can be evidenced experimentally by unusual large or small $^3J_{\text{H,H}}$ values.^[24] Interestingly, in both structures shown in Figure 2.3, the two NOE criteria are fulfilled; this indicates one conformation for **2**. But only with the correct parametrization, does the experimental β angle derived from $^3J_{\text{HN,HB}}$ agree with the calculated structure (see SI, chapter 2.3.2). This example shows impressively that RDCs can be used as a tool to evaluate the correctness of the coordinates of rigid unnatural amino acids in solution, which is a crucial prerequisite for reliable restrained MD simulations, especially for short peptidic foldamers.

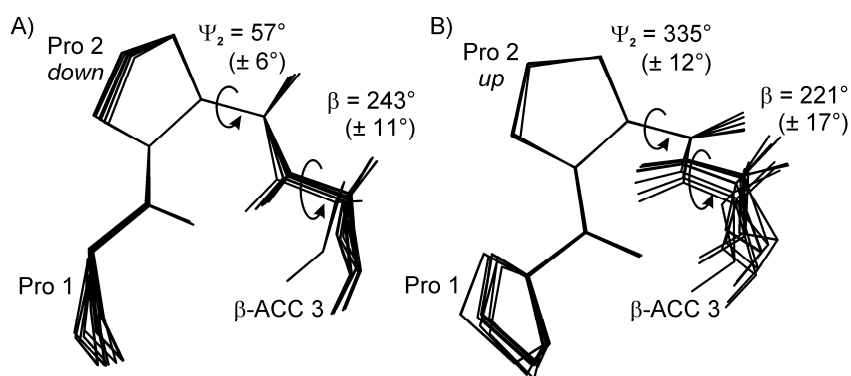


Figure 2.3: Conformational changes of **2** caused by different β -ACC parametrizations derived from A) PRODRG2 or B) an X-ray structure of **3**. In both cases, the 50 structures with the lowest NOE energies are displayed, fitted on the N, C $^\alpha$ and CO of Pro2. The C-terminal benzyl protecting group is omitted for the sake of clarity.

RDCs for the backbone conformation analysis of a β -ACC containing foldamer

Inspired by the excellent performance of *cis*- β -ACC in the RDC back-calculation, we used *cis*- β -ACC as a probe for molecular alignment, and thus exploited the potential of RDCs as a source of conformational information for the structure refinement of short peptidic foldamers. In principle, the reported applications of β -ACC-containing foldamers in medicinal chemistry and organocatalysis suggest that conformational investigations should be performed at room temperature. Since the degradation of **2** into the Pro-Pro-diketopiperazine is observed even at 273 K, **1** was selected for structural investigations with RDCs. At 300 K, the NOE interpretation of **1** was severely hampered by exchange processes involving the amide proton of β -ACC, which impeded NOE interpretation at this prominent position in the NOE network. In this case, RDC data are expected to be particularly valuable, because they allow for the determination of the orientation of vectors in the different amino acids relative to the alignment tensor.

Even in foldamers, linear tripeptides are very likely to show remaining internal dynamics or, even more seriously, several interconverting conformations; these situations would lead to a complex averaging of the experimental NMR parameters, including RDCs. In order to find out if parts of **2** were conformationally restricted enough to reduce the influence of conformational averaging to a minimum, and thus, to allow for RDC interpretation, the conformational stability of **1** was investigated at 240 K, and the resulting structure analyzed according to the NOE and *J* criteria discussed above. The NOE-restrained MD simulations indicated a surprisingly limited conformational flexibility as far as rotations around the backbone angles α and β are concerned (see Figure 2.4A for nomenclature and Figure 2.9 for the calculated structure ensemble). The predominance of the conformation shown in Figure 2.9 at 240 K was revealed by the fulfillment

of all NOE restraints and by observable NOEs for all interproton distances below 3.5 Å. The unexpected stability of the β angle was experimentally confirmed by the unusual $^3J_{\text{HN,HB}}$ ^[24] of 9.69 Hz (see Supporting Information, chapter 2.3.3). At 300 K, small changes in the chemical shifts (≤ 0.07 ppm, except for the amide proton), a qualitatively identical NOE intensity pattern and the slight decrease in the $^3J_{\text{HN,HB}}$ (from 9.69 Hz to 8.89 Hz) showed that this conformation was still preferred and only slightly loosened at higher temperatures. The formation of an intraresidual hydrogen-bond, which is hinted at by IR spectroscopy at room temperature,^[18] corroborates this conformation. On the other hand, the orientations of Pro1 and the benzyl protecting group are less defined. Therefore, only those RDCs solely affected by rotations around the angles α and β (with respect to the alignment probe *cis*- β -ACC) can be interpreted without significant conformational averaging, and thus, were used for a structural refinement of the backbone conformation of **1**.

Based on this structural model of **1** and *cis*- β -ACC as an alignment probe, RDC information was gathered on the angles α and β , which describe the orientation of the adjacent parts of the peptide relative to the probe (Figure 2.4A). For the angle β , $^3D_{\text{HN,HB}}$ was determined from 1D ^1H spectra, and $^1D_{\text{C}\alpha,\text{H}\alpha}$ within Pro3 (from P.E.HSQC spectra) was chosen as the sensor for the rotation around α , as it is the only α -relevant RDC that is practically independent of the proline side-chain conformation. The conformational space to be investigated by RDC analysis was mapped by calculating structures of **1** without any distance restraints. The alignment tensors for these structures were then determined by the six RDCs within the rigid *cis*- β -ACC residue, and the two RDCs relevant for α and β were back-calculated and checked against experimental values. Figure 2.4 displays the results of the relative NOE and RDC evaluation for α and β .

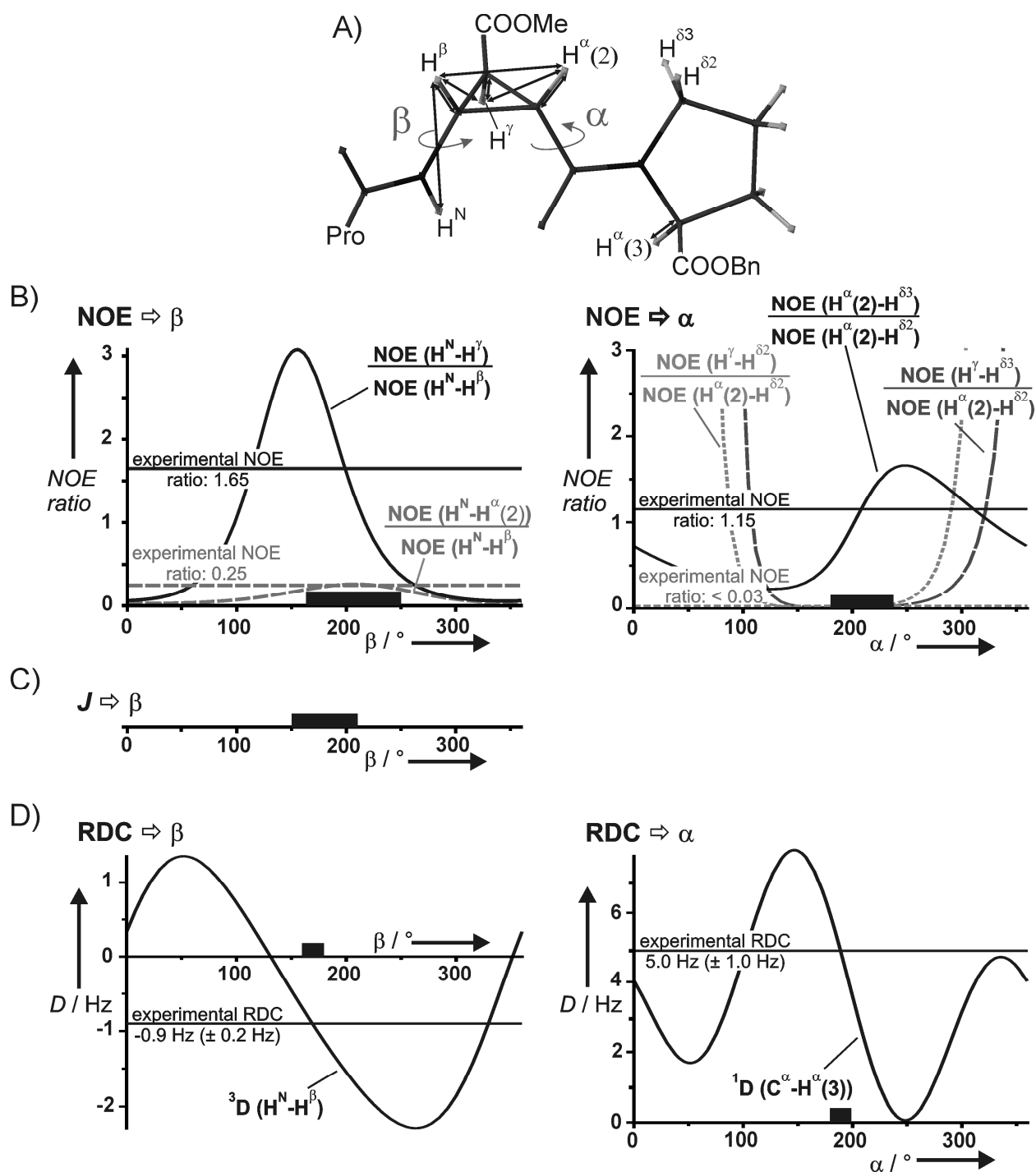


Figure 2.4: A) Conformational information on the angles α and β in **1** derived from B) NOEs, C) $^3J_{HN,HB}$ and D) RDCs. The black bars mark angle regions in agreement with the experimental parameters.

For α and β , the RDC evaluation matches angles of 175° – 200° and 160° – 180° , respectively, which are within the angle ranges derived from the relative NOE intensity pattern (Figure 2.4). In addition, the β angle range determined by RDCs is supported by an estimated Karplus curve for $^3J_{HN,HB}$ (8.89 Hz at 300 K) that indicates an angle of $180 \pm 30^\circ$ (Figure 2.4C; see Supporting Information, chapter 2.3.3, for details). Order parameters, which take remaining

internal dynamics into account, had not been included in the RDC interpretation so far. Therefore, the good agreement of the RDC data with other NMR parameters, which are each dynamically averaged in different ways, can be interpreted as further proof of a considerably stable core conformation of **1** in CDCl_3 at room temperature.

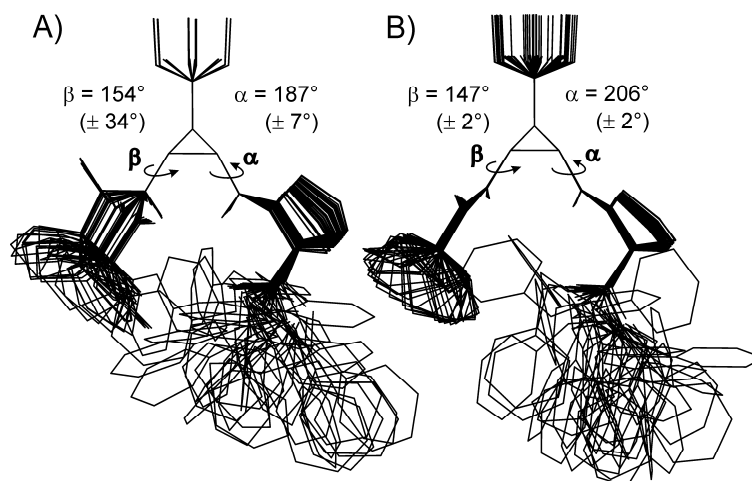


Figure 2.5: Comparison of A) NOE- and B) RDC-derived structures of **1** at room temperature. In both cases, the 40 structures with the lowest energies are presented, which are based on α/β -relevant NOEs or RDCs only.

Focusing on the backbone rotations around α and β , we applied the RDC data in MD simulations with the software system CNS (Crystallography & NMR System).^[25] Our set of eight RDCs (supplemented by the α -relevant $^1D_{\text{C}\delta, \text{H}\delta 2}$, $^1D_{\text{C}\delta, \text{H}\delta 3}$ and $^2D_{\text{H}\delta 2, \text{H}\delta 3}$) were used as the restraints on the basis of the alignment tensor determined for *cis*- β -ACC. For comparison, we quantified the α - and β -relevant NOE contacts, as far as this was possible for the exchange-affected NOEs, and applied them as distance restraints in separate calculations. The resulting structures (presented in Figure 2.5) show similar α and β values and a remarkable correspondence of the entire conformation for both parameter sets. The reduced conformational flexibility of the RDC-derived structures compared to that of the NOE-derived structures can be explained by the limited precision with which the NOEs could be obtained due to exchange contributions; this required the use of relatively large error bounds for NOEs. In contrast, the RDCs could be determined very precisely. This example shows that, even in short linear peptides at natural abundance, conformational information can be derived from RDCs in the case of a conformationally stable compound and the presence of a reliable probe for molecular alignment.

RDCs for the detection of preferred proline side-chain conformations

Besides providing information on the peptide backbone, in principle, RDCs can also be used to gain insight into proline side-chain conformations. In order to cancel the influence of variable backbone conformations on the proline RDCs, separate alignment tensors were calculated for Pro1 and Pro3. As a result, the RDC analysis reflects the averaging of the proline side-chain conformations only and should allow for the detection of preferences. Based on a two-state model assumption for proline conformations (“*up*” and “*down*”, Figure 2.6A),^[26-27] structures of **1** were calculated in which *J* coupling restraints forced the proline residues into one of the two conformations. These structures were used to establish the conformation-dependent correlations of experimental and back-calculated proline RDCs (10 for Pro1 and 6 for Pro3) displayed in Figure 2.6B and C.

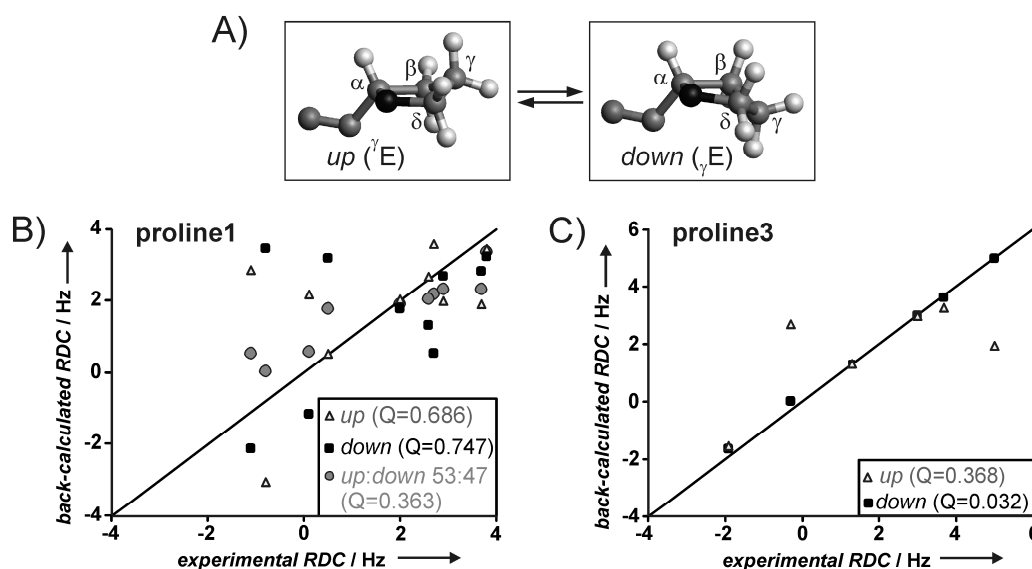


Figure 2.6: A) *Up* and *down* conformations of proline and experimental and back-calculated RDCs for B) Pro1 and C) Pro3.

For Pro3, the excellent match of the down conformation and the experimental RDCs (Figure 2.6C) indicates a distinct preference of this conformation, which is supported by an analysis of scalar coupling constants.^[28] For Pro1 on the other hand, the Q factors are poor for both the *up* and *down* conformations (0.686 and 0.747, respectively, Figure 2.6B). It can be optimized to 0.363 by assuming an equilibrium *up/down* population of 53:47, which is in agreement with the *J* analysis of Pro1.^[28] The significantly larger Q factor of Pro1 compared to that of Pro3 can be explained by the presence of fast internal motion at single sites in Pro1 or the population of other conformations beside *up* and *down*.

Conclusion

In summary, we have presented an RDC-based approach to select appropriate structures for the force field parametrization of rigid non-standard amino acids. Conformational analyses of H-(L)-Pro-(L)-Pro- \blacktriangledown -OBn show that even slight alterations in the proton positions of unnatural amino acids can lead to significant deviations in backbone and side-chain conformations. In the presence of *cis*- β -ACC as a probe for molecular alignment, RDCs allowed us to obtain conformational information on the backbone of the short linear peptide H-(L)-Pro- \blacktriangledown -(L)-Pro-OBn, being especially valuable if the NOE analysis is affected by chemical exchange. In addition, RDCs were employed to detect the preferences of proline side-chain conformations. This study shows that even in the case of short linear peptides with unnatural amino acids, RDCs at natural abundance can provide essential structural information. This example demonstrates that the RDC approach can be expanded to open-chain structures not only in the case of configuration determination, but also in the field of conformational analyses. In the context of β -ACC, RDC-supported conformational studies are expected to help establish the structure activity/selectivity relationships of neuropeptide Y (NPY) analogues, integrin ligands and organocatalysts that have been developed with this amino acid.

2.3 Supporting Information

2.3.1 Experimental Section

Compounds **1** and **2** were synthesized following the published protocol.^[17] NMR spectra were recorded on a Bruker Avance III 600 spectrometer (600.13 MHz) (temperature was controlled by a BVT 3000 unit) and on a Bruker Avance III 600 (600.25 MHz) equipped with a TCI cryoprobe with z-gradient.

Sample concentrations of 40 mM to 140 mM were applied for NMR measurements of **1** at 240 K and 300 K depending on sensitivity requirements of the different spectra, while aggregation in this concentration and temperature range could be excluded by comparison of chemical shifts and by diffusion measurements with convection artifact suppression.^[29] Due to the relatively small size of the investigated molecules and therefore slow NOE build-up a mixing time of 350 ms had to be used in the 2D ^1H , ^1H -NOESY spectra. ^1H , ^{13}C -P.E.HSQC^[22] spectra for the determination of RDCs were measured in CDCl_3 and in a strained PDMS/ CDCl_3 gel^[23] which provided a CDCl_3 line splitting of 20.5 Hz. ^1H , ^1H -NOESY and ^1H , ^{13}C -HSQC-NOESY spectra (due to severe signal overlap) of a 270 mM sample of **2** were recorded in CDCl_3 at 273 K. NMR data were processed and evaluated with Bruker's TOPSPIN 2.1 and the included DAISY program was used for spectra simulation whenever necessary. NOESY spectra were integrated and evaluated with AUREMOL,^[30] its REFINE module was used for full relaxation matrix calculations.

Assignments of proton and carbon resonances of the conformations with Xxx-Pro *trans*-peptide bonds of **1** and **2** were obtained by the use of one- and two-dimensional NMR spectra. ^1H -spectra and ^{13}C -spectra (gated decoupled, power-gated, DEPT-135) in combination with ^1H , ^1H -COSY, ^1H , ^1H -NOESY, ^1H , ^{13}C -HSQC and ^1H , ^{13}C -HMBC allowed for almost complete assignment of all resonances of **1** and **2** (see Table 2.1).

MD simulations were performed with CNS 1.1 (Crystallography & NMR System).^[25] The simulated annealing protocol included a high temperature stage (2,000 steps at 50,000 K of 7.5 fs each) in torsion angle space, an annealing stage to 0 K (2,000 250 K-steps of 7.5 fs each) and a final energy minimization following the conjugate gradient method in ten cycles of 200 steps each.

The unnatural amino acid *cis*- β -ACC was implemented into CNS on the basis of the DFT minimized structures, as discussed in 2.2, and force field parameters were created by the Dundee

The solvent for structure refinement was simulated by a cubic box of 50 Å length filled with 1,000 molecules of chloroform (obtained from VEGA ZZ 2.0.8^[32]), for which periodic boundary conditions were assumed. The CHCl₃ geometry as well as atomic charges were taken from literature data^[33] and force field parameters were generated by XPLO2D.

Calculated structures were visualized and evaluated with MOLMOL 2K.2.^[34]

The chemical structure of the β -ACC molecule is shown, highlighting the Pro 1, Pro 3, and OBn domains. The structure is a complex polypeptide chain with various side chains and functional groups. Key features include:

- Pro 1 domain:** Located on the left, it features a proline ring (Pro 1) with atoms labeled HB1, HB2, HG1, HG2, HD1, HD2, and HT1. It is connected to a carbonyl group (C=O) and a side chain containing NAA, HAB, and HA.
- β -ACC domain:** The central part of the molecule, containing a proline ring (Pro 3) with atoms labeled HD1, HD2, HG1, HG2, HB1, HB2, and HA. It is connected to a carbonyl group (C=O) and a side chain containing OAF, OAH, OAJ, CAI, HAI1, HAI2, HAI3, CAE, CAB, CAC, and CAD.
- OBn domain:** Located on the right, it features a proline ring (Pro 3) with atoms labeled HB1, HB2, HG1, HG2, HD1, HD2, and HE1. It is connected to a carbonyl group (C=O) and a side chain containing OAA, OAH, OAJ, CAI, HAI1, HAI2, HAI3, CAE, CAB, CAC, and CAD.

Figure 2.7: Nomenclature of **1** as used for CNS. The same atom names were used for **2**. Only the primarily populated conformation of **1** (with a *trans* Xxx-Pro peptide bond) is depicted as only this one was investigated in detail.

Resonance assignment of **1** and **2****Table 2.1:** Assignment of proton and carbon resonances of **1** and **2** (major conformation with *trans* peptide bonds only, see Figure 2.7 for atom nomenclature). Chemical shifts were referenced to solvent signals ($\delta(^1\text{H})_{\text{CHCl}_3} = 7.26$ ppm, $\delta(^{13}\text{C})_{\text{CDCl}_3} = 77.16$ ppm).

resonance assignment of 2 (CDCl ₃ , 273 K)				
amino acid	proton	$\delta(^1\text{H})$ / ppm	carbon	$\delta(^{13}\text{C})$ / ppm
Pro 1	HT1	---	C	---
	HA	3.89	CA	58.8
	HB1	2.15	CB	30.1
	HB2	1.8		
	HG1	1.81	CG	26
	HG2	1.73		
	HD1	2.92	CD	47.3
	HD2	3.13		
Pro 2	HA	4.53	C	---
	HB1	1.9	CA	59.9
	HB2	2.19	CB	27.5
	HG1	1.88-1.92	CG	24.7
	HG2			
	HD1	3.47	CD	46.5
	HD2	3.4		
β-ACC	HAB	7.65	CAD	---
	HAB1	3.91	CAB	35.8
	HAC1	2.52	CAC	26.5
	HAE1	2.31	CAE	28.2
	HAI*	3.65	CAG	---
			CAI	52.2
OBn	HB1	5.06; 5.08	CB	66.9
	HB2			
	HD*	7.31	CG	134.8
	HE*	7.33	CD*	127.9
			CE*	128.4
	HZ	7.31-7.32	CZ	128.3

resonance assignment of 1 (CDCl ₃ , 240 K)				
amino acid	proton	$\delta(^1\text{H})$ / ppm	carbon	$\delta(^{13}\text{C})$ / ppm
Pro 1	HT1	---	C	176.2
	HA	3.75	CA	59.9
	HB1	2.09	CB	30.4
	HB2	1.9		
	HG1	1.59	CG	26
	HG2	1.68		
	HD1	2.87	CD	46.8
	HD2	2.74		
β-ACC	HAB	8.97	CAD	166.8
	HAB1	4.18	CAB	36.2
	HAC1	2.61	CAC	25.4
	HAE1	2.46	CAE	27.8
	HAI*	3.67	CAG	171
			CAI	52.4
Pro 3	HA	4.53	C	171.2
	HB1	2.17	CA	58.5
	HB2	2	CB	28.8
	HG1	2.02-2.05	CG	24.3
	HG2			
	HD1	3.65	CD	47.2
	HD2	3.91		
OBn	HB1	5.04; 5.09	CB	66.5
	HB2			
	HD*	7.34	CG	134.8
	HE*	7.36	CD*	127.9
			CE*	128.4
	HZ	7.33	CZ	128.2

resonance assignment of 1 (CDCl ₃ , 298/300 K)				
amino acid	proton	$\delta(^1\text{H})$ / ppm	carbon	$\delta(^{13}\text{C})$ / ppm
Pro 1	HT1	2.08	C	176.4
	HA	3.7	CA	60.8
	HB1	2.07	CB	30.8
	HB2	1.91		
	HG1	1.59	CG	26.2
	HG2	1.69		
	HD1	2.87	CD	47.2
	HD2	2.81		
β-ACC	HAB	8.58	CAD	167.1
	HAB1	4.12	CAB	36.6
	HAC1	2.58	CAC	26.1
	HAE1	2.44	CAE	28
	HAI*	3.69	CAG	171.2
			CAI	52.4
Pro 3	HA	4.55	C	171.6
	HB1	2.17	CA	59.1
	HB2	2	CB	29.3
	HG1	2.01; 2.06	CG	24.7
	HG2			
	HD1	3.65	CD	47.5
	HD2	3.87		
OBn	HB1	5.09; 5.12	CB	66.7
	HB2			
	HD*	7.32	CG	135.7
	HE*	7.34	CD*	128.1
			CE*	128.7
	HZ	7.31	CZ	128.4

2.3.2 Quality check of different *cis*- β -ACC coordinates with RDC data

In order to generate an appropriate β -ACC parametrization for MD simulations, various *cis*- β -ACC coordinate files were generated with the help of the Spartan 06 program package^[35] (Table 2.2). Three different starting structures were used for that purpose: One structure that was directly built within Spartan, a second structure which was generated by the Dundee PRODRG2 server, and a third one by inverting the stereocenters of a crystal structure of the enantiomer of **3**^[18] followed by addition of hydrogen atoms with Spartan. Different equilibrium geometry calculation algorithms were applied to these structures: a molecular mechanics approach (MMFF force field), a semi-empirical calculation (RM1 method) and an *ab initio* calculation (Hartree-Fock with 6-31G* basis set). In addition, density functional theory calculations (B3LYP, 6-31G* basis set) on the crystal structure and its MM minimized offspring were performed. All these structures were fitted to 6 RDCs within the rigid β -ACC moiety with the help of the PALES^[20-21] bestFit module (using singular-value decomposition). The results in terms of alignment tensors and bond and angle parameters as well as quality factors Q are summarized in Figure 2.8 and Table 2.2 (see footnote of Table 2.2 for structure code).

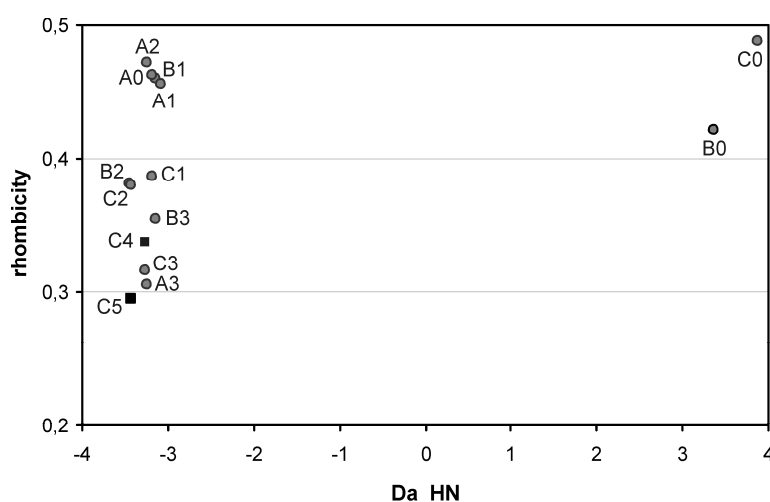


Figure 2.8: Alignment tensors (represented by their normalized axial components and their rhombicities) based on experimental β -ACC RDCs and the 14 different coordinate sets of **3** (see Table 2.2).

It can be concluded that B0 and C0 (the PRODRG structure and the crystal structure to which hydrogen atoms had been added simply by Spartan) yielded insufficient Q factors and erroneous alignment tensors due to the wrong hydrogen positions (decisive parameters are highlighted in Table 2.2). All the other equilibrium geometry calculation methods, however, resulted in acceptable Q factors and both similar parameters and alignment tensors within the

range of experimental errors. The two geometries obtained by the DFT calculations were used as the basis for the applied CNS parametrization of *cis*- β -ACC.

Table 2.2: Comparison of geometric parameters of the generated β -ACC coordinates of **1** and their RDC evaluation with PALES.

bond lengths / Å			A0	A1	A2	A3	B0	B1	B2	B3	C0	C1	C2	C3	C4	C5
CAB	CAC		1.56	1.51	1.53	1.50	1.56	1.51	1.53	1.50	1.47	1.51	1.53	1.50	1.52	1.52
CAB	CAE		1.56	1.52	1.52	1.51	1.57	1.52	1.53	1.52	1.54	1.52	1.53	1.51	1.52	1.52
CAC	CAE		1.56	1.51	1.53	1.50	1.56	1.51	1.53	1.50	1.51	1.51	1.53	1.49	1.54	1.50
CAB	NAA		1.47	1.44	1.44	1.42	1.51	1.43	1.43	1.42	1.44	1.44	1.43	1.42	1.42	1.43
CAC	CAD		1.53	1.48	1.50	1.50	1.58	1.49	1.49	1.50	1.48	1.49	1.50	1.50	1.50	1.51
CAE	CAG		1.53	1.49	1.49	1.50	1.56	1.48	1.48	1.49	1.50	1.48	1.48	1.49	1.49	1.49
CAB	HAB1		1.10	1.09	1.11	1.07	1.00	1.09	1.11	1.07	1.10	1.09	1.11	1.07	1.08	1.08
CAC	HAC1		1.10	1.09	1.11	1.07	1.00	1.09	1.11	1.07	1.10	1.09	1.10	1.07	1.08	1.08
CAE	HAE1		1.10	1.09	1.11	1.07	1.00	1.09	1.11	1.07	1.10	1.09	1.11	1.07	1.09	1.09
NAA	HAB		1.01	1.01	1.01	1.00	1.00	1.02	1.02	1.00	1.01	1.02	1.02	1.00	1.02	1.01

bond angles / °			A0	A1	A2	A3	B0	B1	B2	B3	C0	C1	C2	C3	C4	C5
CAB	CAC	CAE	60.0	59.8	60.1	60.0	59.8	59.5	60.0	59.7	60.3	59.7	60.0	59.3	59.5	59.2
CAC	CAE	CAB	60.0	59.8	60.2	59.5	60.0	60.1	60.2	59.3	57.5	60.0	60.2	60.1	59.5	60.2
CAE	CAB	CAC	60.0	60.4	59.7	60.6	60.2	60.4	59.8	61.0	62.2	60.3	59.9	60.6	61.0	60.6
NAA	CAB	CAC	117.3	121.7	118.1	121.9	121.2	121.0	119.8	112.1	118.8	121.5	118.8	121.5	121.3	120.8
NAA	CAB	CAE	117.3	121.1	118.2	121.0	121.3	121.5	117.7	121.2	116.3	121.0	117.2	118.7	120.5	119.2
CAD	CAC	CAB	117.3	121.9	119.2	121.0	122.7	122.0	118.4	120.6	118.2	120.2	117.4	118.0	118.5	117.1
CAD	CAC	CAE	117.3	118.6	117.1	117.3	121.7	118.4	117.1	116.9	119.1	119.5	117.0	116.4	115.8	115.8
CAG	CAE	CAB	117.3	120.9	116.9	118.5	122.3	119.7	116.1	118.1	123.3	119.4	118.9	120.5	120.6	120.7
CAG	CAE	CAC	117.3	117.5	116.0	117.2	121.4	119.6	116.1	117.2	119.9	120.5	119.3	120.6	120.9	121.0
HAB1	CAB	CAC	117.3	116.6	118.9	114.8	135.0	116.1	116.9	115.0	135.1	116.2	117.7	115.2	116.6	115.5
HAB1	CAB	CAE	117.3	116.7	119.1	115.7	134.9	117.0	118.5	115.6	133.1	116.7	119.1	117.4	117.0	117.5
HAC1	CAC	CAB	117.3	116.8	118.8	113.8	134.6	114.0	117.6	113.6	135.3	116.9	119.1	115.5	115.1	115.6
HAC1	CAC	CAE	117.3	115.4	118.5	113.6	135.6	118.5	117.6	114.2	134.5	115.8	117.5	116.4	114.7	116.6
HAE1	CAE	CAB	117.3	113.9	118.2	114.9	134.6	115.9	119.2	116.6	134.6	117.0	120.4	117.6	116.2	117.4
HAE1	CAE	CAC	117.3	118.6	119.6	115.7	135.4	117.1	120.4	116.7	137.6	117.6	119.0	115.4	115.3	114.2
HAB1	CAB	NAA	116.0	111.7	113.1	113.3	88.4	112.0	113.9	112.7	93.0	112.1	113.9	113.6	111.9	113.5
HAC1	CAC	CAD	116.0	113.8	113.3	118.0	87.3	114.0	115.2	118.4	91.7	114.2	114.9	118.1	119.2	118.8
HAE1	CAE	CAG	116.0	115.2	115.1	118.0	87.7	114.1	114.5	116.7	88.1	112.8	110.9	112.9	113.9	113.4

PALES-output			A0	A1	A2	A3	B0	B1	B2	B3	C0	C1	C2	C3	C4	C5
Q RDC_RMS			0.054	0.098	0.081	0.036	0.357	0.039	0.066	0.058	0.310	0.062	0.057	0.007	0.021	0.036
Da_HN			-3.18	-3.07	-3.25	-3.23	3.37	-3.13	-3.44	-3.14	3.87	-3.19	-3.42	-3.27	-3.27	-3.43
rhombicity			0.46	0.46	0.47	0.30	0.42	0.46	0.38	0.35	0.49	0.39	0.38	0.32	0.34	0.29

Structure code:

A	structure built within Spartan		
B	PRODRG structure	0	starting structure
C	crystal structure	1	molecular mechanics: MMFF
		2	semi-empirical: RM1
C4	DFT: B3LYP, 6-31G*, starting from C0	3	Hartree-Fock: 6-31G*
C5	DFT: B3LYP, 6-31G*, starting from C1		

2.3.3 Structure investigation of **1**

Structure investigations of **1** at 240 K based on NOEs:

28 negative NOE contacts (spin diffusion limit), detected in 2D ^1H , ^1H -NOESY (350 ms mixing time) spectra at 240 K, were used as restraints in MD simulations. At first, relatively loose distance restraints were used to restrict the available conformational space, employing uniform upper and lower bounds of 0.500 nm and 0.175 nm, respectively. Using the standard simulated annealing protocol, described in chapter 2.3.1, 100 structures were calculated. Of these, 5 structures with low total and NOE energies were selected as a representative set for further analysis. Each member of this ensemble together with the NOESY cross peak volumes (determined with AUREMOL) was used as input for the full relaxation matrix calculation (with the REFINE module (to be published) included in AUREMOL) in order to take spin diffusion effects into account. The refined sets of distance restraints were then applied for the next round of structure calculations. In total 5 rounds of structure calculations were performed until convergence of both distance restraints and calculated structures was reached. Solvent refined structures were obtained by subsequent refinement employing a chloroform box with periodic boundary conditions. Figure 2.9 shows the obtained structure ensemble.

NOE derived structures in chloroform (240 K)

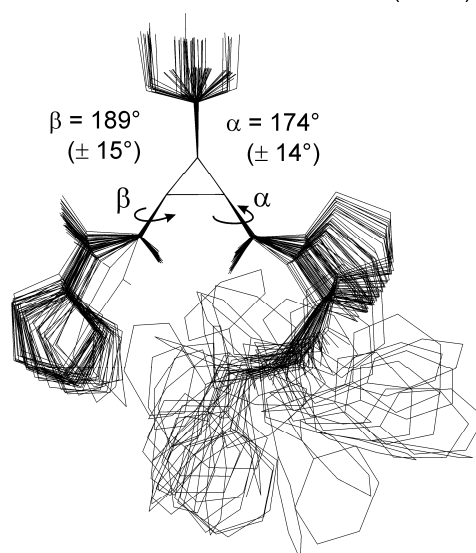


Figure 2.9: Ensemble of 50 structures refined in a chloroform box with 28 NOE distance restraints at 240 K derived from full relaxation matrix calculations.

The range of the β angle populated by the structure ensemble is in agreement with the large J coupling between the amide proton and the β -proton of *cis*- β -ACC (9.69 Hz at 240 K). As no Karplus curve has become available for *cis*- β -ACC so far, the quantum mechanically calculated Karplus curve for **4**^[36] was compared to the one calculated for **5** by an empirically generalized Karplus equation.^[37]

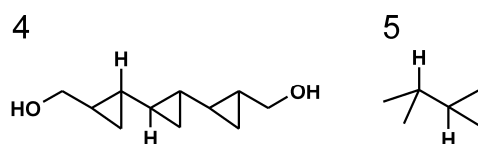


Figure 2.10: Model compounds for the calculation of the Karplus curve.

Thus, it was concluded that the cyclopropane ring scales down the scalar coupling constant in comparison to aliphatic chains as substituents. This was transferred onto the well-known Karplus curve for $^3J_{\text{HN,H}\alpha}$ of natural α -amino acids.^[38] Hence, the observed J coupling of 9.69 Hz was interpreted in terms of a population of β values of $180^\circ \pm 30^\circ$ (Figure 2.4C).

Structure investigation of **1** at 300 K based on NOEs:

At 300 K, only four NOEs carrying quantifiable α - and β -relevant structural information could be identified (HAC1 - HD*(Pro3) for α and HAB - HAC1 as well as HAB - HAE1 for β). The quantification of this NOE information was additionally hampered by chemical exchange processes involving the amide proton. Therefore, no global calibration of NOE intensities was possible at 300 K and the REFINE module of AUREMOL could not be applied for spin diffusion corrections either.

When trying to translate relative NOE intensities relevant for α directly into angular information as shown in Figure 2.4B (right), proline side chain conformations become important as they influence interatomic distances, too. In order to take this into account, a two-state approximation was made for Pro3 (the two conformations of low energy are usually referred to as “*up*” and “*down*”)^[39] and the population of these two conformations was estimated to be approximately 30 % : 70 % *up* : *down* with the help of J couplings.^[28] This ratio was used for the theoretical calculation of NOE intensities (Figure 2.4B, it was also used for Figure 2.4D) which included the assumption that the populations of α and proline side chain conformations are independent.

In order to additionally obtain upper limit distance restraints for MD simulations, the structurally relevant four NOEs that carry conformational information about the angles α and β were quantified according to equation (2.1): Two β -relevant contacts involving the amide proton were calibrated to the NOE HAB-HAB1 ($r_{\text{ref}} = 3.0 \text{ \AA}$) whose distance cannot exceed 3 \AA , so that the applied restraints represent upper limits on any account. Two further restraints, meaningful for α , were calibrated to the geminal peak of the δ -protons of Pro3. The upper limit of all these restraints was extended to $1.07 \cdot r_{\text{ref}}$ ($\approx 1.5 \cdot \text{NOE}_{\text{ref}}/\text{NOE}_{\text{XY}}$) in order to concede spin diffusion influences and shortcomings in NOE integration. The generated structure ensemble is displayed in Figure 2.1.

$$r_{xy} = r_{\text{ref}} \cdot \left(\frac{\text{NOE}_{\text{ref}}}{\text{NOE}_{xy}} \right)^{\frac{1}{6}} \quad (2.1)$$

Structure investigation of **1** at 298 K based on RDCs:

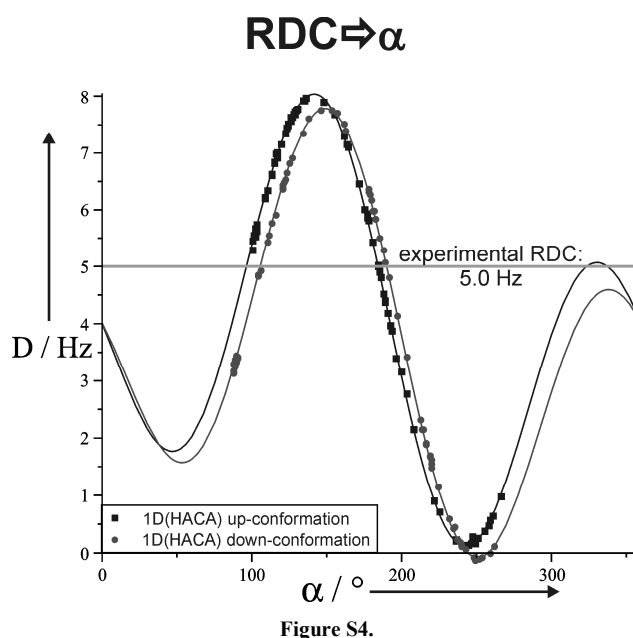
A second set of structures was calculated employing residual dipolar couplings (RDCs) as conformational restraints. 23 RDCs could be determined experimentally from well-resolved 1D proton spectra and P.E.HSQC spectra at 298 K. They are summarized together with their estimated errors in Table 2.3. However, only 8 of them (highlighted in Table 2.3) were suited for interpretation as all the others were heavily influenced by internal dynamics.

Experimental errors of 0.2 Hz were assumed for $^3D_{\text{HH}}$ determined from multiplet analysis of 1D proton spectra. For $^1D_{\text{CH}}$ from P.E.HSQC spectra, the error was estimated to be 1 Hz in case the RDC could be extracted directly from peak splitting in $\omega 2$ and 2 Hz in case the multiplets in $\omega 2$ had to be simulated with DAISY due to higher order influences. Errors in $^2D_{\text{HH}}$ from the peak tilt in P.E.HSQC spectra were estimated dependent on the peak quality as 0.4 Hz or 0.7 Hz. These errors were also used for the alignment tensor determination and Q factor calculation with PALES.

Concerning the angle α , the RDCs $^2D_{\text{H}\delta 2, \text{H}\delta 3}$, $^1D_{\text{C}\delta, \text{H}\delta 2}$, $^1D_{\text{C}\delta, \text{H}\delta 3}$ and $^1D_{\text{C}\alpha, \text{H}\alpha}$ beared conformational information, but in principle they all depend on the proline side chain conformation which impeded their straightforward interpretation. However, $^1D_{\text{C}\alpha, \text{H}\alpha}$ showed almost no dependence on the proline side chain conformation (Figure 2.11) and was therefore suited to extract information on α .

Table 2.3: Experimentally determined residual dipolar couplings.

			D / Hz	ΔD / Hz	source	
Pro1	$^1D_{CH}$	CA	HA	0,1	1,0	P.E.HSQC
		CB	HB1	0,5	1,0	P.E.HSQC
			HB2	2,7	1,0	P.E.HSQC
		CG	HG1	2,6	1,0	P.E.HSQC
			HG2	3,7	1,0	P.E.HSQC
		CD	HD1	-0,8	1,0	P.E.HSQC
			HD2	-1,1	1,0	P.E.HSQC
	$^2D_{HH}$	HB1	HB2	2,9	0,4	P.E.HSQC
		HG1	HG2	3,8	0,4	P.E.HSQC
		HD1	HD2	2,0	0,4	P.E.HSQC
β -ACC	$^1D_{CH}$	CAB	HAB1	-7,4	1,0	P.E.HSQC
		CAC	HAC1	5,2	2,0	P.E.HSQC
		CAE	HAE1	2,9	2,0	P.E.HSQC
	$^3D_{HH}$	HAB	HAB1	-0,9	0,2	1D- 1H
		HAB1	HAC1	-0,3	0,2	1D- 1H
		HAB1	HAE1	0,5	0,2	1D- 1H
		HAC1	HAE1	1,8	0,2	1D- 1H
		CA	HA	5,0	1,0	P.E.HSQC
Pro3	$^1D_{CH}$	CD	HD1	-1,9	1,0	P.E.HSQC
			HD2	-0,3	1,0	P.E.HSQC
	$^2D_{HH}$	HD1	HD2	3,7	0,7	P.E.HSQC
	$^3D_{HH}$	HA	HB1	3,0	0,2	1D- 1H
			HB2	1,3	0,2	1D- 1H

**Figure 2.11:** $^1D_{C\alpha,H\alpha}$ shows almost no dependence on the side chain conformation of Pro3 (a ratio of 30:70 up:down was used for Figure 2.4D).

For the use of RDCs as CNS restraints, the alignment tensor defined for the *cis*- β -ACC residue was applied. As the “axial” input in CNS is dependent on D_{\max} , i.e. on the internuclear distance, three different scaling factors for the “axial” value of $^3D_{\text{HN,H}\beta}$ (the only applied RDC for which the distance cannot be assumed to be fixed) were used which were supposed to cover the available distance range. However, the structures of low energy generated with these three different scaling factors were identical, resulting in the 40 structures (out of 300) that are displayed in Figure 2.5B.

2.3.4 Structure investigation of 2

54 positive NOE contacts (extreme narrowing limit) detected in $^1\text{H}, ^1\text{H}$ -NOESY (350 ms mixing time) spectra at 273 K were used as restraints in MD simulations employing a procedure analogue to **1** (chapter 2.3.3). Because of similar chemical shifts of some protons and therefore ambiguous assignment of some NOESY peaks, a $^1\text{H}, ^{13}\text{C}$ -HSQC-NOESY was measured. Nevertheless, eight NOESY contacts remained ambiguous and one twofold ambiguous. All NOESY contacts to the aromatic protons have been included only qualitatively with uniform upper and lower bounds of 0.500 nm and 0.175 nm, respectively. Of the 54 NOE contacts, four had to be replaced by corresponding signals from other NOESY spectra because of poor peak quality. These peaks were checked carefully and their upper and lower bounds were extended by 0.020 nm.

The relatively high number of restraints for such a small peptide and especially the high number of long range contacts (Figure 2.12) leads to very well defined final structures (see Figure 2.3).

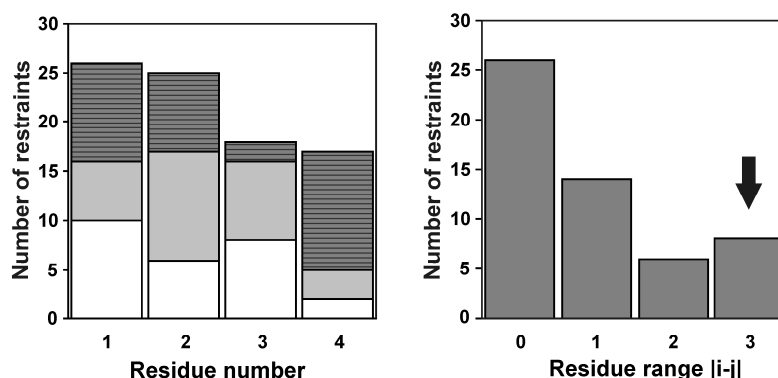


Figure 2.12: Distance restraints of **2**. Left: For each residue white = intraresidual; pale grey = $i+|i+1|$; dark grey = long range restraints. Right: Restraints for the whole molecule vs. the distance between the interacting residues.

The calculated structures of **2** already converged after two cycles of structure calculations (Figure 2.13). This could be interpreted, in addition to the high number of restraints, in terms of a very good reliability of the calculated structures.

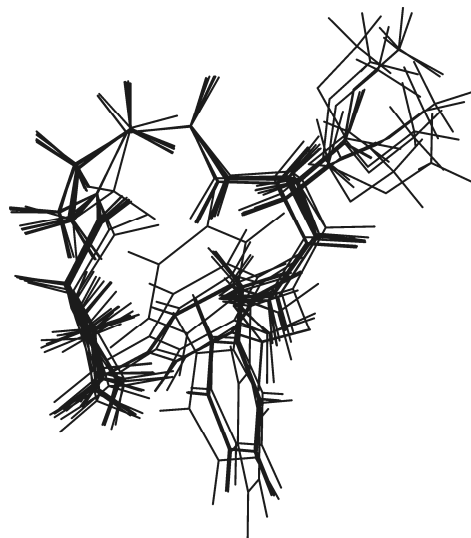


Figure 2.13: Ensemble of the lowest energy structures of **2** for each step in the spin diffusion cycle. The structures are self-consistent.

Validation of the MD calculations for **2**:

Small chemical shift changes ($\Delta\delta(300\text{ K}-240\text{ K}) < 0.72\text{ ppm}$) showed that this conformation was still preferred at higher temperatures.

Analogously to **1**, the range of the β angle populated by the structure ensemble of **2** ($221^\circ \pm 17^\circ$) was in very good agreement with the J coupling between the amide proton and the β -proton of *cis*- β -ACC (6.63 Hz at 273 K), which indicated β values between $225^\circ \pm 15^\circ$ (following the estimation procedure described in chapter 2.3.3).

All distances below 3.5 Å that occurred in more than the half low-energy CNS structures give rise to cross peaks in the NOESY spectra.

Table 2.4: All H-H distances below 3.5 Å in the calculated structures of **2**.

H-H-distances in calculated structures below 3.5 Å						NOESY cross peaks	used as distance restraints
1	PRO	HA	2	PRO	HD1	yes	yes
1	PRO	HA	2	PRO	HD2	yes	yes
1	PRO	HB1	2	PRO	HD1	yes	yes
1	PRO	HB1	2	PRO	HD2	yes	yes
1	PRO	HB1	4	BZA	HD2	yes	yes
1	PRO	HB2	2	PRO	HD1	yes	yes
1	PRO	HB2	2	PRO	HD2	yes	yes
1	PRO	HB2	3	β-ACC	HAB	yes	yes
1	PRO	HB2	4	BZA	HB1	yes	yes
1	PRO	HB2	4	BZA	HB2	yes	yes
1	PRO	HB2	4	BZA	HD2	yes	yes
1	PRO	HB2	4	BZA	HD1	yes	yes
1	PRO	HB2	4	BZA	HE2	yes	yes
1	PRO	HG2	3	β-ACC	HAB	yes	yes
1	PRO	HG2	4	BZA	HB1	yes	yes
1	PRO	HG2	4	BZA	HB2	yes	yes
1	PRO	HG2	4	BZA	HD2	yes	yes
2	PRO	HB2	3	β-ACC	HAB	yes	yes
2	PRO	HB2	4	BZA	HB1	t1 noise	---
2	PRO	HB2	4	BZA	HD1	very small	---
2	PRO	HB1	4	BZA	HE1	yes	yes
2	PRO	HG2	4	BZA	HD1	yes	yes
2	PRO	HG2	4	BZA	HE1	yes	yes
2	PRO	HG2	4	BZA	HZ	yes	yes
2	PRO	HD2	3	β-ACC	HAB	yes	yes
2	PRO	HD2	4	BZA	HB1	yes	yes
2	PRO	HD2	4	BZA	HD1	yes	yes
2	PRO	HD2	4	BZA	HE1	overlap	---
2	PRO	HD2	4	BZA	HZ	yes	yes
3	β-ACC	HAB	4	BZA	HB1	small	---
3	β-ACC	HAB	4	BZA	HB2	small	---
3	β-ACC	HAB	4	BZA	HD1	near diag.	---
3	β-ACC	HAB1	4	BZA	HB2	t1 noise	---
3	β-ACC	HAC1	4	BZA	HB2	yes	yes
3	β-ACC	HAC1	4	BZA	HB1	yes	c

2.3.5 Statistical information on the calculated structures of 1 and 2

Table 2.5: Statistical information on the calculated structure ensembles.

	Figure 2.3B	Figure 2.9	Figure 2.5A	Figure 2.5B
number of selected structures	50	50	40	40
number of restraints (NOE/RDC, respectively)	54	28	4	11
rmsd (heavy atoms without OBn residue) ^[a] / Å	0.39 ± 0.27	0.61 ± 0.24	0.52 ± 0.20 ^[a]	0.31 ± 0.14 ^[a]
E(NOE/RDC) / kJ mol ⁻¹	2.0 ± 0.1	1.4 ± 1.8	< 1	< 1
E(total) / kJ mol ⁻¹	39.2 ± 0.1	-153.0 ± 11.3	12.0 ± 0.2	19.7 ± 2.6

[a] only those heavy atoms being directly affected by the applied restraints were concerned for rmsd calculation.

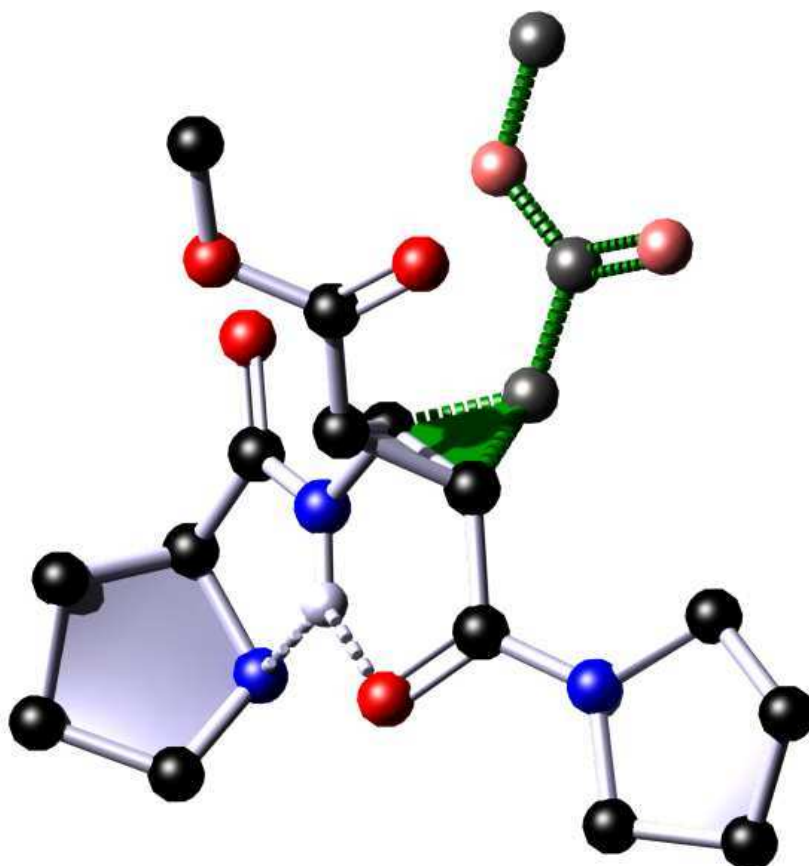
2.4 References

- [1] J. H. Prestegard, C. M. Bougault, A. I. Kishore, *Chem. Rev.* **2004**, *1004*, 3519-3540.
- [2] B. Simon, M. Sattler, *Angew. Chem. Int. Ed.* **2002**, *41*, 437-440.
- [3] C. Farès, J. Hassfeld, D. Menche, T. Carlomagno, *Angew. Chem. Int. Ed.* **2008**, *47*, 3722-3726.
- [4] C. M. Thiele, *Concepts in Magnetic Resonance Part A* **2007**, *30A*, 65-80.
- [5] C. M. Thiele, S. Berger, *Org. Lett.* **2003**, *5*, 705-708.
- [6] C. M. Thiele, A. Marx, R. Berger, J. Fischer, M. Biel, A. Giannis, *Angew. Chem. Int. Ed.* **2006**, *45*, 4455-4460.
- [7] J. Klages, C. Neubauer, M. Coles, H. Kessler, B. Luy, *ChemBioChem* **2005**, *6*, 1672-1678.
- [8] U. M. Reinscheid, J. Farjon, M. Radzom, P. Haberz, A. Zeeck, M. Blackledge, C. Griesinger, *ChemBioChem* **2006**, *7*, 287-296.
- [9] A. Schuetz, J. Junker, A. Leonov, O. F. Lange, T. F. Molinski, C. Griesinger, *J. Am. Chem. Soc.* **2007**, *129*, 15114-15115.
- [10] A. Schuetz, T. Murakami, N. Takada, J. Junker, M. Hashimoto, C. Griesinger, *Angew. Chem. Int. Ed.* **2008**, *47*, 2032-2034.
- [11] S. A. Dames, R. Aregger, N. Vajpai, P. Bernado, M. Blackledge, S. Grzesiek, *J. Am. Chem. Soc.* **2006**, *128*, 13508-13514.
- [12] S. Ohnishi, D. Shortle, *Proteins: Structure, Function and Genetics* **2003**, *50*, 546-551.
- [13] R. Beumer, C. Bubert, C. Cabrele, O. Vielhauer, M. Pietsch, O. Reiser, *J. Org. Chem.* **2000**, *65*, 8960-8969.
- [14] S. De Pol, C. Zorn, C. D. Klein, O. Zerbe, O. Reiser, *Angew. Chem. Int. Ed.* **2004**, *43*, 511-514.
- [15] N. Koglin, C. Zorn, R. Beumer, C. Cabrele, C. Bubert, N. Sewald, O. Reiser, A. G. Beck-Sickinger, *Angew. Chem. Int. Ed.* **2003**, *42*, 202-205.
- [16] S. Urman, K. Gaus, Y. Yang, U. Strijowski, N. Sewald, S. DePol, O. Reiser, *Angew. Chem. Int. Ed.* **2007**, *46*, 3976-3978.
- [17] V. D'Elia, H. Zwicknagl, O. Reiser, *J. Org. Chem.* **2008**, *73*, 3262-3265.
- [18] C. Zorn, PhD thesis, University of Regensburg (Regensburg (Germany)), **2001**.
- [19] A. W. Schüttelkopf, D. M. F. van Aalten, *Acta Crystallographica* **2004**, *D60*, 1355.
- [20] M. Zweckstetter, A. Bax, *J. Am. Chem. Soc.* **2000**, *122*, 3791-3792.
- [21] M. Zweckstetter, *Nat. Protocols* **2008**, *3*, 679-690.
- [22] P. Tzvetkova, S. Simova, B. Luy, *J. Magn. Reson.* **2007**, *186*, 193-200.
- [23] J. C. Freudenberger, P. Spiteller, R. Bauer, H. Kessler, B. Luy, *J. Am. Chem. Soc.* **2004**, *126*, 14690-14691.
- [24] H. J. Dyson, P. E. Wright, *Annu. Rev. Biophys. Biophys. Chem.* **1991**, *20*, 519-538.
- [25] A. T. Brünger, P. D. Adams, G. M. Clore, W. L. DeLano, P. Gros, R. W. Grosse-Kunstleve, J.-S. Jiang, J. Kuszewski, M. Nilges, N. S. Pannu, R. J. Read, L. M. Rice, T. Simonson, G. L. Warren, *Acta Crystallogr., Sect. D* **1998**, *54*, 905-921.
- [26] M. Cai, Y. Huang, J. Liu, R. Krishnamoorthi, *J. Biomol. NMR* **1995**, *6*, 123-128.
- [27] Z. L. Madi, C. Griesinger, R. R. Ernst, *J. Am. Chem. Soc.* **1990**, *112*, 2908-2914.
- [28] M. Schmid, Diploma thesis, University of Regensburg (Germany) **2007**.
- [29] A. Jerschow, N. Müller, *J. Magn. Reson.* **1997**, *125*, 372-375.
- [30] W. Gronwald, H. R. Kalbitzer, *Progr. in NMR Spectr.* **2004**, *44*, 33-96.
- [31] G. J. Kleywegt, K. Henrick, E. J. Dodson, D. M. F. van Aalten, *Structure* **2003**, *11*, 1051-1059.
- [32] A. Pedretti, L. Villa, G. Vistoli, *J. Comp. Aid. Mol. Des.* **2004**, *18*, 167.
- [33] M. E. Martín, A. Muñoz Losa, I. F. Galván, M. A. Aguilar, *THEOCHEM* **2006**, *775*, 81-86.
- [34] R. Koradi, M. Billeter, K. Wüthrich, *J. Mol. Graphics* **1996**, *14*, 51-56.
- [35] <http://www.wavefun.com>.
- [36] A. G. M. Barrett, R. A. James, G. E. Morton, P. A. Procopiou, C. Boehme, A. de Meijere, C. Griesinger, U. M. Reinscheid, *J. Org. Chem.* **2006**, *71*, 2756-2759.
- [37] C. A. G. Haasnoot, F. A. A. M. de Leeuw, C. Altona, *Tetrahedron* **1980**, *36*, 2783.
- [38] V. F. Bystrov, *Progress in NMR Spectroscopy* **1976**, *10*, 41-81.
- [39] G. N. Ramachandran, A. V. Lakshminarayanan, R. Balasubramanian, G. Tegoni, *Biochimica et Biophysica Acta (BBA) - Protein Structure* **1970**, *221*, 165-181.

3 Foldamers with Tunable Orientation of the Steric Shielding

Full Paper:

“Tripeptides with (\pm)- β -ACC: Foldamers with tunable orientation of the steric shielding”



Matthias Fleischmann, Markus Schmid, Valerio D’Elia,
Oliver Reiser, Ruth M. Gschwind

ChemBioChem **2011**, to be submitted.

The synthesis of the peptides was performed by V. D’Elia
and the enamine detection was performed by M. Schmid.

3.1 Abstract

Foldamers containing the unnatural amino acids (\pm)-*cis*- β -aminocyclopropane carboxylic acids ((\pm)-*cis*- β -ACC) often provide high activities and selectivities in organocatalytic and pharmaceutical applications. There, the configuration of the β -ACC was found to be decisive, however, a direct structural impact has not yet been reported so far. Therefore, in this NMR and MD study the influence of either (+) or (-) *cis*- β -ACC on the conformational preferences of three tripeptidic foldamers composed of one β -ACC and proline and/or hydroxyproline-derived residues was investigated. In all three peptides and independent of the β -ACC configuration an unexpected high conformational stability of the backbone was detected, stabilized by a bifurcated H-bond network and allylic strain. Therefore, β -ACC provides the ability to manipulate the orientation of the cyclopropane ring and its methoxy substituent by the configuration of β -ACC without changing the peptide conformation. This may explain the different selectivities found in the applications of β -ACC in organocatalysis and medicinal chemistry and allow for further improved selectivities. In addition, for the first time the detection of a peptidic enamine in organocatalytic aldol reactions is reported.

3.2 Manuscript

Introduction

In biological systems and organocatalysis, specific conformations of peptides often provide high activities and selectivities.^[1] Therefore, the development of foldamers,^[2] e.g. of oligopeptides with stable conformations in solution, is an active research field in medicinal chemistry and organocatalysis.^[3-4] Especially, unnatural amino acids such as β -amino acids, were found to induce strong conformational preferences in peptides. Sometimes these foldamers show promisingly high activities and selectivities in pharmaceutical or organocatalytic applications, as for example reported for the unnatural amino acid (\pm)-*cis*- β -aminocyclopropane carboxylic acid ((\pm)-*cis*- β -ACC).^[5] In the field of medicinal chemistry oligopeptides containing β -ACC provide extremely high selectivities for the NPY Y₁ receptor,^[6] which belong to the pharmaceutical very important class of GPCR receptor proteins, and are active as integrin ligands.^[7] Additionally, in organocatalytic applications tripeptides with β -ACC and proline residues showed organocatalytic activities in inter- and intramolecular aldol reactions yielding high diastereo- and enantioselectivities.^[8] Interestingly, in these applications the configuration of the β -ACC was found to be decisive for the reactivity and/or selectivity of these foldamers. Thus, exclusively (+)- β -ACC containing NPY analogues showed the desired selectivity towards the NPY Y₁ receptor^[6] and tripeptides with inverse β -ACC configuration showed only very poor selectivities in organocatalytic reactions.^[8] Therefore, foldamers containing the β -ACCs are promising targets to investigate structure/reactivity or structure/selectivity correlations, especially by addressing the influence of the configuration on the foldamer structure.

In previous structural investigations of peptides containing β -ACC residues so far, β -ACCs have been shown to induce stable helical conformations in α/β peptides even with only five to nine amino acids.^[9] There only slight differences in the helical induction for both enantiomers of β -ACC have been reported.^[9] IR, CD and MD investigations for di- to pentapeptides with alternating β -ACC and Ala/Phe units revealed distinct hydrogen bond patterns in six-, eight- and nine-membered ring conformations.^[10] However, in this study the influence of the configuration was not addressed. In addition, in our working group first RDC supported structural investigations on two open chain tripeptides revealed unexpected high conformational stabilities of these peptides,^[11] but only (-)- β -ACC containing tripeptides were

investigated. Therefore, in this study the influence of the configuration of *cis*- β -ACC was investigated.

Here, we present NMR solution studies on tripeptides containing either (+)- or (-)- β -ACC. The detected preferences regarding the peptide backbone and side chain conformations are compared to each other, revealing the structure inducing effects of both enantiomers of β -ACC. In addition, first peptide enamines were detected.

Results and Discussion

For the investigation of the influence of the configuration of *cis*- β -ACC, the tripeptide H-(L)-*trans*-4-Hyp(OBn)-(+)-*cis*- β -ACC-(L)-Pro-OBn **3** was selected, which possesses a high sequence homology towards our previously investigated tripeptides **1** and **2**,^[11] but with (+)- β -ACC instead of (-)- β -ACC (see Figure 3.1). The exchange of proline against O-benzyl protected hydroxyproline Hyp(OBn) at the N-terminus was supposed to further stabilize the proline side chain conformation, since Hyp exclusively adopts the *up* conformation.^[12-13] In addition, **3** was selected due to the higher organocatalytic activity and selectivity of its C-terminal deprotected derivative **5** compared to its only proline containing analogue.

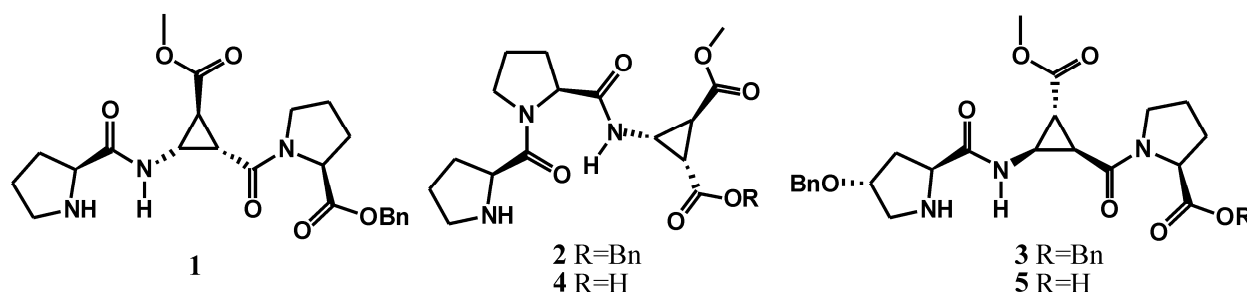


Figure 3.1: H-(L)-Pro- \blacktriangledown -(L)-Pro-OBn **1**, H-(L)-Pro-(L)-Pro- \blacktriangledown -OBn **2**, H-(L)-*trans*-4-Hyp(OBn)- \blacktriangle -(L)-Pro-OBn **3**, H-(L)-Pro-(L)-Pro- \blacktriangledown -OH **4** and H-(L)-*trans*-4-Hyp(OBn)- \blacktriangle -(L)-Pro-OH **5**; \blacktriangledown = (-)-*cis*- β -ACC, \blacktriangle = (+)-*cis*- β -ACC.

Parametrization of the unnatural amino acids Hyp and Hyp(OBn)

In conformational studies of small molecules and non-standard amino acids, the appropriate parametrization of these compounds is essential for reliable MD simulations. For β -ACC the parametrization was based on a crystal structure of a model compound, which was refined by DFT equilibrium geometry calculations and then checked with RDCs (residual dipolar couplings) for correctness of the hydrogen positions in the rigid cyclopropane ring.^[11] In this study, the DFT calculations based on either an energy minimized *in silico* structure or on the

crystal structure led to very similar results, which shows that an accurate parametrization of such unnatural amino acids can be achieved even in the absence of a crystal structure. Therefore, the parametrization of Hyp and Hyp(OBn) was based solely on DFT and HF calculations.^[14] In order to test the applicability of this approach also for proline-derived unnatural amino acids, several coordinate files were generated for proline and were compared to the established proline parametrization for MD calculations in CNS (Crystallography and NMR System).^[15] Four equilibrium geometry calculation algorithms were applied for that purpose, all of them starting from an MM-minimized *in silica* structure: Two *ab initio* calculations (Hartree-Fock with 6-31G* and 6-311++G** basis sets) and two density functional theory calculations (B3LYP, 6-31G* and 6-311++G** basis sets) were performed. For the differently optimized geometries, the maximum differences of the calculated bond lengths were found to be below 0.02 Å and of the calculated angles below 0.5°, which shows the high congruence of the DFT- and HF derived structures. These structures were then compared to the proline structure implemented in CNS, revealing maximum differences of the bond lengths below 0.04 Å and of the angles below 4°. Since these small differences for proline demonstrate the applicability of the *in silico* method for the amino acid parametrization, the HF and DFT approach was used for the Hyp and Hyp(OBn) parametrization, too.

Next, the same calculations were performed for Hyp and Hyp(OBn). The differences of the four calculated structures in each case were again very small (max. 0.03 Å and 2.5°), so the mean structure of the four geometries was used as the basis for the CNS parametrizations of Hyp and Hyp(OBn), respectively (see Table 3.3 in the SI). The obtained geometrical parameters for Pro and Hyp were in very good agreement with similar calculations in the literature^[16] and the results indicate that the optimized torsion angle values of the hydroxyproline residue closely resemble those of the proline residue.^[17] These angle parameters were then used in the following MD simulations in the torsion angle space.

MD calculations of **3**

For the MD calculations of **3** at 273 K in CDCl₃, 50 positive NOE contacts (extreme narrowing limit), detected in 2D ¹H,¹H-NOESY spectra (350 ms mixing time) at 273 K, were used as distance restraints (see Table 3.4 in the SI). Using the standard simulated annealing protocol, described in the SI, 100 structures with relatively loose distance restraints were calculated. Of these, three structures with lowest total and NOE energies were selected as a representative set for further analysis. Each member of this ensemble together with the NOESY cross peak volumes was used as input for the full relaxation matrix calculation in AUREMOL^[18]

in order to take spin diffusion effects into account. The refined sets of distance restraints were then applied for the next set of structure calculations. In total four cycles of structure calculations were performed, although convergence of both distance restraints and calculated structures was obtained already after two cycles. Figure 3.2a shows the obtained structure ensemble of **3** at 273 K in vacuo. Solvent refined structures were generated by subsequent refinement employing a chloroform box with periodic boundary conditions.

To elucidate the influence of temperature on the conformation and the conformational stability, the NOESY experiments and MD calculations described above were repeated for **3** at 240 K. 43 negative NOE contacts (slow tumbling limit) at 240 K were used as restraints in MD simulations employing an analogous procedure to the one for **3** at 273 K. For the calculation of the distance restraints in the REFINE module of AUREMOL the correlation time τ_c was estimated in a first step to be 2.7 ns with the help of an approximated NOE build up curve and the ratio of the cross peak volumes at 300 and 240 K. However, the calculation of some very large distance restraints, which would require to break covalent bonds, indicated that this rough estimation leads to too large correlation times. Therefore, an extension of the τ_c algorithm^[19] in the REFINE module of AUREMOL was made for our solvent CDCl_3 leading to a correlation time τ_c of 1.1 ns, which generated reasonable distance restraints for the MD calculations. The obtained structure shows a good congruence to the structure at 273 K regarding the backbone angle β and the conformational stability and confirms the accuracy of the MD calculations (see Figure 3.2b).

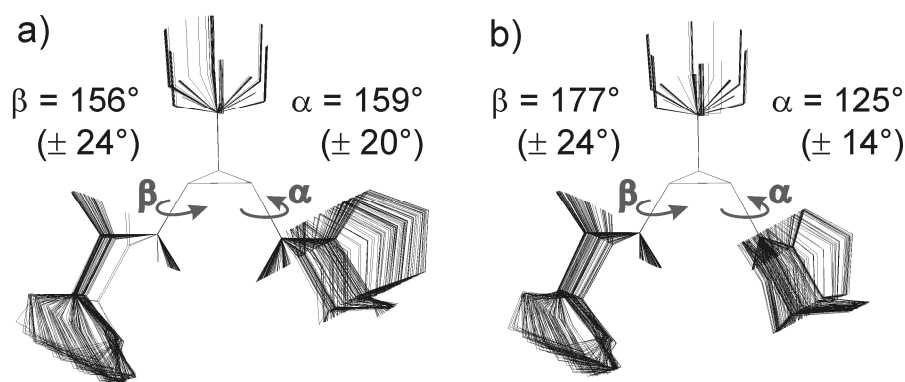


Figure 3.2: Ensembles of 100 structures of **3** at a) 273 K and b) 240 K in vacuo with NOE distance restraints derived from full relaxation matrix calculations. Hydrogen atoms except H^{N} (β -ACC) and the two benzyl groups are omitted for the sake of clarity. For the complete structures see Figure 3.7 and Figure 3.8 in the SI.

Validation of the MD calculations

In conformational studies of such small molecules as **3**, it is essential to check whether the experimental NMR parameters originate from one prevalent conformation or are averaged over several coexisting or interconverting conformations. As criteria for the dominant population of a particular conformation of short linear peptides, it has been proposed, that all interproton distances below 3.5 Å occurring in more than half of the calculated structures give rise to detectable NOEs and that no NOE restraints are violated.^[9] In addition, the predominant adoption of one well-folded form can be evidenced experimentally by unusual large or small $^3J_{\text{HH}}$ values.^[20] The MD simulations of **3** indicated – similar to **1** and **2**^[11] – again a limited conformational flexibility at both temperatures as far as rotations around the backbone angles Ψ_1 , α and β and the side chain conformation of Hyp(OBn) are concerned (see Figure 3.2). As expected, the orientations of the benzyl protecting groups are less defined (see Figure 3.7 and Figure 3.8 in the SI). The predominance of this conformation shown in Figure 3.2a is revealed by the excellent agreement of the experimental β angles derived from $^3J_{\text{HN-H}\beta}$ values with the calculated structures for **3** (and also for **1** and **2**), see Table 3.1. In addition, the fulfillment of all NOE restraints for **3** at 273 K and 240 K and the existence of observable NOE cross peaks for all distances below 3.5 Å for **3** at 273 K indicated one conformation for **3** at 273 K. However, for **3** at 240 K, the calculated distance of 3.46 Å between H^{N} (β -ACC) and $\text{H}^{\delta 1}$ (Pro3) was not represented by a NOE cross peak, indicating an incorrect α value for **3** at 240 K. In addition, this calculated α angle of **3** at 240 K strongly differed from the α angle of **3** at 273 K. The resulting small distance of Pro3 and the β -ACC moiety (see Figure 3.2b) for **3** at 240 K was not reflected by the experimental NOE cross peak and could therefore successfully be identified as artifact from the MD calculations. The most probably explanation for this rotation around α compared to **3** at 273 K could be the overestimation of the NOE restraints from H^{β} (β -ACC) to the H^{δ} protons of Pro3, since these structure decisive cross peaks were near the diagonal in the NOESY spectrum.

However, the unexpected limited flexibility and the values of the β angle of **3** at 273 and 240 K are experimentally confirmed by the unusual large $^3J_{\text{HN-H}\beta}$ value of 9.54 Hz at 240 K (see SI). The slight decrease in the $^3J_{\text{HN-H}\beta}$ coupling constant from 9.54 Hz at 240 K to 8.88 Hz at 273 K and the only slight difference of the calculated structures at both temperatures also indicate a high conformational stability. In addition, the linearity of the temperature coefficient $\Delta\delta/\Delta T$ of the amide proton H^{N} of β -ACC and small changes in the ^1H chemical shifts

($\Delta\delta(298\text{ K} - 240\text{ K}) = 0.32\text{ ppm}$ for the amide proton and $\Delta\delta \leq 0.12\text{ ppm}$ for the other protons) show that this conformation is still preferred at higher temperatures.

Table 3.1: Comparison of calculated and experimental β angles derived from $^3J_{\text{HN-H}\beta}$ and calculated α angles of **1**, **2** and **3** at varying temperatures.

	1	2	3	
T / K	240	273	273	240
$^3J_{\text{HN-H}\beta}$ / Hz	9.69 ^[a]	6.63 ^[a]	8.88	9.54
β_{exp}	$180^\circ \pm 30^\circ$ ^[a]	$215^\circ \pm 15^\circ$ ^[a]	$157^\circ \pm 13^\circ$	$180^\circ \pm 30^\circ$
$\beta_{\text{calc,vac}}$	$151^\circ \pm 11^\circ$	$221^\circ \pm 17^\circ$ ^[a]	$156^\circ \pm 24^\circ$	$177^\circ \pm 24^\circ$
$\beta_{\text{calc,solv}}$	$189^\circ \pm 15^\circ$	$192^\circ \pm 13^\circ$	$152^\circ \pm 23^\circ$	$199^\circ \pm 19^\circ$
$\alpha_{\text{calc,solv}}$	$174^\circ \pm 15^\circ$	$(271^\circ \pm 76^\circ)$ ^[b]	$168^\circ \pm 25^\circ$	$(118^\circ \pm 13^\circ)$ ^[c]

[a] From Ref^[11]. [b] Orientation of the benzyl group less defined. [c] MD artifact.

Beside the restricted conformational flexibility of the backbone angles, the MD simulations reveal preferred proline and hydroxyproline side chain conformations. For proline it has been found that two distinct envelope conformations are preferentially adopted, designated as C^γ -exo “*up*” and C^γ -endo “*down*”.^[12, 21-23] In contrast, hydroxyproline was reported to adopt only the *up* conformation.^[12-13] Likewise, in this study the O-benzyl protected hydroxyproline Hyp(OBn) was found to adopt almost exclusively the *up* conformation, which is supported by the analysis of all $^3J_{\text{HH}}$ couplings within the pyrrolidine ring of Hyp(OBn) and by the existence of a strong w-coupling of 2.2 Hz from $H^{\beta 1}$ to $H^{\delta 1}$ (Hyp(OBn)) in the ^1H spectra at 273 K. The existence of this 4J long range coupling and its only slightly reduction to 1.9 Hz at 298 K emphasizes the stability of the *up* conformation of the Hyp(OBn) side chain, even at higher temperatures.^[24] In contrast, for the N-terminal Pro in **1** and **2** no preference for *up* or *down* was observed, while proline in position two and three slightly prefers the *down* conformation (see Figure 3.3). Altogether, these MD findings are corroborated by all experimental $^3J_{\text{HH}}$ couplings and are analogous to the literature for Pro and Hyp containing peptides.^[12-13, 21-23] Thus, the incorporation of β -ACC does not induce unusual conformational preferences in the adjacent proline rings.

Structural motifs induced by the unnatural amino acids β -ACC

For a detailed understanding of the role of β -ACC in the reported applications of β -ACC containing foldamers in medicinal chemistry and organocatalysis, a comparison of the conformational preferences inherent in the β -ACC containing foldamers was conducted next. In previous studies using IR spectroscopy and molecular modeling, it was shown that β -ACC and its derivatives are able to induce several H-Bond patterns:^[10, 25] Beside a hydrogen bond in a six-membered ring conformation from the H^N (β -ACC) to the amide oxygen (β -ACC), which bears the disadvantage of a constrained N-H \cdots O geometry, also H-bond patterns with eight or nine-membered ring conformations were reported, especially, when strong H-bond donors and acceptors are in the vicinity of the β -ACC moiety. Furthermore, with poor H-bond acceptors e.g. esters instead of the stronger H-bond acceptor amide,^[26-27] at the C-terminus, the formation of the hydrogen bond in the six-membered ring conformation is disfavored for β -ACC derivatives.^[10] But due to the sequence of the investigated tripeptides, which provide a tertiary amide as H-bond acceptor for the six-membered ring conformation and lack alternative strong H-bond donors and acceptors^[28-29] in the vicinity of the β -ACC unit, the formation of the hydrogen bond in the 6- rather than 8- or 9-membered ring conformation was strongly favored for **1-3**.

Interestingly, the MD calculations of **1** and **2** with (-)- β -ACC and **3** with (+)- β -ACC showed, independent of the configuration of β -ACC, a curved turn structure with an unexpected stability concerning the backbone angles α and β (see Figure 3.2 and Table 3.1 for the angle values and Figure 3.3 for the structures), which is most probably induced by a combination of H-bonds and sterical hindrance. First the hydrogen bond pattern is discussed: The stability of the backbone angles α and β leads to a nearly constant distance of the H^N (β -ACC) to the O(=C) (β -ACC) of 2.03 ± 0.05 Å in **1**, **2** (distance to -O- instead of O(=C)) and **3** at 273 K. In addition, the angle formed by the atoms N-H^N \cdots O(=C) in **1**, **2** and **3** at 273 K is $116^\circ \pm 10^\circ$, see Figure 3.3a-c. No H-bond is indicated for **3** at 240 K due to the slightly incorrect α angle value (see Figure 3.3d and discussion above). These conformational preferences are most probably induced by a weak to moderate hydrogen bond within the β -ACC moiety from its H^N to its amide oxygen (in **1** and **3**) or to the sp³ ester oxygen (in **2**), respectively. This hydrogen bond is expected to be stronger at lower temperatures, as experimentally corroborated by the downfield shift of the amide proton from 8.58 ppm at 298 K to 8.89 ppm at 240 K.^[30-32] In addition, titration experiments with competing H-bond acceptors^[33-35] for **1** showed the existence of this H-bond: Upon the stepwise addition of DMSO the ¹H chemical shift of the H^N (β -ACC) (downfield shift below 0.08 ppm) and the ³J_{HN-H β} coupling constant remained nearly constant. The correlated

stabilities of $\delta(\text{H}^{\text{N}})$ and $^3J_{\text{HN-H}\beta}$ could hence be taken as a further support for the suggestion that an intraresidual H-bond within β -ACC contributes considerably to the conformational backbone stabilization. Furthermore, DFT and HF calculations for **3** (data not shown) and the MD calculations for **1**, **2** and **3** at 273 K showed the existence of this H-bond, independent of the configuration of β -ACC (see Figure 3.3a-c). Only in the MD calculations of **3** at 240 K (see Figure 3.3d), the H-bond within β -ACC was not reproduced. However, this can be attributed to the overestimation of the NOE restraint discussed above.

Interestingly, in **2** the -O- instead of O(=C) oxygen acts as the hydrogen bond acceptor (C6' ring). Usually esters act at the sp^2 rather than sp^3 oxygen atom as H-bond acceptor,^[27] but this kind of hydrogen bond with -O- as H-bond acceptor was also observed e.g. for Boc-Ala-(+)*cis*- β -ACC-OBn in molecular modeling studies.^[10] This preference of the H-bond geometry with the weaker H-bond acceptor might be attributed to stabilizing CH- π interactions of the benzyl group with the H^β and H^γ protons of Pro1, as indicated by NOESY contacts from the H^β , H^γ and $\text{H}^{\delta 2}$ protons to the aromatic protons of the benzyl group. An MD trajectory in the CDCl_3 box for **2** showed a distance of the H^β and H^γ protons to the midpoint M of the aromatic ring of 3-4 Å and an angle C-H--M larger than 120° (data not shown), typical for H-bonds with π -acceptors in proteins.^[29, 36]

Furthermore, a second, but weaker hydrogen bond between N (Pro_{*i-1*}/Hyp(OBn)_{*i-1*}) and H^{N} (β -ACC_{*i*}) is indicated for **1**, **2** and **3** at 273 and 240 K by the nearly constant distance from the N (Pro_{*i-1*}/Hyp(OBn)_{*i-1*}) to H^{N} (β -ACC_{*i*}) of 2.27 ± 0.06 Å and a nearly constant angle value for the corresponding N... H^{N} -N angle of $104^\circ \pm 2^\circ$ (see Figure 3.3a-d). This H-bond stabilizes the Ψ_{i-1} angle and induces a kink in the peptide chain, which is independent of the configuration of β -ACC. This geometry is further stabilized in **2** by an additional third weak H-bond from the amide oxygen O(Pro_{*i-2*}) to H^{N} (β -ACC_{*i*}), as indicated by the corresponding distance and angle values (distance O... H^{N} : 2.28 Å; angle O... H^{N} -N: 114° , see Figure 3.3b). This arrangement involving three amino acids stabilized by a $\text{O(=C)}_{i-2} \rightarrow \text{H}^{\text{N}}_i$ hydrogen bond with the corresponding Ψ angle of -9° and a ϕ angle of $+10^\circ$ for the second residue (Pro_{*i-1*}) can be regarded as distorted inverse γ -turn.^[10, 37] Interestingly, such bifurcated (in **1** and **3**) and even trifurcated (in **2**) H-bonds have not yet been reported in earlier IR studies of di- to pentapeptide containing alternating Ala/Phe and either (+) or (-)- β -ACC.^[10] One possible explanation is that bi- or trifurcated hydrogen bonded states are indistinguishable from single hydrogen bonded states by means of their NH valence bond vibration.

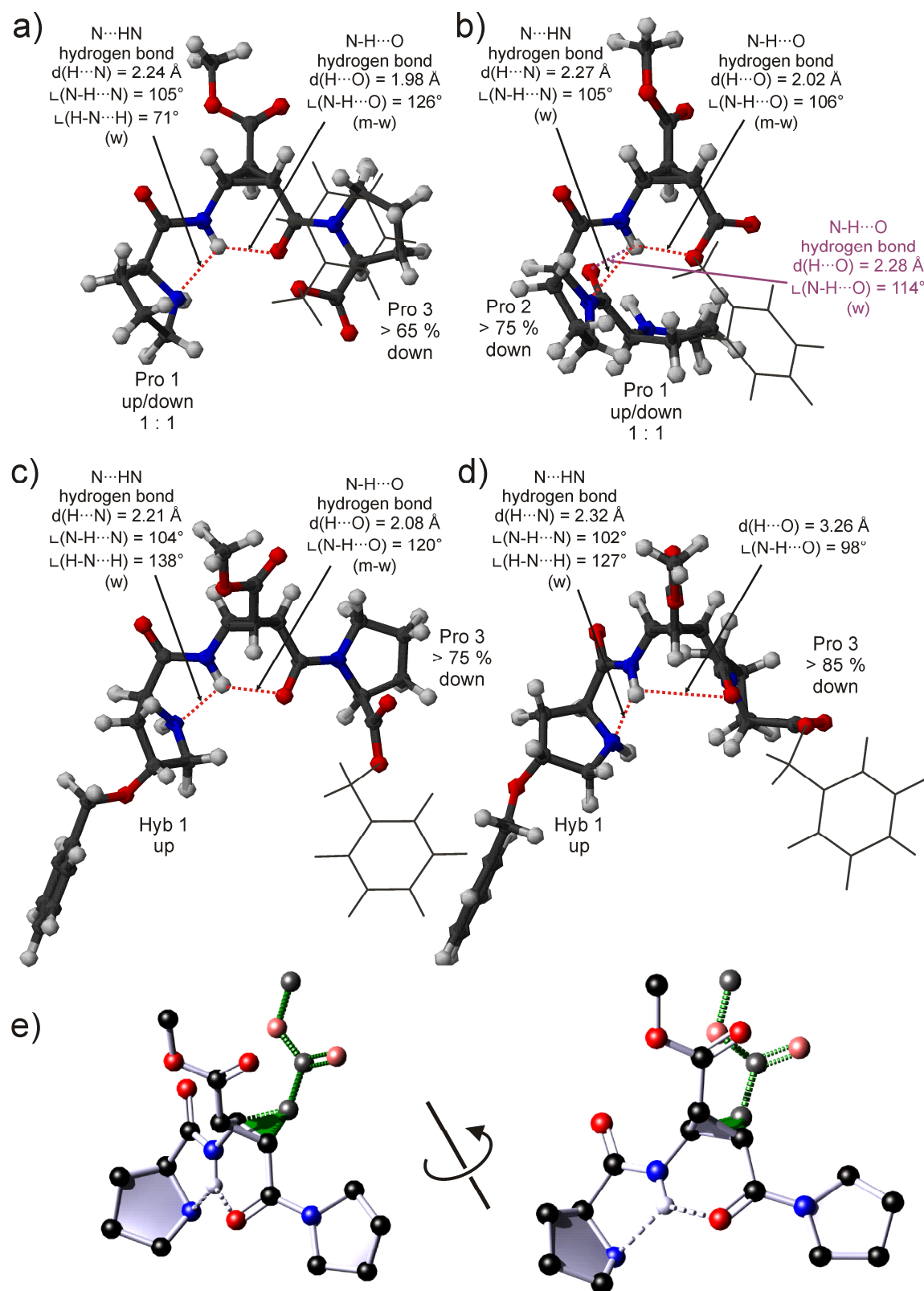


Figure 3.3: Proline puckering and hydrogen bonds of a) **1** at 240 K, b) **2** at 273 K, c) **3** at 273 K and d) **3** at 240 K refined in $CDCl_3$. The C-terminal benzyl group is plotted as line for the sake of clarity. Hydrogen bond strength classification (m moderate, w weak) according to Jeffrey.^[38] e) Scheme of the merged backbone conformations of **1** and **3** highlighting the different orientations of the cyclopropane ring and its methoxy substituent. Color code: red: oxygen, blue: nitrogen, black: carbon, grey: hydrogen.

Together with the bifurcated hydrogen bond network, the stability of the α angle seems to be also induced by steric interactions between the C^β and C^γ substituents of β -ACC with the H^δ protons of Pro3, following the well known concept of allylic 1,3-strain of Z configured allyl compounds,^[39] exemplarily shown in Figure 3.4. There the conformational equilibrium strongly favors **6a**, while **6b** represents an energy maximum determining the rotational barrier due to the allylic 1,3 strain.^[39] Due to the partial double bond character of the peptide bond and similar geometry of the β -ACC-Pro3 sub unit compared to allylic compounds, the β -ACC-Pro sub unit also adopts an eclipsed conformation with α values of 174° for **1** (with (-)- β -ACC) and 168° for **3** (with (+)- β -ACC) at 273 K (see Table 3.1). The allylic strain in combination with the hydrogen bond in the six-membered ring conformation both induced, independent of the configuration of β -ACC, in a cooperative manner the conformational stability of the backbone angles α and β .

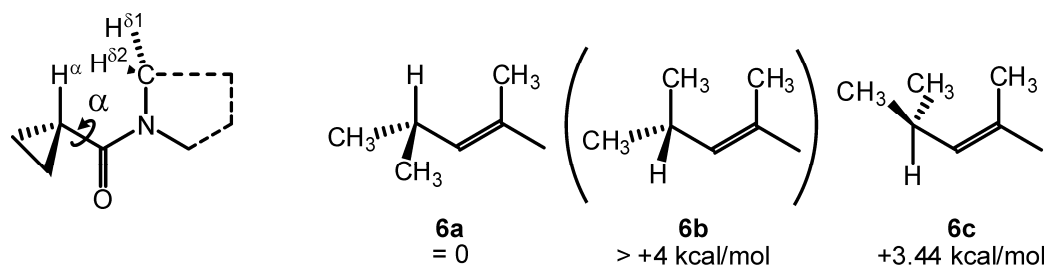


Figure 3.4: Scheme of the allylic 1,3-strain in a model compound^[39] and in the β -ACC-Pro sub unit.

Altogether, the high conformational preferences of the tripeptides **1-3** were stabilized by a bifurcated H-bond network induced by β -ACC together with allylic 1,3-strain in the β -ACC-Pro3 sub unit in **1** and **3**. Despite inversion of the configuration of β -ACC from **1** to **3**, identical hydrogen bond pattern and very similar backbone conformations were observed. This demonstrates that the tripeptide backbone and also the proline side chain conformation of **1-3** were independent of the configuration of β -ACC and only the cyclopropane ring and its methoxy substituent is oriented towards different sides dependent on the configuration. This is visualized by a scheme shown in Figure 3.3e. There, the structures of **1** and **3** are merged, highlighting the different orientations of the cyclopropane platform and its methoxy substituent. Therefore, β -ACC provides the ability to manipulate the orientation of the cyclopropane ring and its methoxy substituent by an inversion of the configuration without changing the backbone and therefore the overall peptide structure. This structural feature of β -ACC may explain the reported differences in selectivities in organocatalysis and medicinal chemistry upon a change of the β -ACC configuration. Especially, for organocatalytic applications the steric shielding by the

cyclopropane ring and its methoxy substituent might play a role in the selectivity of the organocatalysts and might be further improved with larger substituents at the cyclopropane ring. In this context, the detailed investigations on the conformational preferences induced by (\pm)- β -ACC presented herein should allow for an improvement of the β -ACC involving applications in organocatalysis and medicinal chemistry.

Deprotected organocatalysts and enamine formation

Inspired by the high conformational stability of **1-3**, we wanted to investigate the conformations of **4** and **5** (= unprotected **2** and **3**), which act as organocatalysts in aldol and mannich reactions.^[8, 40-41] For both tripeptides, a deprotection at the C-terminus leads to the formation of zwitterionic species, which aggregate in CDCl₃ to dimers for **4** and trimers for **5**, as observed by DOSY spectroscopy^[42-43] (for details see SI). Due to the presence of very strong salt bridges in CDCl₃, which are supposed to alter the hydrogen bonding pattern,^[28] structure alterations were expected and indeed, the absence of strong Pro1-Pro2 NOESY cross peaks for **4** indicated a reorientation of the Pro1-Pro2 sub unit compared to **2** and a change of the H^N (β -ACC) from a doublet at 7.65 ppm for **2** to a broad singlet at 9.68 ppm for **4** at 273 K indicated an alteration of the β angle. Conformational changes compared to **2** were also observed in quantum mechanical calculations for dimeric **4** (for details see SI). These conformational changes further evidenced the hydrogen bond within β -ACC together with the allylic 1,3-strain as main source of the conformational preferences of **1-3** and emphasized the importance of this hydrogen bond beside the allylic 1,3-strain for the high conformational stability. Further NMR investigations of **4** were hampered by its degradation into the Pro-Pro-diketopiperazine^[44-45] and severe signal overlap of Pro1, Pro2 and the diketopiperazine (see ¹H spectra in Figure 3.10b in the SI). In addition, for **5** five to seven conformations with almost equal populations could be identified. Therefore, no further structure investigations of **4** and **5** were performed.

Instead, a stabilization of enamines of the tripeptides seemed to be more promising. First, enamines of short peptidic organocatalysts have never been detected so far; second, our previous studies on enamines derived from proline and prolinol catalysts^[46-47] showed that the formation of enamines leads to a deaggregation to monomeric enamines. In a first attempt experimental conditions close to the structural investigations described above and close to the catalytic conditions used in the organocatalysis^[8] were used. 1:1 and 1:2 mixtures of **4** with p-nitrobenzaldehyde, acetone, benzophenone and cyclohexanone, respectively, were prepared in CDCl₃. But in agreement with our recent studies on proline and prolinol enamines, which were

only detectable in solvents with good H-bond acceptor and poor H-bond donor abilities like DMSO,^[46-47] enamines could not be detected (see SI). Therefore, we investigated next **1** with propionaldehyde in DMSO-d₆, using the same experimental conditions that had successfully been applied for the detection of proline enamines: Freshly distilled propionaldehyde (1 µL, 0.014 mmol) was added to a mixture of **1** (approx. 0.004 mmol) and DMSO-d₆ (0.6 mL) and the ongoing events were monitored by one-dimensional proton spectra at 300 K (see Figure 3.5). The macroscopic solubility of the tripeptide in DMSO was rather poor, leading to extremely low signal to noise ratios (see Figure 3.12 in the SI). In addition, the broad lines of the amide proton resonances indicate spectroscopically that the dissolved tripeptide molecules are heavily aggregated similar to the situation of **4** and **5** reported above. Upon the addition of an excess of propionaldehyde, two significant changes are observed in the 1D ¹H NMR spectra (see Figure 3.12 in the SI). First, two doublets of 13.7 Hz each at 6.04 ppm and 5.98 ppm, respectively, as well as two doublets of quartets close to 4 ppm and two broad singlets at about 1.55 ppm are observed. These signals, agreeing excellently with the previously reported data for the propionaldehyde-derived proline enamine,^[46] clearly evidence that two different *E*-configured enamine species (in a ratio of about 5:4) are formed from propionaldehyde and **1** in DMSO. Following our earlier conformational studies on this tripeptide, these enamines might be *cis-trans*-isomers with respect to the conformation of the β-ACC-Pro peptide bond (*cis:trans* ratio of the catalyst in chloroform: 1:4 at 240 K and 1:3 at 300 K).^[48] Second, the formation of the enamines also has an impact on the spectral appearance of the amide proton resonances of β-ACC: The broad amide proton resonances of the tripeptide, at about 8.65 ppm in DMSO for both isomers, experience a significant upfield shift to 8.25 ppm and 7.81 ppm in the enamine and the reduced line widths indicate that the formation of the enamine is indeed accompanied by the deaggregation of the tripeptide. However, a long-term stabilization of the enamine species could not be achieved in this experimental system. After 3 hours, no enamine can be detected any longer (see Figure 3.5); instead, low amounts of the self-condensation product of propionaldehyde are observed. Still, the lifetime of the enamine species in combination with the chemical shifts of the H1 proton at the enamine double bond allowed for a rough conformational characterization by ¹H, ¹H-NOESY analyses. The enamine resonances at 6.04 ppm and 5.98 ppm show cross peaks to signals at 3.49 ppm and 3.47 ppm, most probably belonging to the H^α (Pro1) protons in the two enamine species. Hence, this can be interpreted as a first evidence for the population of the *s-trans* conformation around the exocyclic N-C double bond; obviously, this conformation, which had been observed for proline enamines, is also preferred in the case of

peptide enamines. Further detailed studies concerning the possible adaption of conformational preferences upon the formation of enamines as reported for prolinol (ether) enamines could not be performed on the tripeptides **1-5** due to their low solubility in DMSO. Nevertheless, this is to our knowledge the first detection of peptidic enamines and constitutes a first insight into the stereoinduction exerted by *N*-terminal prolyl peptides^[49] in asymmetric enamine organocatalysis.

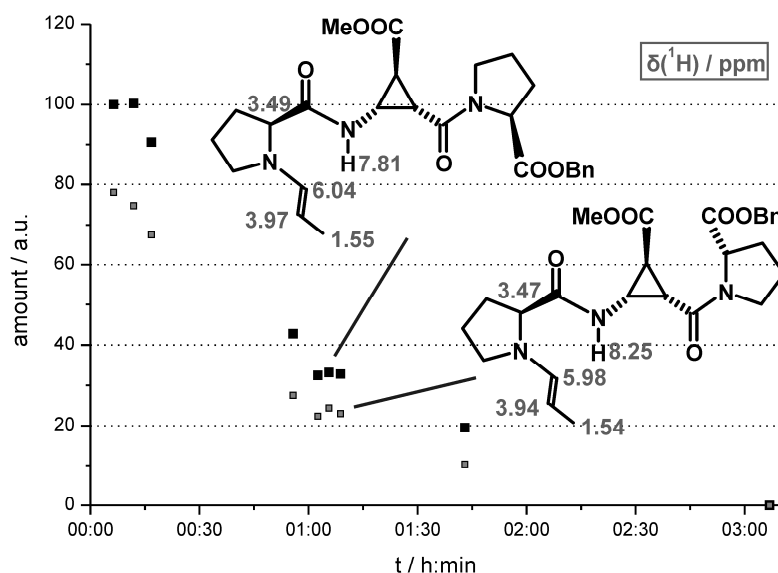


Figure 3.5: Decrease of the amounts of enamines formed of **1** with propionaldehyde in DMSO- d_6 at 300 K, followed by ^1H spectra. Because of the poor signal-to-noise ratio, an absolute quantification of the enamine amount was not possible; the amount of the major isomer detected in the first spectrum was therefore set to 100 arbitrarily.

Conclusion

In summary, we have presented a NMR and MD derived approach for the investigation of conformational preferences of different tripeptides containing the unnatural amino acid β -ACC and proline-like residues, revealing the structure induction and, especially, the influence of the configuration of β -ACC. A remarkable conformational stability regarding the backbone and the Hyp(OBn) side chain conformation was observed for H-(L)-*trans*-4-Hyp(OBn)-(+) -*cis*- β -ACC-(L)-Pro-OBn **3** at 273 and 240 K, which was similar to H-(L)-Pro-(-)-*cis*- β -ACC-(L)-Pro-OBn **1** and H-(L)-Pro-(L)-Pro-(-)-*cis*- β -ACC-OBn **2**. These high conformational preferences of the tripeptides **1-3** were stabilized in a cooperative manner by a bifurcated H-bond network induced by β -ACC and for **1** and **3** additionally by allylic 1,3-strain in the β -ACC-Pro3 sub unit. Despite inversion of the configuration of β -ACC from **1** to **3**, an identical hydrogen bond pattern and, thus, very similar backbone conformation was observed, demonstrating that both cooperative

stabilizing effects and thus the backbone conformation were independent of the configuration of β -ACC. Therefore, β -ACC provides the ability to manipulate the orientation of the cyclopropane ring and its methoxy substituent by an inversion of the configuration without changing the backbone and therefore the overall peptide structure. This may explain the different selectivities found in the applications of β -ACC in organocatalysis and medicinal chemistry. Thus, our study suggests that by using larger substituents at the cyclopropane ring an improved sterical shielding of one halfspace of the peptide may be achieved, which should lead to improved selectivities in β -ACC applications. In addition, for the first time the detection of a peptide enamine in organocatalytic aldol reactions is reported. In this context, the detailed investigations on the conformational preferences induced by (\pm)- β -ACC presented herein should allow for an improvement of the β -ACC involving applications in organocatalysis and medicinal chemistry.

3.3 Supporting Information

3.3.1 Experimental Section

Compounds **1**, **2** and **3** were synthesized following the published protocol.^[8, 50] NMR spectra were recorded on a Bruker Avance III 600 spectrometer equipped with a low temperature 5 mm TBI $^1\text{H}/^{31}\text{P}$ -BB probe and on a Bruker Avance III 600 equipped with a TCI cryoprobe, both with z-gradients and BVT 3000 temperature control unit. NMR data were processed and evaluated with Bruker's TOPSPIN 2.1 and 3.0.

Sample concentrations of 60 mM to 90 mM were applied for NMR measurements of **3** at 298 K, 273 K and 240 K, while aggregation in this concentration and temperature range could be excluded by diffusion measurements with convection artifact suppression.^[42] Assignment of proton and carbon resonances of all conformations of **3** was obtained by the use of one- and two-dimensional NMR spectra. ^1H -, ^{13}C -, $^1\text{H}, ^1\text{H}$ -COSY, $^1\text{H}, ^{13}\text{C}$ -HSQC, $^1\text{H}, ^{13}\text{C}$ -HMBC, $^1\text{H}, ^1\text{H}$ -NOESY and $^1\text{H}, ^{13}\text{C}$ -HSQC-NOESY spectra allowed for complete resonance assignment for almost all conformations of **3**. Due to the relatively small size of the investigated molecules and therefore slow NOE build-up a mixing time of 350 ms was used in the 2D $^1\text{H}, ^1\text{H}$ -NOESY and $^1\text{H}, ^{13}\text{C}$ -HSQC-NOESY spectra.

The peptide showed one main conformation with 62 % and some minor conformations with 15 %, 9 %, 7 % and 5 %. All conformations, except the 15 % minor conformation, showed a *trans* Xxx-Pro peptide bond proved by the ^{13}C chemical shift difference between the $\text{C}\beta$ and $\text{C}\gamma$ of Pro3.^[51-52] The assignment of all conformations was performed to identify overlapping NOESY peaks and to exclude these peaks from the MD calculations, but only the assignment of the main conformation is depicted in Table 3.2

NOESY spectra were integrated and evaluated with AUREMOL 2.2.2 and 2.3.1,^[18] its REFINE module was used for full relaxation matrix calculations. The calculation algorithm^[19] for the internal correlation time τ_c needed for the REFINE module was extended about the solvents CDCl_3 , CHCl_3 and CH_2Cl_2 . The viscosity, molecular mass and density data of these solvents were taken from the literature^[53-55] and were fitted with the Curve Fitting Tool of MATLAB 7.5.0 R2007b. The resulting fit parameters from the polynomial fit routine were incorporated into the internal AUREMOL solvent database (extension will be part of the next Auremol release).

MD simulations were performed with CNS 1.1 and 2.0 (Crystallography & NMR System).^[56] The simulated annealing protocol included a high temperature stage (2,000 steps at

50,000 K of 7.5 fs each) in torsion angle space, an annealing stage to 0 K (2,000 250 K-steps of 7.5 fs each) and a final energy minimization following the conjugate gradient method in ten cycles of 200 steps each.

The unnatural amino acid *cis*- β -ACC was implemented into CNS on the basis of the DFT minimized structures and the benzyl protecting group was parameterized on the basis of the available data for the natural amino acid phenylalanine.^[11] The O-benzyl protected hydroxyproline Hyp(OBn) was implemented into CNS on the basis of HF and DFT calculations computed with SPARTAN 06,^[57] as discussed in chapter 3.1, and force field parameter definitions readable by CNS were created by the Dundee PRODRG2 server^[58] and XPLO2D.^[59]

The solvent for structure refinement was simulated by a cubic box of 50 Å length filled with 1,000 molecules of chloroform (obtained from VEGA ZZ 2.0.8^[60]), for which periodic boundary conditions were assumed. The CHCl₃ geometry as well as atomic charges were taken from literature data^[61] and force field parameters were generated by XPLO2D.

Calculated structures were visualized and evaluated with MOLMOL 2K.2.^[62]

Nomenclature of 3

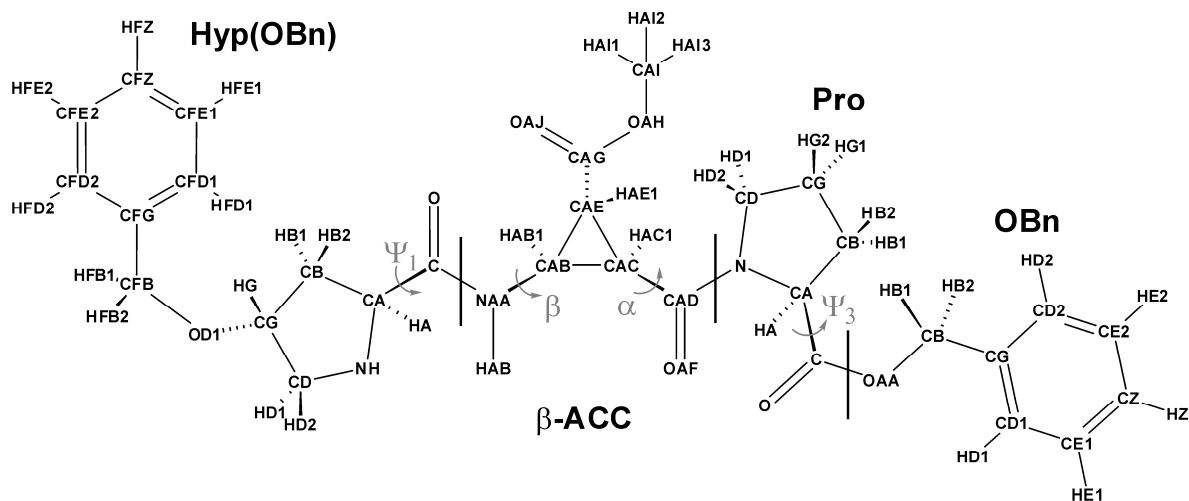


Figure 3.6: Nomenclature of 3 as used for CNS. The same atom names were used for 1 and 2. Only the primarily populated conformation of 3 (with a *trans* Xxx-Pro peptide bond) is depicted as only this one was investigated in detail.

Resonance assignment of **3****Table 3.2:** Assignment of proton and carbon resonances of **3** in CDCl₃ (major conformation with *trans* peptide bonds only, see Figure 3.6 for atom nomenclature). Chemical shifts were referenced to the chloroform signal ($\delta(^1\text{H}) = 7.26$ ppm, $\delta(^{13}\text{C}) = 77.16$ ppm).

Amino acid	Carbon	$\delta(^{13}\text{C})$ / ppm at 298 K	Proton	$\delta(^1\text{H})$ / ppm		
				at 298 K	at 273 K	at 240 K
Hyp(OBn)	CFB	70.79	HFB2 HFB1	4.43/4.49	4.41/4.47	4.40/4.46
	CFG	138.26				
	CFD*	127.73	HFD*	7.30	---	---
	CFE*	128.58	HFE*	7.33	---	---
	CFZ	127.82	HFZ	7.30	---	---
	C	175.84	HT1	2.20	---	---
	CA	59.96	HA	3.88	3.91	3.93
	CB	36.49	HB2 HB1	1.93 2.41	1.92 2.43	1.93 2.47
	CG	80.38	HG	4.07	4.07	4.09
	CD	52.71	HD2 HD1	2.74 3.14	2.73 3.16	2.68 3.20
	C	166.97	HAB	8.58	8.69	8.89
	CAC	26.71	HAC1	2.58	2.59	2.61
β -ACC	CAB	36.48	HAB1	4.03	4.06	4.16
	CAE	27.69	HAE1	2.46	2.47	2.49
	CAG	171.22				
	CAI	52.42	HAI*	3.71	3.70	3.70
Pro	C	171.75				
	CA	59.11	HA	4.57	4.57	4.60
	CB	29.34	HB2 HB1	2.00 2.20	2.00 2.20	2.03 2.23
	CG	24.67	HG2 HG1	2.01-2.06 2.01-2.06	2.06-2.01 2.06-2.01	2.01-2.05 2.01-2.05
	CD	47.60	HD2 HD1	3.78 3.76	3.79 3.73	3.84 3.71
	CB	67.04	HB2 HB1	5.09/5.23	5.08/5.22	5.06/5.21
	CG	135.72				
OBn	CD*	128.23	HD*	7.32	---	7.36
	CE*	128.68	HE*	7.36	---	7.36

3.3.2 Parametrization of Hyp and Hyp(OBn)

Angle and bond length values for Hyp and Hyp(OBn) were based on DFT and HF calculations generated with the program SPARTAN 06. (see Table 3.3). The charge distribution was according to the natural amino acids threonine and proline.

Table 3.3: Geometric parameters of the Pro, Hyp and Hyp(OBn) residues as used in the MD calculations.

	CNS	Pro	Hyp	Hyp(OBn)
bond length / Å	N-CA	1.486	1.4860	1.4860
	CA-CB	1.530	1.5300	1.5300
	CB-CG	1.490	1.5300	1.5300
	CG-CD	1.504	1.5255	1.5255
	CD-N	1.474	1.4740	1.4740
	CG-HG	1.080	1.0800	1.0800
	CG-O/CG-HG1	1.080	1.4195	1.4195
angle	CB-CG-O/CB-CG-HG1	109.955°	111.9325°	111.9325°
	CB-CG-CD	106.100°	102.0275°	102.0275°
	HG-CG-O/HG2-CG-HG1	110.456°	110.6150°	110.6150°
	CD-CG-HG	110.382°	112.6675°	112.6675°
	CD-CG-O	110.382°	106.4850°	106.4850°
	CG-O-CFB	---	109.3175°	116.9775°
	CG-CD-N	103.688°	105.0200°	105.0200°
	CB-CG-HG	109.955°	109.2487°	109.2487°
	CG-CD-HD2	110.382°	111.3275°	111.3275°
	CG-CD-HD1	110.382°	111.3275°	111.3275°
	O-CFB-CFG	---	---	113.7200°
improper angle	HA-N-C-CB	66.327°	66.3265°	66.3265°
	HB1-HB2-CA-CG	-71.939°	-69.6639°	-69.6639°
	OH1-HG-CB-CD	-71.899°	-73.2775°	-73.2775°
	HD1-HD2-CG-N	-71.902°	-71.9225°	-71.9225°
dihedral	CFG-OD1-HFB1-HFB2	---	---	-71.0400°

3.3.3 Structure investigation of **3** at 273 K

50 positive NOE contacts (extreme narrowing limit), were detected in 2D ^1H , ^1H -NOESY (350 ms mixing time) spectra at 273 K and used as restraints in MD simulations. At first, relatively loose distance restraints were used to restrict the available conformational space, employing uniform upper and lower bounds of 0.500 nm and 0.175 nm, respectively. Using the standard simulated annealing protocol, described in chapter 3.3.1, 100 structures were calculated. Of these, 3 structures with low total and NOE energies were selected as a representative set for further analysis. Each member of this ensemble together with the NOESY cross peak volumes was used as input for the full relaxation matrix calculation (with the REFINE module included in AUREMOL) in order to take spin diffusion effects into account. The refined sets of distance restraints were then applied for the next round of structure calculations.

In the first round of structure calculations three families were identified, but one of them could be excluded due to its violation of distance restraints. In the second round the two remaining families interconverted into one and reproduced itself in the following rounds of structure calculations. The obtained structure ensemble is shown in Figure 3.7 (and without the benzyl groups in Figure 3.2a).

In total four rounds of structure calculations were performed, at which after two rounds convergence of both distance restraints and calculated structures was obtained. Solvent refined structures were obtained by subsequent refinement employing a chloroform box with periodic boundary conditions.

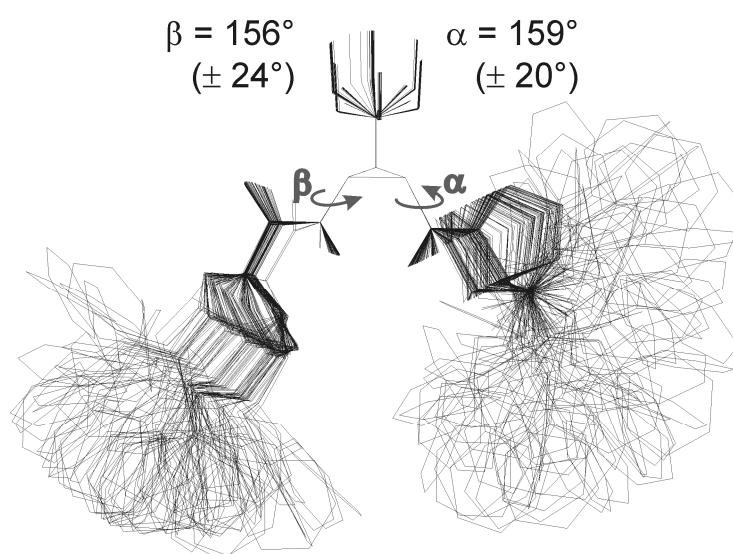


Figure 3.7: Ensemble of 100 structures of **3** at 273 K in vacuo with 50 NOE distance restraints derived from full relaxation matrix calculations.

Table 3.4: 50 distance restraints of **3** at 273 K derived from full relaxation matrix calculations.

assign	(resid 1 and name HA)	(resid 1 and name HB2)	2.85	0.29	0.29
assign	(resid 1 and name HA)	(resid 1 and name HD2)	3.96	0.43	0.43
assign	(resid 1 and name HA)	(resid 1 and name HD1)	3.85	0.41	0.41
assign	(resid 1 and name HA)	(resid 2 and name HAB)	3.56	0.36	0.36
assign	(resid 1 and name HB2)	(resid 1 and name HB1)	1.78	0.19	0.19
assign	(resid 1 and name HB2)	(resid 1 and name HG)	2.25	0.23	0.23
assign	(resid 1 and name HB2)	(resid 1 and name HD2)	3.32	0.34	0.34
assign	(resid 1 and name HB2)	(resid 1 and name HD1)	4.02	0.45	0.45
assign	(resid 1 and name HB2)	(resid 1 and name HFB1)	3.67	0.90	1.40
assign	(resid 1 and name HB2)	(resid 1 and name HFB2)	4.12	1.55	0.95
assign	(resid 1 and name HB2)	(resid 2 and name HAB)	3.25	0.34	0.34
assign	(resid 1 and name HB1)	(resid 1 and name HG)	2.77	0.31	0.30
assign	(resid 1 and name HB1)	(resid 1 and name HD1)	3.85	0.45	0.42
assign	(resid 1 and name HB1)	(resid 1 and name HFB1)	2.48	0.77	0.77
assign	(resid 1 and name HB1)	(resid 1 and name HFB2)	2.52	0.77	0.77
assign	(resid 1 and name HG)	(resid 1 and name HD2)	2.37	0.24	0.24
assign	(resid 1 and name HG)	(resid 1 and name HD1)	2.83	0.29	0.29
assign	(resid 1 and name HG)	(resid 1 and name HFB1)	3.03	0.94	0.83
assign	(resid 1 and name HG)	(resid 1 and name HFB2)	3.17	0.84	0.94
assign	(resid 1 and name HD2)	(resid 1 and name HD1)	1.78	0.19	0.19
assign	(resid 1 and name HD2)	(resid 1 and name HFB1)	3.60	0.91	2.10
assign	(resid 1 and name HD2)	(resid 1 and name HFB2)	4.86	2.22	1.04
assign	(resid 1 and name HD2)	(resid 2 and name HAB)	2.50	0.27	0.27
assign	(resid 1 and name HD1)	(resid 1 and name HFB1)	2.48	0.77	1.57
assign	(resid 1 and name HD1)	(resid 1 and name HFB2)	3.29	1.66	0.86
assign	(resid 1 and name HD1)	(resid 2 and name HAB)	3.68	0.41	0.41
assign	(resid 1 and name HFB1)	(resid 1 and name HFD*)	2.84	0.81	1.11
assign	(resid 1 and name HFB2)	(resid 1 and name HFD*)	3.13	1.16	0.84
assign	(resid 2 and name HAB)	(resid 2 and name HAB1)	2.96	0.30	0.30
assign	(resid 2 and name HAB)	(resid 2 and name HAC1)	3.69	0.38	0.38
assign	(resid 2 and name HAB)	(resid 2 and name HAE1)	2.84	0.29	0.29
assign	(resid 2 and name HAB)	(resid 3 and name HA)	3.89	0.44	0.43
assign	(resid 2 and name HAB)	(resid 3 and name HD2)	4.89	0.56	0.54
assign	(resid 2 and name HAB1)	(resid 2 and name HAC1)	2.46	0.25	0.25
assign	(resid 2 and name HAB1)	(resid 2 and name HAE1)	3.12	0.32	0.32
assign	(resid 2 and name HAC1)	(resid 3 and name HA)	4.74	0.51	0.52
assign	(resid 2 and name HAC1)	(resid 3 and name HD2)	2.19	0.23	0.24
assign	(resid 2 and name HAC1)	(resid 3 and name HD1)	2.75	0.29	0.30
assign	(resid 2 and name HAE1)	(resid 3 and name HD2)	4.84	0.63	0.54
assign	(resid 2 and name HAE1)	(resid 3 and name HD1)	5.19	0.66	0.58
assign	(resid 3 and name HA)	(resid 3 and name HB2)	2.71	0.29	0.29
assign	(resid 3 and name HA)	(resid 3 and name HB1)	2.30	0.26	0.25
assign	(resid 3 and name HA)	(resid 3 and name HD2)	4.10	0.44	0.45
assign	(resid 3 and name HA)	(resid 3 and name HD1)	3.61	0.40	0.40
assign	(resid 3 and name HB1)	(resid 3 and name HD2)	3.87	0.44	0.43
assign	(resid 3 and name HB1)	(resid 3 and name HD1)	2.98	0.36	0.33
assign	(resid 3 and name HG1)	(resid 3 and name HD2)	2.57	0.27	0.28
assign	(resid 3 and name HG1)	(resid 3 and name HD1)	2.30	0.26	0.25
assign	(resid 4 and name HB1)	(resid 4 and name HD*)	3.26	1.65	0.85
assign	(resid 4 and name HB2)	(resid 4 and name HD*)	2.42	0.76	1.56

3.3.4 Structure investigation of **3** at 240 K

43 negative NOE contacts (slow tumbling limit) detected in $^1\text{H}, ^1\text{H}$ -NOESY (350 ms mixing time) spectra at 240 K were used as restraints in MD simulations employing a procedure analogue to **3** at 273 K (chapter 3.2).

Due to the ambiguous assignment of the benzylic protons NOESY distance restraints to both of these protons have been extended to include both protons and additionally about 0.05 nm. Or they have been included only qualitatively with uniform upper and lower bounds of 0.600 nm and 0.300 nm, when only one contact was observed.

After the extension of the τ_c algorithm in the REFINE module of AUREMOL, a τ_c of 1.1 ns was calculated generating reasonable distance restraints for the MD calculations (see Figure 3.8).

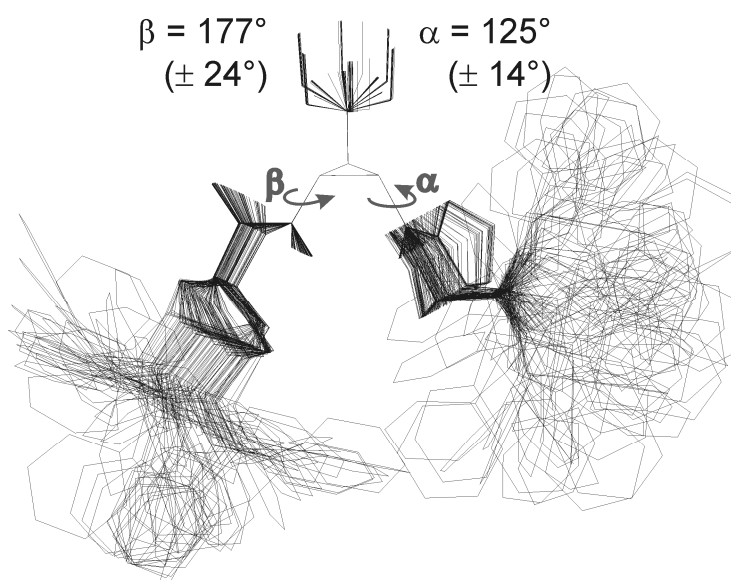


Figure 3.8: Ensemble of 100 structures of **3** at 240 K in vacuo with 43 NOE distance restraints derived from full relaxation matrix calculations.

3.3.5 Validation of the calculated β angles

From the well-known Karplus curve for $^3J_{\text{HN-H}\alpha}$ of natural α -amino acids^[63-64] (see Figure 3.9) in combination with the scaling effect of the cyclopropane ring,^[11, 65] the observed J coupling of 9.54 Hz for **3** at 240 K was interpreted in terms of a population of β values of $180^\circ \pm 30^\circ$. The same had been earlier for **1** and **2**.^[11] For all tripeptides the experimental β angles, derived from $^3J_{\text{HN-H}\beta}$ values, were in excellent agreement with the calculated structures (see Table 3.1).

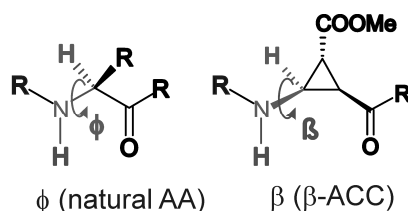


Figure 3.9: β angle in β -ACC as analogue to the ϕ angle in natural amino acids.

3.3.6 NMR investigations on the organocatalysts **4** and **5**

Degradation of **4** into the Pro-Pro-diketopiperazine and severe signal overlap

The organocatalytic precursor **2** decomposed under ring closure to the cyclic Pro-Pro-diketopiperazine. This is known from peptide chemistry, where especially the Pro-Pro-dipeptide sequence is prone to form diketopiperazines.^[44, 66] Since the unprotected catalyst **4** also possesses this detrimental sequence, but without the deleterious electron lone pair at the N-terminus, a slow decomposition of **4** could be observed in dry CDCl_3 just as well and more pronounced in CDCl_3 containing traces of water.^[45] The acceleration of the decay by more polar, protic solvents could be confirmed in MeOH, where a complete decay could be observed within 12 days. For the catalytic reaction, this slow decomposition of the catalyst **4** was not considered as problematic because of the subsequent separation of the decay product by the work-up.

In contrast, for a meaningful conformational analysis of **4**, a purification of the compound was necessary. Therefore several attempts were performed, but a complete separation of the decomposition product was not possible with the lowest amount of the decay product around 10 %. Due to the proceeding decomposition and the striking signal overlap of Pro1, Pro2 and the diketopiperazine in the ^1H spectra (see Figure 3.10b), this experimental system was considered to be too complex for detailed and meaningful conformational investigations of **4**. Thus, no

conformational analysis, but only aggregation studies and attempts to stabilize intermediates with some additives have been made for **4**.

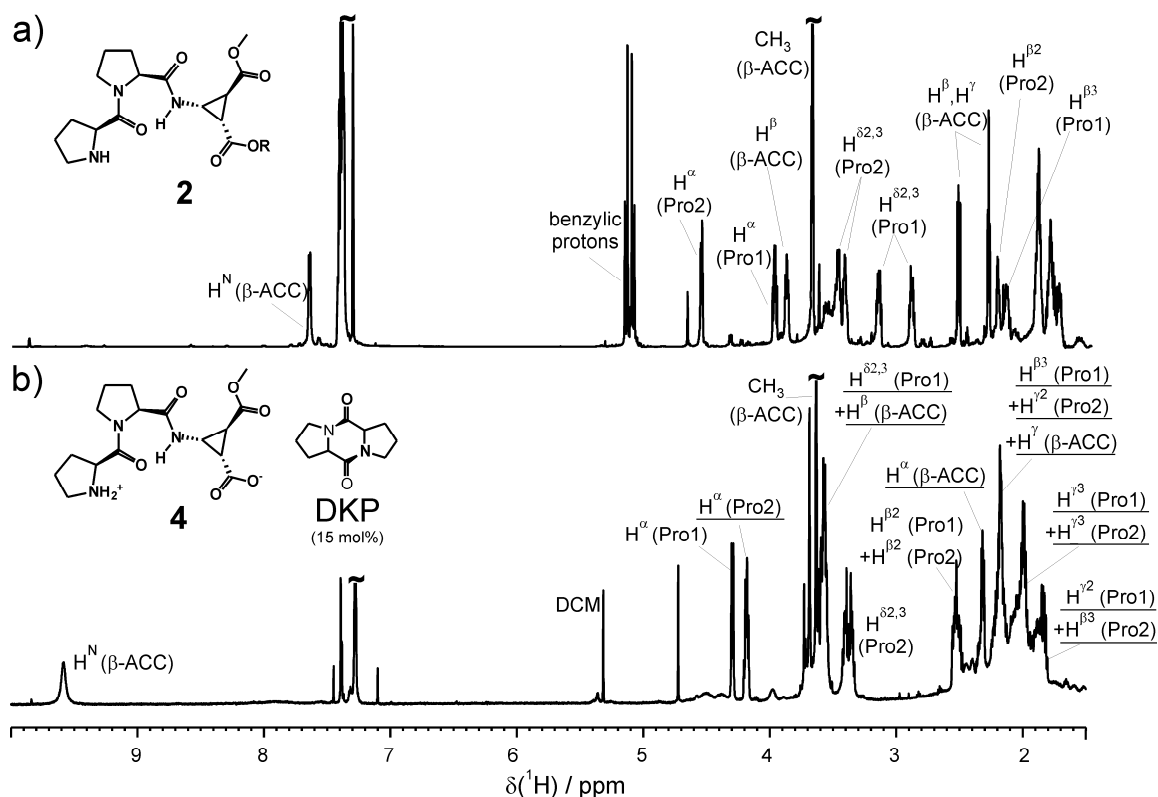


Figure 3.10: a) ^1H spectrum of **2** in CDCl_3 at 270 K with sufficient chemical shift dispersion. b) ^1H spectra of **4** in CDCl_3 at 300 K with striking signal overlap of Pro1, Pro2 and the diketopiperazine DKP degradation product. Proton signals of **2** overlapped with signals of the DKP are marked with an underline.

NMR investigations of **5** at 300 K

Sample concentrations of 160-190 mM in CDCl_3 were applied for the 2D NMR measurements of **5** at 300 K resulting in only poor spectral quality, which could not be improved by dilution or by lowering the temperature. Five to seven conformations with almost equal populations could be identified in a ^1H , ^{13}C -HSQC at 298 K. The severe signal overlap owing to the high number of conformations with similar chemical shift pattern and the large line widths of the signals, due to aggregation and presumably exchange between the conformations, hampered a complete assignment of the proton and carbon resonances and impeded a conformational analysis for **5**.

Aggregation studies of **4** and **5**

From diffusion-ordered spectroscopy (DOSY)^[43, 67] the translational self-diffusion coefficients of molecules in solution can be calculated according to the Stejskal-Tanner equation.^[68] On this basis and with the diffusion coefficient of TMS as reference, the relative diffusivity $D_{\text{rel}} = D_{\text{TMS}}/D_{\text{analyt}}$ of an analyt can be gained, from which the molecular mass M of the molecule can be estimated empirically following equation (3.1) (parametrized for organic solvents).^[69]

$$M = 84.5 \frac{\text{g}}{\text{mol}} \cdot D_{\text{rel}}^{1.72} \quad (3.1)$$

The comparison of the estimated mass with the actual molecular mass of the analyte then allows for an estimation of the aggregation behavior of the analyte in solution.

DOSY experiments^[42] for **4** in CDCl_3 at 300 K in the concentration range from 1-5 mM revealed mass estimations of 630-700 g mol^{-1} .^[69] By comparison with the actual mass ($M=353.4 \text{ g mol}^{-1}$), these values could be interpreted as dimer over the whole concentration range with only a slight deaggregation upon dilution. The dimerization of **4** bears analogy to proline catalyzed aldol reactions in DMSO, where proline is initially a dimeric species and subsequently forms a monomeric enamine intermediate in the course of the reaction.^[70]

Table 3.5: DOSY-based molecular mass estimations for **4**, the Pro-Pro-diketopiperazine DKP and the different additives in CDCl_3 at 300 K.

c / mM ^[a]	c / mM ^[b]	additive	mass estimation / g mol^{-1}			
			4 ($M=353$)	DKP ($M=194$)	additive	pure additive
29	5	---	697	285	---	---
22	4	---	688	265	---	---
10	2	---	658	281	---	---
5	1	---	626	283	---	---
10	4	1:1 p-nitro benzaldehyde	743	711	145	125
10	4	1:2 p-nitro benzaldehyde	713	645	140	
10	3	1:1 benzophenone	731	696	180	177
10	3	1:2 benzophenone	749	672	169	
10	4	1:1 acetone	693	664	78	67
10	4	1:2 acetone	667	600	72	
10	3	1:1 cyclohexanone	744	683	130	107
10	3	1:2 cyclohexanone	697	653	116	

[a] concentration according to the net weight. [b] concentration OMS corrected due to precipitation of **4**.

To allow for NMR investigations on **4** as a monomer and to investigate potential enamine intermediates of the catalytic reaction, **4** should be stabilized and disaggregated by an increase of the polarity of the solvent (dielectric constant ϵ of CDCl_3 : 4.8)^[55] and/or by the formation of enamine (or oxazolidinone-like) intermediates. Therefore, p-nitro benzaldehyde and benzophenone (ϵ : 12.62/27° C)^[55] were selected to increase the solubility of **4** by an increase of the polarity of the solvent. Additionally, cyclohexanone (ϵ : 16.1/20° C)^[55] and acetone (ϵ : 21.1/20° C)^[55] bearing the potential to form enamine intermediates with the catalyst, were selected. Each compound was added to samples of **4** in CDCl_3 at 300 K to end up in a molar ratio **4**:additive of 1:1 and 1:2, respectively. The corresponding DOSY-based mass estimations of **4**, the diketopiperazine and of the additives are summarized in Table 3.5. For comparison, the mass estimations for pure additives (10 mM in CDCl_3) are also given in the last column. For **4**, no disaggregation upon addition of the carbonyl compounds was observed. In contrast, for the diketopiperazine a more than twofold increase of the estimated mass was observed, from 260-290 g mol⁻¹ without additives to 640-710 g mol⁻¹ with additives. The masses of all additives are unaffected (within the error range) by the presence of **4** and the diketopiperazine compared to the pure additive samples. This suggested that there is no direct interaction of the additives with **4** or with the decomposition product. The aggregation of the diketopiperazine may be attributed to the increase of the polarity of the solution rather than the formation of an aggregate with the additives.

Altogether, no disaggregation of the catalyst with the additives neither as a soluble intermediate nor by an increase of the solvent polarity could be achieved. Recent investigations on the stabilization trends of enamines showed, that CDCl_3 was not the appropriate solvent, since proline enamines are stabilized by solvents with good H-bond acceptor (β) and at the same time poor H-bond donor (α) properties like DMSO (β 0.76, α 0.00).^[46, 71] In contrary, CDCl_3 is only a very poor H-bond acceptor ($\beta=0.1$). Therefore, the non-detection of enamine intermediates in these investigations can be attributed to the misfit solvent and also misfit carbonyl compounds.

However, an increase of the amount of (still aggregated) **4** in solution by a factor of 2 was observed upon the addition of the additives (see Table 3.5).

DOSY experiments^[42] for **5** in CDCl₃ at a concentration of 160 mM in the temperature range from 300 to 220 K delivered always the same diffusion coefficient for the five to seven conformations of **5**. This means that the simultaneously existing species were not different aggregates of **5**, but different conformations with the same aggregation behavior. By a comparison with the actual mass ($M = 459.5$ g/mol), the DOSY-based mass estimations of 1423-1550 g/mol could be interpreted as trimer for all conformers over the whole temperature range.^[69] The potential influence of the high concentration was ruled out by dilution experiments, which revealed scarcely alteration of the chemical shift pattern in the ¹H spectra. Therefore similar aggregation behavior was expected for **5** also at lower concentrations. This was supported by dilution of **4** down to 1 mM, in which only a slight disaggregation was observed by DOSY experiments (see Table 3.5).

This higher aggregation of **5** compared to its monomeric precursor **3** was reflected by the different rotational correlation time τ_c indicated by the sign of NOESY cross peaks: While **3** (and also **1** and **2**) was in the extreme narrowing regime down to 273 K indicating fast motion typical for a monomeric species, **5** was in the slow tumbling regime even at 300 K indicating a aggregated species with a relatively high rotational correlation time τ_c .

3.3.7 Quantum mechanical calculations for dimeric **4**

Quantum mechanical calculations (HF, 6-31G*)^[57] for a dimer of **4** in vacuo showed one molecule with an intact intramolecular hydrogen bond in the six-membered ring conformation, while the second one possessed an intramolecular salt-bridge from its N- to its C-terminus. Furthermore, the Pro2- β -ACC peptide bond of the second molecule interacted as hydrogen bond donor and acceptor with the N- and C-terminus of the other molecule (see Figure 3.11). However, the QM calculations were performed in vacuo, therefore the energy gain due to the formation of hydrogen bonds and salt bridges was presumably overestimated and no experimental restraints were included in the calculation. Therefore, it is unclear, whether these results are consistent with the experimental data, e.g. the existence of two inequivalent molecules was not indicated by the NMR spectra. But the survival of the C₆ hydrogen bond in one of the molecules further hinted at the high conformational preference of this C₆ conformation.

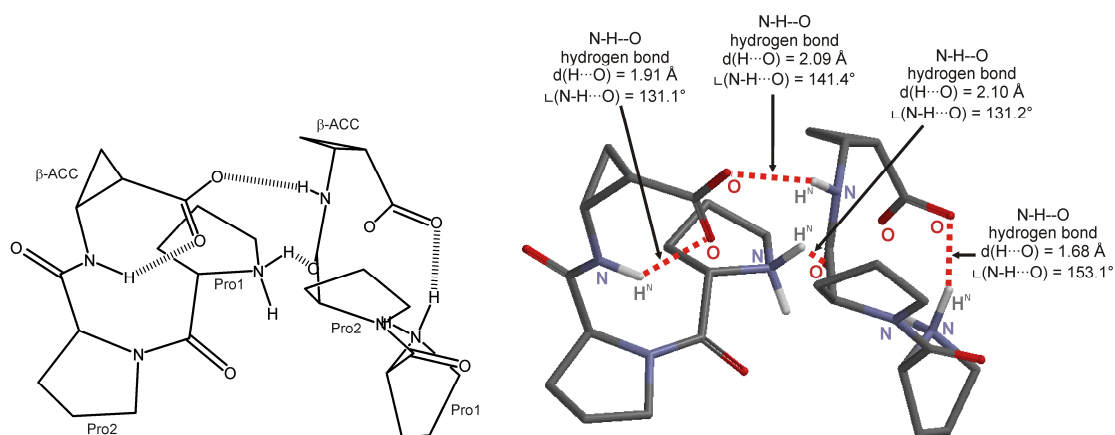


Figure 3.11: Hartree-Fock-based^[57] structure model of dimeric **4** with intra- and intermolecular H-bonds. Methoxy esters of β -ACC and hydrogen atoms (except H^N) are omitted for the sake of clarity.

3.3.8 Enamine detection for **1**

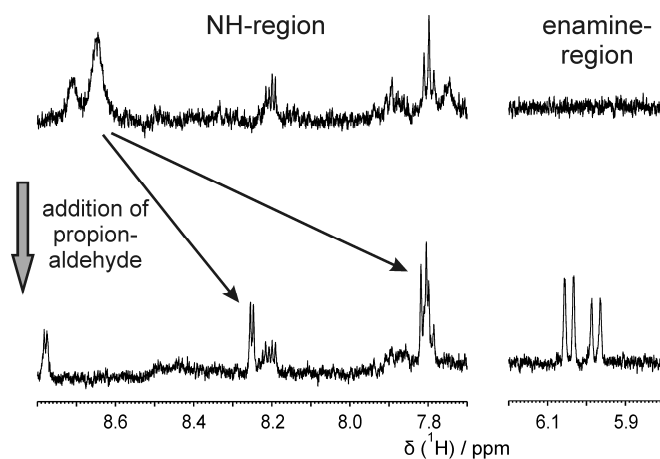


Figure 3.12: Proton spectra of **1** in DMSO- d_6 before (top) and after (bottom) the addition of an excess of propionaldehyde.

3.3.9 Statistical information on the calculated structures of **3**

Table 3.6: Statistical information on the calculated structure ensembles.

	Figure 3.2a \equiv Figure 3.7	Figure 3.2b \equiv Figure 3.8
number of selected structures	100	100
number of restraints	50	43
rmsd (backbone without benzyl groups) / Å	0.44 ± 0.15	0.40 ± 0.12
$E(\text{NOE})_{\text{max}} / \text{kJ mol}^{-1}$	3.08	1.9
$E(\text{total})_{\text{max}} / \text{kJ mol}^{-1}$	18.8	16.6

3.4 Additional experimental findings

3.4.1 Preparation of PDMS/ CDCl_3 gels

In chapter 2, it was shown that in the presence of *cis*- β -ACC as a probe for molecular alignment, RDCs allowed to obtain conformational information on the backbone and proline side-chain conformations of **1**. In order to use this valuable tool for the structure determination of **3** in addition to the NOE derived information, PDMS/ CDCl_3 gels^[72-73] for the RDC determination of **3** were prepared. PDMS gels with a higher cross linking (PDMS with a irradiation dose of 200 kGy instead of 100 kGy)^[72-73] were used to increase the alignment and therefore the magnitude of the RDCs of **3** in the PDMS-200/ CDCl_3 gel compared to **1** in a PDMS-100 gel (see Table 3.8). The alignment and homogeneity of the gel was investigated with the magnitude of the CDCl_3 quadrupole splitting $\Delta\nu_Q$ and the line widths in deuterium spectra. As expected for PDMS gels,^[48] the line widths in the ^1H and ^2H spectra decreased below 2 Hz and the CDCl_3 quadrupole splitting in the ^2H spectra increased in the course of the homogenization process from 40 to 50 Hz (see Figure 3.13 and Figure 3.14). However, after 130 days a smaller quadrupole splitting of 22.6 Hz was observed indicating mechanical reorientation and relaxation processes in the aged gel.^[48] After homogenization of the gel, 12.5 mg of **3** were added into the solvent above the gel for diffusion into the gel, leading to a concentration of 21 mM of **3** in the gel (distribution coefficient taken into account).^[48]

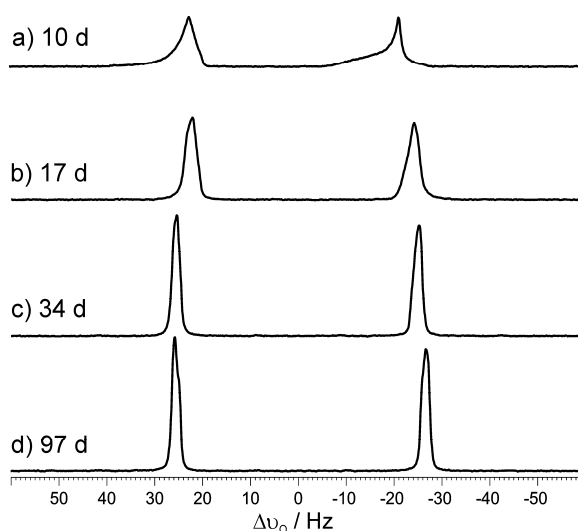


Figure 3.13: CDCl_3 quadrupole splitting in the ^2H spectra of a PDMS-200/ CDCl_3 gel after a) 10, b) 17, c) 34 and d) 97 days, each at 300 K and 600 MHz.

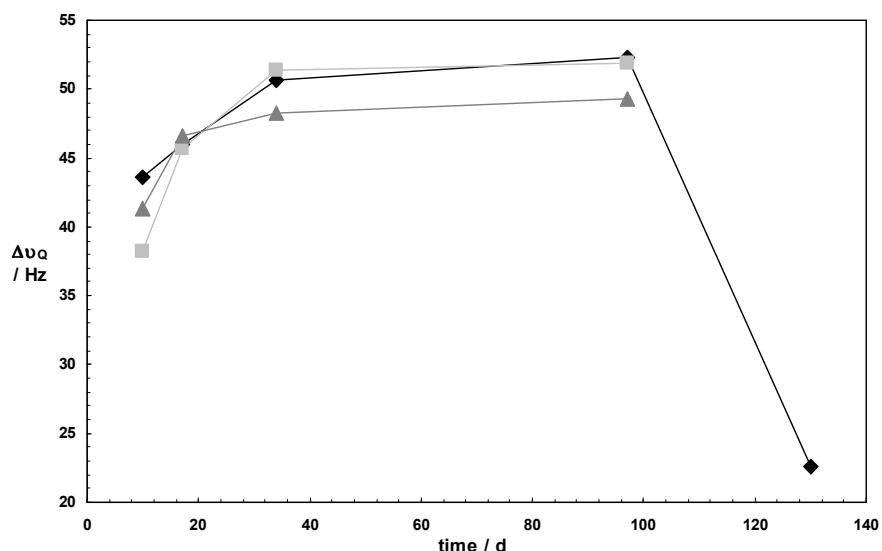


Figure 3.14: Time-dependence of the CDCl_3 quadrupole splitting of three PDMS-200/ CDCl_3 gels.

3.4.2 Determination of RDCs

For the determination of RDCs of **3** at 298 K ^1H spectra and $^1\text{H}, ^{13}\text{C}$ -P.E.HSQC^[74] spectra were measured in CDCl_3 and in a strained PDMS-200/ CDCl_3 gel^[72] which provided a CDCl_3 line splitting of 22.6 Hz. 29 RDCs could be determined experimentally from well-resolved 1D proton spectra and P.E.HSQC spectra at 298 K. They are summarized together with their estimated errors in Table 3.7.

Experimental errors of 0.2 Hz for well-resolved, 0.4 Hz for distorted and therefore partially simulated and 0.7 Hz for completely simulated multiplets were assumed for $^3D_{\text{HH}}$ determined from multiplet analysis of 1D proton spectra. For $^1D_{\text{CH}}$ from P.E.HSQC spectra, the error was estimated to be 1 Hz in case the RDC could be extracted directly from peak splitting in ω_2 , and 2 Hz in case the multiplets in ω_2 had to be simulated with DAISY due to higher order influences or overlap with minor conformations. Errors in $^2D_{\text{HH}}$ from the peak tilt in P.E.HSQC spectra were estimated dependent on the peak quality as 0.4 Hz, 0.7 Hz (one P.E.HSQC row distorted) or 2.0 Hz, if both P.E.HSQC rows could be not analyzed without remaining uncertainties.

Table 3.7: Experimentally determined residual dipolar couplings of **3** at 298 K.

RDC			D / Hz	Δ D / Hz	source			
Hyp(OBn) 1	$^1D_{CH}$	CA	HA	10.0	± 1.0	P.E.HSQC		
		CB	HB1	-2.7	± 2.0	P.E.HSQC		
			HB2	3.2	± 2.0	P.E.HSQC		
		CG	HG	9.6	± 2.0	P.E.HSQC		
		CD	HD1	-0.7	± 2.0	P.E.HSQC		
			HD2	3.4	± 2.0	P.E.HSQC		
	$^2D_{HH}$	HB1	HB2	0.5	± 0.7	P.E.HSQC and 1D- 1H		
		HD1	HD2	-0.6	± 0.4	P.E.HSQC and 1D 1H		
	$^3D_{HH}$	HA	HB1	-0.2	± 0.4	1D 1H		
			HB2	1.9	± 0.4	1D 1H		
		HB2	HG	-8	± 0.4	1D 1H		
	β -ACC	$^1D_{CH}$	CAB	HAB1	-4.7	± 1.0	P.E.HSQC	
CAC			HAC1	-0.7	± 2.0	P.E.HSQC		
CAE			HAE1	4.4	± 1.0	P.E.HSQC		
$^3D_{HH}$		HAB	HAB1	-0.8	± 0.4	1D 1H		
		HAB1	HAC1	-1.5	± 0.7	1D 1H		
		HAB1	HAE1	0.4	± 0.2	1D 1H		
		HAC1	HAE1	2.0	± 0.2	1D 1H		
		Pro 3	$^1D_{CH}$	CA	HA	-6.5	± 1.0	P.E.HSQC
				CB	HB1	7.8	± 2.0	P.E.HSQC
HB2	-12.5				± 2.0	P.E.HSQC		
CG	HG1/HG2			3.1	± 8.0	P.E.HSQC		
$^2D_{HH}$	CD		HD1/HD2	-1.3	± 8.0	P.E.HSQC		
	HB1		HB2	-7.3	± 0.7	P.E.HSQC		
		HD1	HD2	-6.9	± 2.0	P.E.HSQC		
	$^3D_{HH}$	HA	HB1	3.1	± 0.2	1D 1H		
			HB2	-0.4	± 0.2	1D 1H		

Table 3.8: Quadrupole splitting and maximum absolute values of the experimental RDCs of **1** in a PDMS-100 and **3** in a PDMS-200 gel, both at 298 K. The higher cross-linking of the PDMS-200 gel leads to larger RDC values.

PDMS gel	100	200
$\Delta\nu_Q$ / Hz	22	22.6
peptide	1	3
$^1D_{CH}$ / Hz	7.4	12.5
$^3D_{HH}$ / Hz	3	3.1
$^2D_{HH}$ / Hz	3.8	7.3

3.5 References

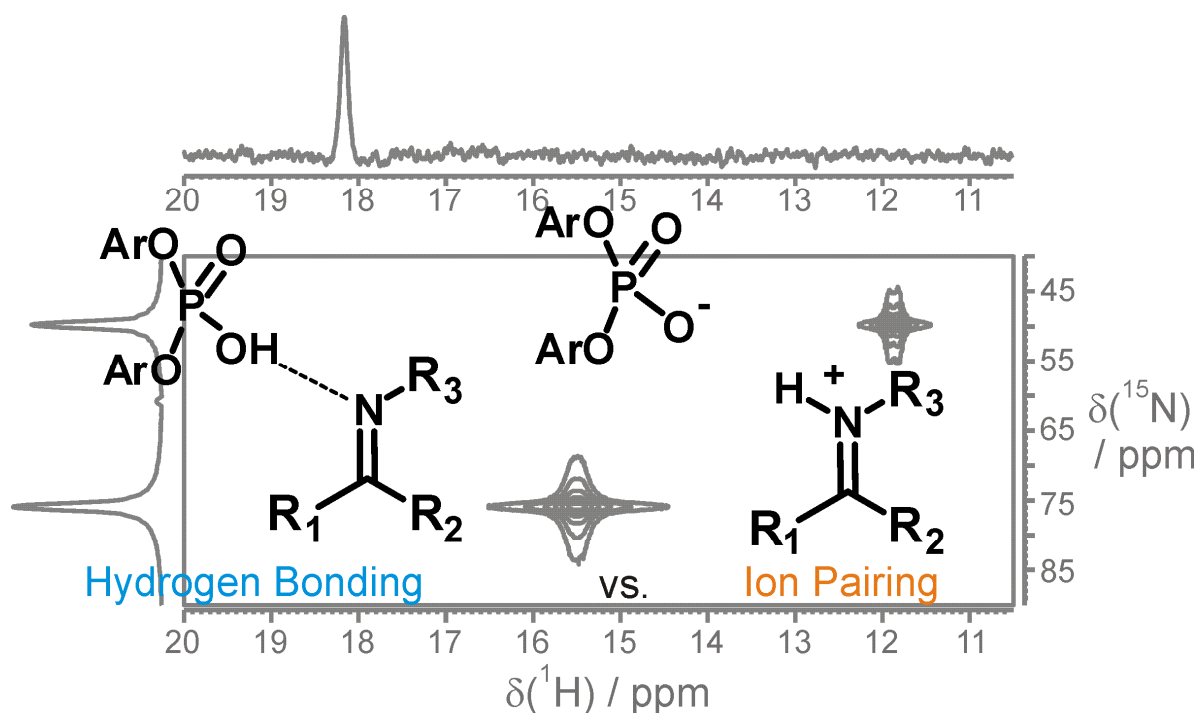
- [1] E. A. C. Davie, S. M. Mennen, Y. Xu, S. J. Miller, *Chem. Rev.* **2007**, *107*, 5759-5812.
- [2] G. Licini, L. Prins, P. Scrimin, *Eur. J. Org. Chem.* **2005**, 969-977.
- [3] J. D. Revell, H. Wennemers, *Curr. Opin. Chem. Biol.* **2007**, *11*, 269-278.
- [4] S. J. Miller, *Acc. Chem. Res.* **2004**, *37*, 601-610.
- [5] R. Beumer, C. Bubert, C. Cabrele, O. Vielhauer, M. Pietsch, O. Reiser, *J. Org. Chem.* **2000**, *65*, 8960-8969.
- [6] N. Koglin, C. Zorn, R. Beumer, C. Cabrele, C. Bubert, N. Sewald, O. Reiser, A. G. Beck-Sickinger, *Angew. Chem. Int. Ed.* **2003**, *42*, 202-205.
- [7] S. Urman, K. Gaus, Y. Yang, U. Strijowski, N. Sewald, S. DePol, O. Reiser, *Angew. Chem. Int. Ed.* **2007**, *46*, 3976-3978.
- [8] V. D'Elia, H. Zwicknagl, O. Reiser, *J. Org. Chem.* **2008**, *73*, 3262-3265.
- [9] S. De Pol, C. Zorn, C. D. Klein, O. Zerbe, O. Reiser, *Angew. Chem. Int. Ed.* **2004**, *43*, 511-514.
- [10] C. Zorn, PhD thesis, University of Regensburg (Regensburg (Germany)), **2001**.
- [11] M. B. Schmid, M. Fleischmann, V. D'Elia, O. Reiser, W. Gronwald, R. M. Gschwind, *ChemBioChem* **2009**, *10*, 440-444.
- [12] C. A. G. Haasnoot, F. A. A. M. De Leeuw, H. P. M. De Leeuw, C. Altona, *Biopolymers* **1981**, *20*, 1211-1245.
- [13] A. E. Aliev, D. Courtier-Murias, *J. Phys. Chem. B* **2007**, *111*, 14034-14042.
- [14] I. K. Song, Y. K. Kang, *J. Phys. Chem. B* **2006**, *110*, 1915-1927.
- [15] A. T. Brünger, P. D. Adams, G. M. Clore, W. L. DeLano, P. Gros, R. W. Grosse-Kunstleve, J.-S. Jiang, J. Kuszewski, M. Nilges, N. S. Pannu, R. J. Read, L. M. Rice, T. Simonson, G. L. Warren, *Acta Crystallogr., Sect. D* **1998**, *54*, 905-921.
- [16] R. Improta, C. Benzi, V. Barone, *J. Am. Chem. Soc.* **2001**, *123*, 12568-12577.
- [17] J. S. W. Lam, J. C. P. Koo, I. Hudáky, A. Varro, J. G. Papp, B. Penke, I. G. Csizmadia, *THEOCHEM* **2003**, *666-667*, 285-289.
- [18] W. Gronwald, H. R. Kalbitzer, *Progr. in NMR Spectr.* **2004**, *44*, 33-96.
- [19] J. H. Schreiber, Diploma thesis, University of Regensburg (Germany) **2003**.
- [20] H. J. Dyson, P. E. Wright, *Annu. Rev. Biophys. Biophys. Chem.* **1991**, *20*, 519-538.
- [21] Z. L. Madi, C. Griesinger, R. R. Ernst, *J. Am. Chem. Soc.* **1990**, *112*, 2908-2914.
- [22] M. Cai, Y. Huang, J. Liu, R. Krishnamoorthi, *J. Biomol. NMR* **1995**, *6*, 123-128.
- [23] G. N. Ramachandran, A. V. Lakshminarayanan, R. Balasubramanian, G. Tegoni, *Biochimica et Biophysica Acta (BBA) - Protein Structure* **1970**, *221*, 165-181.
- [24] M. C. Reddy, B. P. N. Reddy, J. Ramakrishna, *Spectrochimica Acta Part A: Molecular Spectroscopy* **1985**, *41*, 1229-1233.
- [25] S. N. Rao, S. J. Profeta, V. N. Balaji, *Protein Pept. Lett.* **1998**, *5*, 41-48.
- [26] E. M. Arnett, E. J. Mitchell, T. S. S. R. Murty, *J. Am. Chem. Soc.* **1974**, *96*, 3875-3891.
- [27] J.-Y. Le Questel, C. Laurence, A. Lachkar, M. Helbert, M. Berthelot, *J. Chem. Soc., Perkin Trans. 2* **1992**, 2091-2094.
- [28] T. Steiner, *Angew. Chem. Int. Ed.* **2002**, *41*, 48-76.
- [29] T. Steiner, G. Koellner, *J. Mol. Biol.* **2001**, *305*, 535-557.
- [30] S. Sharif, G. S. Denisov, M. D. Toney, H.-H. Limbach, *J. Am. Chem. Soc.* **2007**, *129*, 6313-6327.
- [31] S. Sharif, E. Fogle, M. D. Toney, G. S. Denisov, I. G. Shenderovich, G. Buntkowsky, P. M. Tolstoy, M. C. Huot, H.-H. Limbach, *J. Am. Chem. Soc.* **2007**, *129*, 9558-9559.
- [32] S. Sharif, D. Schagen, M. D. Toney, H.-H. Limbach, *J. Am. Chem. Soc.* **2007**, *129*, 4440-4455.
- [33] A. Jansma, Q. Zhang, B. Li, Q. Ding, T. Uno, B. Bursulaya, Y. Liu, P. Furet, N. S. Gray, B. H. Geierstanger, *J. Med. Chem.* **2007**, *50*, 5875-5877.
- [34] D. Yang, J. Qu, B. Li, F.-F. Ng, X.-C. Wang, K.-K. Cheung, D.-P. Wang, Y.-D. Wu, *J. Am. Chem. Soc.* **1999**, *121*, 589-590.
- [35] G. V. M. Sharma, P. Nagendar, P. Jayaprakash, P. Radha Krishna, K. V. S. Ramakrishna, A. C. Kunwar, *Angew. Chem. Int. Ed.* **2005**, *44*, 5878-5882.
- [36] M. Brandl, M. S. Weiss, A. Jabs, J. Sühnel, R. Hilgenfeld, *J. Mol. Biol.* **2001**, *307*, 357-377.
- [37] K. Brickmann, Z. Yuan, I. Sethson, P. Somfai, J. Kihlberg, *Chem. Eur. J.* **1999**, *5*, 2241-2253.
- [38] G. A. Jeffrey, *An Introduction to Hydrogen Bonding*, Oxford University Press, Oxford, **1997**.
- [39] R. W. Hoffmann, *Chem. Rev.* **1989**, *89*, 1841-1860.
- [40] S. Bahmanyar, K. N. Houk, H. J. Martin, B. List, *J. Am. Chem. Soc.* **2003**, *125*, 2475-2479.
- [41] B. List, L. Hoang, H. J. Martin, *Proc. Natl. Acad. Sci.* **2004**, *101*, 5839-5842.

- [42] A. Jerschow, N. Müller, *J. Magn. Reson.* **1997**, *125*, 372-375.
- [43] C. S. Johnson, *Prog. Nucl. Magn. Reson. Spectrosc.* **1999**, *34*, 203-256.
- [44] P. M. Fischer, *J. Pept. Sci.* **2003**, *9*, 9-35.
- [45] C. Goolcharran, R. T. Borchardt, *J. Pharm. Sci.* **1998**, *87*, 283-288.
- [46] M. B. Schmid, K. Zeitler, R. M. Gschwind, *Angew. Chem. Int. Ed.* **2010**, *49*, 4997-5003.
- [47] M. B. Schmid, K. Zeitler, R. M. Gschwind, *J. Am. Chem. Soc.* **2011**, *133*, 7065-7074.
- [48] M. Fleischmann, Diploma thesis, University of Regensburg (Germany) **2007**.
- [49] E. R. Jarvo, S. J. Miller, *Tetrahedron* **2002**, *58*, 2481-2495.
- [50] V. D'Elia, PhD thesis, University Regensburg (Regensburg (Germany)), **2009**.
- [51] D. E. Dorman, F. A. Bovey, *J. Org. Chem.* **1973**, *38*, 2379-2383.
- [52] C. Grathwohl, K. Wüthrich, *Biopolymers* **1976**, *15*, 2025-2041.
- [53] T. W. Phillips, K. P. Murphy, *J. Chem. Eng. Data* **1970**, *15*, 304-307.
- [54] I. B. Rabinovich, A. A. Lobashov, V. I. Kucheryavii, *Zhurnal Fizicheskoi Khimii* **1960**, *34*, 2202-2204.
- [55] D. R. Lide, *CRC Handbook of Chemistry and Physics*, 90. ed., Taylor & Francis, **2009**.
- [56] A. T. Brünger, P. D. Adams, G. M. Clore, W. L. DeLano, P. Gros, R. W. Grosse-Kunstleve, J.-S. Jiang, J. Kuszewski, M. Nilges, N. S. Pannu, R. J. Read, L. M. Rice, T. Simonson, G. L. Warren, *Acta Cryst.* **1998**, *D54*, 905-921.
- [57] <http://www.wavefun.com/>.
- [58] A. W. Schüttelkopf, D. M. F. van Aalten, *Acta Cryst.* **2004**, *D60*, 1355-1363.
- [59] G. J. Kleywegt, K. Henrick, E. J. Dodson, D. M. F. van Aalten, *Structure* **2003**, *11*, 1051-1059.
- [60] A. Pedretti, L. Villa, G. Vistoli, *J. Comput.-Aided Mol. Des.* **2004**, *18*, 167-173.
- [61] M. E. Martín, A. Muñoz Losa, I. F. Galván, M. A. Aguilar, *J. Mol. Struct. (THEOCHEM)* **2006**, *775*, 81-86.
- [62] R. Koradi, M. Billeter, K. Wüthrich, *J. Mol. Graphics* **1996**, *14*, 51-55.
- [63] C. A. G. Haasnoot, F. A. A. M. de Leeuw, C. Altona, *Tetrahedron* **1980**, *36*, 2783-2792.
- [64] V. F. Bystrov, *Prog. Nucl. Magn. Reson. Spectrosc.* **1976**, *10*, 41-82.
- [65] A. G. M. Barrett, R. A. James, G. E. Morton, P. A. Procopiou, C. Boehme, A. deMeijere, C. Griesinger, U. M. Reinscheid, *J. Org. Chem.* **2006**, *71*, 2756-2759.
- [66] M. C. Khosla, R. R. Smeby, F. M. Bumpus, *J. Am. Chem. Soc.* **1972**, *94*, 4721-4724.
- [67] W. S. Price, *Concepts Magn. Reson.* **1998**, *10*, 197-237.
- [68] E. O. Stejskal, J. E. Tanner, *The Journal of Chemical Physics* **1965**, *42*, 288-292.
- [69] C. A. Crutchfield, D. J. Harris, *J. Magn. Reson.* **2007**, *185*, 179-182.
- [70] M. B. Schmid, PhD thesis, University Regensburg (Regensburg (Germany)), **2011**.
- [71] Y. Marcus, *Chem. Soc. Rev.* **1993**, *22*, 409-416.
- [72] J. C. Freudenberger, P. Spiteller, R. Bauer, H. Kessler, B. Luy, *J. Am. Chem. Soc.* **2004**, *126*, 14690-14691.
- [73] J. Klages, C. Neubauer, M. Coles, H. Kessler, B. Luy, *ChemBioChem* **2005**, *6*, 1672-1678.
- [74] P. Tzvetkova, S. Simova, B. Luy, *J. Magn. Reson.* **2007**, *186*, 193-200.

4 Brønsted Acid Catalysis – Hydrogen Bonding vs. Ion Pairing

Communication:

“Brønsted Acid Catalysis – Hydrogen Bonding versus Ion Pairing in Imine Activation”



Matthias Fleischmann, Diana Drettwan,
Erli Sugiono, Magnus Rueping, Ruth M. Gschwind

Angew. Chem. **2011**, 123, 6488-6493

Angew. Chem. Int. Ed. **2011**, 50, 6364-6269

<http://dx.doi.org/10.1002/ange.201101385>

<http://dx.doi.org/10.1002/anie.201101385>

The synthesis of the compounds was performed by Erli Sugiono.

The NMR investigations were performed in close collaboration with Diana Drettwan.

4.1 Abstract

NMR spectroscopy was used to distinguish hydrogen-bonding and ion pairing in the activation of imines by a phosphate catalyst. Hydrogen-bond strength and the amount of the hydrogen-bonded species present are decisive for the catalytic reaction and can be manipulated by introducing substituents with different electronic properties. This insight should guide the development of more efficient catalytic systems.

4.2 Manuscript

Despite the crucial role of hydrogen-bonding interactions and proton transfer in organocatalysis, especially in the reactions involving Brønsted acid catalysts,^[1-6] fundamental understanding of the nature of catalyst-substrate complexes in solution is rather limited. One reason for the challenges associated with investigation of the catalytically active species in Brønsted acid catalysis is their lack of experimental accessibility. This difficulty is valid in particular for 1,1'-binaphthalene-2,2'-diol (binol) phosphoric acids,^[7-24] with which the activation of the substrate takes place either through proton transfer or hydrogen-bonding, with or without charge assistance by the catalyst. To improve the catalytic performance of Brønsted acid catalysts, it is essential to identify the different catalytic species present in solution. Schrader et al. were able to detect key intermediates in a cascade reaction involving a binol-derived phosphoric acid catalyst by electrospray ionization mass spectroscopy (ESI-MS).^[25] However, with this method, it was not possible to differentiate between proton transfer and hydrogen-bond formation. Owing to our tremendous interest in the further development of binol-derived phosphoric acids and derivatives as efficient Brønsted acid catalysts for application in various transformations involving imines,^[7-10, 13-24] we decided to conduct experiments which would help identify the activation mode in these reactions.

NMR spectroscopy has emerged as a powerful technique for the investigation of both hydrogen-bonding and ion pair systems.^[26-27] Limbach and co-workers showed in marvelous studies on the hydrogen-bond networks in various pyridoxal 5'-phosphate derived Schiff bases that the intermolecular hydrogen-bonds could be characterized by a combination of ^1H and ^{15}N NMR spectroscopy.^[28-31] A correlation between the ^1H and ^{15}N chemical shifts, the corresponding coupling constants $^1J_{\text{H,N}}$, and the hydrogen-bond strength was found. In principle, the direct detection of 1D, 2D, and 3D correlations caused by intermolecular $^2J_{\text{H,P}}$ and $^1J_{\text{H,N}}$ couplings is possible; however, sharp line widths, which indicate slow relaxation, are required. Only few studies dealing with the detection of magnetization transfer through hydrogen-bonds in non-biomolecules in organic solvents have been reported. For example, we investigated artificial arginine and acylguanidine complexes by NMR spectroscopy.^[32-33]

Hence, we chose NMR spectroscopy as an adequate tool to identify the species present in various Brønsted acid/imine mixtures and to examine the influence of temperature and concentration on imine protonation.^[34-41]

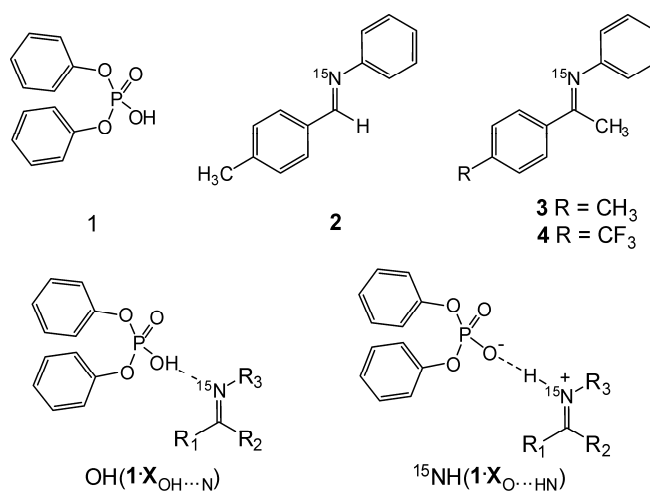


Figure 4.1: Investigated model systems with the phosphorus-based acid catalyst diphenyl phosphate **1** and different imines **2-4**.

The model compounds selected for our investigations are depicted in Figure 4.1. Diphenyl phosphate (DPP, **1**, $pK_a < 2$) was selected as an achiral phosphate used in Brønsted acid catalyzed transformations.^[7-24] Imines **2** and **3** were selected as substrates to identify the main trends between aldimines and ketimines. The effect of electron density was investigated with the aid of ketimines **3** and **4** bearing aromatic substituents with different electronic properties. For the setup of the optimal experimental conditions, the NMR properties of the complex **1·2** were investigated in dichloromethane, chloroform and toluene, the typical solvents used in synthetic applications.^[7-24] Toluene was found to provide by far the best chemical shift dispersion and solubility. To enable the detection of the hydrogen-bonding properties of the analyzed complexes **1·2**, **1·3**, and **1·4**, 1:1 mixtures of the phosphate and the imine were used, and the highest possible concentration was chosen for each individual complex (100, 40, and 20 mM, respectively).¹ To enable the determination of $^1J_{^{15}\text{N},^1\text{H}}$ coupling constants and to facilitate ^1H , ^{15}N magnetization transfer, we synthesized ^{15}N -labeled imines **2-4**. Since the NMR spectra of the three complexes investigated were very similar, the NMR spectroscopic approach used to identify the position of the crucial proton is explained exemplarily for complex **1·2**. All NMR spectroscopic data of **1·2**, **1·3**, and **1·4** are summarized in Table 4.3 in the Supporting Information.

At 300 K the ^1H spectrum of **1-2** showed only one averaged signal for the acidic proton (Figure 4.2a). Therefore, we carried out low-temperature studies to identify chemical exchange processes, which are highly probable at room temperature between the proposed species formed by intermolecular hydrogen-bonding and proton transfer species. Indeed, below 280 K, three

¹ Deviations from the 1:1 ratio between **1** and imine lead to an extreme acceleration of the chemical exchange of the acidic proton, which prevent the NMR detection of individual H-bonded species even at low temperatures.

signals were observed for the acidic proton. These signals become sharper as the temperature was decreased to 240 K (Figure 4.2a), at which temperature a singlet at $\delta=18.16$ ppm and two doublets at $\delta=15.50$ and 11.87 ppm with $^1J_{\text{H,N}}$ coupling constants of 86.0 ± 1 and 69.5 ± 1 Hz were observed.^{II} Upon further cooling, each of the two signals above 15 ppm split into a group of signals, which indicated similar binding properties of the acidic proton but structurally slightly deviating species. (the complete temperature series is depicted in Figure 4.6 in the Supporting Information). In contrast, in the ^{31}P spectra only one averaged singlet was observed at all temperatures (Figure 4.2b).

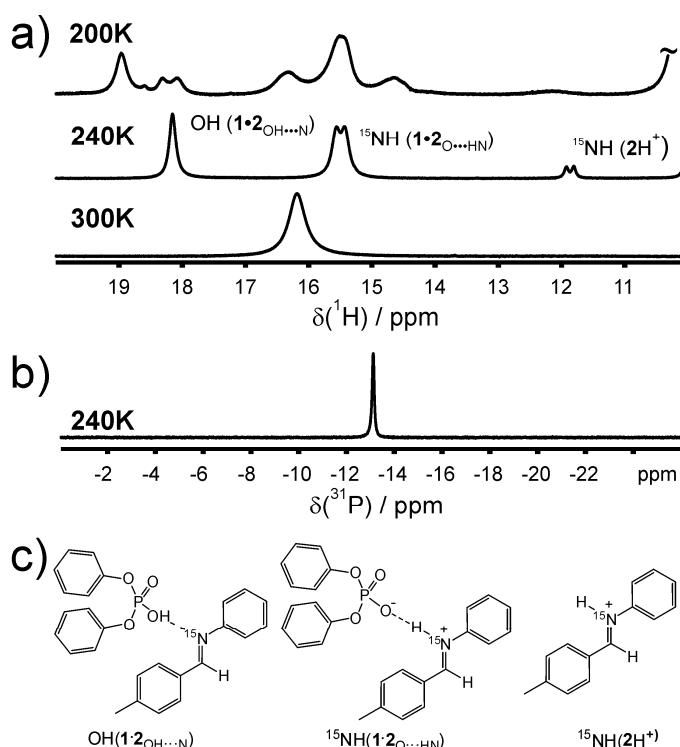


Figure 4.2: a) Temperature dependence of the ^1H spectra of 1-2. b) ^{31}P spectrum of 1-2 at 240 K in $[\text{D}_8]\text{toluene}$ at 600 MHz. c) Identified species.

In the temperature study, extremely broad proton signals (line widths up to 480 Hz) were detected (see Figure 4.2a and also Figure 4.6 in the Supporting Information). This broadness indicates very short transversal relaxation times and exchange, which severely hamper the detection of magnetization transfer as required for the differentiation of hydrogen-bonded and proton transfer complexes. Therefore, for the subsequent NMR spectroscopic investigations, we chose a temperature of 240 K, which provides the smallest line widths (165, 105, and 50 Hz) and shows one averaged signal for each of the three main species (Figure 4.2c). In principle, it should

^{II} The unusually small coupling constant of 69.5 Hz for $\text{NH}(2\text{H}^+)$ is probably a result of partial decoupling caused by the pronounced exchange with the two complex species observed in NOESY spectra at 240 K.

be possible to identify the bonding properties of the acidic proton in these three species from ^1H , ^{31}P -HMBC and ^1H , ^{15}N -HMQC spectra. For POH compounds, ^1H , ^{31}P -HMBC cross peaks are expected, and for HN^+ compounds, ^1H , ^{15}N -HMQC cross peaks should be observed. Indeed, two cross peaks were detected in the ^1H , ^{15}N -HMQC spectrum (Figure 4.3c). These cross peaks enabled the assignment of the signals at $\delta=15.50$ and 11.87 ppm to HN^+ species. For the third proton signal at $\delta=18.16$ ppm, no cross peak was observed despite extensive magnetization-transfer-delay optimizations in various ^1H , ^{15}N -HMBC experiments and experimental times up to 10 h. No cross peaks were observed in the corresponding ^1H , ^{31}P -HMBC spectra even when various spectroscopic parameters were used. This lack of cross peaks can be explained by the short transversal relaxation times of the three proton signals in combination with small $^2J_{\text{H,P}}$ coupling constants. Therefore, we carried out time-shared ^{31}P , ^1H -INEPT experiments (INEPT = insensitive nuclei enhanced by polarization transfer), which show significantly higher signal-to-noise ratios for systems with long ^{31}P T_2 times and short ^1H T_2 times.^[32] However, even in transfer-delay-optimized ^{31}P , ^1H -INEPT spectra with experimental times around 10 h, only one cross peak to the signal at $\delta=18.16$ ppm was detected (Figure 4.3b). These ^1H , ^{15}N -HMQC and ^{31}P , ^1H -INEPT spectra show that in a 1:1 mixture of **1** and **2**, one POH and two HN^+ species exist simultaneously, and that the detection of magnetization transfer through potential hydrogen-bonds in these species is hampered by short ^1H relaxation times and small $^{\text{nh}}J$ values.

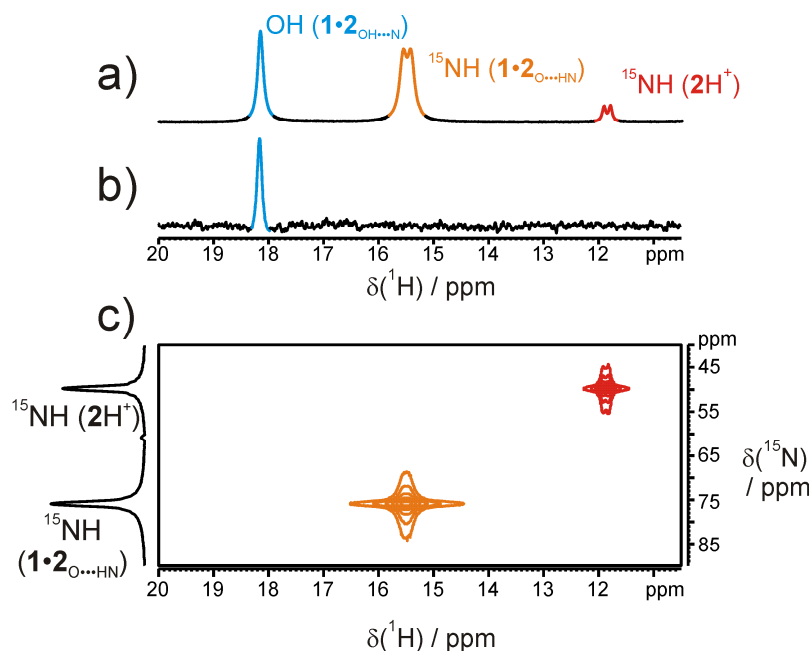


Figure 4.3: NMR spectroscopic characterization of the 1:1 complex of **1** and **2** at 240 K in $[\text{D}_8]\text{toluene}$ at 600 MHz: a) OH region of the ^1H spectrum indicating three different species. b) 1D ^{31}P , ^1H -INEPT spectrum. c) 2D ^1H , ^{15}N -HMQC spectrum.

First, the POH species ($\delta(^1\text{H})=18.16$ ppm) was identified. In principle, this signal could either belong to **1** or to the expected $\text{OH}(\mathbf{1}\cdot\mathbf{2}_{\text{OH}\cdots\text{N}})$ complex (Figure 4.2c). To differentiate between these two possibilities, we investigated the chemical shifts and aggregation levels of the pure catalyst **1** and compared them to those of the **1**·**2** sample. At 240 K, pure **1** showed a significantly highfield shifted OH signal at $\delta(^1\text{H})=13.80$ ppm, which is close to the value for dimethyl phosphate.^[42] This signal did not split into several signals at temperatures below 240 K as found for **1**·**2** (for spectra see Figure 4.9 in the SI). Furthermore, diffusion measurements showed different values for **1** and $\text{OH}(\mathbf{1}\cdot\mathbf{2}_{\text{OH}\cdots\text{N}})$, and when the temperature was lowered for **1**, a trend from the formation of dimers to the formation of trimers was observed, as similarly reported for dimethyl phosphate (for details see SI).^[42] Therefore, the presence of pure **1** in the **1**·**2** sample can clearly be excluded.

For the POH species in the **1**·**2** sample, the diffusion values were in agreement with the formation of a **1**·**2** complex (for details, see the Supporting Information), which we refer to herein as the DPP-aldimine complex $\text{OH}(\mathbf{1}\cdot\mathbf{2}_{\text{OH}\cdots\text{N}})$ (Figure 4.2c). The remarkable downfield shift of the OH proton signal in the spectrum of $\text{OH}(\mathbf{1}\cdot\mathbf{2}_{\text{OH}\cdots\text{N}})$ compared to the OH proton signal of the **1**·**1** dimer suggests the presence of a stronger hydrogen-bond in $\text{OH}(\mathbf{1}\cdot\mathbf{2}_{\text{OH}\cdots\text{N}})$ than in the **1**·**1** dimer. However, anisotropy effects of the aldimine substituents in $\text{OH}(\mathbf{1}\cdot\mathbf{2}_{\text{OH}\cdots\text{N}})$ may also contribute to the observed chemical shift difference.

Next, the two HN^+ species were assigned. In principle, these signals could belong to 2H^+ , $2\cdot 2\text{H}^+$, or the expected $\text{NH}(\mathbf{1}\cdot\mathbf{2}_{\text{O}\cdots\text{HN}})$ complex (Figure 4.2c). To differentiate between these possibilities, we simulated the chemical shifts and/or aggregation levels of 2H^+ and $2\cdot 2\text{H}^+$ with samples of **2** combined with 1.0 and 0.5 equivalents of HBF_4 , respectively. The experiments with **2** and one equivalent of HBF_4 resulted in a proton signal for 2H^+ at $\delta=11.39$ ppm, very close to that at $\delta=11.87$ ppm for the **1**·**2** sample. This result indicates the existence of the free protonated aldimine $\text{NH}(2\text{H}^+)$ in the **1**·**2** sample (see Figure 4.2c for the complexes and for spectra see Figure 4.10 in the Supporting Information). The presence of $\text{NH}(2\text{H}^+)$ was confirmed by ^1H -DOSY experiments, which revealed a temperature- and viscosity-corrected diffusion coefficient of $D_{\text{corr}}(\text{NH}(2\text{H}^+)) = 4.40\cdot 10^{-10} \text{ m}^2 \text{ s}^{-1}$, indicative for a monomeric aldimine. The experiments with **2** and 0.5 equivalents of HBF_4 resulted in a proton signal at $\delta=12.14$ ppm for the $2\cdot 2\text{H}^+$ complex. This chemical shift is close to that observed for monomeric 2H^+ ; however, a downfield shift by 3.36 ppm was observed for the second HN^+ signal observed in the **1**·**2** sample at $\delta=15.50$ ppm. Therefore, the formation of $2\cdot 2\text{H}^+$ in the **1**·**2** sample could be excluded. The remarkably higher chemical shift of the main HN^+ species relative to those of 2H^+ and $2\cdot 2\text{H}^+$ can be interpreted as a strong hint for the formation of a hydrogen-bond to the phosphoric acid.

Therefore, this species was assigned as $\text{NH}(\mathbf{1}\cdot\mathbf{2}_{\text{O}\cdots\text{HN}})$ (Figure 4.2c). Furthermore, the DOSY value, $D_{\text{corr}} = 1.39 \cdot 10^{-10} \text{ m}^2 \text{ s}^{-1}$, obtained for $\text{NH}(\mathbf{1}\cdot\mathbf{2}_{\text{O}\cdots\text{HN}})$ clearly indicates the formation of a complex. The calculated hydrodynamic volume of $\text{NH}(\mathbf{1}\cdot\mathbf{2}_{\text{O}\cdots\text{HN}})$ is puzzling at a first glance, because it is two times larger than that of $\text{OH}(\mathbf{1}\cdot\mathbf{2}_{\text{OH}\cdots\text{N}})$, see SI. However, if one considers that toluene was used as the solvent and that, in contrast to $\text{OH}(\mathbf{1}\cdot\mathbf{2}_{\text{OH}\cdots\text{N}})$, $\text{NH}(\mathbf{1}\cdot\mathbf{2}_{\text{O}\cdots\text{HN}})$ is a contact ion pair, which offers additional possibilities for electrostatic and cation- π interactions, this greater hydrodynamic volume is in accordance with the assignment of the two complex species. Another possible explanation for the increased volume is stabilization by additional acid molecules, as previously found by Limbach and co-workers.^[43]

Thus, the combined NMR spectroscopic results discussed above show that the complex **1·2** does not form solely a hydrogen-bonded species or a contact ion pair in solution, but that both species $\text{OH}(\mathbf{1}\cdot\mathbf{2}_{\text{OH}\cdots\text{N}})$ and $\text{NH}(\mathbf{1}\cdot\mathbf{2}_{\text{O}\cdots\text{HN}})$ coexist simultaneously. Furthermore, minor amounts of the free protonated aldimine $\text{NH}(\mathbf{2}\text{H}^+)$ are present.

In synthetic applications, variations in reactivity have been reported for aldimines and differently substituted ketimines upon modification of the electron density of the imine moiety.^[7-25] Therefore, we investigated the effect of an aldimine versus a ketimine as well as the effect of different substituents in the ketimine on the ratio of the hydrogen-bonded species to the contact ion pair in these Brønsted acid/imine complexes. To elucidate the influence of ketimines, we chose the structurally closest complex **1·3**; for the investigation of substituent effects, the complex **1·4** was selected additionally (for structures see Figure 4.1).

Again, the ^1H spectra of **1·3** and **1·4** showed one averaged signal each for the acidic proton at 300 K (for spectra see Figure 4.7 and Figure 4.8 in the SI). Low-temperature measurements in combination with the spectroscopic assignment procedures described above again revealed the coexistence of three species, $\text{OH}(\mathbf{1}\cdot\mathbf{3}/\mathbf{4}_{\text{OH}\cdots\text{N}})$, $\text{NH}(\mathbf{1}\cdot\mathbf{3}/\mathbf{4}_{\text{O}\cdots\text{HN}})$, and $\text{NH}(\mathbf{3}/\mathbf{4}\text{H}^+)$, in both samples (see Figure 4.4). However, the low-temperature ^1H spectra of **1·3** and **1·4** showed that the absolute chemical shift differences and the ratio of the $\text{OH}(\mathbf{1}\cdot\mathbf{X}_{\text{OH}\cdots\text{N}})$, $\text{NH}(\mathbf{1}\cdot\mathbf{X}_{\text{O}\cdots\text{HN}})$, and $\text{NH}(\mathbf{X}\text{H}^+)$ species vary according to the properties of the imine (see Figure 4.4 and Table 4.1).

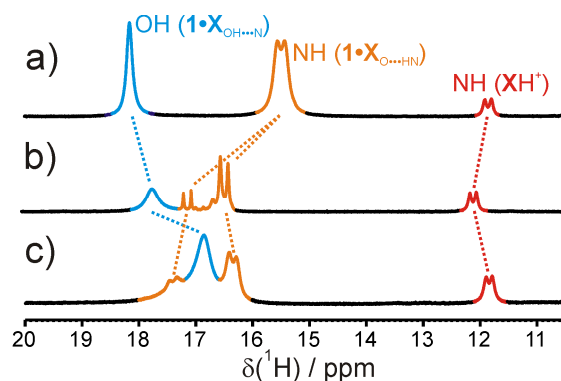


Figure 4.4: ^1H spectra of the different imine-catalyst complexes in $[\text{D}_8]\text{toluene}$ at 600 MHz: a) **1·2** at 240 K; b) **1·3** at 220 K; c) **1·4** at 210 K. The best chemical shift dispersion and the best line widths of the proton signals were detected at different temperatures for the three samples.


Table 4.1: Relative amounts of $\text{OH}(\mathbf{1}\cdot\text{X}_{\text{OH}\cdots\text{N}})$ and $\text{NH}(\mathbf{1}\cdot\text{X}_{\text{O}\cdots\text{HN}})$ in the different samples **1·2**, **1·3**, and **1·4** at 220 K.

Sample	$\text{OH}(\mathbf{1}\cdot\text{X}_{\text{OH}\cdots\text{N}})$	$\text{NH}(\mathbf{1}\cdot\text{X}_{\text{O}\cdots\text{HN}})$
1·2	0.33	0.67
1·3	0.42	0.58
1·4	0.61	0.39

In **1·2**, the chemical shift difference between $\text{OH}(\mathbf{1}\cdot\mathbf{2}_{\text{OH}\cdots\text{N}})$ and $\text{NH}(\mathbf{1}\cdot\mathbf{2}_{\text{O}\cdots\text{HN}})$ was the largest ($\Delta\delta=2.66$ ppm). In the ketimine sample **1·3**, the chemical shift difference between $\text{OH}(\mathbf{1}\cdot\mathbf{3}_{\text{OH}\cdots\text{N}})$ and $\text{NH}(\mathbf{1}\cdot\mathbf{3}_{\text{O}\cdots\text{HN}})$ was decreased to $\Delta\delta=1.76$ ppm (weighted average of the two $\text{NH}(\mathbf{1}\cdot\mathbf{3}_{\text{O}\cdots\text{HN}})$ species), and in **1·4**, the signals for the different subspecies $\text{OH}(\mathbf{1}\cdot\mathbf{4}_{\text{OH}\cdots\text{N}})$ and $\text{NH}(\mathbf{1}\cdot\mathbf{4}_{\text{O}\cdots\text{HN}})$ even overlap. This stepwise decrease in the $\Delta\delta(^1\text{H})$ values indicates a decrease in the hydrogen-bond strengths within the three complexes, whereby **1·2**>**1·3**>**1·4**. According to the outstanding and very detailed studies of Limbach and co-workers on the strength of hydrogen-bonds to an enzymatic cofactor,^[28–31] such a decrease in hydrogen-bond strength should correlate with an increase in the ^1H and ^{15}N chemical shift values and a decrease in the $^1J_{\text{H,N}}$ values of the $\text{NH}(\mathbf{1}\cdot\text{X}_{\text{O}\cdots\text{HN}})$ species. Indeed, these trends fit perfectly with those observed for $\text{NH}(\mathbf{1}\cdot\mathbf{2}_{\text{O}\cdots\text{HN}})$ and the two $\text{NH}(\mathbf{1}\cdot\mathbf{3}_{\text{O}\cdots\text{HN}})$ species (Table 4.2). Thus, the different species found for the investigated Brønsted acid/imine complexes are hydrogen-bonded complexes with varying hydrogen-bond strengths in different stages of the proton transfer reaction. In accordance with this concept,^[44] the ratios of the $\text{OH}(\mathbf{1}\cdot\text{X}_{\text{OH}\cdots\text{N}})$ and $\text{NH}(\mathbf{1}\cdot\text{X}_{\text{O}\cdots\text{HN}})$ species also vary (Table 4.1). In **1·2**, which has the strongest hydrogen-bonds, the proton transfer reaction is most pronounced, and the highest amount of $\text{NH}(\mathbf{1}\cdot\mathbf{2}_{\text{O}\cdots\text{HN}})$ was also observed. Samples **1·3** and **1·4** showed

decreasing amounts of $\text{NH}(\mathbf{1}\cdot\mathbf{3}/\mathbf{4})_{\text{O}\cdots\text{HN}}$ in agreement with the decreased hydrogen-bond strength indicated by the NMR spectroscopic parameters discussed above.

Table 4.2: Hydrogen-bond characteristics of the three complexes **1·2**, **1·3** and **1·4**.

	$\Delta\delta(^1\text{H})^{[\text{a}]} / \text{ppm}$	$\delta(^1\text{H})^{[\text{b}]} / \text{ppm}$	$\delta(^{15}\text{N})^{[\text{b}]} / \text{ppm}$	$^1J_{\text{HN}}^{[\text{b}]} / \text{Hz}$	H-bond strength
1·2 ^[c]	2.66	15.50	75.9	86.0±1.0	
1·3 ^[d]	1.33	16.28	77.3	84.5±0.2	
1·3 ^[d]	0.64	16.97	79.0	83.8±0.2	
1·4 ^[e]	0.56	16.13	n.d.	n.d.	
1·4 ^[e]	-0.56	17.25	n.d.	n.d.	

[a] $\Delta\delta(^1\text{H}) = \delta(\text{OH}(\mathbf{1}\cdot\mathbf{X}_{\text{OH}\cdots\text{N}})) - \delta(\text{NH}(\mathbf{1}\cdot\mathbf{X}_{\text{O}\cdots\text{HN}}))$. [b] The value for $\text{NH}(\mathbf{1}\cdot\mathbf{X}_{\text{O}\cdots\text{HN}})$ is given. [c] At 240 K, [d] At 220 K, [e] At 210 K. n.d.=not determined.

Next, we investigated the influence of concentration and temperature on the appearance of the different hydrogen-bonded species to estimate the relative amounts of $\text{OH}(\mathbf{1}\cdot\mathbf{X}_{\text{OH}\cdots\text{N}})$ and $\text{NH}(\mathbf{1}\cdot\mathbf{X}_{\text{O}\cdots\text{HN}})$ species under experimental conditions used in Brønsted acid catalyzed reactions. Dilution experiments with **1·2** showed no influence of the absolute concentration on the ratio of $\text{OH}(\mathbf{1}\cdot\mathbf{X}_{\text{OH}\cdots\text{N}})$ to $\text{NH}(\mathbf{1}\cdot\mathbf{X}_{\text{O}\cdots\text{HN}})$ within the experimentally accessible concentration range (see Table 4.4 in the Supporting Information). In contrast, integration of the ^1H signals of the different species in **1·2**, **1·3**, and **1·4** at different temperatures showed pronounced temperature effects on the relative amounts of $\text{OH}(\mathbf{1}\cdot\mathbf{X}_{\text{OH}\cdots\text{N}})$ and $\text{NH}(\mathbf{1}\cdot\mathbf{X}_{\text{O}\cdots\text{HN}})$ (Figure 4.5).^{III} In all samples, exclusively linear temperature dependencies were observed within the whole temperature range, in which integration was possible because of sufficient chemical shift dispersion.

^{III} The amount of the solvent separated protonated imines $\text{NH}(\text{XH}^+)$ remained constant in all samples.

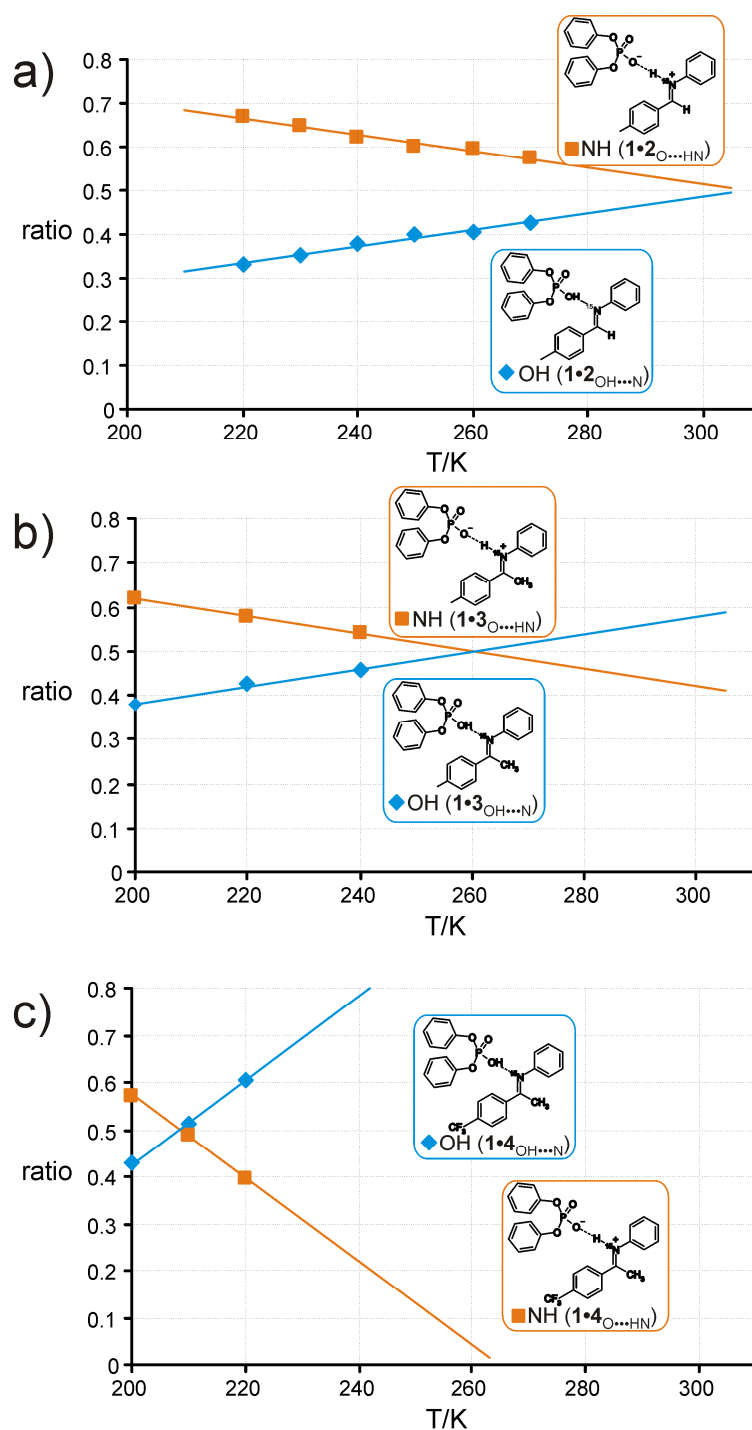


Figure 4.5: Extrapolation of the temperature dependence of the amounts of $\text{OH}(1 \cdot \text{X}_{\text{OH} \cdots \text{N}})$ and $\text{NH}(1 \cdot \text{X}_{\text{O} \cdots \text{HN}})$ in a) 1·2, b) 1·3 and c) 1·4.

Figure 4.5 shows that in general at low temperatures, the ion pairs $\text{NH}(1 \cdot \text{X}_{\text{O} \cdots \text{HN}})$ are stabilized, whereas at increasing temperatures, the hydrogen-bonded complexes $\text{OH}(1 \cdot \text{X}_{\text{OH} \cdots \text{N}})$ become favored. This effect might be explained by additional stabilizing cation- π interactions with the aromatic rings as flexibility is decreased^[45-46] and/or improved electrostatic compensation in higher aggregated complexes. Both hypotheses are experimentally corroborated

by the considerably higher hydrodynamic volume of $\text{NH}(\mathbf{1}\cdot\mathbf{2}_{\text{O}\cdots\text{HN}})$ relative to that of $\text{OH}(\mathbf{1}\cdot\mathbf{2}_{\text{OH}\cdots\text{N}})$ (see Table 4.6 in the Supporting Information). In detail, for **1·2** and **1·3**, different ratios of ion pairs to hydrogen-bonded complexes but similar temperature-dependent slopes were detected (see Figure 4.5 and Table 4.1). Samples **1·2** and **1·3** have deviating hydrogen-bond strengths but identical aromatic substituents. Thus, the relative amounts of $\text{OH}(\mathbf{1}\cdot\mathbf{X}_{\text{OH}\cdots\text{N}})$ and $\text{NH}(\mathbf{1}\cdot\mathbf{X}_{\text{O}\cdots\text{HN}})$ at 220 K fit well with the hydrogen-bond strengths, and the similar slopes seem to be caused by the identical aromatic substituents and their π - π interactions^[47-48] with the solvent toluene. In contrast, in **1·4** with the electron-withdrawing CF_3 substituent, the decrease in the amount of $\text{NH}(\mathbf{1}\cdot\mathbf{4}_{\text{O}\cdots\text{HN}})$ and the increase in the amount of $\text{OH}(\mathbf{1}\cdot\mathbf{4}_{\text{OH}\cdots\text{N}})$ with increasing temperature are much stronger than for **1·2** and **1·3**. These significantly steeper slopes might be caused by stronger intermolecular π - π interactions of the electron-deficient aromatic ring of the imine, for example, with the electron-rich solvent toluene. The strong increase in the amount of the $\text{NH}(\mathbf{1}\cdot\mathbf{4}_{\text{O}\cdots\text{HN}})$ species at very low temperatures seems to indicate that either these π - π interactions or cation- π interactions enable partial electron transfer to the imine. This interaction may enhance the basicity of the imine, in analogy with the well-known concept of charge-transfer complexes. This interpretation in terms of intermolecular interactions is in accordance with the rapid loss of such interactions at slightly elevated temperatures, because it is estimated that above 260 K exclusively $\text{OH}(\mathbf{1}\cdot\mathbf{4}_{\text{OH}\cdots\text{N}})$ is present (Figure 4.5c). We therefore concluded that the OH species is the reactive intermediate for this particular substrate.

In summary, we have been able to demonstrate that NMR spectroscopy is the method of choice to clearly distinguish between the activation modes of hydrogen-bonding and ion pairing in Brønsted acid catalysis. Before this study, it was assumed that full protonation of the imine resulted in the formation of an ion pair, which would subsequently react with a nucleophile. However, our experiments clearly show that besides ion pairing, hydrogen-bonding exists. The relative hydrogen-bond strength in $\text{OH}(\mathbf{1}\cdot\mathbf{X}_{\text{OH}\cdots\text{N}})$ (**2>3>4**) and the relative amount of $\text{OH}(\mathbf{1}\cdot\mathbf{X}_{\text{OH}\cdots\text{N}})$ at room temperature (**4>3~2**) show that both hydrogen-bond strength and the amount of the OH species are decisive for the reaction. Furthermore, the ratio between hydrogen-bonding and ion pairing (OH, NH) can be manipulated readily by simply introducing substituents with different electronic properties. These results provide insight into the different activation modes in Brønsted acid catalysis and are expected to guide the development of more efficient catalytic systems.

4.3 Supporting Information

4.3.1 Experimental Section

NMR spectra were recorded on a Bruker Avance III 600 spectrometer equipped with a low temperature 5 mm TBI $^1\text{H}/^{31}\text{P}$ -BB probe with z-gradient (temperature was controlled by a BVT 3000 unit). NMR data were processed and evaluated with Bruker's TOPSPIN 3.0 and the included DAISY program was used for line shape analysis.

Sample concentrations of 100 mM, 40 mM and 20 mM in [D8]toluene were applied for NMR measurements of the complexes **1·2**, **1·3**, and **1·4**, respectively, depending on the solubility of the different complexes. Aggregation in this concentration and temperature range was controlled by diffusion measurements with convection artefact suppression.^[49] Assignments of proton and carbon resonances of the catalyst **1**, the imines **2-4**, and of the complexes **1·2**, **1·3**, and **1·4** were obtained by one- and two-dimensional NMR spectra (^1H , gated decoupled and power-gated ^{13}C , ^1H , ^1H -COSY, ^1H , ^1H -NOESY, ^1H , ^{13}C -HSQC, and ^1H , ^{13}C -HMBC spectra). In addition, ^{15}N and ^{31}P signals were assigned with 1D ^{15}N -, ^{31}P -, and ^{31}P , ^1H -INEPT spectra in combination with 2D ^1H , ^{31}P -HMBC and ^1H , ^{15}N -HMQC spectra. The ^1H and ^{13}C chemical shifts are referenced to the methyl group of the residual toluene signal ($\delta(^1\text{H}) = 2.36$ ppm and $\delta(^{13}\text{C}) = 19.97$ ppm). For the calibration of the ^{15}N and ^{31}P chemical shifts the Ξ values corresponding to TMS were applied.

Table 4.3: NMR data of the species in the **1·2**, **1·3**, and **1·4** samples.

Sample	OH(1·X _{OH...N})			NH(1·X _{O...HN})					NH(XH ⁺)				
	$\delta(^1\text{H})$ / ppm	rel. amount	$V_{\text{H}} / \text{\AA}^3$	$\delta(^1\text{H})$ / ppm	$\delta(^{15}\text{N})$ / ppm	$^1J_{\text{NH}} /$ Hz	rel. amount	$V_{\text{H}} / \text{\AA}^3$	$\delta(^1\text{H}) /$ ppm	$\delta(^{15}\text{N}) /$ ppm	$^1J_{\text{NH}} /$ Hz	rel. amount	$V_{\text{H}} / \text{\AA}^3$
1·2 ^[a]	18.16	0.38	900	15.50	75.9	86.0±1.0	0.62	1746	11.87	49.7	69.5±1.0	0.08	149
1·3 ^[b]	17.61	0.42	572	16.28 ^[d]	77.3	84.5±0.2	0.58 ^[e]	613	11.71	49.7	70.0±1.0	0.18	191
				16.97 ^[d]	79.0	83.8±0.2		613					
1·4 ^[c]	16.69	0.51	n.d.	16.13 ^[d]	n.d.	n.d.	0.49 ^[e]	n.d.	11.38	62.7 ^[a]	66.6±1.0	0.11	n.d.
				17.25 ^[d]	n.d.	n.d.		n.d.					

[a] 240 K; [b] 220 K; [c] 210 K; [d] sub species of NH(**1·X**_{O...HN}); [e] sum of the NH(**1·X**_{O...HN}) sub species.

4.3.2 Temperature dependence of the complexes **1·2**, **1·3** and **1·4**

Temperature dependence of the complex **1·2**

In the ^1H spectrum of **1·2** at 300 K only one averaged signal for the acidic proton was detected. Upon cooling below 280 K, three signals were observed for the acidic proton, which became sharper until 240 K and showed a singlet at 18.16 ppm and two doublets at 15.50 and 11.87 ppm belonging to the three detected complex species $\text{OH}(\mathbf{1}\cdot\mathbf{2}_{\text{OH}\cdots\text{N}})$, $\text{NH}(\mathbf{1}\cdot\mathbf{2}_{\text{O}\cdots\text{HN}})$, and $\text{NH}(\mathbf{2}\text{H}^+)$. Upon further cooling each of the two signals at higher ppm values split into a group of signals indicating several structurally slightly deviating species with similar binding properties of the acidic proton (see Figure 4.6).

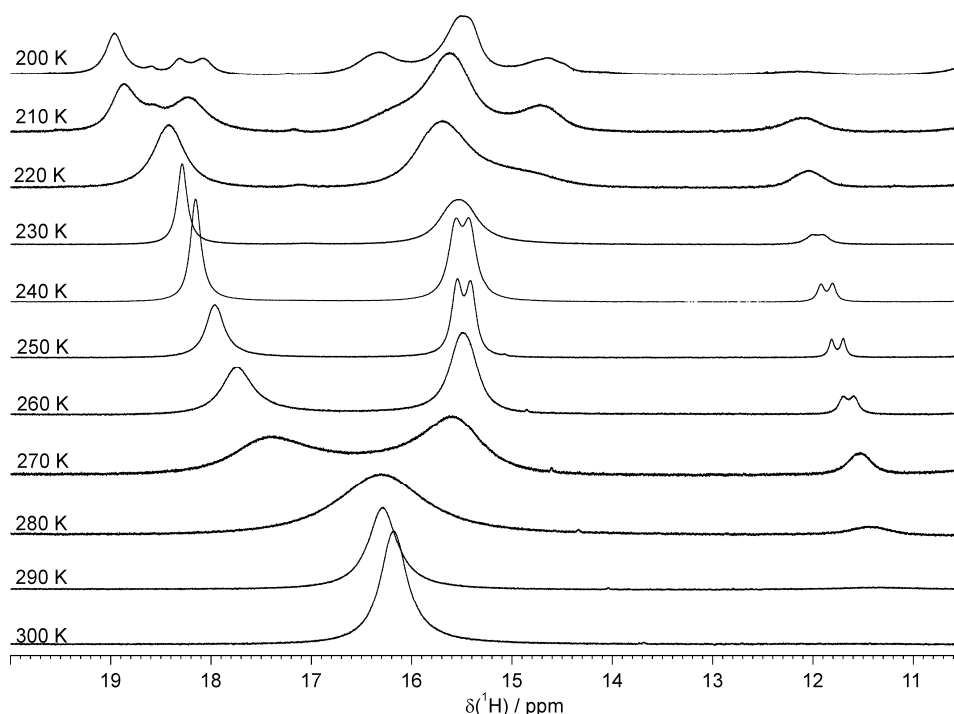


Figure 4.6: Temperature dependence of the OH/NH region of the ^1H spectra of **1·2**.

Temperature dependence of the complex **1·3**

Similar to **1·2**, in the ^1H spectrum of **1·3** at 300 K one averaged signal for the acidic proton was detected. By cooling below 240 K, at least three signals were observed for the acidic proton, which became sharper until 220 K and showed a singlet at 17.61 ppm, two doublets at 16.97 ppm and 16.43 ppm and a doublet at 11.71 ppm, belonging to the three detected complex species $\text{OH}(\mathbf{1}\cdot\mathbf{3}_{\text{OH}\cdots\text{N}})$, $\text{NH}(\mathbf{1}\cdot\mathbf{3}_{\text{O}\cdots\text{HN}})$ and $\text{NH}(\mathbf{3}\text{H}^+)$, see Figure 4.7.

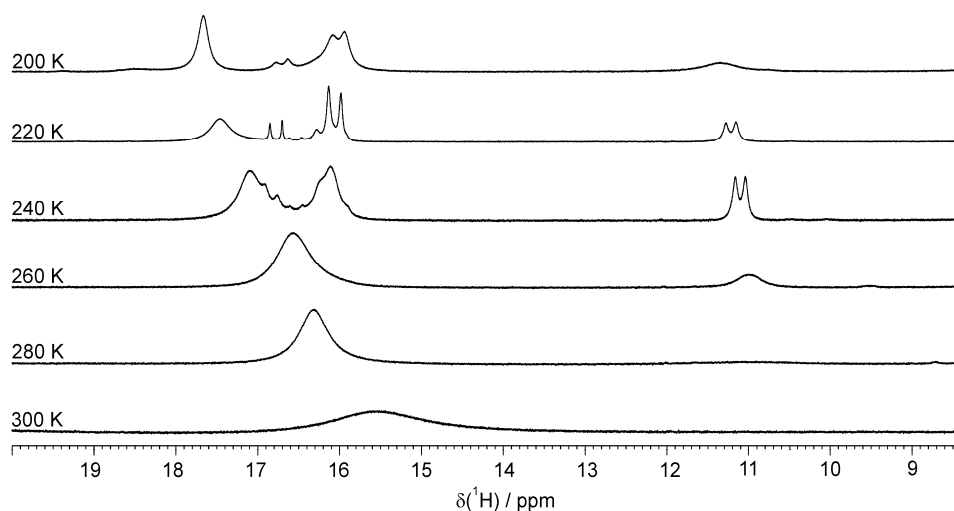


Figure 4.7: Temperature dependence of the OH/NH region of the ^1H spectra of **1-3**.

Temperature dependence of the complex **1-4**

In the ^1H spectrum of **1-4** at 300 K two averaged signals for the acidic proton were detected. By cooling below 240 K, four signals were observed for the acidic proton, which became sharper until 210 K and showed a singlet at 16.67 ppm, two doublets at 17.25 and 16.13 ppm, and a doublet at 11.38 ppm, belonging to the three detected complex species $\text{OH}(\mathbf{1-4}_{\text{OH}\cdots\text{N}})$, $\text{NH}(\mathbf{1-4}_{\text{O}\cdots\text{HN}})$ and $\text{NH}(\mathbf{4H}^+)$, see Figure 4.8.

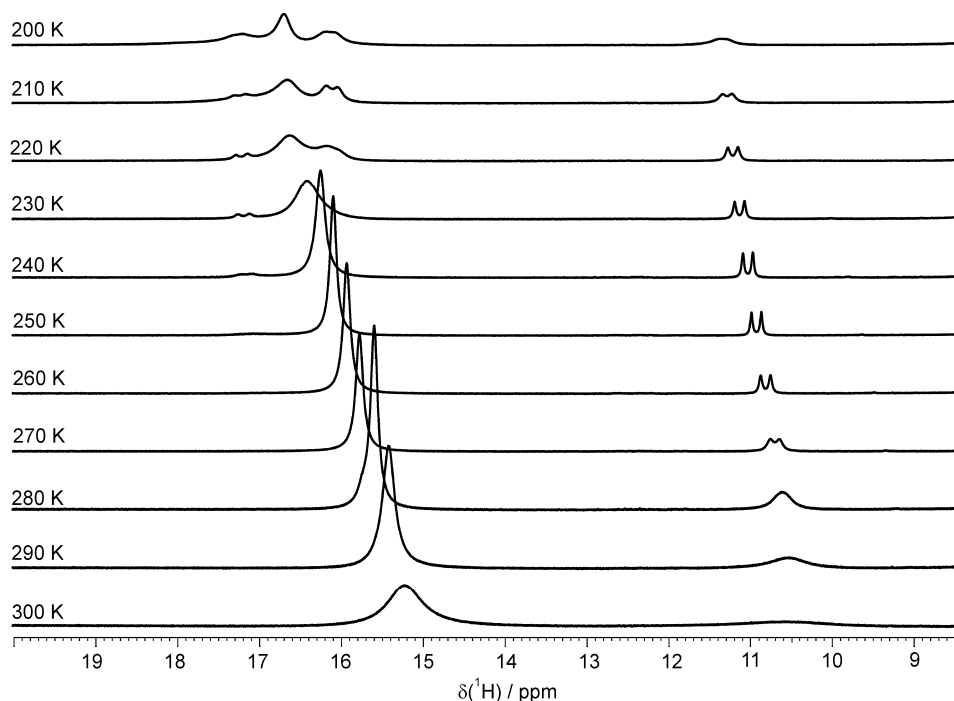


Figure 4.8: Temperature dependence of the OH/NH region of the ^1H spectra of **1-4**.

4.3.3 Evaluation of other potentially existing species

Exclusion of the existence of a 1·1 dimer in the complex samples

The presence of a **1·1** dimer in the **1·2** sample was excluded by the comparison of the temperature dependence of the OH proton signal of the **1·2** complex species (see Figure 4.9b) and a sample containing only pure **1** (see Figure 4.9a). At 240 K pure **1** showed a significant highfield shifted OH signal at 13.80 ppm ($\Delta\delta = -4.36$ ppm). In addition, at temperatures below 240 K no splitting of the OH proton signal into more signal groups, as found in the **1·2** sample, was observed. Because of these and other findings, the presence of a **1·1** dimer in the **1·2** sample could be clearly excluded.

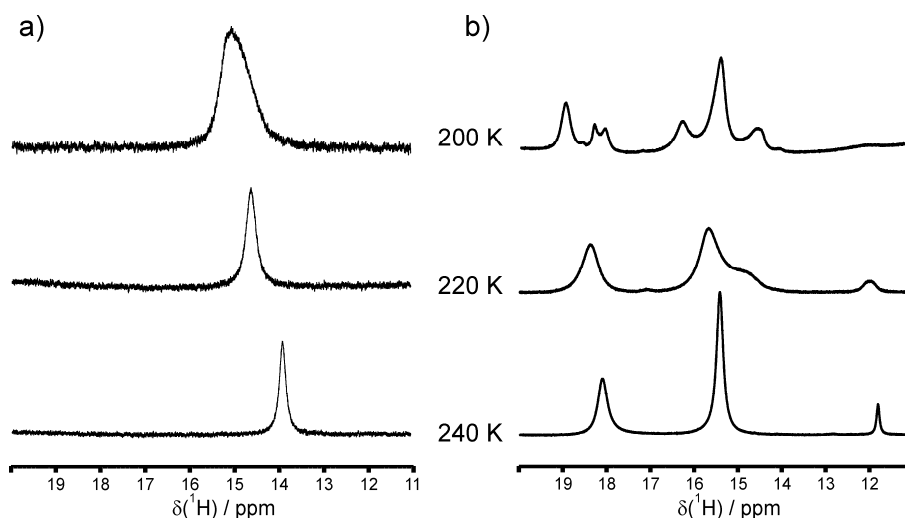


Figure 4.9: Temperature dependence of the OH proton signal a) of the **1·1** dimer and b) of the **1·2** sample.

Exclusion of the $2\cdot 2H^+$ and evidence of $NH(2H^+)$ species

The exclusion of the $2\cdot 2H^+$ and the evidence of the $2H^+$ species in the complex samples was obtained among other findings by comparison with samples containing the imine and the strong acid HBF_4 , whose corresponding base BF_4^- was expected to coordinate the iminium cation only weakly. Samples containing the imine **2** and 0.5 eq. HBF_4 were prepared for the preparation of a protonated $2\cdot 2H^+$ species (with the only weakly coordinating BF_4^- counter anion). In addition, a 1:1 mixture of **2** and HBF_4 was produced for a $2H^+$ species.

In the 1H spectrum of the 1:1 mixture the chemical shift of the $2H^+$ species at 11.39 ppm was very similar to the protonated aldimine in the complex sample of **1·2** (see Figure 4.10a and c). Therefore, the existence of a hardly coordinated $2H^+$ species in the **1·2** sample was confirmed in accordance to DOSY and other findings. In contrast, the 1H spectrum of the 1:0.5 mixture

showed a different chemical shift around 12 ppm for the **2·2** dimer compared to the $\text{NH}(\mathbf{1}\cdot\mathbf{2}_{\text{O}\cdots\text{HN}})$ species at 15.50 ppm (see Figure 4.10b and c). This was one argument for the exclusion of the **2·2** dimer in the **1·2** sample. Altogether, by HBF_4 and DOSY experiments the signal at 15.50 ppm in the ^1H spectra of the **1·2** sample was identified to be not a **2·2** dimer, but a $\text{NH}(\mathbf{1}\cdot\mathbf{2}_{\text{O}\cdots\text{HN}})$ species and the signal at 11.87 ppm is identified as the protonated aldimine 2H^+ .

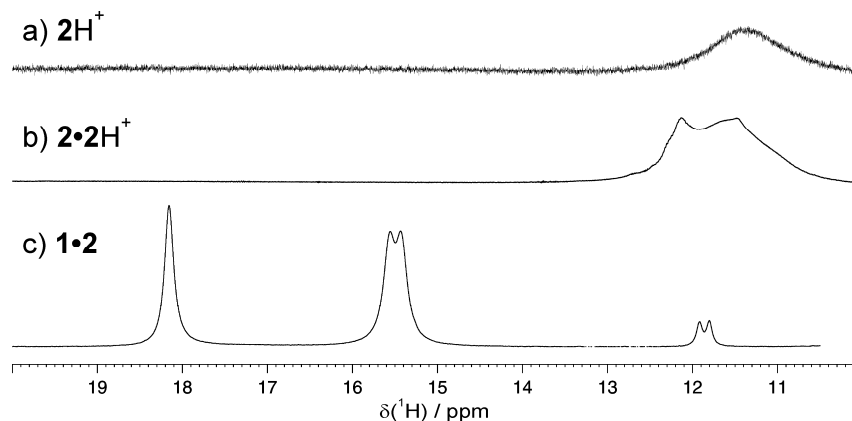


Figure 4.10: Exclusion of the $2\cdot 2\text{H}^+$ dimer and evidence of the $\text{NH}(2\text{H}^+)$ species with the help of HBF_4 experiments: ^1H spectra at 240 K of a) a dry sample of aldimine **2** with 1 eq. $\text{HBF}_4\cdot\text{OEt}_2$. b) **2** with 0.5 eq. $\text{HBF}_4\cdot\text{OEt}_2$. c) the **1·2** sample.

4.3.4 Concentration dependence of the different complex species

Table 4.4: Concentration dependence of the amounts of $\text{OH}(\mathbf{1}\cdot\mathbf{2}_{\text{OH}\cdots\text{N}})$ and $\text{NH}(\mathbf{1}\cdot\mathbf{2}_{\text{O}\cdots\text{HN}})$ in the **1·2** sample at 240 K. The relative amounts of the two complex species remained constant in the whole concentration range.

$c(\mathbf{1}\cdot\mathbf{2}) / \text{mM}$	$\text{OH}(\mathbf{1}\cdot\mathbf{2}_{\text{OH}\cdots\text{N}})$	$\text{NH}(\mathbf{1}\cdot\mathbf{2}_{\text{O}\cdots\text{HN}})$
69	0.35	0.65
62	0.32	0.68
53	0.34	0.66
50	0.34	0.66
47	0.31	0.69
45	0.34	0.66
42	0.34	0.66
39	0.33	0.67
37	0.34	0.66
36	0.35	0.65
32	0.34	0.66

4.3.5 DOSY experiments of pure 1-3 and the 1·2 and 1·3 complex species

From diffusion-ordered spectroscopy (DOSY)^[50-51] the translational self-diffusion coefficients of molecules in solution can be calculated according to the Stejskal-Tanner equation,^[52] see equation (4.1), adapted for a convection compensating double stimulated echo sequence (DSTE) including an eddy current delay t_e and bipolar gradient pulses, shown in Figure 4.11.^[49-51]

$$I = I_0 \cdot \exp \left[-D \gamma^2 g^2 \delta^2 \left(\Delta - \frac{2\delta}{3} - \tau_g \right) \right] \quad (4.1)$$

with intensity attenuation I/I_0 , gyromagnetic ratio γ , amplitude of the gradient pulses g with duration δ , diffusion time Δ and gradient refocusing delay τ_g .

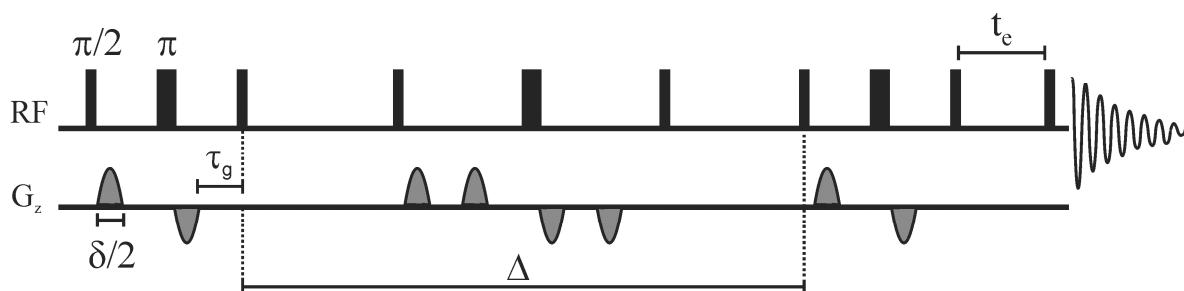


Figure 4.11: DSTE with bipolar gradient pulses and eddy current delay t_e

With the diffusion coefficients D of the analyte and of TMS (acting as viscosity reference), the hydrodynamic radius r_H of the analyte can be estimated following the Stokes-Einstein equation (see equation (4.2)).^[53] The comparison of the estimated hydrodynamic volume with theoretical volumes then allows for an estimation of the aggregation behavior of the analyte in solution.

$$D = \frac{k_B T}{F \cdot c \cdot \pi \cdot \eta \cdot r_H} \quad (4.2)$$

with Boltzmann constant k_B , absolute temperature T , shape factor F , scaling factor c and viscosity η .

With our experimental setup the usual standard deviation for diffusion coefficients is $\pm 3\%$. We checked the validity of this error range for compound **1** and found it working. For the complexes investigated the determination of diffusion values was quite challenging, because of severe signal overlap of the aromatic signals leading to erroneous results. In addition, the OH/NH proton signals could not be detected in the diffusion measurements because of their short relaxation times and/or exchange. Therefore, in the complex samples the methyl groups of the imines were used for the determination of the diffusion coefficients (see Figure 4.12). The assignment of the different methyl groups to the corresponding species was accomplished by the equal ^1H integral ratios of the OH/NH signals and the Me groups. In addition, the Me and OH/NH signals possess the same coalescence behavior in the low temperature NMR studies.

For reliable diffusion coefficients only baseline separated signals can be used. Therefore, only several samples allowed for the determination of reliable diffusion coefficients depending on the temperature, the general line widths of the signals in the sample, and the position of the methyl group of toluene, see Table 4.6 and Table 4.7.

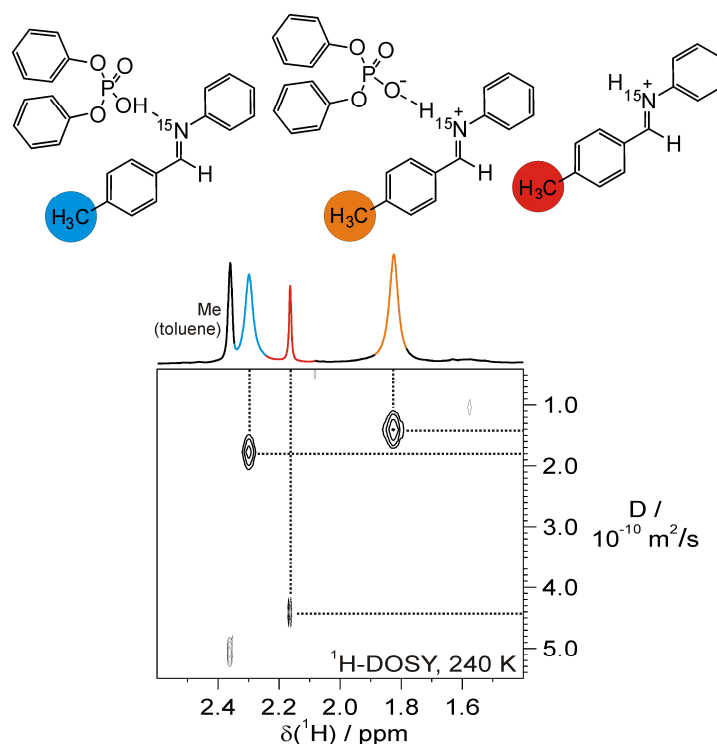


Figure 4.12: Methyl region of the ^1H -DOSY spectrum and the corresponding species in the **1·2** sample at 240 K.

Table 4.5: Diffusion coefficients and experimental hydrodynamic volumes of **1-3** at 300 and 240 K, respectively.

sample	T / K	η / mPa s	$D_{\text{exp}} / 10^{-10} \text{ m}^2/\text{s}$	$D_{\text{corr}} / 10^{-10} \text{ m}^2/\text{s}^{[a]}$	$V_{\text{H, monomer}} / \text{\AA}^3$
2	300	0.510	14.82	3.31	216 ^[b]
3	300	0.537	14.24	3.35	208 ^[b]
1	300	0.497	9.01	1.96	376 ^[c]
	240	1.261	2.27	1.57	648 ^[c]

[a] temperature and viscosity referenced to the **1-2** sample at 240 K. [b] $V_{\text{H, shaped}}$. [c] $V_{\text{H, globular}}$ of the **1-1** dimer divided by 2.

The hydrodynamic volumes V_{H} of **1-2** and **1-3** were estimated as sum of the V_{H} of the single species to be $V_{\text{H}}(\mathbf{1-2}) = 592 \text{ \AA}^3$ and $V_{\text{H}}(\mathbf{1-3}) = 584 \text{ \AA}^3$, respectively (see Table 4.5).

Table 4.6: Diffusion coefficients and experimental hydrodynamic volumes of the different species in the **1-2** sample at 300 and 240 K.

sample	T / K	species	$D_{\text{exp}} / 10^{-10} \text{ m}^2/\text{s}$	$D_{\text{corr}} / 10^{-10} \text{ m}^2/\text{s}^{[a]}$	$V_{\text{H, globular}} / \text{\AA}^3$
1-2	300	average of OH(1-2 _{OH...N}) and NH(1-2 _{O...HN})	9.70	2.43	469
		NH(2-H ⁺)	23.16	5.80	95
		OH(1-2 _{OH...N})	1.82	1.82	900
	240	NH(1-2 _{O...HN})	1.39	1.39	1746
		NH(2-H ⁺)	4.40	4.40	149

[a] temperature and viscosity referenced to the **1-2** sample at 240 K.

Table 4.7: Diffusion coefficients and experimental hydrodynamic volumes of the different species in the **1-3** sample at 300, 240 and 220 K.

sample	T / K	species	$D_{\text{exp}} / 10^{-10} \text{ m}^2/\text{s}$	$D_{\text{corr}} / 10^{-10} \text{ m}^2/\text{s}^{[a]}$	$V_{\text{H, globular}} / \text{\AA}^3$
1-3	300	average of OH(1-3 _{OH...N}) and NH(1-3 _{O...HN})	11.76	2.69	379
		NH(3-H ⁺)	17.15	3.92	183
		average of OH(1-3 _{OH...N}) and NH(1-3 _{O...HN})	2.49	2.30	524
	240	NH(3-H ⁺)	4.21	3.90	184
		OH(1-3 _{OH...N})	1.18	2.22	572
	220	NH(1-3 _{O...HN})	1.14	2.15	613
		NH(3-H ⁺)	2.03	3.82	191

[a] temperature and viscosity referenced to the **1-2** sample at 240 K.

4.4 Additional experimental findings

4.4.1 Influence of the water content.

For a long time the use of water as solvent in asymmetric catalysis has remained in the shadow. Since the positive effect of water on the reactivity and selectivity in Diels–Alder and other reactions has been shown, the situation has changed significantly. Several asymmetric metal catalyzed reactions carried out in the presence of water have subsequently been developed.^[54] In the field of organocatalysis, Schreiner and co-workers have recently shown that activation via hydrogen-bond formation in the presence of water is possible,^[55] despite the excellent hydrogen-bond donor/acceptor abilities of water. This observation can be explained by hydrophobic effects. The formation of such hydrogen-bonds results in the nonpolar components being oriented such that the contact surface between these molecules and water is minimized (hydrophobic hydration). Rueping et al. recently introduced the asymmetric transfer hydrogenation of quinolines in pure water with chiral binol-phosphate based Brønsted acid catalysts. They concluded that diametrical polarities of the ion pair and the reaction medium are required in order to achieve hydrophobic hydration and to avoid weakening of the contact ion pair.^[22] In view of the coexistence of hydrogen-bonded and ion paired species in our diphenyl phosphate-imine samples, we investigated the influence of the water content on the sample.

The influence of the amount of water upon the formation of the complex species and the equilibrium of the species was investigated using **1·2** and **1·3** samples with varying water contents from 0.0 eq. to 0.6 eq. H₂O relative to **1** and monitored the effect by low temperature proton spectra. By addition of 0.13 eq H₂O to a **1·2** sample the proton chemical shift pattern remained unaffected, just the amount of NH(**1·2**_{O⋯HN}) increased from 63 to 67 % at the expense of OH(**1·2**_{OH⋯N}) and NH(2H⁺) (see Table 4.8). But due to the large OH/NH line width and therefore large error range of integration this alteration seems not significant enough for a reliable interpretation.

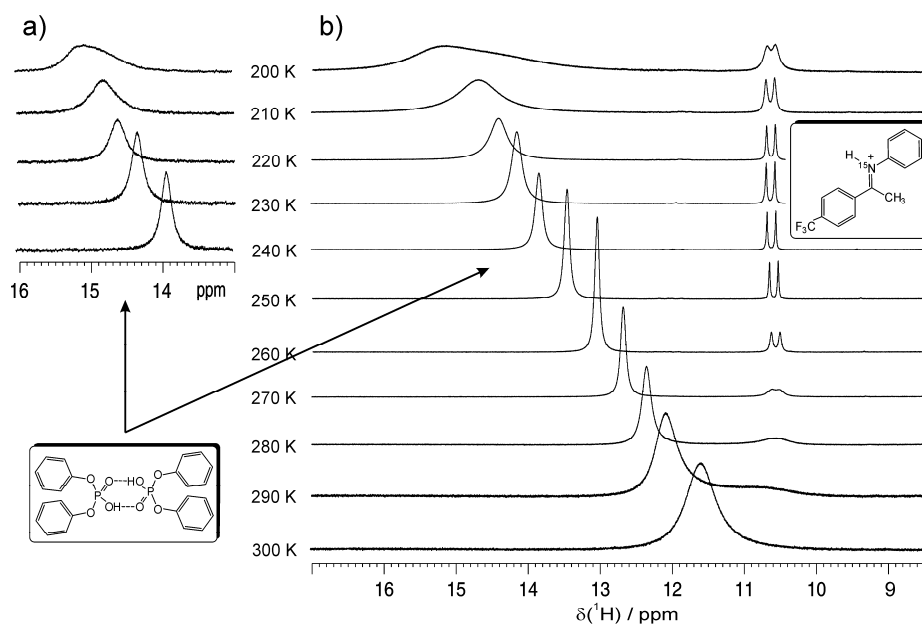


Figure 4.13: Temperature dependence of the OH/NH proton signals of a) pure **1** and b) **1·3** with 0.6 eq. H₂O.

In contrast, a further increase of the water content up to 0.6 eq. led to a complete change of the **1·3** sample (see Figure 4.13B vs. Figure 4.7). The most significant difference was observed for the chemical shift of the OH proton, which appeared at 11.61 ppm at 300 K, 4.2 ppm upfield shifted compared to the dry sample ($\delta(^1\text{H})=15.80$ ppm). At lower temperatures the OH signal split up into a doublet at 10.6 ppm and a second broad singlet which was shifted further downfield by lowering the temperature. The identification of the doublet at 11.61 ppm as $\text{NH}(\text{3H}^+)$ with a $^1J_{\text{HN}}$ coupling constant of 72.5 ± 0.5 Hz was confirmed by $^1\text{H}\{^{15}\text{N}\}$, $^1\text{H}, ^{15}\text{N}$ -HMQC and DOSY experiments (data not shown). The singlet could be identified as OH proton of the **1·1** dimer by comparison with pure **1** (see Figure 4.13A). At 240 K, the singlet showed the same chemical shift of 13.80 ppm as the OH proton of pure **1**. At temperatures below 240 K no splitting into more signal groups, as found in the dry **1·2** sample (for spectra see Figure 4.7), was observed in accordance to pure **1**. In addition, the temperature and viscosity corrected diffusion coefficients of this species resembled that of a **1·1** dimer. Altogether, it can be concluded that in the **1·3** sample with 0.6 eq. water, instead of the two complex species $\text{OH}(\text{1·3}_{\text{OH}\cdots\text{N}})$ and $\text{NH}(\text{1·3}_{\text{O}\cdots\text{HN}})$, the **1·1** dimer in addition to $\text{NH}(\text{3H}^+)$ was present.

To summarize, the influence of the amount of water was investigated with different samples with varying water content. While 0.13 eq. H₂O relative to **1** were tolerated without significant alterations compared to the dry sample, a content of 0.6 eq. H₂O led to the formation of a **1·1** dimer instead of the two complex species. In contrast, the amount of the $\text{NH}(\text{XH}^+)$

remained unaffected in the water content range under investigation (see Table 4.8 and for an overview of the ^1H spectra at 200–240 K see Figure 4.14).

Table 4.8: Amount of the different species by varying water content at 220 K.

sample	eq. H_2O	amount of			
		1·1	$\text{OH}(\mathbf{1}\cdot\mathbf{X}_{\text{OH}\cdots\text{N}})$	$\text{NH}(\mathbf{1}\cdot\mathbf{X}_{\text{O}\cdots\text{HN}})$	$\text{NH}(\mathbf{X}\text{H}^+)$
1·2	0.0	---	31	63	6
	0.13	---	29	67	4
1·3	0.0	---	36	49	15
	0.6	85	---	---	15
1·4	0.07	---	54	35	11

A possible explanation for this behavior might be the high affinity of **1** to water. This interaction can be seen in the ^1H spectra of **1** with varying H_2O content. Even at 200 K, the exchange of water protons with the OH proton of **1** is still observed. Furthermore, the OH proton exchange, within the **1·1** dimer or with water, could be responsible for the non-detection of the $^2J_{\text{P-OH}}$ coupling in pure **1**; only the $^nJ_{\text{PH}}$ couplings to the carbon bound protons (including the very small $^6J_{\text{PH}}$ coupling)^[56–58] could be detected in ^{31}P , ^1H -INEPT spectra. The high affinity of **1** to water can additionally be seen in the different solubility with and without water; dry **1** showed no precipitation (tested up to 100 mM) in $[\text{D}_8]\text{toluene}$, while in the presence of water **1** is soluble only up to 20 mM (concentration calculated with external standard). The precipitate formed upon the addition of water might be an insoluble complex formed of water and **1**.

These findings could be of high importance for Brønsted acid catalysis in general, since one of the complex species was considered to be the catalytically active species in all Brønsted acid catalyzed reactions. In contrast to the extended binol-phosphates with large nonpolar substituents, the relatively small diphenyl phosphate is not suited for hydrophobic interactions,^[22] so that no stabilization of ion paired or hydrogen-bonded complexes inside a hydrophobic pocket is possible.^[22] Instead of stabilizing hydrophobic interactions, hydrophilic **1**/water interactions are likely to impede the formation of the complex species with the imines. If the water content exceeds the tolerated amount, no activated complex species could be detected. Hence, in the absence of the complexes, the low amount of the non-coordinated activated iminium cations, which could offer activity without the desired selectivity, could reduce the selectivity of the whole catalytic system. It seems therefore highly recommendable for Brønsted acid catalyzed reactions in organic solvents to dry all reagents before use.

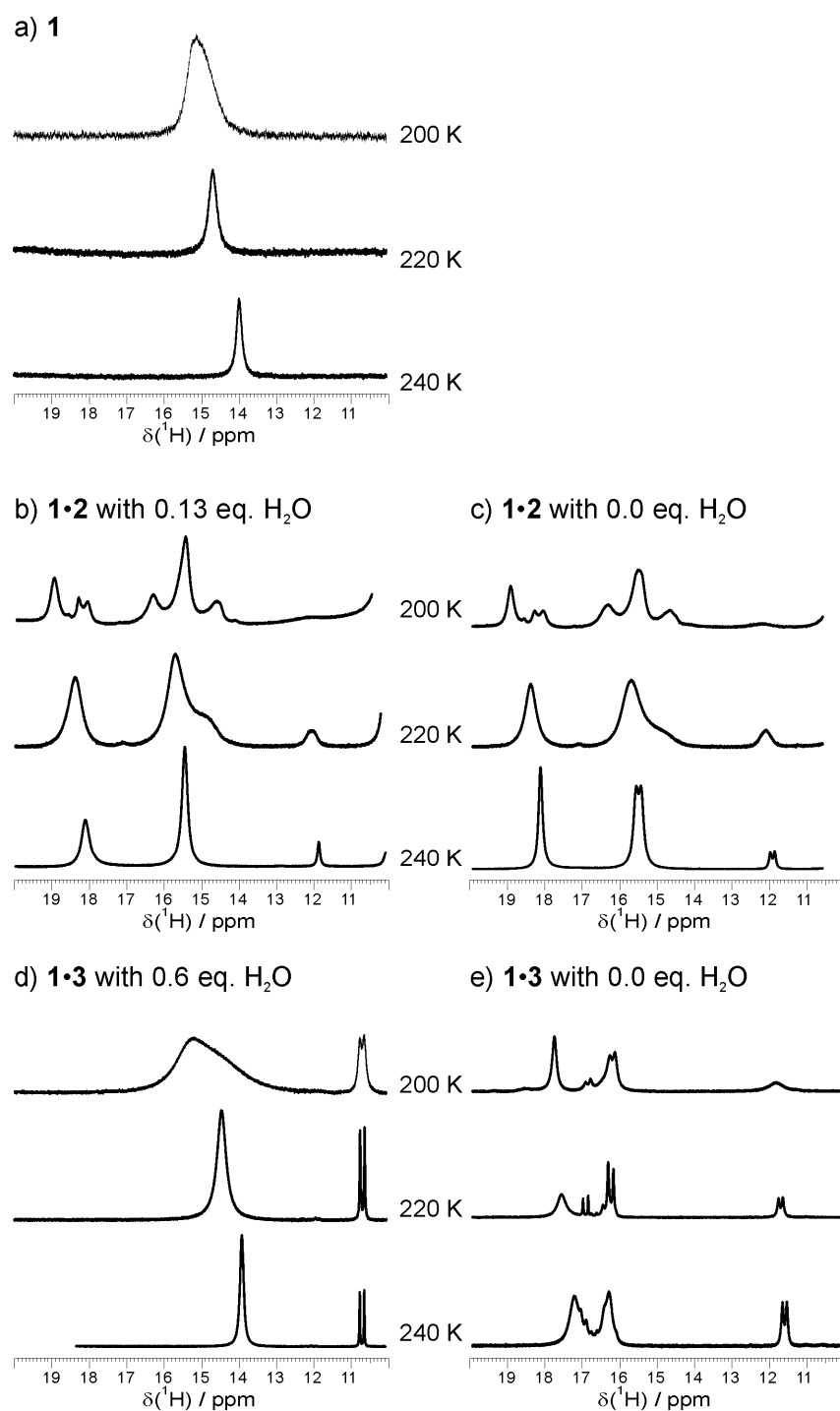


Figure 4.14: Overview of the ^1H spectra of the different samples with varying water content at 200, 220 and 240 K.

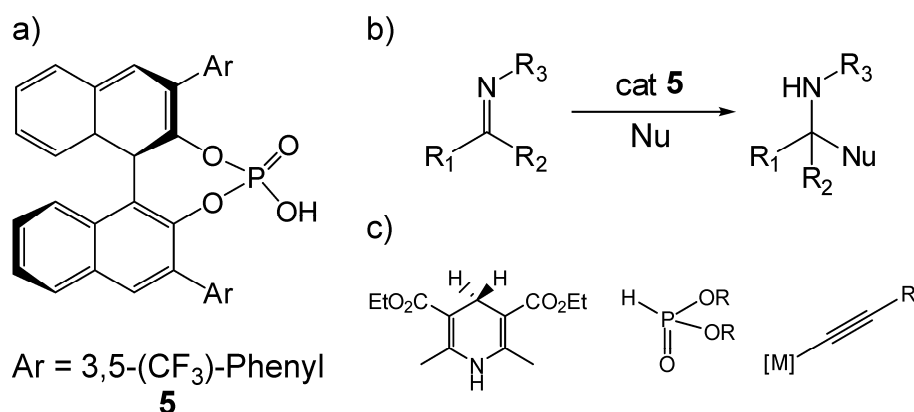
4.4.2 Investigations of a chiral CF₃-substituted binol-phosphate catalyst

Figure 4.15: a) Binol-phosphate based catalyst **5**, b) typical reaction scheme for imines with c) different nucleophiles.

After the investigations of the substrate scope with different imines and achiral **1** and investigation of the influence of the water content on the catalytic system, we were further interested in exploring the overwhelming catalyst scope, which evolved for such chiral binol phosphate based catalysts in the last years.^[7-13] For that purpose, we selected the 3,5-(CF₃)₂-phenyl substituted binol phosphate **5**, which was used as catalyst in transfer hydrogenations,^[59] hydrophosphonylations^[60-62] and alkynylation^[63] of imines (see Figure 4.15B and C) and in other type of reactions.^[64-66] In addition, **5** was used as chiral ligand in gold catalysis for an intramolecular hydroamination of allenes.^[67]

Investigations on the detection of the OH proton of pure **5**:

For pure **1** and the **1·2·1·4** samples, different species could be detected in low temperature proton spectra and were subsequently identified in ¹H, ¹⁵N-HMQC and ³¹P, ¹H-INEPT spectra. Thus, for further investigations on chiral catalysts like **5**, the detection of the OH/NH proton in ¹H spectra is an absolute prerequisite. But, in a sample containing pure **5** in toluene no OH proton signal could be detected at 298/300 K in several ¹H spectra. This finding might in principle be explained by e.g. deprotonation and chemical exchange of the acidic proton against an other cation, fast exchange with water molecules or with another molecule of **5** by formation of aggregates leading to broadening/vanishing of the signal. Furthermore, the low solubility in general leading to insufficient sensitivity or formation of hydrogen-bonds with the CF₃ groups at the phenyl substituents might be responsible for the non-detection of the OH proton.

To rule out the influence of water, samples have been dried carefully, but the OH proton was still undetectable. The potentially insufficient sensitivity owing to the low solubility of **5** in

toluene (<1 mM, calculated with external OMS standard) was investigated spectroscopically with a cryo probe and/or intense signal sampling, but no OH proton could be detected. In another approach, acetonitrile was used as solvent providing good solubility for **5** (up to 10 mM was tested without precipitation), but again no OH proton signal was detectable. Next, the aggregation behavior was investigated by DOSY experiments. In contrast to **1**, which forms a hydrogen-bonded dimer in toluene, **5** forms a monomeric species in toluene and CD₃CN.^[68] This can be attributed to the sterically demanding 3,5-(CF₃)-phenyl substituents of the catalyst effectively impeding the catalyst dimerization.

Another possibility for the non-detection of the OH proton could be the formation of hydrogen-bonds from the OH proton to the CF₃ groups leading to fast exchange between the different binding motifs.^[44] This hypothesis was corroborated indirectly by the line broadening of both the ortho and the para protons of the phenyl ring beside the CF₃ groups in both solvents. In CD₃CN the line widths of the ortho and para protons of the phenyl ring are 15 and 7 Hz, respectively, compared to 4-6 Hz for the naphthyl protons. In toluene this effect is even more pronounced with a line broadening for the phenyl protons up to 16 and 8 Hz, respectively, compared to around 4 Hz for the protons at the naphthyl moiety. This line broadening could be interpreted as hydrogen-bonding interaction from the carbon bound phenyl protons to the CF₃ groups^[44] and this effect should be even more pronounced for the OH proton.

To summarize, the OH proton could not be detected for pure **5**, which presumably could be attributed to the formation of hydrogen-bonds to the CF₃ groups leading to broadening/vanishing of the signal. Therefore, no further attempts have been made to detect the ²J_{PH} coupling to the OH proton in INEPT or HMBC type spectra.

Investigations on **5**·**2** samples:

For the characterization of pure **5** and subsequently for the identification of species in samples of **5** and the imines, the OH proton possesses a decisive role. Since the detection of the OH proton for pure **5** was not possible, we turned our interests in investigations on potential complex species formed of **5** and an imine. Therefore, a **5**·**2** sample in the ratio of 1:1 should be prepared in toluene, but due to the low solubility and precipitation of **5** a 1:1 ratio was not achievable. In the ¹H spectra at 298 K only the signal sets of the pure compounds **5** and **2**, but no complex species as found in **1**·**2**-**1**·**4**, were detected.

To improve the solubility, a second **5**·**2** sample in toluene with 10 % DMSO was prepared, but the addition of DMSO hardly increased the solubility, but instead altered the chemical shift pattern tremendously. In addition, the diffusion coefficient of **5** increased drastically indicating

the formation of at least a pentamer at 250 K.^[68] This experimental system was therefore considered to be too complex for detailed and meaningful investigations. Thus, so far no further efforts have been made towards the investigation for **5**.

Thus, no further attempts have been made for the investigation of pure **5** or **5·2** samples. Instead, to elucidate the catalyst scope of the Brønsted acid catalysis, other chiral catalyst, preferably without the complicating H-bonding CF₃ substituent, should be investigated.

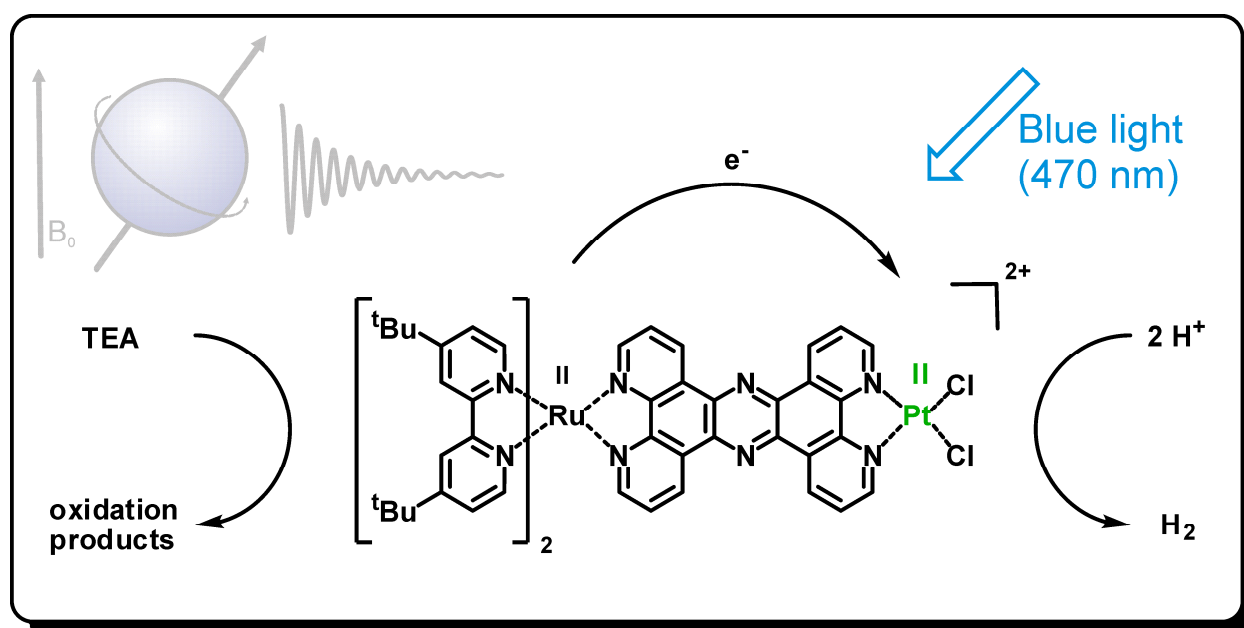
4.5 References

- [1] T. Akiyama, *Chem. Rev.* **2007**, *107*, 5744-5758.
- [2] T. Akiyama, J. Itoh, K. Fuchibe, *Adv. Synth. Catal.* **2006**, *348*, 999-1010.
- [3] M. S. Taylor, E. N. Jacobsen, *Angew. Chem. Int. Ed.* **2006**, *45*, 1520-1543.
- [4] A. G. Doyle, E. N. Jacobsen, *Chem. Rev.* **2007**, *107*, 5713-5743.
- [5] H. Yamamoto, N. Payette, in *Hydrogen Bonding in Organic Synthesis* (Ed.: P. M. Pikhov), Wiley-VCH, Weinheim, **2009**, pp. 73-140.
- [6] D. Kampen, C. M. Reisinger, B. List, *Top. Curr. Chem.* **2010**, *291*, 395-456.
- [7] M. Terada, *Chem. Commun.* **2008**, 4097-4112.
- [8] M. Terada, *Synthesis* **2010**, 1929-1982.
- [9] M. Terada, *Bull. Chem. Soc. Jpn.* **2010**, *83*, 101-119.
- [10] A. Zamfir, S. Schenker, M. Freund, S. B. Tsogoeva, *Organic & Biomolecular Chemistry* **2011**, *8*, 5262-5276.
- [11] T. Akiyama, J. Itoh, K. Yokota, K. Fuchibe, *Angew. Chem. Int. Ed.* **2004**, *43*, 1566-1568.
- [12] D. Uraguchi, M. Terada, *J. Am. Chem. Soc.* **2004**, *126*, 5356-5357.
- [13] M. Rueping, E. Sugiono, F. R. Schoepke, *Synlett* **2010**, *2010*, 852-865.
- [14] M. Rueping, E. Sugiono, T. Theissmann, A. Kuenkel, A. Köckritz, A. Pews-Davtyan, N. Nemati, M. Beller, *Org. Lett.* **2007**, *9*, 1065-1068.
- [15] M. Rueping, E. Sugiono, S. A. Moreth, *Adv. Synth. Catal.* **2007**, *349*, 759-764.
- [16] M. Rueping, A. P. Antonchick, *Org. Lett.* **2008**, *10*, 1731-1734.
- [17] M. Rueping, T. Theissmann, S. Raja, J. W. Bats, *Adv. Synth. Catal.* **2008**, *350*, 1001-1006.
- [18] M. Rueping, A. P. Antonchick, *Angew. Chem. Int. Ed.* **2008**, *47*, 10090-10093.
- [19] M. Rueping, A. P. Antonchick, E. Sugiono, K. Grenader, *Angew. Chem. Int. Ed.* **2009**, *48*, 908-910.
- [20] M. Rueping, F. Tato, F. R. Schoepke, *Chemistry – A European Journal* **2010**, *16*, 2688-2691.
- [21] M. Rueping, M.-Y. Lin, *Chemistry – A European Journal* **2010**, *16*, 4169-4172.
- [22] M. Rueping, T. Theissmann, *Chemical Science* **2010**, *1*, 473-476.
- [23] M. Rueping, C. Brinkmann, A. P. Antonchick, I. Atodiresci, *Org. Lett.* **2010**, *12*, 4604-4607.
- [24] M. Rueping, E. Merino, R. M. Koenigs, *Adv. Synth. Catal.* **2010**, *352*, 2629-2634.
- [25] W. Schrader, P. P. Handayani, Z. Jian, B. List, *Angew. Chem. Int. Ed.* **2009**, *48*, 1463-1466.
- [26] Y. Cohen, L. Avram, L. Frish, *Angew. Chem. Int. Ed.* **2005**, *44*, 520-554.
- [27] P. S. Pregosin, *Pure Appl. Chem.* **2009**, *81*, 615-633.
- [28] S. Sharif, G. S. Denisov, M. D. Toney, H.-H. Limbach, *J. Am. Chem. Soc.* **2007**, *129*, 6313-6327.
- [29] S. Sharif, D. Schagen, M. D. Toney, H.-H. Limbach, *J. Am. Chem. Soc.* **2007**, *129*, 4440-4455.
- [30] S. Sharif, E. Fogle, M. D. Toney, G. S. Denisov, I. G. Shenderovich, G. Buntkowsky, P. M. Tolstoy, M. C. Huot, H.-H. Limbach, *J. Am. Chem. Soc.* **2007**, *129*, 9558-9559.
- [31] M. Chan-Huot, S. Sharif, P. M. Tolstoy, M. D. Toney, H.-H. Limbach, *Biochemistry* **2010**, *49*, 10818-10830.
- [32] R. M. Gschwind, M. Armbrüster, I. Z. Zubrzycki, *J. Am. Chem. Soc.* **2004**, *126*, 10228-10229.
- [33] G. Federwisch, R. Kleinmaier, D. Drettwan, R. M. Gschwind, *J. Am. Chem. Soc.* **2008**, *130*, 16846-16847.
- [34] X.-Q. Zhu, Q.-Y. Liu, Q. Chen, L.-R. Mei, *J. Org. Chem.* **2009**, *75*, 789-808.
- [35] H. Mayr, A. R. Ofial, *Tetrahedron Lett.* **1997**, *38*, 3503-3506.
- [36] S. Lakhdar, T. Tokuyasu, H. Mayr, *Angew. Chem. Int. Ed.* **2008**, *47*, 8723-8726.
- [37] C. Rabiller, J. P. Renou, G. J. Martin, *J. Chem. Soc., Perkin Trans. 2* **1977**, 536-541.
- [38] H. Mayr, A. R. Ofial, E.-U. Wärrthwein, N. C. Aust, *J. Am. Chem. Soc.* **1997**, *119*, 12727-12733.
- [39] R. Knorr, K. Ferchland, *Liebigs Annalen* **1995**, *1995*, 419-425.
- [40] M. Bissonnetteh, H. L. Thanh, D. Vocelle, *Can. J. Chem.* **1985**, *63*, 2298-2302.
- [41] G. M. Sharma, O. A. Roels, *J. Org. Chem.* **1973**, *38*, 3648-3651.
- [42] C. Detering, P. M. Tolstoy, N. S. Golubev, G. S. Denisov, H. H. Limbach, *Doklady Physical Chemistry* **2001**, *379*, 191-193.
- [43] N. S. Golubev, S. N. Smirnov, V. A. Gindin, G. S. Denisov, H. Benedict, H.-H. Limbach, *J. Am. Chem. Soc.* **1994**, *116*, 12055-12056.
- [44] T. Steiner, *Angew. Chem. Int. Ed.* **2002**, *41*, 48-76.
- [45] D. A. Dougherty, *Science* **1996**, *271*, 163-168.
- [46] J. C. Ma, D. A. Dougherty, *Chem. Rev.* **1997**, *97*, 1303-1324.
- [47] J. Santos, B. Grimm, B. M. Illescas, D. M. Guldi, N. Martin, *Chem. Commun.* **2008**, 5993-5995.
- [48] S. Viel, L. Mannina, A. Segre, *Tetrahedron Lett.* **2002**, *43*, 2515-2519.

- [49] A. Jerschow, N. Müller, *J. Magn. Reson.* **1997**, *125*, 372-375.
- [50] W. S. Price, *Concepts Magn. Reson.* **1998**, *10*, 197-237.
- [51] C. S. Johnson, *Prog. Nucl. Magn. Reson. Spectrosc.* **1999**, *34*, 203-256.
- [52] E. O. Stejskal, J. E. Tanner, *The Journal of Chemical Physics* **1965**, *42*, 288-292.
- [53] A. Macchioni, G. Ciancaleoni, C. Zuccaccia, D. Zuccaccia, *Chem. Soc. Rev.* **2008**, *37*, 479-489.
- [54] U. M. Lindström, *Chem. Rev.* **2002**, *102*, 2751-2772.
- [55] C. M. Kleiner, P. R. Schreiner, *Chem. Commun.* **2006**, 4315-4317.
- [56] C. E. Griffin, M. Gordon, *J. Am. Chem. Soc.* **1967**, *89*, 4427-4431.
- [57] S. Chikkali, D. Gudat, *Eur. J. Inorg. Chem.* **2006**, *2006*, 3005-3009.
- [58] J. Heinicke, E. Musina, N. Peulecke, A. A. Karasik, M. K. Kindermann, A. B. Dobrynin, I. A. Litvinov, Z. *Anorg. Allg. Chem.* **2007**, *633*, 1995-2003.
- [59] M. Rueping, E. Sugiono, C. Azap, T. Theissmann, M. Bolte, *Org. Lett.* **2005**, *7*, 3781-3783.
- [60] T. Akiyama, H. Morita, J. Itoh, K. Fuchibe, *Org. Lett.* **2005**, *7*, 2583-2585.
- [61] T. Akiyama, H. Morita, P. Bachu, K. Mori, M. Yamanaka, T. Hirata, *Tetrahedron* **2009**, *65*, 4950-4956.
- [62] P. S. Bhadury, Y. Zhang, S. Zhang, B. Song, S. Yang, D. Hu, Z. Chen, W. Xue, L. Jin, *Chirality* **2009**, *21*, 547-557.
- [63] M. Rueping, A. P. Antonchick, B. C., *Angew. Chem. Int. Ed.* **2007**, *46*, 6903-6906.
- [64] R. I. Storer, D. E. Carrera, Y. Ni, D. W. C. MacMillan, *J. Am. Chem. Soc.* **2005**, *128*, 84-86.
- [65] M. J. Wanner, R. N. S. van der Haas, K. R. de Cuba, J. H. van Maarseveen, H. Hiemstra, *Angew. Chem. Int. Ed.* **2007**, *46*, 7485-7487.
- [66] D. J. Cox, M. D. Smith, A. J. Fairbanks, *Org. Lett.* **2010**, *12*, 1452-1455.
- [67] K. Aikawa, M. Kojima, K. Mikami, *Angew. Chem. Int. Ed.* **2009**, *48*, 6073-6077.
- [68] C. A. Crutchfield, D. J. Harris, *J. Magn. Reson.* **2007**, *185*, 179-182.

5 NMR Investigations on the Photocatalytic Water Reduction

“NMR investigations on the photocatalytic water reduction –
utilization of the $^3J_{\text{H},195\text{Pt}}$ coupling as a sensor for a potential cleavage of the Pt unit.”



Matthias Fleischmann, Michael Pfeffer,
Sven Rau, Ruth M. Gschwind

Dalton Transactions **2011**, to be submitted.

The synthesis of the compounds was performed by Michael Pfeffer.

5.1 Introduction

Light driven organometallic catalysis by heteronuclear Ru(II) complexes

In the light of limited resources and of mankind's ever increasing energy demand, attention has been directed towards the development of new photocatalytic systems. The underlying idea is to model nature's photosynthesis,^[1] which converts $3\text{--}5\cdot 10^{11}$ t CO₂ into biomass by using not more than 0.05 % of the complete sun light, that reaches the surface of the earth (10^{22} kJ per year).^[2] In recent studies, supramolecular devices were able to perform light-driven catalytic reactions such as the reduction of CO₂, olefin transformations and hydrogen production.^[1] Especially the conversion and storage of solar energy by means of light-driven water splitting in analogy to the natural archetype has gained great attention. There the solar energy is converted to the storable energy carrier oxygen and hydrogen, the latter is in nature usually fixed by a substrate, e.g. NADP⁺. To simulate this complex process of the water cleavage in the photosystems in plants, the simultaneously proceeding water oxidation to oxygen and water reduction to hydrogen should be investigated independently. In the last decades several model systems for water oxidation^[3] as well as water reduction^[4] have been developed.

In principle, the systems for photocatalytic hydrogen production consist of a transition metal as a photo sensitizer for light absorption, a ligand acting as an electron transmitter/reservoir^[5-6] and a catalytic metal center, which catalyzes the reduction of water to molecular hydrogen. After the development of intermolecular systems,^[4, 7-8] single-molecule approaches, which combine all of the desired functionalities intramolecularly, have been introduced.^[9-11]

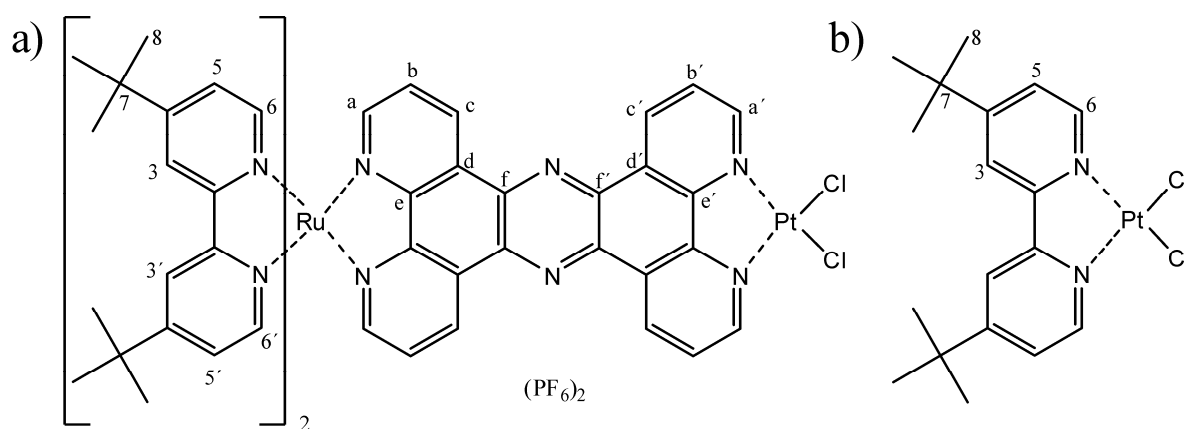


Figure 5.1: a) The photocatalyst [(tbbpy)₂Ru(tpphz)PtCl₂](PF₆)₂ and b) the model system (tbbpy)PtCl₂.

In this context, monomolecular Ru(II)-polypyridyl light-harvesting complexes have been shown to be efficient photocatalysts.^[1, 10-11] One representative of this kind composed of a Ru-photosensitizer, a tpphz-bridging ligand and a PtCl₂ or PdCl₂ unit as the catalytic center was developed by Rau et al.^[12] The binuclear photocatalyst [(tbbpy)₂Ru(tpphz)PtCl₂]²⁺ (tbbpy = 4,4'-di-*t*-butyl-2,2'-bipyridine, tpphz = tetrapyridophenazine) and its Pt-analogue, shown in Figure 5.1a, catalyze the water reduction to molecular hydrogen and the *cis*-selective hydrogenation of tolane.^[12]

Mechanistic proposal of the photocatalytic water reduction

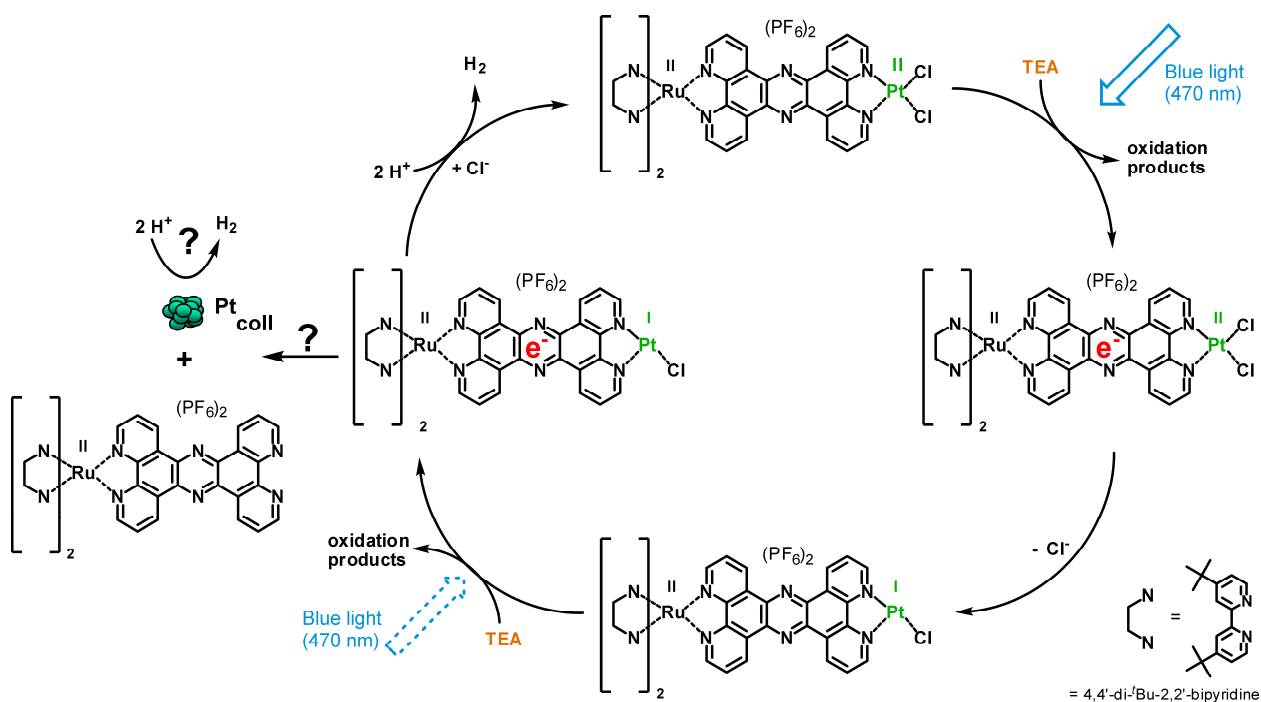


Figure 5.2: Proposed reaction mechanism of the photocatalytic water cleavage with $[(\text{tbbpy})_2\text{Ru}(\text{tpphz})\text{PtCl}_2](\text{PF}_6)_2$.^[1, 12-13]

On the example of the above mentioned photocatalyst, the mechanistic proposal of the water reduction with intramolecular binuclear catalysts is shown in Figure 5.2: The reaction starts with the photoinduced excitation of the ruthenium (II) center into a $^3\text{MLCT}$ -state (MLCT = metal to ligand charge transfer), followed by an electron transfer to the bridging ligand. The generated Ru(III) is reduced back to Ru(II) by the sacrificial electron donor triethylamine (TEA). An electron transfer from the tpphz-ligand onto the Pt center regenerates the photoactive Ru(II)-tpphz subunit, which subsequently accepts a second electron from TEA. It is unknown, whether or not this process involves the anew absorption of a photon. In this step an electron carrying tpphz ligand in combination with a Pt(I) center is formed. This twofold

reduced catalyst enables the formation of molecular hydrogen from protons (from the CD₃CN-water mixture or in the absence of water from TEA) while regenerating the catalyst.

Beside this catalytic cycle involving the intramolecular complex as catalyst, an alternative reaction pathway involving Pt(0)- and Pd(0)-colloids is discussed,^[1-3, 9-11, 13-15] since mechanistic investigations with GC, XPS (X-ray photoelectron spectroscopy) and TEM (transmission electron microscopy) showed, that Pd(0) colloids are formed upon irradiation with visible light from covalently linked Ru(bpy)₃ and (bpy)PdCl₂ moieties connected via a dimethoxy benzene spacer (Ru(dmb)Pd complexes).^[14] In addition, the formation of Pd(0)-colloids is also known for the [(tbbpy)₂Ru(tpphz)PdCl₂]²⁺ from dynamic light scattering (DLS) and X-ray absorption spectroscopy (XAS) performed in the research group of Prof. Rau. Based on the observed correlation of the dissociation of Pd(0) and an induction period of hydrogen formation, Lei et al. supposed that the colloidal metal particles might play a decisive role in the hydrogen formation.^[14]

This hypothesis is in conflict with the observations made by Rau et al. for the hydrogenation of tolane to stilben with [(tbbpy)₂Ru(tpphz)PdCl₂](PF₆)₂. The exclusively formation of the *cis*-product as well as the inactivity of the palladium-free mononuclear complex have been interpreted that Pd(II) must be involved in this reaction.^[12] Furthermore, in contrast to its Pd-analogue, for [(tbbpy)₂Ru(tpphz)PtCl₂](PF₆)₂, which provides similar reactivity, only low amounts of Pt(0)-colloids (<10 %) are detected by XAS and TEM. Furthermore, Sakai and co-workers showed, that for several other Pt(II)-catalyst-based systems no colloids are present in solution after the catalytic hydrogen formation.^[11] The different behaviors of Pd- and Pt-based catalysts were recently supported by Rau and co-workers through deactivation-experiments of Pd- and Pt-colloids with Hg. By the addition of Hg, the catalytic activity of the Pd-based catalysts was drastically reduced, while the activity of the Pt-based catalysts even slightly increased. These findings indicated that the Pt-based catalysts are more stable compared to the Pd-based ones and that Pt-colloids – in contrast to Pd-colloids - do not play a decisive role in the H₂ production.

In addition, DFT calculations showed that the photo reduction of the phenazine induces a dissociation of the chloride ligand from the palladium center, which is connected with the subsequent electron transfer from the tpphz ligand to the palladium center.^[12] The relevance of this theoretical finding could be proven experimentally, since the addition of chloride ions results in the inhibition of hydrogen production,^[12] but no spectroscopic proof could be obtained so far.

Since it has not been proven undoubtedly yet, whether the monomolecular binuclear catalysts themselves or photodecomposition products derived thereof, such as colloidal metal particles, play the decisive role in the catalysis of H₂ formation, the behavior of [(tbbpy)₂Ru(tpphz)PtCl₂](PF₆)₂ under irradiation with visible light was investigated by NMR spectroscopy. To this end, the ³J_{IH,195Pt} coupling was used as a sensor for a potential cleavage of the PtCl₂ unit from the ruthenium phenazin scaffold.^[16] In addition, the proposed dissociation of the chloride or Cl⁻/OH⁻ exchange was investigated.

5.2 Results and Discussion

5.2.1 NMR investigations on the model compound (tbbpy)PtCl₂

In this project the behavior of the Pt unit, especially a potential Pt cleavage upon irradiation, was investigated by means of ¹⁹⁵Pt NMR spectroscopy, enabled by the favorable NMR spectroscopic properties of ¹⁹⁵Pt (spin quantum number I = 1/2, gyromagnetic ratio γ(¹⁹⁵Pt) = 5.768·10⁷ rad s⁻¹ T⁻¹, natural abundance 33.8 %).^[17] The ¹⁹⁵Pt chemical shift is highly sensitive to the metal oxidation state, to the ligand substitution and to the coordination sphere of the ¹⁹⁵Pt nucleus.^[17-18] In addition to the chemical shift, the ³J_{IH,195Pt} coupling in pyridine-like Pt(II) complexes, which is typically in the range of 20 Hz or beyond,^[16, 19-20] is also a direct probe for alterations in the Pt binding situation. Alternatively, the ²J_{13C,195Pt} coupling, which is typically in the range of 10-20 Hz,^[21] or the ¹J_{15N,195Pt} coupling in the known range from 88 to 755 Hz could be analyzed,^[19-20] typically from the satellite pattern in 2D coherence transfer experiments.^[20, 22]

Generally, ¹⁹⁵Pt NMR has a couple of spectroscopic advantages, but, caused by the ¹⁹⁵Pt relaxation behavior, it also comes along with some challenges for the direct observation of ¹⁹⁵Pt and for the detection of any kind of couplings to ¹⁹⁵Pt. For large compounds like [(tbbpy)₂Ru(tpphz)PtCl₂](PF₆)₂, the chemical shift anisotropy (CSA) is the dominant relaxation mechanism for ¹⁹⁵Pt (beside CSA, the spin rotation relaxation is important for small, highly symmetrical complexes like PtCl₄²⁻ and PtCl₆²⁻).^[17] CSA relaxation increases with the square of the applied magnetic field strength B₀², the square of the nuclear screening anisotropy (Δσ)², with the molecular weight, the solvent viscosity and with decreasing temperature (as the reorientational correlation time τ_c will be increased).^[17] This suggests that ¹⁹⁵Pt studies should be carried out at low to intermediate magnetic field strengths with a demand for high temperature stability, as CSA effects will be smaller under these conditions, see equation (5.1).^[23]

$$\left[\frac{1}{T_1(Pt)} \right] (CSA) = \frac{6}{7} \cdot \left[\frac{1}{T_2(Pt)} \right] (CSA) = \frac{2}{15} \gamma_{Pt}^2 \cdot B_0^2 \cdot (\Delta\sigma)^2 \cdot \tau_c \quad (5.1)$$

with gyromagnetic moment γ , magnetic field strength B_0 , nuclear screening anisotropy $\Delta\sigma$ and reorientational correlation time τ_c .

Due to the challenges in ^{195}Pt NMR for such extended and therefore very fast relaxing molecules like the investigated photocatalyst, an intensive optimization of spectroscopic parameters is an absolute prerequisite for the successful application of the different experiments. Therefore, (tbbpy)PtCl₂ (see Figure 5.1b) was used as a model compound to optimize the detection methods for the $\delta(^{195}\text{Pt})$ and $^3J_{1\text{H},^{195}\text{Pt}}$ coupling, before the real photocatalyst was investigated.

B_0 field strength dependency of the ^{195}Pt relaxation

The influence of the field strength on the CSA relaxation of (tbbpy)PtCl₂ in CD₂Cl₂ and therefore the detectability of the $^3J_{1\text{H},^{195}\text{Pt}}$ coupling in ^1H spectra was investigated at 400 and 600 MHz (see Figure 5.3). As already mentioned, the CSA relaxation becomes more effective at higher magnetic field strength, which leads to a partial decoupling due to relaxation. This is shown in Figure 5.3, where the ^{195}Pt satellites are clearly visible at 400 MHz, but hardly observable at 600 MHz. This shows that it is of advantage to carry out ^{195}Pt studies at 400 MHz rather than 600 MHz.

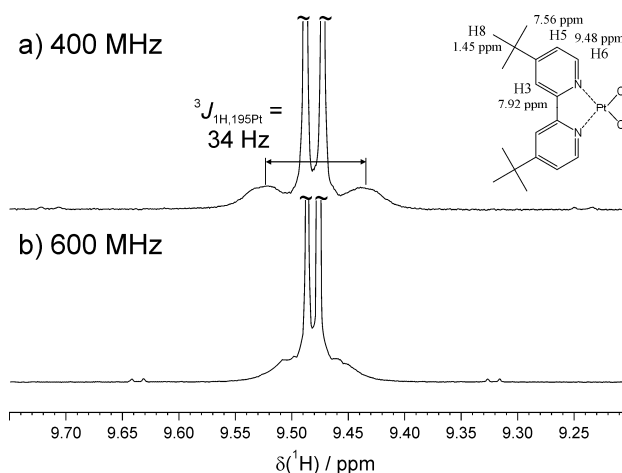


Figure 5.3: ^1H signal of proton H6 of (tbbpy)PtCl₂ in CD₂Cl₂ at 300 K a) at 400 MHz and b) at 600 MHz.

Solvent dependency of the ^{195}Pt relaxation

According to equation (5.1), the ^{195}Pt relaxation and consequently the detectability of the $^3J_{\text{H},^{195}\text{Pt}}$ coupling strongly depend on the reorientational correlation time τ_c . This effect was investigated with ^1H spectra in DMSO- d_6 , CDCl_3 , CD_2Cl_2 and CD_3CN . (see Figure 5.4). Along with the decreasing viscosity from a)-d) (η at 25°C in $\text{mPa}\cdot\text{s}$: DMSO: 1.987, CHCl_3 : 0.537, CD_2Cl_2 : 0.413, CD_3CN 0.369)^[24] the correlation time τ_c decreases. This leads to decelerated relaxation and therefore to a better observability of the coupling in low viscous solvents. Because of the good solubility of $(\text{tbbpy})\text{PtCl}_2$ in CD_2Cl_2 and the low viscosity of CD_2Cl_2 , it was used as the solvent for the following experiments.

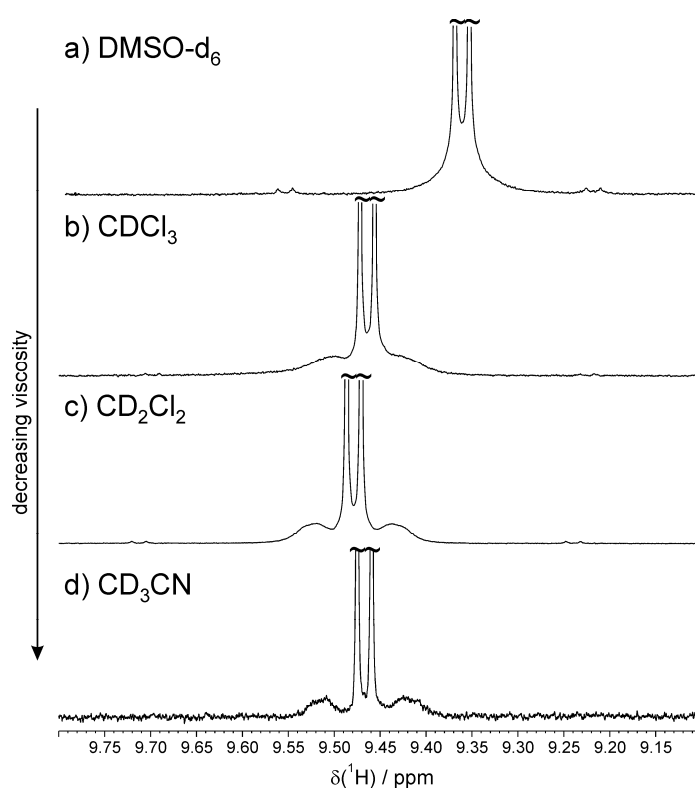


Figure 5.4: ^1H signal of H6 proton of $(\text{tbbpy})\text{PtCl}_2$ at 300 K and 400 MHz in different solvents: a) DMSO- d_6 , b) CDCl_3 , c) CD_2Cl_2 , b), d) CD_3CN . a)-c) 64 scans, d) 256 scans.

^{195}Pt spectra of the model compound

Because of the large chemical shift range of Pt(II) complexes of 5000 ppm, a series of ^{195}Pt spectra of (tbbpy)PtCl₂ in CD₂Cl₂ was necessary in order to cover the complete chemical shift range of Pt(II) complexes. For (tbbpy)PtCl₂ in CD₂Cl₂, one singlet at $\delta(^{195}\text{Pt}) = -2341$ ppm with a line width of 780 Hz was found at 600 MHz (see Figure 5.5). The ^{195}Pt chemical shift is in excellent agreement with a similar square-planar Pt complex with two chloride and one phenantroline ligand ($\delta(^{195}\text{Pt}) = -2336$ ppm)^[25] and other pyridine-derived Pt complexes containing chloride ligands.^[16-17, 20] The enormous line width of 780 Hz can be attributed to the fast CSA relaxation at the high field strength of 600 MHz and can be diminished to 740 Hz at 400 MHz (data not shown). This only slight reduction hints at additional relaxation mechanisms like spin-rotation relaxation.^[17] In addition, relaxation contributions of the adjacent nitrogen atoms due to the presence of larger $^1J_{\text{N,Pt}}$ values (often hundreds of Hz in Pt(II) complexes)^[19] in combination with considerable ^{14}N relaxation rates may cause an additional shortening of the T_2 time of ^{195}Pt .^[20]

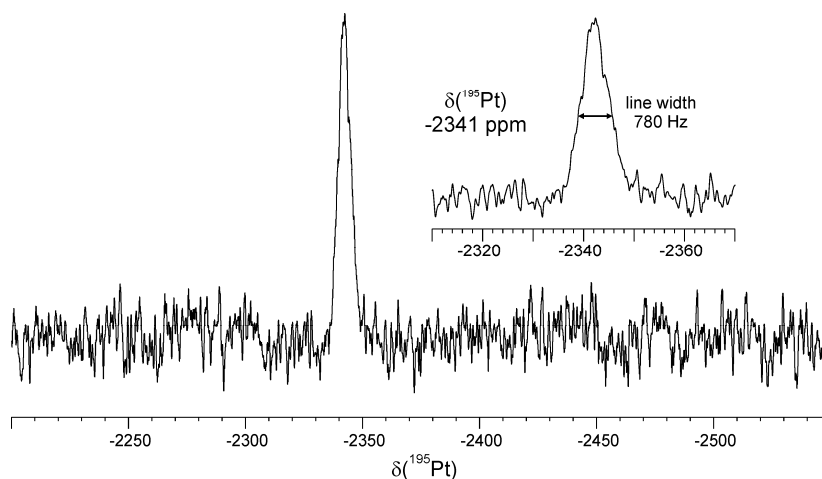


Figure 5.5: ^{195}Pt spectrum of (tbbpy)PtCl₂ in CD₂Cl₂ at 300 K and 600 MHz. Referenced to Na₂PtCl₆ in D₂O (see SI).

To estimate the influence of the solvent on the ^{195}Pt chemical shift of (tbbpy)PtCl₂, a ^{195}Pt spectrum in CD₃CN at 300 K and 400 MHz was measured. Due to the low solubility in CD₃CN, 170k scans were necessary leading to a measurement time of more than two days. The chemical shift in CD₃CN ($\delta(^{195}\text{Pt}) = -2340$ ppm, data not shown) was very similar to the value in CD₂Cl₂, indicating that the solvent has only a diminished influence on the chemical shift for this particular compound.

Detection of the $^3J_{\text{H},^{195}\text{Pt}}$ coupling in 1D and 2D $^1\text{H},^{195}\text{Pt}$ -HMBC spectra

In principle, a direct detection of $^nJ_{\text{H},^{195}\text{Pt}}$ couplings is possible using 1D and 2D $^1\text{H},^{195}\text{Pt}$ -HMBC spectra. Therefore, an optimal balance between relaxation induced exponential signal decay and sinusoidal coupling evolution is essential, which can be adjusted with an optimized magnetization transfer delay D6. In addition, in all spectra with gradient pulses utilized for coherence selection, the gradient strength pattern has to be adjusted, so that the effects of all gradients cancel at the end of the pulse sequence, see equation (5.2) for the $^1\text{H},^{195}\text{Pt}$ -HMBC pulse sequence used in this approach.

$$\sum G_z = -(\gamma_H + \gamma_X)G_1 + (\gamma_H - \gamma_X)G_2 + \gamma_H G_3 = 0 \quad (5.2)$$

with gyromagnetic moment γ and gradients G_1 , G_2 and G_3 .

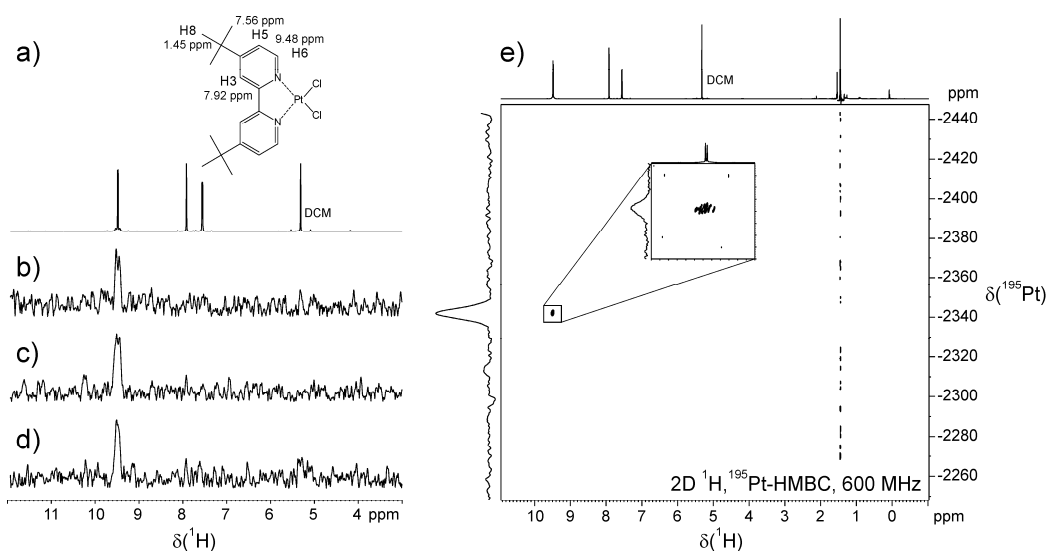


Figure 5.6: 1D and 2D $^1\text{H},^{195}\text{Pt}$ -HMBC spectra of $(\text{tbbpy})\text{PtCl}_2$ in CD_2Cl_2 at 300 K with optimized D6 delay of 10 ms. a) ^1H spectrum and b-d) 1D $^1\text{H},^{195}\text{Pt}$ -HMBC spectra at 400 MHz with ns 600 and different gradient strength pattern $\text{GPZ}_{1/2/3}$: b) 30/30/12.94, c) 40/30/25.09 d) 60/30/49.40; e) 2D $^1\text{H},^{195}\text{Pt}$ -HMBC spectrum at 600 MHz with ns 256 and $\text{GPZ}_{1/2/3}$ 60/30/49.40.

The optimum transfer delay D6 was determined in a series of 1D $^1\text{H},^{195}\text{Pt}$ -HMBC spectra with varying D6 delays to be 10 ms (at 400 and 600 MHz, data not shown). For the coherence selection three different gradient strength patterns have been calculated (expressed in percentage of the maximum gradient power): $\text{GPZ}_{1/2/3}$ 30/30/12.94, 40/30/25.09, and 60/30/49.40, all in accordance with equation (5.2). The corresponding 1D $^1\text{H},^{195}\text{Pt}$ -HMBC spectra exhibited only marginal deviations in the signal intensities for the different gradient strength pattern (see Figure 5.6b-d). Therefore, all following 1D and 2D $^1\text{H},^{195}\text{Pt}$ -HMBC spectra were performed with

GPZ_{1/2/3} 60/30/49.40 (see Figure 5.6e). To conclude, the $^3J_{\text{H},^{195}\text{Pt}}$ coupling could be detected in 1D and 2D $^1\text{H},^{195}\text{Pt}$ -HMBC spectra.

Detection of the $^3J_{\text{H},^{195}\text{Pt}}$ coupling by the comparison of ^1H and $^1\text{H}\{^{195}\text{Pt}\}$ spectra

1D and 2D $^1\text{H},^{195}\text{Pt}$ -HMBC spectra gave direct evidence for the $^3J_{\text{H},^{195}\text{Pt}}$ coupling between the proton H6 and the Pt center. However, this method is very time consuming and seems not suited for online-monitoring of fast photocatalytic reactions. Therefore, $^1\text{H}\{^{195}\text{Pt}\}$ spectra with inverse or power gated decoupling scheme with a typical time demand of seconds to minutes are a time-saving alternative. By comparison of the $^1\text{H}\{^{195}\text{Pt}\}$ and the normal ^1H spectrum protons carrying a Pt coupling can be identified. A variation of the decoupling power in inverse gated $^1\text{H}\{^{195}\text{Pt}\}$ spectra revealed the optimum decoupling power with complete decoupling of the $^3J_{\text{H},^{195}\text{Pt}}$ coupling and only marginal line shape distortions for the other signals (see Figure 5.7b). These residual distortions could be eliminated with the power gated decoupling scheme (Figure 5.7c). This is exemplarily shown for the Pt coupled H6 proton on the left side of Figure 5.7 and for the uncoupled H3 and H5 protons on the right side of Figure 5.7.

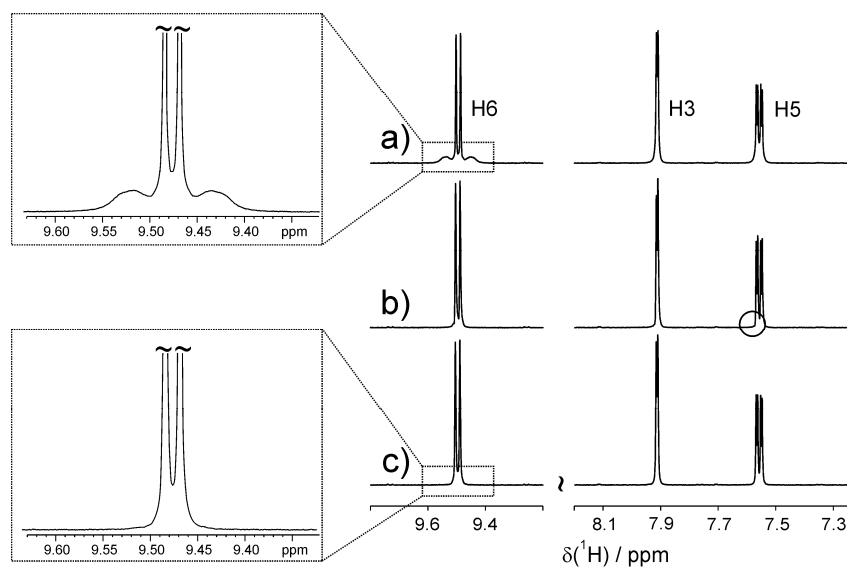


Figure 5.7: a) ^1H spectrum and b) inverse gated and c) power gated $^1\text{H}\{^{195}\text{Pt}\}$ spectra of (tbbpy) PtCl_2 in CD_2Cl_2 at 300 K and 400 MHz. Left and right sections are scaled independently.

5.2.2 NMR investigations on the photocatalyst $[(\text{tbbpy})_2\text{Ru}(\text{tpphz})\text{PtCl}_2](\text{PF}_6)_2$

After implementation of different detection methods, $[(\text{tbbpy})_2\text{Ru}(\text{tpphz})\text{PtCl}_2](\text{PF}_6)_2$ was investigated in analogy to the model compound. Acetonitrile was used as the solvent because of its low viscosity and its application in the photocatalytic water reduction. To allow for fast and reliable NMR measurements, the catalyst concentration was increased from 10^{-2} mM (catalytic reaction conditions)^[12] to 9 mM, the highest concentration without precipitation.

^{195}Pt spectra

In the ^{195}Pt spectra one singlet at -2297 ppm with a line width of 670 Hz at 600 MHz and 360 Hz at 400 MHz (see Figure 5.8) was detected. This strong reduction of the line width at lower magnetic field indicates that the ^{195}Pt relaxation of the photocatalyst is dominated by the CSA mechanism (in contrast to the model compound). The downfield shift of 43 ppm compared to $(\text{tbbpy})\text{PtCl}_2$ ($\delta(^{195}\text{Pt}) = -2340$ ppm in CD_3CN) is in the same range as observed for an attachment of a second metal fragment to similar $\text{Pt}(\text{bpym})(\text{CH}_3)_3\text{Cl}$ complexes (bpym = 2,2'-bipyrimidine).^[20]

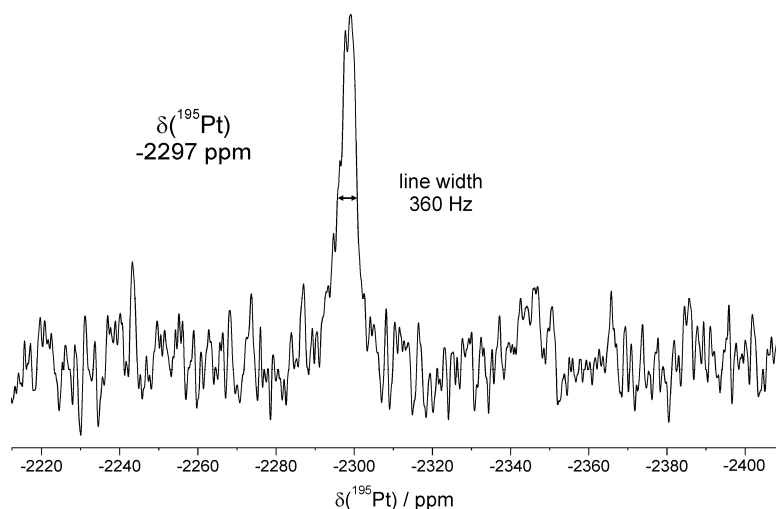


Figure 5.8: ^{195}Pt spectrum of $[(\text{tbbpy})_2\text{Ru}(\text{tpphz})\text{PtCl}_2](\text{PF}_6)_2$ in CD_3CN at 300 K and 400 MHz.

Comparison of the magnitude of the coupling for the model compound and the photocatalyst

The coupling constant of the model compound was about 34 Hz, as is visible as satellite splitting in the ^1H spectrum, see Figure 5.3. This quite big constant leads to a relatively easy detection and makes this compound ideal for testing. However, for the real photocatalyst the $^3J_{\text{H},^{195}\text{Pt}}$ coupling is not visible as satellite splitting but just as line broadening, even at 300 MHz, the lowest applied field strength. Therefore, its magnitude was estimated by line shape analysis of the Ha' proton (see Figure 5.9). In this simulation the coupling constant was varied from 0 to 20 Hz and the line width of the signal was iterated accordingly (see Table 5.1), at which the best fit with the experimental spectrum was obtained with a simulated coupling constant of 8 ± 2 Hz (see Figure 5.9).

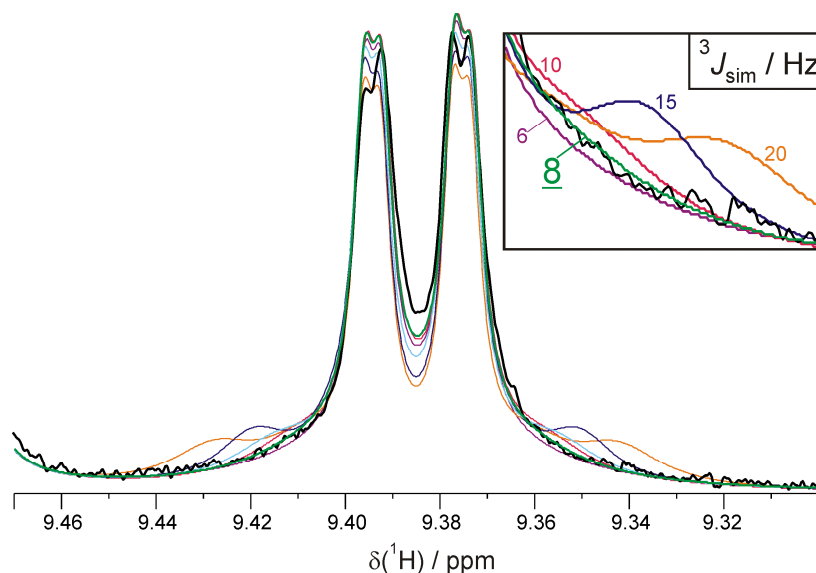


Figure 5.9: Simulations of the coupling pattern of the Ha' proton of $[(\text{tbbpy})_2\text{Ru}(\text{tpphz})\text{PtCl}_2](\text{PF}_6)_2$ in CD_3CN at 300 K and 300 MHz.

Table 5.1: Simulated coupling constants from 0 to 10 Hz and corresponding line widths for the Ha' proton signal at 300 MHz and theoretical HMBC peak intensities with optimized D6 delay.

Ha' proton		$^1\text{H}, ^{195}\text{Pt}$ -HMBC	
$^3J_{\text{H},^{195}\text{Pt}} / \text{Hz}$	line width / Hz	opt. D6 delay / ms	rel. peak intensity
0	15.7	---	---
2	15.4	21	0.05
4	14.6	21	0.10
6	12.9	23	0.16
8	9.2	28	0.28
10	6.9	---	---
12	6.4	---	---
15	6.3	---	---
20	6.2	---	---

Detection of the $^3J_{\text{H},^{195}\text{Pt}}$ coupling in 1D ^1H , ^{195}Pt -HMBC and $^1\text{H}\{^{195}\text{Pt}\}$ spectra

For this small coupling constant of 8 ± 2 Hz, the corresponding optimized D6 delay in the HMBC is 28 ms at 300 MHz (see Table 5.1). At higher field strengths, the relaxation induced signal decay is accelerated and therefore shorter D6 delays have been utilized. This can be seen in the 1D ^1H , ^{195}Pt -HMBC spectra at 400 MHz with varying D6 delay from 0.5 to 6 ms in Figure 5.10b-f, where the highest signal intensity was obtained with a D6 delay of 4 ms at 400 MHz. At 600 MHz this tendency was even more pronounced: In a series of 1D HMBC spectra with varying D6 delay, each of them with 10k scans (data not shown), only for the smallest D6 delay of 1 ms a small coupling peak could be detected. Therefore, the optimum D6 delay was 28 ms at 300 MHz, 4 ms at 400 MHz and below 1 ms at 600 MHz.

As mentioned for the model compound, this method is very time consuming and instead a comparison of ^1H and $^1\text{H}\{^{195}\text{Pt}\}$ spectra is preferred for the detection of the $^3J_{\text{H},^{195}\text{Pt}}$ coupling (see Figure 5.10g). For the Ha' proton the coupling could be observed by the comparison of the $^1\text{H}\{^{195}\text{Pt}\}$ spectrum (red) and the ^1H spectrum (black). Exemplarily, the Hc' proton at 9.50 ppm is also depicted to demonstrate the unchanged line shapes of all other protons.

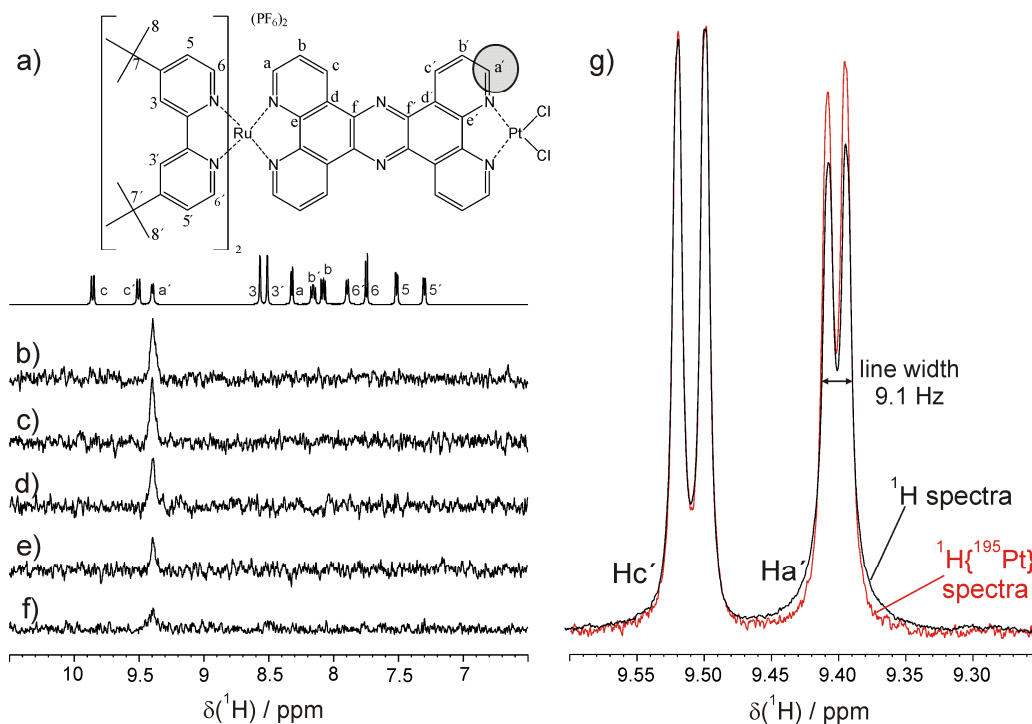


Figure 5.10: Detection of the $^3J_{\text{H},^{195}\text{Pt}}$ coupling of $[(\text{tbbpy})_2\text{Ru}(\text{tpphz})\text{PtCl}_2](\text{PF}_6)_2$ in CD_3CN at 300 K and 400 MHz: a) ^1H spectrum. b)-f) 1D ^1H , ^{195}Pt -HMBC spectra with ns 10k and D6 delay of b) 6 ms, c) 4 ms, d) 2 ms, e) 1 ms, f) 0.5 ms. g) Comparison of ^{195}Pt -coupled ^1H spectrum (black) and power gated decoupled $^1\text{H}\{^{195}\text{Pt}\}$ spectrum (red), each with 8 scans.

Determination of the hydrodynamic volume with DOSY experiments

^1H -DOSY experiments^[26] are interesting with regard to aggregation/deaggregation of the catalyst before or in the course of the catalytic reaction. From the diffusion coefficient ($6.00 \pm 0.18 \cdot 10^{-10} \text{ m}^2 \text{ s}^{-1}$ at 298 K) a hydrodynamic volume of $V_{\text{H}} = 4.1 \pm 0.4 \cdot 10^3 \text{ \AA}^3$ could be calculated (with globular shape approximation).^[27] With the help of the theoretical hydrodynamic volume of 1193 \AA^3 (calculated on the molecular mechanics level),^[28] the aggregation tendency of the compound can be estimated very roughly to be a trimer or tetramer. But due to the very rough estimations, this aggregation value has to be handled with care and further investigations would be necessary.

This formation of aggregates has been shown to be induced by π - π -stacking interactions of the aromatic ligands,^[29] and mainly dimers are found for mononuclear $[(\text{bpy})_2\text{Ru}(\text{tpphz})](\text{PF}_6)_2$ and similar complexes in CD_3CN in the concentration range of 1-10 mM.^[30-31] In addition, the theoretical increase of the ^1H diffusion value upon a cleavage of the PtCl_2 unit is within the error range of the measurement. Therefore, ^1H -DOSY values cannot be reliably interpreted with regard to a potential cleavage of the PtCl_2 unit. Alternative ^{195}Pt - or ^{35}Cl -DOSY experiments are not feasible due to the fast CSA and quadrupolar relaxation, respectively.^[32-33]

5.2.3 NMR investigations under catalytic conditions

For the photocatalytic water reduction, acetonitrile-water mixtures are used as the solvent, triethylamine (TEA) is used as the sacrificial electron donor and the solution is irradiated with light of 470 nm wavelength. To get stepwise closer to the catalytic conditions, several test systems were investigated. In first control experiments the change of the solvent from pure CD_3CN to $\text{CD}_3\text{CN}/\text{D}_2\text{O}$ mixtures was investigated with or without irradiation with blue light (470 nm). In the next step, TEA was added similarly to the catalytic conditions and the behavior of the sample with and without irradiation was again investigated by means of ^1H , $^1\text{H}\{^{195}\text{Pt}\}$, ^{195}Pt and ^{35}Cl spectra (for experimental details see SI).

In these investigations, a similar irradiation setup as in the catalysis, but with NMR tubes instead of GC vials, was used to be as close to the catalytic conditions as possible. The setup was composed of a stick with 30 LEDs emitting blue light ($470 \pm 15 \text{ nm}$) and four air coolers near the LED stick for heat dissipation (see Figure 5.11).

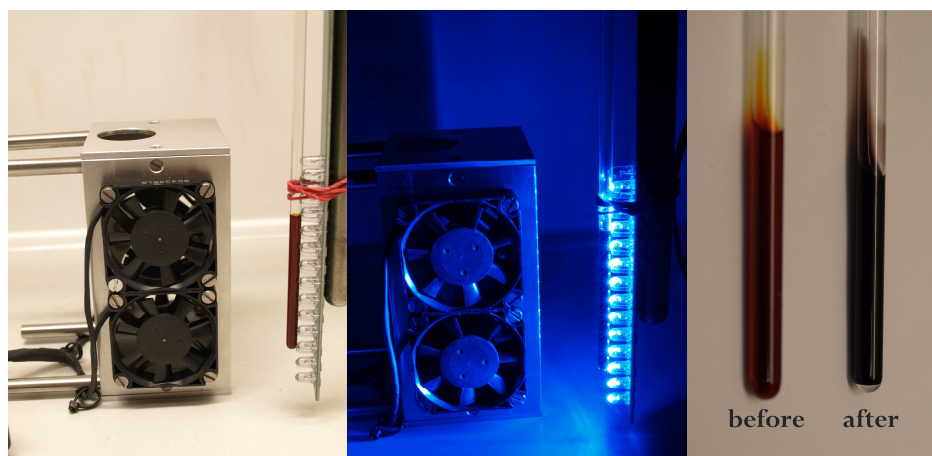


Figure 5.11: Irradiation setup used for the NMR investigations composed of a stick with 30 LEDs and four air cooler for heat removal and samples containing the catalyst and TEA in aqueous solution before and after irradiation.

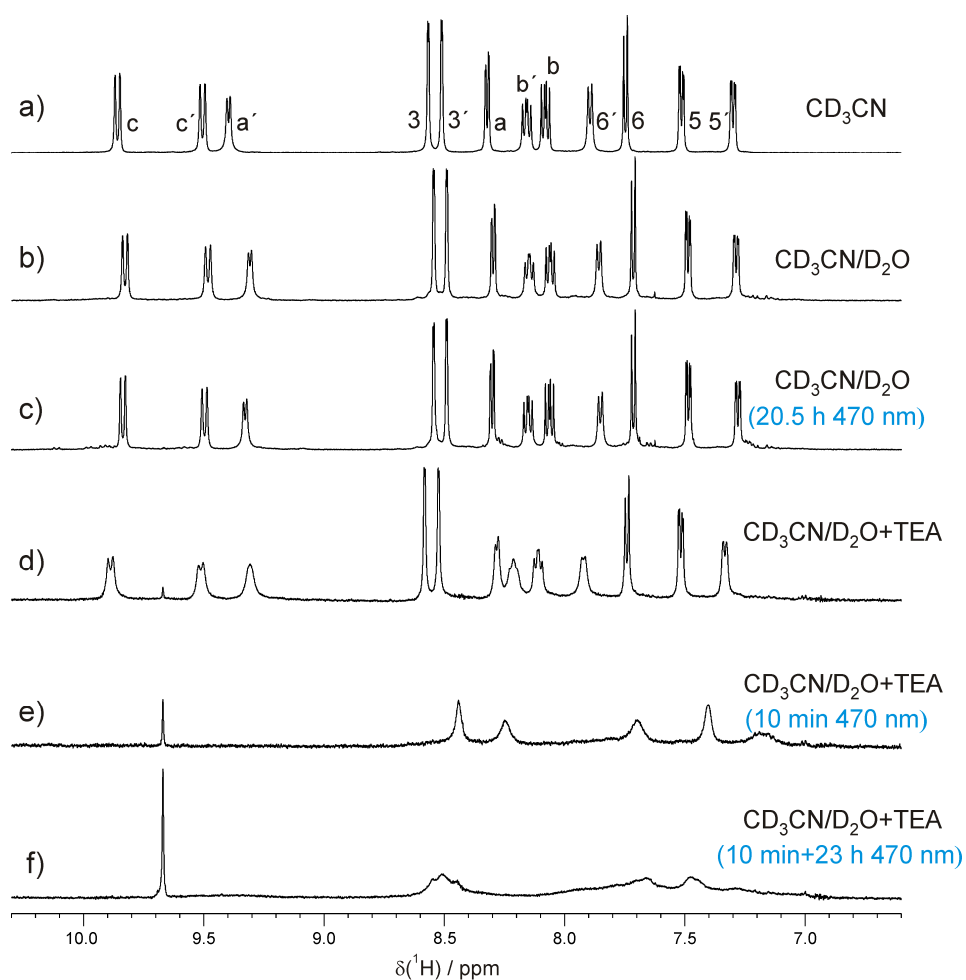


Figure 5.12: Aromatic section of the ^1H spectra of $[\text{tbbpy}]_2\text{Ru}(\text{tpphz})\text{PtCl}_2(\text{PF}_6)_2$ in a) CD_3CN , b) $\text{CD}_3\text{CN}/\text{D}_2\text{O}$, c) $\text{CD}_3\text{CN}/\text{D}_2\text{O}$ after 10 min irradiation, d) $\text{CD}_3\text{CN}/\text{D}_2\text{O}+\text{TEA}$ e) $\text{CD}_3\text{CN}/\text{D}_2\text{O}+\text{TEA}$ after 10 min irradiation and f) $\text{CD}_3\text{CN}/\text{D}_2\text{O}+\text{TEA}$ after 10 min+23 h irradiation with 470 nm LED light.

In CD₃CN/D₂O, the proton signals were downfield shifted by 0.02-0.03 ppm (Ha' proton 0.09 ppm) compared to pure CD₃CN, see Figure 5.12a and b. Upon irradiation for 20.5 h no alterations of the ¹H chemical shifts or coupling fine structure could be observed (see Figure 5.12c). In particular, the ³J_{1H,195Pt} coupling of the Ha' proton was still detected. In addition, the ¹⁹⁵Pt chemical shift of the signal did not change upon irradiation (data not shown). Since for a Cl⁻/OH⁻ exchange a downfield shift of more than 300 ppm is expected,^[34] it can be clearly excluded that a Cl⁻/OH⁻ exchange occurs for [tbbpy]₂Ru(tpphz)PtCl₂](PF₆)₂ by irradiation at 470 nm for 20.5 h in aqueous solution (at least without TEA as sacrificial electron donor). This finding was confirmed by ³⁵Cl spectra, since in a ³⁵Cl spectrum with 64k scans no ³⁵Cl signal from a released chloride anion could be detected (for details see SI).

In the next step a large excess of TEA was added leading to a reduced spectral resolution of the aromatic protons (see Figure 5.12d). This could be attributed to the high dynamic range (e.g. ratio of signal intensities Ha' / CH₃(NEt₃): 0.0004 / 1) leading to reduced resolution for small signals in presence of the very intense signals of TEA. ¹H spectra with selective excitation of the aromatic protons of the catalyst reduced the intensities of the TEA signals and improved the ratio to 0.1 / 1, but no increase in spectral resolution could be obtained (data not shown).

After irradiation for 10 min five broad singlets between 7 and 8.5 ppm (7.18, 7.40, 7.70, 8.25, 8.44 ppm) emerged in the aromatic region in the ¹H spectra (see Figure 5.12e), whereas the line shape and intensities of the solvent and TEA signals remained unchanged. In addition, no ¹⁹⁵Pt signal could be detected any longer (data not shown). After a further irradiation period of 23 h three broad signals at 8.51, 7.67 and 7.48 ppm were detected in the aromatic region and no ¹⁹⁵Pt signal could be detected in the typical Pt(II) chemical shift range of -500 ppm to -5500 ppm (data not shown). These findings strongly hint at a decomposition of the photocatalyst in the presence of TEA upon irradiation, already after 10 min.

One reason for the decomposition of the photocatalyst could be the high luminance intensity of the LED stick in combination with the different sample geometry in the NMR tube compared to the assembly used in the photocatalytic reactions (GC vials). Another explanation might be the high concentration of the catalyst of 1.52 mM compared to 10⁻² mM under catalytic conditions^[12] leading to a drastically increased concentration of photo excited species upon irradiation. This assumption is confirmed by the drastically increased speed of the color change of the reaction mixture from red to black (see Figure 5.11). It occurs within few minutes in this setup whereas it takes minutes to hours for the GC vial-setup typically employed under catalytic conditions.

5.3 Conclusion and Outlook

To summarize, this project dealt with the formation and catalytic relevance of Pt-colloids and the spectroscopic evidence for the proposed cleavage of a chloride from the catalyst. Therefore, the $^3J_{1\text{H},195\text{Pt}}$ coupling should be used as sensor for a potential cleavage of the complete PtCl_2 unit from the catalyst. In addition, the ^{195}Pt chemical shift and ^{35}Cl spectra should reveal a spectroscopic evidence for the proposed cleavage of a chloride.

With $(\text{tbbpy})\text{PtCl}_2$ in CD_2Cl_2 , acting as a model compound, the spectroscopic parameters that are essential for the successful investigations of Pt compounds have been optimized: The solvent and B_0 field dependence of the ^{195}Pt relaxation was investigated with various solvents at 400 and 600 MHz spectrometer revealing low viscous solvents and low magnetic field strength to be favorable for the detectability of the coupling. In the ^{195}Pt spectrum one singlet at $\delta(^{195}\text{Pt}) = -2341$ ppm in CD_2Cl_2 and $\delta(^{195}\text{Pt}) = -2340$ ppm in CD_3CN was found. The direct detection of the $^3J_{1\text{H},195\text{Pt}}$ coupling was achieved with 1D and 2D ^1H , ^{195}Pt -HMBC spectra and by the comparison of ^1H and $^1\text{H}\{^{195}\text{Pt}\}$ spectra.

After optimization of the detection methods with the help of the model compound, the photocatalyst $[\text{tbbpy}]_2\text{Ru}(\text{tpphz})\text{PtCl}_2](\text{PF}_6)_2$ in CD_3CN was investigated and the $^3J_{1\text{H},195\text{Pt}}$ coupling could be detected in $^1\text{H}\{^{195}\text{Pt}\}$ and 1D ^1H , ^{195}Pt -HMBC spectra. The addition of water and the following irradiation with blue light (470 nm) had no significant effect on the ^{195}Pt and ^1H chemical shift or the $^3J_{1\text{H},195\text{Pt}}$ coupling. For $[\text{tbbpy}]_2\text{Ru}(\text{tpphz})\text{PtCl}_2](\text{PF}_6)_2$ in $\text{CD}_3\text{CN}/\text{D}_2\text{O}$ without the sacrificial electron donor TEA, a Cl^-/OH^- exchange or Cl^- cleavage can be clearly excluded after irradiation for 20.5 h. Upon the addition of a large excess of TEA, the spectral resolution decreased. Upon irradiation in the presence of TEA, the photocatalyst decomposed, probably due to the high luminance intensity and/or the high catalyst concentration.

For further investigations a reduction of the amount of TEA (down to a 1:1 ratio to the catalyst) seems advisable to avoid the deterioration of the spectral resolution and to decelerate the decomposition. Additionally, the light intensity and/or the catalyst concentration should be reduced to decrease the decomposition rate.

Another approach for the observation of the Pt-cleavage would be the ^{15}N labeling of the nitrogen atoms directly attached to the platinum, since this might decelerate the ^{195}Pt relaxation and thereby facilitate the detection of the small $^3J_{1\text{H},195\text{Pt}}$ coupling and additionally might allow for 1D triple resonance (^1H , ^{15}N , ^{195}Pt) experiments.

Furthermore, the currently applied setup impeded a simultaneous irradiation and NMR observation, which would facilitate the investigation of photocatalytic reactions in general. Therefore, a glass fiber-based NMR-illumination unit was developed. In addition, this new setup allows an adaption of the light intensity to the particular requirements (see chapter 7). First tests in the field of flavin photocatalysis have been performed successfully with this new setup, but due to the very recent construction no attempts have been made in the field of the photocatalytic water reduction so far.

5.4 Supporting Information

Experimental Section

NMR spectra were recorded on a Bruker Avance 400 MHz spectrometer equipped with a BBO probe with z-gradient (temperature was controlled by a BVT 2000 unit) and a Bruker Avance 600 III spectrometer equipped with a TBI $^1\text{H}/^{31}\text{P}$ -BB probe with z-gradient and BVT 3000 unit at 300 K. The NMR data were processed and evaluated with Bruker's TOPSPIN 3.0 and the included DAISY program was used for line shape analysis.

Assignments of proton and carbon resonances were obtained by one- and two-dimensional NMR spectra (^1H , ^1H , ^1H -COSY, ^1H , ^1H -NOESY, ^1H , ^{13}C -HSQC, and ^1H , ^{13}C -HMBC spectra). In addition, ^{195}Pt signals were assigned with 1D ^{195}Pt -, and ^1H , ^{195}Pt -HMBC spectra. The ^1H and ^{13}C chemical shifts are internally referenced to TMS, the ^{195}Pt chemical shifts were referenced to 0.25 M Na_2PtCl_6 in D_2O and the ^{35}Cl chemical shifts were referenced to 1M LiCl in D_2O .

For the ^{195}Pt spectra of both compounds, the 90° pulse length was adapted from a sample of 0.25 M Na_2PtCl_6 in D_2O (which was used before for the setup of the ^{195}Pt parameter set), since variations of the 90° pulse length for the ^{195}Pt signal of (tbbpy) PtCl_2 in CD_2Cl_2 showed the optimal pulse length similar to those of 0.25 M Na_2PtCl_6 in D_2O .

In general, ^{195}Pt spectra demand high temperature stability due to the CSA relaxation in combination with the high temperature dependency of the ^{195}Pt chemical shift.^[18] This prerequisite was not fulfilled at a 400 MHz spectrometer without BCU temperature control unit, where insufficient temperature control impeded the detection of any signal for (tbbpy) PtCl_2 in CD_2Cl_2 in ^{195}Pt as well as 1D and 2D ^1H , ^{195}Pt -HMBC spectra (data not shown).

In a ^{35}Cl spectrum of 0.25 M Na_2PtCl_6 in D_2O a sharp singlet at $\delta(^{35}\text{Cl}) = -0.45$ ppm with a line width of 16 Hz was detected. Due to the chemical shift and line width,^[35] this signal could be assigned to a released chloride anion from $\text{PtCl}_6^{2-} \rightarrow 2 \text{Cl}^- + \text{PtCl}_4$. This shows the release of Cl^- from PtCl_2 fragments in aqueous solution. In contrast, for the irradiated photocatalyst in aqueous solution without TEA, no signal attributable to a released chloride anion was found in ^{35}Cl spectra.

Sample preparation and irradiation setup

For (tbbpy)PtCl₂ in CD₂Cl₂, a sample concentration of 55 mM was applied for the optimization of NMR spectroscopic parameters. For [tbbpy)₂Ru(tpphz)PtCl₂](PF₆)₂ in CD₃CN a concentrations of 9 mM (8.5 mg; 5.4 μmol in 0.6 mL CD₃CN) without and 1-2 mM with irradiation were applied. Higher concentrations led to the precipitation of the catalyst. Similar attempts in CD₂Cl₂ were not feasible due to the very low solubility of the catalyst in CD₂Cl₂.

[tbbpy)₂Ru(tpphz)PtCl₂](PF₆)₂ in CD₃CN/D₂O without TEA:

All NMR investigations were conducted under an inert atmosphere of argon at all times to prevent oxidation/quenching of the reaction by oxygen. All solvents were carefully degassed before use. [tbbpy)₂Ru(tpphz)PtCl₂](PF₆)₂ (1.7 mg; 1.08 μmol; 1 eq.) was dissolved in 0.43 mL CD₃CN and 0.07 mL D₂O yielding a catalyst concentration of 2.16 mM. The resulting water content of 16 vol% was chosen since the maximum turn over number (TON, mol product/mol catalyst) of the photocatalytic water reduction was observed at this particular content.^[36] The bright red solution was illuminated for 20.5 h with blue light (470 ± 15 nm) with 30 LEDs, which were fixed at a stick in close proximity to the NMR tube. Air coolers near the LED stick were used for temperature regulation. No color changes of the sample were observed visually upon irradiation.

[tbbpy)₂Ru(tpphz)PtCl₂](PF₆)₂ in CD₃CN/D₂O with TEA:

To the above mentioned solution 0.21 mL degassed TEA (0.15 g; 1.51 mmol) were added, resulting in a catalyst concentration of 1.52 mM (1 eq.) and a TEA concentration of 2.13 M (1400 eq.), to be as close to the catalytic conditions as possible.^[12] The solution was irradiated for 10 min with the LED stick, which was accompanied by a color change from bright red to black (see Figure 5.11). Further irradiation periods of 10 min and additionally 23 h were applied.

^1H - and ^{13}C resonance assignment

^1H - and ^{13}C resonance assignment for $[(\text{tbbpy})_2\text{Ru}(\text{tpphz})\text{PtCl}_2](\text{PF}_6)_2$ in CD_3CN at 300 K, for nomenclature see Figure 5.13. All homonuclear coupling constants have been simulated with the DAISY program.

^1H -NMR (CD_3CN , T = 300 K, ref: TMS 0.00 ppm): $\delta(^1\text{H})[\text{ppm}] =$

9.85 (Hc, 2H, dd, $^3J_{\text{Hb,Hc}} = 8.31$ Hz, $^4J_{\text{Ha,Hc}} = 1.21$ Hz); 9.50 (Hc', 2H, dd, $^3J_{\text{Hb',Hc'}} = 8.35$ Hz, $^4J_{\text{Ha',Hc'}} = 1.12$ Hz); 9.39 (Ha', 2H, dd, $^3J_{\text{Ha',Hb'}} = 5.72$ Hz, $^4J_{\text{Ha',Hc'}} = 1.12$ Hz); 8.57 (H3, 2H, d, $^4J_{\text{H3,H5}} = 1.81$ Hz); 8.52 (H3', 2H, d, $^4J_{\text{H3',H5'}} = 1.86$ Hz); 8.32 (Ha, 2H, dd, $^3J_{\text{Ha,Hb}} = 5.38$ Hz, $^4J_{\text{Ha,Hc}} = 1.21$ Hz); 8.17 (Hb', 2H, dd, $^3J_{\text{Ha',Hb'}} = 5.72$ Hz, $^3J_{\text{Hb',Hc'}} = 8.35$ Hz); 8.08 (Hb, 2H, dd, $^3J_{\text{Ha,Hb}} = 5.38$ Hz, $^3J_{\text{Hb,Hc}} = 8.31$ Hz); 7.90 (H6', 2H, d, $^3J_{\text{H5',H6'}} = 6.17$ Hz); 7.75 (H6, 2H, d, $^3J_{\text{H5,H6}} = 6.04$ Hz); 7.52 (H5, 2H, dd, $^3J_{\text{H5,H6}} = 6.04$ Hz, $^4J_{\text{H3,H5}} = 1.81$ Hz); 7.30 (H5', 2H, dd, $^3J_{\text{H5',H6'}} = 6.17$ Hz, $^4J_{\text{H3',H5'}} = 1.86$ Hz); 1.49 (CH3-tBu, 18H, s); 1.36 (CH3-tBu', 18H, s)

^{13}C -NMR (CD_3CN , T = 300 K, ref: TMS 00.00 ppm): $\delta(^{13}\text{C})[\text{ppm}] =$

163.81 (C7); 163.28 (C7'); 158.26 (C2); 157.48 (C2'); 155.29 (Ca); 154.02 (C6'); 152.16 (C6); 152.62 (Ce); 151.58 (Ca'); 149.89 (Ce'); 142.86 (Cf); 138.71 (Cf'); 137.05 (Cc'); 135.24 (Cc); 131.32 (Cd); 129.23 (Cd'); 129.00 (Cb'); 128.51 (Cb); 126.20 (C5'); 125.67 (C5); 122.61 (C3); 122.27 (C3'); 36.47 (C7); 36.31 (C7'); 30.62 (C8); 30.52 (C8')

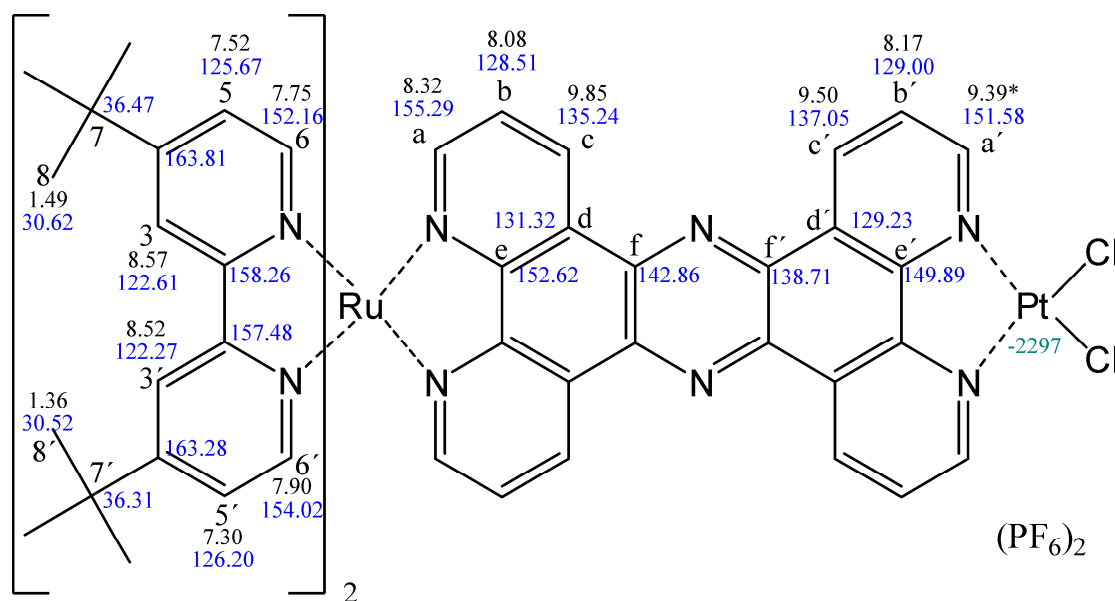


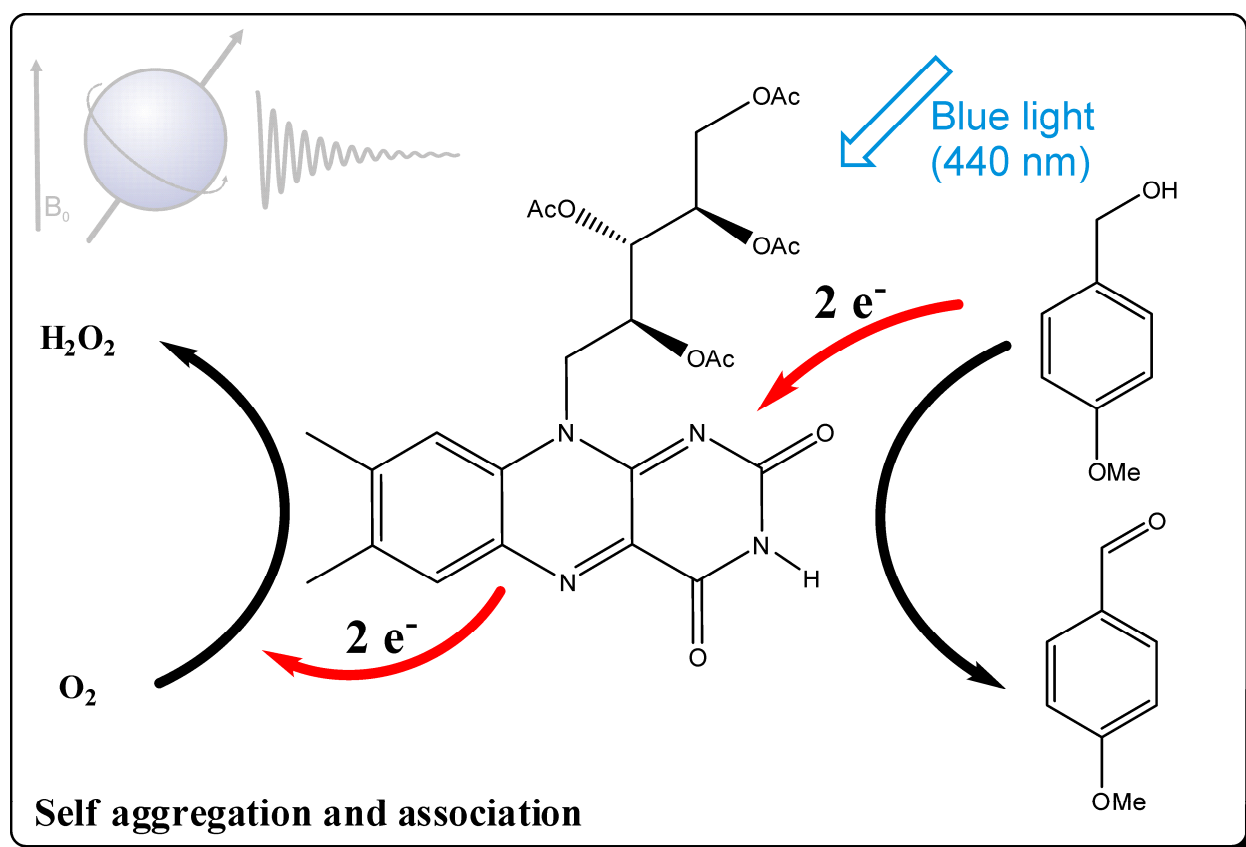
Figure 5.13: Signal assignment of ^1H , ^{13}C and ^{195}Pt resonances of $[(\text{tbbpy})_2\text{Ru}(\text{tpphz})\text{PtCl}_2](\text{PF}_6)_2$ in CD_3CN at 300 K.

5.5 References

- [1] S. Rau, D. Walther, J. G. Vos, *Dalton Transactions* **2007**, 915-919.
- [2] G. Renger, *Chem. unserer Zeit* **1994**, 28, 118-130.
- [3] M. Hara, C. C. Waraksa, J. T. Lean, B. A. Lewis, T. E. Mallouk, *J. Phys. Chem. A* **2000**, 104, 5275-5280.
- [4] K. Kalyanasundaram, J. Kiwi, M. Grätzel, *Helv. Chim. Acta* **1978**, 61, 2720-2730.
- [5] C. Chiorboli, M. A. J. Rodgers, F. Scandola, *J. Am. Chem. Soc.* **2002**, 125, 483-491.
- [6] R. Konduri, H. Ye, F. M. MacDonnell, S. Serroni, S. Campagna, K. Rajeshwar, *Angew. Chem. Int. Ed.* **2002**, 41, 3185-3187.
- [7] M. Kirch, J.-M. Lehn, J.-P. Sauvage, *Helv. Chim. Acta* **1979**, 62, 1345-1384.
- [8] E. Borgarello, J. Kiwi, E. Pelizzetti, M. Visca, M. Graetzel, *J. Am. Chem. Soc.* **1981**, 103, 6324-6329.
- [9] S. Rau, B. Schäfer, D. Gleich, E. Anders, M. Rudolph, M. Friedrich, H. Görls, W. Henry, J. G. Vos, *Angew. Chem.* **2006**, 118, 6361-6364.
- [10] S. Rau, M. Schwalbe, S. Losse, H. Görls, C. McAlister, F. M. MacDonnell, J. G. Vos, *Eur. J. Inorg. Chem.* **2008**, 2008, 1031-1034.
- [11] K. Yamauchi, S. Masaoka, K. Sakai, *J. Am. Chem. Soc.* **2009**, 131, 8404-8406.
- [12] S. Rau, B. Schäfer, D. Gleich, E. Anders, M. Rudolph, M. Friedrich, H. Görls, W. Henry, J. G. Vos, *Angew. Chem. Int. Ed.* **2006**, 45, 6215-6218.
- [13] S. Tschierlei, M. Presselt, C. Kuhnt, A. Yartsev, T. Pascher, V. Sundström, M. Karnahl, M. Schwalbe, B. Schäfer, S. Rau, M. Schmitt, B. Dietzek, J. Popp *Chemistry – A European Journal* **2009**, 15, 7678-7688.
- [14] P. Lei, M. Hedlund, R. Lomoth, H. Rensmo, O. Johansson, L. Hammarström, *J. Am. Chem. Soc.* **2007**, 130, 26-27.
- [15] S. Tschierlei, M. Karnahl, M. Presselt, B. Dietzek, J. Guthmuller, L. González, M. Schmitt, S. Rau, J. Popp, *Angew. Chem. Int. Ed.* **2010**, 49, 3981-3984.
- [16] L. M. Rendina, J. J. Vittal, R. J. Puddephatt, *Organometallics* **1995**, 14, 1030-1038.
- [17] B. M. Still, P. G. A. Kumar, J. R. Aldrich-Wright, W. S. Price, *Chem. Soc. Rev.* **2007**, 36, 665-686.
- [18] Y. Koie, S. Shinoda, Y. Saito, *J. Chem. Soc., Dalton Trans.* **1981**, 1082-1088.
- [19] P. S. Pregosin, in *Annual Reports on NMR Spectroscopy, Vol. Volume 17* (Ed.: G. A. Webb), Academic Press, **1986**, pp. 285-349.
- [20] D. Gudat, A. Dogan, W. Kaim, A. Klein, *Magn. Reson. Chem.* **2004**, 42, 781-787.
- [21] F. D. Rochon, V. Buculei, *Inorg. Chim. Acta* **2004**, 357, 2218-2230.
- [22] V. P. Ananikov, S. A. Mitchenko, I. P. Beletskaya, *Doklady Chemistry* **1998**, 363, 225-227.
- [23] J. B. Robert, A. L. Barra, *Chirality* **2001**, 13, 699-702.
- [24] D. R. Lide, *CRC Handbook of Chemistry and Physics*, 90. ed., Taylor & Francis, **2009**.
- [25] S. A. D. Pascali, D. Migoni, P. Papadia, A. Muscella, S. Marsigliante, A. Ciccarese, F. P. Fanizzi, *Dalton Transactions* **2006**, 5077-5087.
- [26] A. Jerschow, N. Müller, *J. Magn. Reson.* **1997**, 125, 372-375.
- [27] C. S. Johnson, *Prog. Nucl. Magn. Reson. Spectrosc.* **1999**, 34, 203-256.
- [28] <http://www.wavefun.com/>.
- [29] S. D. Bergman, D. Reshef, S. Groysman, I. Goldberg, M. Kol, *Chem. Commun.* **2002**, 2374-2375.
- [30] D. Gut, A. Rudi, J. Kopilov, I. Goldberg, M. Kol, *J. Am. Chem. Soc.* **2002**, 124, 5449-5456.
- [31] S. D. Bergman, M. Kol, *Inorg. Chem.* **2005**, 44, 1647-1654.
- [32] E. Martínez-Viviente, H. Rüegger, P. S. Pregosin, J. López-Serrano, *Organometallics* **2002**, 21, 5841-5846.
- [33] S. R. Heil, M. Holz, T. M. Kastner, H. Weingartner, *J. Chem. Soc., Faraday Trans.* **1995**, 91, 1877-1880.
- [34] T. G. Appleton, J. R. Hall, S. F. Ralph, *Inorg. Chem.* **1985**, 24, 4685-4693.
- [35] J. W. Akitt, in *Multinuclear NMR*, 1 ed. (Ed.: J. Mason), Plenum Press, New York, **1987**.
- [36] M. Pfeffer, Diploma thesis, Friedrich-Alexander Universität (Erlangen (Germany)), **2009**.

6 NMR Investigations on Flavin Photocatalysis

“NMR investigations on the self aggregation of riboflavin tetraacetate and its potential association with para-methoxybenzyl alcohol”



Matthias Fleischmann, Christian Feldmeier,
Burkhard König, Ruth M. Gschwind

The synthesis of RFT was performed in the research group of Prof. König. The RFT self aggregation was studied in close collaboration with Christian Feldmeier. C. F. also investigated the RFT-MBA association.

6.1 Introduction

The use of sunlight for chemical reactions is one of the main challenges in recent research.^{IV} Beside the photocatalytic hydrogen production with the aim of energy storage (see chapter 5), photocatalytic reactions can be used for chemical transformations in organic synthesis.^[1] Inspired by the redox activity of flavins as prosthetic group in natural enzymes,^[2-3] several flavin-mediated photocatalytic oxidations^[4] have been investigated by Fukuzumi,^[5-7] Shinkai^[8-9] and others.^[10-14] To increase the stability and efficiency of the photocatalysts, flavin transition metal complexes^[5, 7] or heterocyclic substrate binding sites^[8-9, 15] have been used. The redox potential of flavin was modulated by transition metal complexation^[16] and hydrogen-bonding.^[17-19] König and co-workers investigated thiourea-enhanced,^[12] Zn²⁺-cyclen substituted^[16, 20] or immobilized^[13-14] flavins for the photooxidation of benzyl alcohols and recently extended the synthetic scope to the photooxidation of activated hydrocarbons^[21] and catalytic cleavage of benzyl protection groups^[22] by flavin tetraacetate.

In cooperation with the research groups of Prof. Dick and Prof. König, Riedle et al. presented detailed mechanistic studies for the photooxidation of para-methoxybenzyl alcohol (MBA) with riboflavin tetraacetate (RFT).^[23] The formation of the flavin triplet state represents the key step for the photooxidation, which is followed by an electron transfer and subsequent proton transfer from the alcohol to the photocatalyst. In contrast, the electron transfer to the flavin singlet state is non-productive due to an immediate charge recombination without significant product formation (see Figure 6.1). The model of a productive triplet channel beside a singlet loss channel is in accordance with the observed concentration dependence of the quantum yields of the reaction with a maximum at 25 mM concentration of MBA and significantly smaller yields for both higher and lower alcohol concentrations.^[23]

Furthermore, based on the observation of an additional component in the femtosecond transient absorption spectra of the flavin kinetics, Riedle and co-workers interpreted this component in accordance with their model as a RFT-MBA associate with an association constant of $K_{\text{ass}}=0.2 \text{ M}^{-1}$ in MeCN/DMSO (98/2, v/v) and $K_{\text{ass}}=0.6 \text{ M}^{-1}$ in MeCN/H₂O (50/50, v/v).^[23]

^{IV} This necessity was realized even one hundred years ago by Giacomo Ciamician: “When all of the coal will have been burnt, it may become necessary to resort to exploiting light energy for the progress of society.”
G. Ciamician, *Science* **1912**, 36, 385.

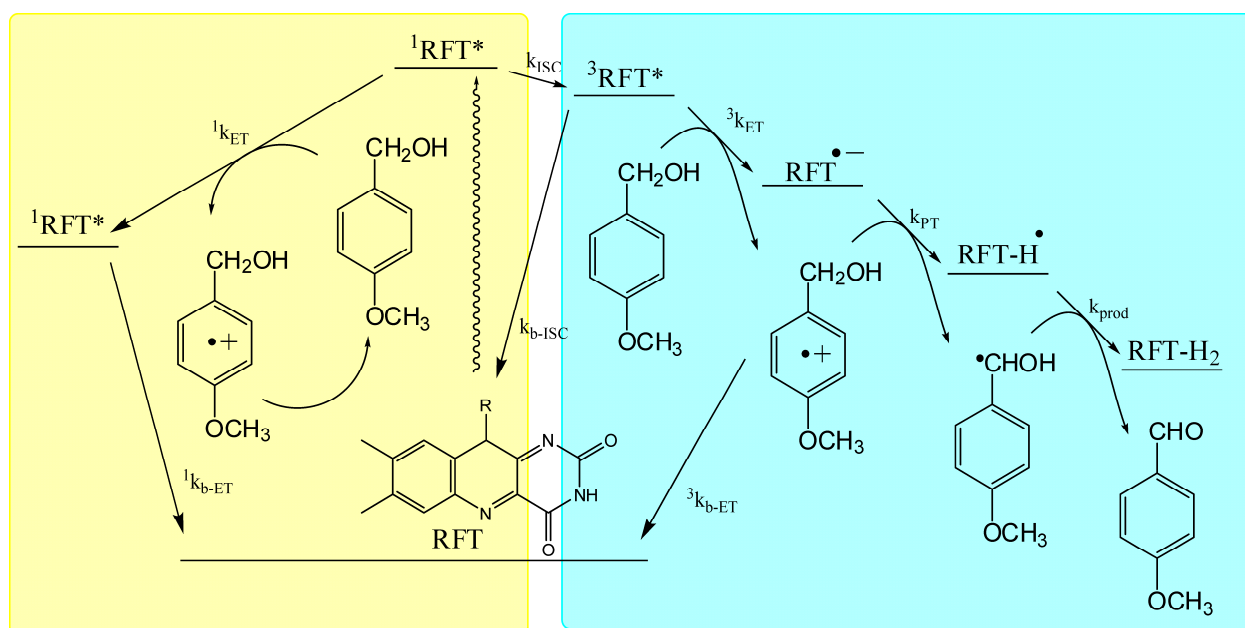


Figure 6.1: Postulated oxidation mechanism of MBA with RFT.^[23] The non-productive singlet pathway (left) returns the excited $^1\text{RFT}^*$ back to the ground state after diffusion controlled electron transfer from MBA and fast charge recombination. In contrast, the reaction of MBA with a triplet $^3\text{RFT}^*$ (right) can lead to product formation via a sequence of electron and proton transfer steps.^[23]

Since these insights into the reaction mechanism are supposed to have a tremendous influence on the design of flavins with higher efficiencies for photocatalytic chemical transformations in general,^[23] these experimental findings and the supposed model were re-investigated by NMR spectroscopy. Therefore, we studied the self aggregation of RFT and the association with MBA at different concentrations and in different solvents.

6.2 Results and Discussion

For the investigation of the RFT self aggregation the diffusion coefficients of RFT were measured in pure CD_3CN , in a $\text{CD}_3\text{CN}/\text{D}_2\text{O}$ 1/1 mixture and in D_2O , i.e. in the solvents typically used for the photooxidation of MBA with flavins.^[12-13, 20] As can be seen in Figure 6.2, the diffusion value of RFT was $1.18 \pm 0.02 \cdot 10^{-9} \text{ m}^2 \text{ s}^{-1}$ in pure CD_3CN and increased to $1.45 \pm 0.02 \cdot 10^{-9} \text{ m}^2 \text{ s}^{-1}$ in $\text{CD}_3\text{CN}/\text{D}_2\text{O}$ 1/1, each in the concentration range from 0.2 to 20 mM. A further increase in the RFT diffusion value to $1.69 \cdot 10^{-9} \text{ m}^2 \text{ s}^{-1}$ has been observed in pure D_2O . Due to the low solubility and precipitation of RFT in pure water, only one sample with an RFT concentration of 0.2 mM could be measured. The diffusion values in the low polarity solvent CD_2Cl_2 are similar to the diffusion values in CD_3CN .

These diffusion studies revealed RFT as a dimer in acetonitrile, whereas in water it is a monomer (for details of the calculation of aggregations levels from self diffusion coefficients see chapter 4.3.5). The formation of monomers in water is similar to flavin and flavin mononucleotide, which form only a low amount of dimers in aqueous solution in the concentration range of 10^{-5} - 10^{-3} M.^[24-25] These findings might be interpreted in that besides π - π stacking, also hydrogen-bonding plays a role for the aggregation behavior of RFT and other flavins.^[24-25] The dimerization in CD_3CN can be reduced either by the addition of water or by an increase of the temperature (see Figure 6.3). At 330 K a similar diffusion value was obtained as in the acetonitrile-water mixture at 300 K.

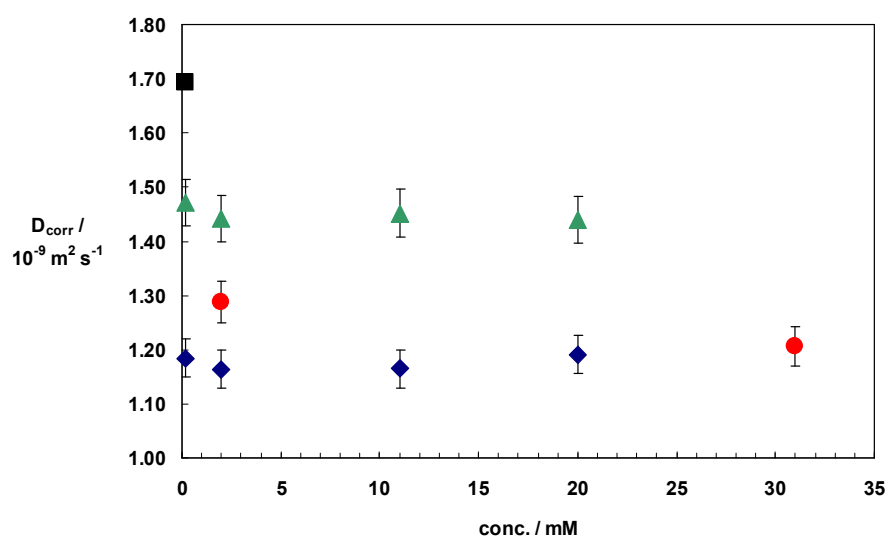


Figure 6.2: Diffusion coefficients of RFT in CD_3CN (◆), $\text{CD}_3\text{CN}/\text{D}_2\text{O}$ (1/1, v/v) (▲), D_2O (■) and CD_2Cl_2 (*) at different RFT concentrations at 300 K. All diffusion coefficients are temperature and viscosity corrected. Measuring inaccuracy of 3 % is assumed for every data point.

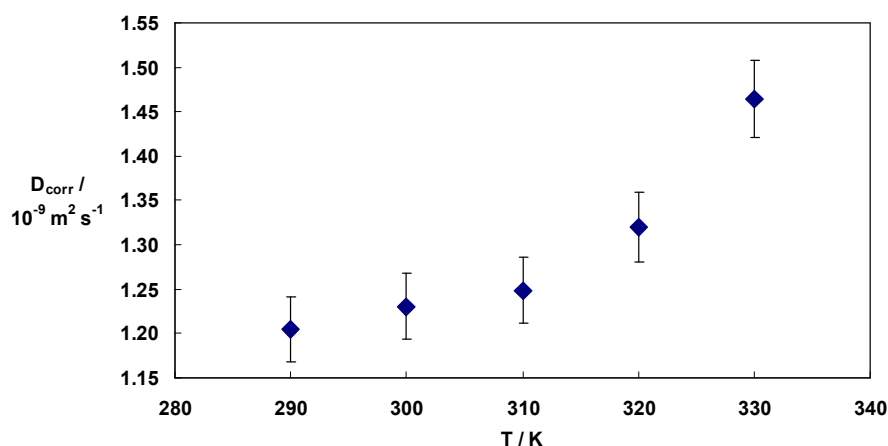


Figure 6.3: Temperature dependence of the diffusion coefficient of 0.2 mM RFT in CD_3CN at 300 K. All diffusion coefficients are temperature and viscosity corrected. Measuring inaccuracy of 3 % is assumed for every data point.

For the photooxidation of MBA with RFT, the quantum yield is higher in the CD₃CN-water mixture compared to pure CD₃CN and pure water (maximum quantum yield of 3 % at a water content of 40 %).^[26-27] The dependency of the reaction rate on the applied solvent^[12-13, 20] could be correlated with the aggregation behavior of RFT: In CD₃CN-water mixtures the highest quantum yields are observed. Possible explanations for the reduced quantum yield in pure water could be the low solubility of the catalyst in pure water reducing the amount of catalyst in solution or the alteration of the favorable hydrogen-bond interactions, which were suggested by Riedle et al. for RFT and MBA in CD₃CN-water mixtures with higher water content.^[23] On the other hand, the reduced quantum yield in pure CD₃CN could be rationalized by the dimerization of RFT in CD₃CN, which is supposed to play a key role in the quenching of the excited state of flavins,^[23] leading to efficient deactivation and therefore reduced quantum yields.

Based on these results, König and co-workers synthesized flavin derivatives with (chiral) bulky substituents in order to diminish the flavin aggregation. Their aggregation behavior in addition to their activity/selectivity is currently under investigation.

Next, the association of RFT and MBA was investigated. Riedle and co-workers obtained from femtosecond spectroscopy the diffusion coefficients of RFT and MBA in D₂O/CD₃CN 1:1 from samples containing RFT and different amounts of MBA (0.5 mM RFT with 2.0-1600 mM MBA).^[23] They found a strong decrease of the experimental diffusion coefficient with increasing MBA concentration and therefore assumed a model including an RFT-MBA associate. To verify these results, these samples were re-investigated by DOSY. Similar diffusion values and a similar increase of the experimental diffusion values were found and thus confirm the experimental findings obtained by femtosecond spectroscopy. But the *viscosity-corrected* diffusion values do not show this increase and revealed that the increase of the experimental diffusion values is due to the high viscosity of the highly concentrated solutions. No hint for an association of RFT and MBA was observed by NMR spectroscopy.

6.3 Conclusion

The self aggregation of RFT and a potential association with MBA at different concentrations and in different solvents have been investigated by DOSY experiments. In pure acetonitrile RFT is a dimer, whereas in water it is a monomer. These aggregation tendencies could be correlated with the solvent dependency of the quantum yield of the photooxidation of MBA with RFT and are used for the design of sterically hindered, chiral flavin derivatives with potentially higher quantum yields. In addition, no hints for an association of RFT and MBA have been observed by NMR spectroscopy.

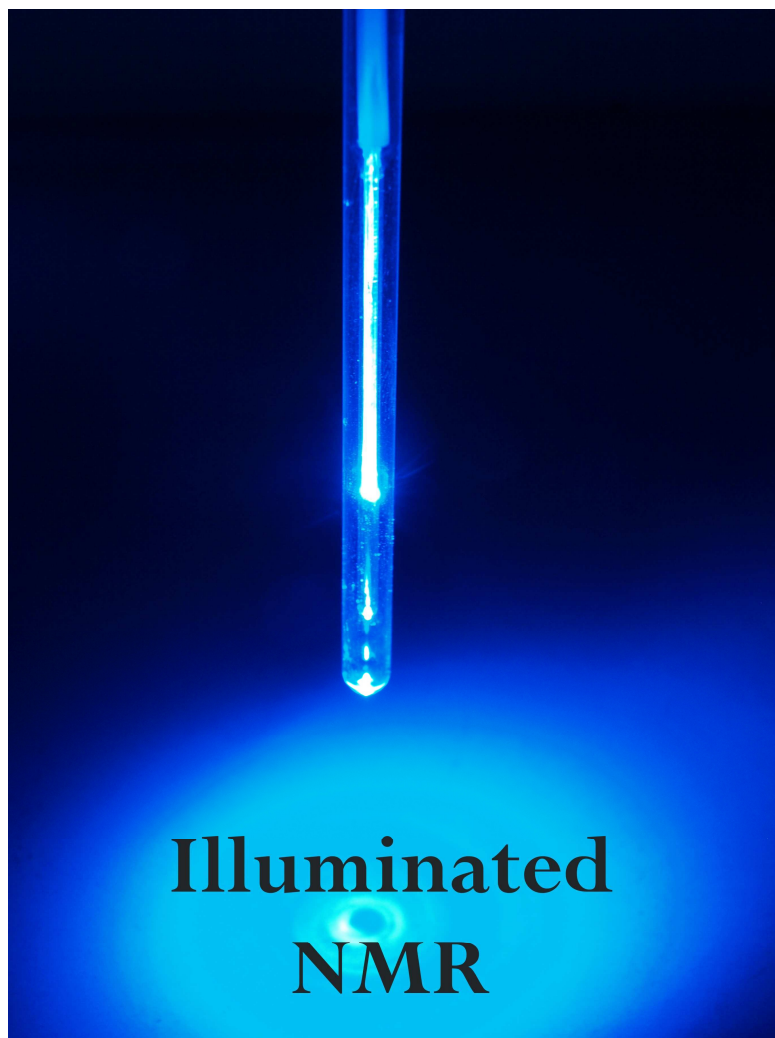
Furthermore, the course of the photooxidation of RFT and MBA was online monitored by ^1H spectra with our NMR-illumination unit (see chapter 7).

6.4 References

- [1] A. Albini, M. Fagnoni, *ChemSusChem* **2008**, *1*, 63-66.
- [2] C. G. Mowat, B. Gazur, L. P. Campbell, S. K. Chapman, *Arch. Biochem. Biophys.* **2010**, *493*, 37-52.
- [3] P. F. Fitzpatrick, *Arch. Biochem. Biophys.* **2010**, *493*, 13-25.
- [4] W. Tong, H. Ye, H. Zhu, V. T. D'Souza, *THEOCHEM* **1995**, *333*, 19-27.
- [5] S. Fukuzumi, S. Kuroda, T. Tanaka, *J. Am. Chem. Soc.* **1985**, *107*, 3020-3027.
- [6] S. Fukuzumi, S. Kuroda, *Res. Chem. Intermed.* **1999**, *25*, 789-811.
- [7] S. Fukuzumi, K. Yasui, T. Suenobu, K. Ohkubo, M. Fujitsuka, O. Ito, *J. Phys. Chem. A* **2001**, *105*, 10501-10510.
- [8] S. Shinkai, K. Kameoka, K. Ueda, O. Manabe, *J. Am. Chem. Soc.* **1987**, *109*, 923-924.
- [9] S. Shinkai, K. Kameoka, K. Ueda, O. Manabe, M. Onishi, *Bioorg. Chem.* **1987**, *15*, 269-282.
- [10] E. Silva, A. M. Edwards, D. Pacheco, *The Journal of Nutritional Biochemistry* **1999**, *10*, 181-185.
- [11] A. Mees, C. Behrens, A. Schwögl, M. Ober, T. Carell, *Eur. J. Org. Chem.* **2003**, *2003*, 2670-2677.
- [12] J. Svoboda, H. Schmaderer, B. König, *Chemistry – A European Journal* **2008**, *14*, 1854-1865.
- [13] H. Schmaderer, P. Hilgers, R. Lechner, B. König, *Adv. Synth. Catal.* **2009**, *351*, 163-174.
- [14] H. Schmaderer, M. Bhuyan, B. König, *Beilstein Journal of Organic Chemistry* **2009**, *5*, 26.
- [15] H. Ye, W. Tong, V. T. D'Souza, *J. Am. Chem. Soc.* **1992**, *114*, 5470-5472.
- [16] B. König, M. Pelka, R. Reichenbach-Klinke, J. Schelter, J. Daub, *Eur. J. Org. Chem.* **2001**, *2001*, 2297-2303.
- [17] S. Shinkai, G.-X. He, T. Matsuda, A. D. Hamilton, H. S. Rosenzweig, *Tetrahedron Lett.* **1989**, *30*, 5895-5898.
- [18] M. Gray, A. J. Goodman, J. B. Carroll, K. Bardon, M. Markey, G. Cooke, V. M. Rotello, *Org. Lett.* **2004**, *6*, 385-388.
- [19] A. S. F. Boyd, J. B. Carroll, G. Cooke, J. F. Garety, B. J. Jordan, S. Mabruk, G. Rosair, V. M. Rotello, *Chem. Commun.* **2005**, 2468-2470.
- [20] R. Cibulka, R. Vasold, B. König, *Chemistry – A European Journal* **2004**, *10*, 6223-6231.
- [21] R. Lechner, S. Kummel, B. König, *Photochemical & Photobiological Sciences* **2010**, *9*, 1367-1377.
- [22] R. Lechner, B. König, *Synthesis* **2010**, 1712-1718.
- [23] U. Megerle, M. Wenninger, R.-J. Kutta, R. Lechner, B. König, B. Dick, E. Riedle, *PCCP* **2011**, *13*, 8869-8880.
- [24] S. Baranovskii, P. Bolotin, *J. Appl. Spectrosc.* **2007**, *74*, 211-218.
- [25] H. Grajek, I. Gryczynski, P. Bojarski, Z. Gryczynski, S. Bharill, L. Kulak, *Chem. Phys. Lett.* **2007**, *439*, 151-156.
- [26] R. Lechner, PhD thesis, University of Regensburg (Regensburg (Germany)), **2010**.
- [27] U. Megerle, R. Lechner, B. König, E. Riedle, *Photochemical & Photobiological Sciences* **2010**, *9*, 1400-1406.

7 Development of an NMR-Illumination Unit

“Development of an NMR-illumination unit
for NMR online-monitoring of photocatalytic reactions”



Matthias Fleischmann, Christian Feldmeier, Ruth M. Gschwind

The design and the test measurements were done in close collaboration with Christian Feldmeier.

7.1 Introduction

For photochemical NMR investigations, several approaches can be performed like CIDNP (chemically induced dynamic nuclear polarization),^[1-5] studies of photoactive compounds^[6-7] or photochemical kinetics.^[8-10] All of these investigations require illumination of the sample inside the NMR spectrometer and therefore several techniques have been developed including illumination from below, from the side or from above.^[11] Illumination from the side or from below has been used for in situ UV/VIS/CF-MAS-NMR spectroscopy (continuous flow-magic angle spinning NMR) by Hunger et al.,^[12] and for low temperature UV/VIS/solution state NMR by Limbach et al.^[13] and others,^[14-15] but has several disadvantages like the required re-arrangement of the probe and non-uniform illumination of optically dense samples.^[11] In contrast, illumination from above with a stepwise tapered optical fiber circumvents these problems, leading to uniform illumination, low deterioration of spectral resolution and a minimum reduction of the volume in the active region of the NMR tube, as demonstrated by Kuprov et al.^[11]

In this thesis, two projects in the field of photocatalysis have been investigated: The water reduction with a ruthenium-platinum catalyst (chapter 5) and the photooxidation and aggregation behavior of methoxybenzyl alcohol with riboflavin tetraacetate (chapter 6). As demonstrated for the photocatalytic water reduction, these photocatalytic reactions are usually very fast and the catalysts can be very sensitive to the light intensity. Thus, irradiation outside the NMR spectrometer and subsequent transfer of the NMR tube into the spectrometer is hardly suited for tracking fast reactions. Instead, to allow for online-monitoring of photocatalytic reactions, the illumination should be performed inside the NMR spectrometer. For this purpose, a glass fiber-based illumination unit was constructed similar to Kuprov et al.,^[11] which allows simultaneous illumination inside the NMR spectrometer.

7.2 Materials and Methods

The optical bench was a Thorlabs KT310 Spatial Filter System equipped with Thorlabs SM1Z-Z-axis Translation Mount, a coated, aspheric lense (Thorlabs C220TME-A, ϕ =9.24 mm, f =11.00 mm, 350-700 nm, NA=0.55, Mounted ECO-550), Thorlabs SM1SMA Series Fiber Adaptor and different LEDs with 440, 470 or 530 nm, which were mounted with a thermal

conductivity-glue on a cooling element (10 mm block of aluminum) as light source (Cree XPEROY D5 15, 460 ± 10 nm, 850 mW @ 700 mA; Cree XPEBLU L1 B4 K2, 470 ± 10 nm, 70.4 lumen @ 700 mA; Cree XPEGRN L1 G4 Q4, 535 ± 10 nm, 200 lumen @ 700 mA). The light was focused into an optical fiber (Thorlabs BFH48-1000 silica fiber (SMA adaptor end, 1000 μ m core diameter, Tefzel coating, NA 0.48 ± 0.02 , UV/VIS range 300 to 1200 nm (High-OH)). The other (mechanically stripped from the Tefzel and hard core cladding) end of the fiber was fixed inside a 5 mm NMR tube by a Wilmad WGS-5BL Stem Coaxial Insert to avoid direct contact of the glass fiber with the analyte solution and to center the glass fiber inside the NMR tube (see Figure 7.1).

Due to the small angle of radiation of the LED in combination with the high Numerical Aperture of the fiber ($NA = \sin(\alpha)$ describes the maximum accepted angle α between the light beam and the optical axis), the highest light intensity in the fiber was obtained without lens by adjusting the fiber directly in front of the LED. With this setup, a reduction of the light intensity in the fiber by a simple de-adjustment of the LED is possible.

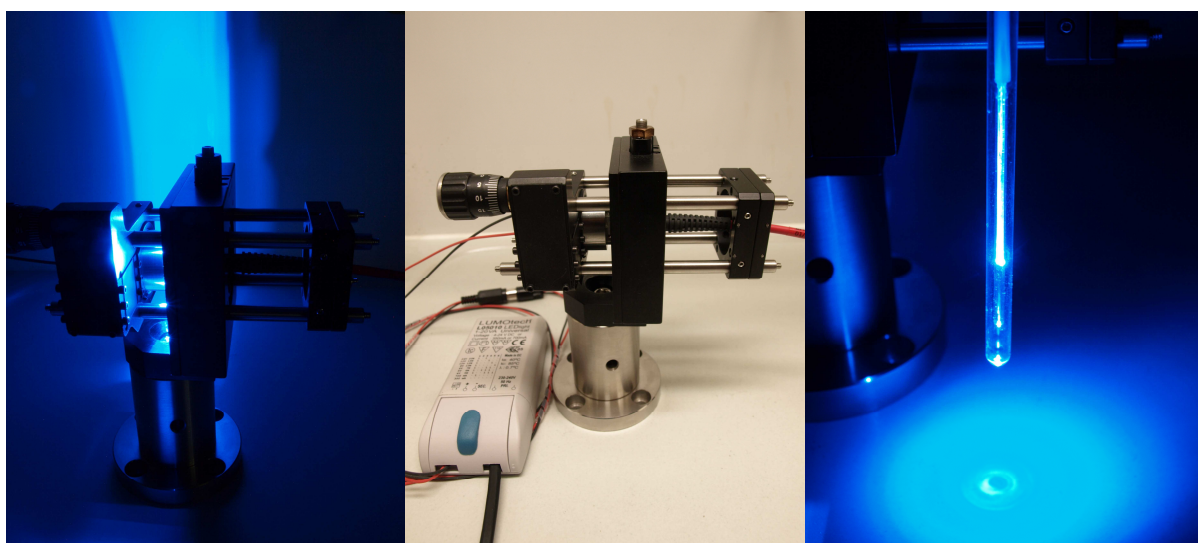
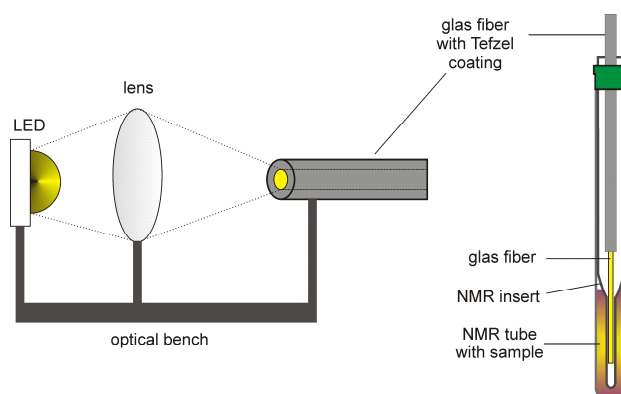


Figure 7.1: Glass fiber-based NMR illumination unit composed of optical bench with LED, lens and glass fiber in combination with NMR insert and tube.

7.3 Results and Discussion

First attempts with the NMR-illumination unit in the field of photocatalysis were made for the photooxidation of MBA with RFT. For that purpose, a sample with 20 mM MBA and 10 mol% photocatalyst in CD₃CN was illuminated with blue light (440 nm) and the reaction was online-monitored with ¹H spectra. In Figure 7.2, the course of the reaction is depicted. The first and the last spectrum were recorded without illumination for comparison of the obtained spectral resolution. Only a slight increase of the line width of the signals upon illumination is observed, e.g. for the ortho (relative to CH₂OH) protons of MBA at 7.27 ppm from 4.2 Hz to 5.6 Hz and for the CH₂ protons from 3.2 Hz to 4.6 Hz, indicating only a slight reduction of the spectral resolution upon illumination. Furthermore, a simultaneous decrease of the MBA signals and increase of the aldehyde signals was detected (see Figure 7.3). Beside the photooxidation, a decomposition of RFT was also observed with a decrease of the RFT signals and the emergence of signals of decomposition products. With decreasing RFT concentration, the MBA oxidation was decelerated. After complete decomposition of RFT, the MBA oxidation stopped and the line width of the signals reduced back to the starting values without illumination.

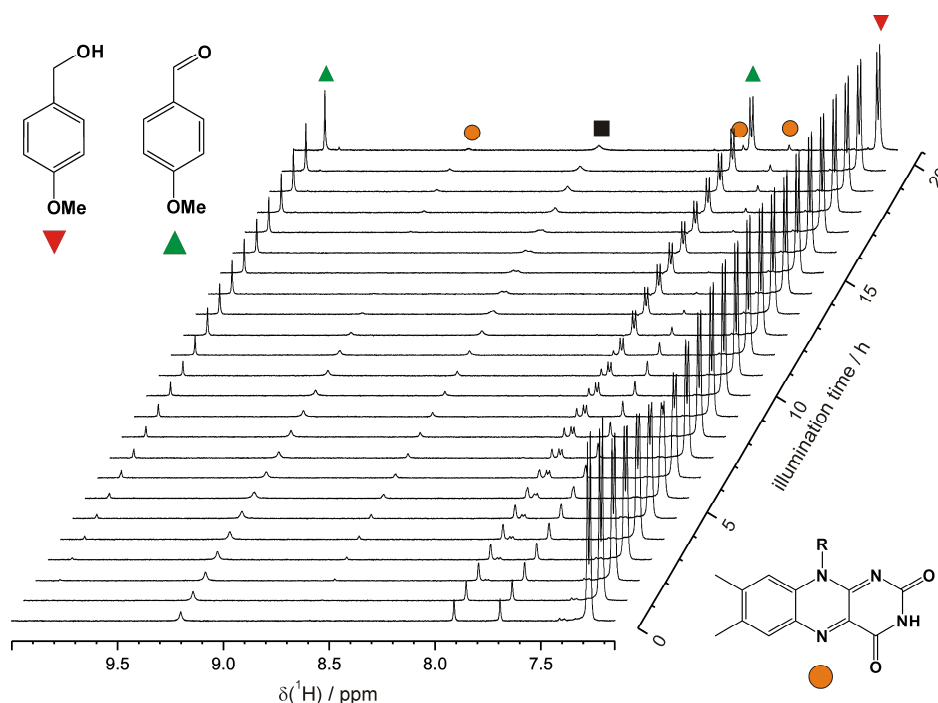


Figure 7.2: Sections of the ¹H spectra during the photooxidation of 20 mM MBA with 2 mM RFT in CD₃CN, illuminated for 20.5 h with 440 nm with the help of the NMR-illumination unit. MBA (▼), MB aldehyde (▲), RFT (●), decomposition product (■).

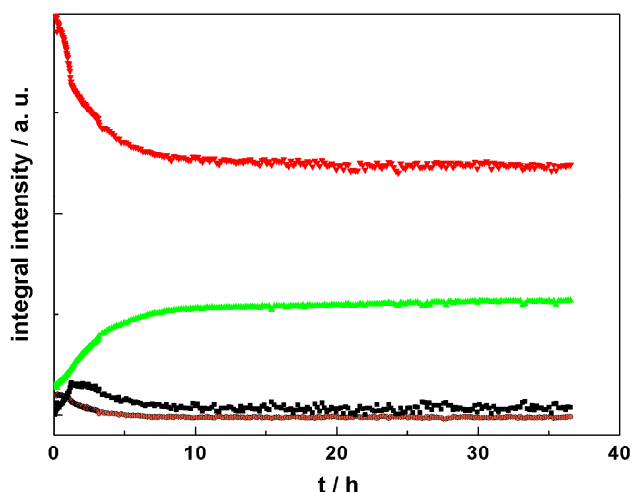


Figure 7.3: Photooxidation of 20 mM MBA with 2 mM RFT in CD_3CN . MBA (\blacktriangledown), MB aldehyde (\blacktriangle), RFT (\bullet), intermediate (\blacksquare).

7.4 Conclusion

To allow for online-monitoring of photocatalytic reactions, a glass fiber-based NMR-illumination unit was constructed, which allows simultaneous illumination inside the NMR spectrometer. The highest light intensity in the fiber was obtained by adjusting the fiber directly in front of the LED, which allows a reduction of the light intensity by a de-adjustment of the LED. This setup was used in the field of photocatalysis for the NMR monitoring of the photooxidation of MBA with RFT. Upon illumination the spectral resolution was only slightly reduced and the decrease of the MBA signals and simultaneous increase of the aldehyde signals could be observed. Furthermore, RFT was decomposed leading to a deceleration and finally to a stop of the MBA oxidation. The RFT decomposition was probably due to the high light intensity, which therefore should be reduced for further investigations. Additionally, the end of the fiber should be stepwise tapered to obtain a more uniform illumination of the complete sample volume.

This NMR-illumination unit opens the door to further investigations of flavin photocatalysis, photocatalytic water reduction with Ru/Pt catalysts and other photocatalytic reactions.

In addition, the applied equipment allows for illumination with a laser light instead of LED light, which provides in principle access to CIDNP measurements for a further insight into mechanisms and intermediates of photocatalytic reactions.

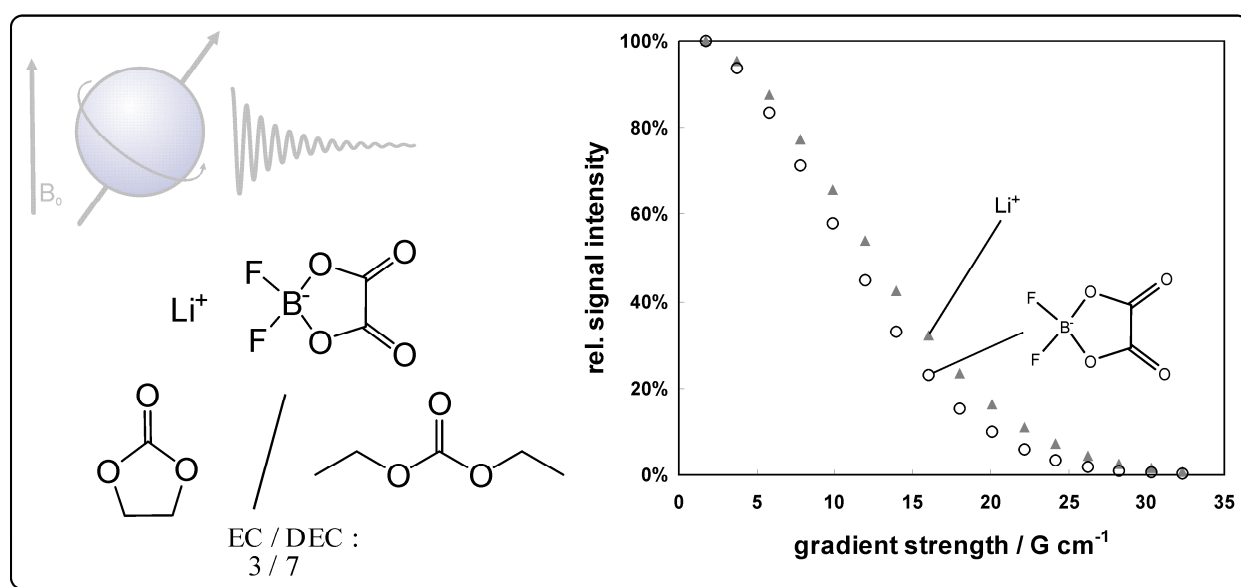
7.5 References

- [1] M. Goez, *Journal of Magnetic Resonance, Series A* **1993**, *102*, 144-150.
- [2] M. Goez, I. Sartorius, *J. Am. Chem. Soc.* **1993**, *115*, 11123-11133.
- [3] M. Goez, I. Sartorius, *J. Phys. Chem. A* **2003**, *107*, 8539-8546.
- [4] J. Matysik, Alia, P. Gast, H. J. van Gorkom, A. J. Hoff, H. J. M. de Groot, *Proceedings of the National Academy of Sciences* **2000**, *97*, 9865-9870.
- [5] M. Goez, *Photochemically Induced Dynamic Nuclear Polarization*, John Wiley & Sons, Inc., **2007**.
- [6] G. Rubinstenn, G. W. Vuister, F. A. A. Mulder, P. E. Dux, R. Boelens, K. J. Hellingwerf, R. Kaptein, *Nat Struct Mol Biol* **1998**, *5*, 568-570.
- [7] G. Rubinstenn, G. W. Vuister, N. Zwanenburg, K. J. Hellingwerf, R. Boelens, R. Kaptein, *J. Magn. Reson.* **1999**, *137*, 443-447.
- [8] P. J. Hore, E. R. P. Zuiderweg, R. Kaptein, K. Dijkstra, *Chem. Phys. Lett.* **1981**, *83*, 376-383.
- [9] O. B. Morozova, Y. P. Tsentalovich, A. V. Yurkovskaya, R. Z. Sagdeev, *J. Phys. Chem. A* **1998**, *102*, 3492-3497.
- [10] O. B. Morozova, A. V. Yurkovskaja, Y. P. Tsentalovich, M. D. E. Forbes, P. J. Hore, R. Z. Sagdeev, *Molecular Physics: An International Journal at the Interface Between Chemistry and Physics* **2002**, *100*, 1187 - 1195.
- [11] I. Kuprov, P. J. Hore, *J. Magn. Reson.* **2004**, *171*, 171-175.
- [12] M. Hunger, W. Wang, *Chem. Commun.* **2004**, 584-585.
- [13] P. M. Tolstoy, B. Koeppe, G. S. Denisov, H.-H. Limbach, *Angew. Chem. Int. Ed.* **2009**, *48*, 5745-5747.
- [14] J. E. Scheffler, C. E. Cottrell, L. J. Berliner, *Journal of Magnetic Resonance (1969)* **1985**, *63*, 199-201.
- [15] C. L. Lerman, M. Cohn, *Biochem. Biophys. Res. Commun.* **1980**, *97*, 121-125.

8 Measurements of Transference Numbers for Li⁺ Ion Electrolytes

Research Paper:

“Measurement of transference numbers for lithium ion electrolytes
via four different methods, a comparative study”



Sandra Zugmann, Matthias Fleischmann, Marius Amereller,
Ruth M. Gschwind, Hans-Dieter Wiemhöfer, Heiner J. Gores

Electrochimica Acta **2011**, 56, 3926-3933

[doi:10.1016/j.electacta.2011.02.025](https://doi.org/10.1016/j.electacta.2011.02.025)

The synthesis of LiDFOB and the electrochemical measurements
were performed by Sandra Zugmann and Marius Amereller.

8.1 Abstract

We report here on comparative measurements of cationic transference numbers of some lithium battery related electrolytes including lithium tetrafluoroborate in propylene carbonate, lithium hexafluorophosphate in blends of ethylene carbonate/diethyl carbonate and ethylene carbonate/propylene carbonate/dimethyl carbonate, as well as lithium difluoromono (oxalate) borate in an ethylene carbonate/diethyl carbonate blend via four different methods. Whereas three electrochemical methods yield transference numbers decreasing with concentration in accordance with electrostatic theories, valid for low to intermediate concentrations of the electrolyte, nuclear magnetic resonance spectroscopy measurements show increasing transference numbers with increasing concentration. The discrepancy is attributed to effects of ion-ion and ion-solvent interaction.

8.2 Manuscript

Introduction

Intrinsic processes such as ion association and solvation, as well as bulk properties such as viscosity, conductivity and mobility of electrolyte solutions are important factors to describe and understand ion transport in solutions.^[1-4] A full characterization of a battery electrolyte, and in particular, the understanding of charge transport and the modeling of the cell properties^[5-6] require knowledge on the transference numbers of the ions. Concentration gradients of the salt develop across a lithium ion cell during current flow and they strongly depend on the lithium transference number. Precipitations of the dissolved salt at the anode and depletion at the cathode are possible consequences at high currents and may cause serious cell failure. Such consequences become probable for lithium salt electrolytes with a low transference number of lithium ions which implies a poor high-rate performance and limits the power output of the cell. Accordingly, a high lithium ion transference number significantly reduces the effects of concentration polarization.^[7] The importance of understanding and controlling lithium ion transference numbers and the corresponding effort to develop a rapid and reliable measurement that gives accurate values becomes more and more apparent in recent years.^[8-11]

The number of precise methods to determine transference numbers in liquid aqueous electrolytes is acceptable.^[12-15] Various methods have already been used for more than a hundred years.^[16] In contrast, accurate data for non-aqueous liquid electrolytes, especially with respect to lithium salts, are very rare. Among the few currently used methods, such as potentiostatic polarization and NMR,^[17-21] several inherent restrictions are often not taken into account. As a consequence, the reported results have to be applied with caution. The situation becomes even worse, as different methods for transference number determinations yield contradictory results in the literature, either for the transference numbers themselves as well as for their concentration dependence.^[22]

In the present study, four different techniques are used and compared to study the lithium transference of non-aqueous electrolytes containing a lithium salt, namely the potentiostatic polarization (PP) method, the galvanostatic polarization (GP) method, the emf (electromotive force) method and the determination by pfg-NMR. Organic carbonates were taken as solvents. The lithium ion transference numbers are reported for solutions of lithium tetrafluoroborate (LiBF₄), lithium hexafluorophosphate (LiPF₆), and the recently synthesized lithium difluoro-mono(oxalato)borate (LiDFOB).^[23-24]

Experimental

The lithium salts LiPF₆ and LiBF₄ were purchased from *Stella* (high purity), LiDFOB was prepared by the synthesis route introduced by Schreiner et al.^[23] resulting in a fine white powder (yield: 99.7%), and tetraethyl ammonium tetrafluoroborate (TEABF₄) was purchased from *Merck KGaA* (selectipure). The solvents ethylene carbonate (EC), diethyl carbonate (DEC), propylene carbonate (PC) and dimethyl carbonate (DMC) were purchased from *Merck KGaA* (p.a.). The carbonate mixtures used as solvents were EC/DEC = 3/7 by wt. and EC/PC/DMC = 2/1/4 by wt., respectively. The water content of the electrolytes was $< 5 \cdot 10^{-5}$, checked by Karl-Fischer titration (*Mettler*, type Karl Fischer Titrator DL18). All solutions were prepared in a glove box (*Mecaplex GB80*) with low mass fraction of water ($< 1 \cdot 10^{-6}$) and oxygen ($< 5 \cdot 10^{-6}$). The electrochemical measurements were done using a Reference 600 potentiostat / galvanostat (*Gamry Instruments*) in a thermostatted T-shaped cell, placed in a Faraday-cage to avoid perturbation of very small currents, see Figure 8.1.

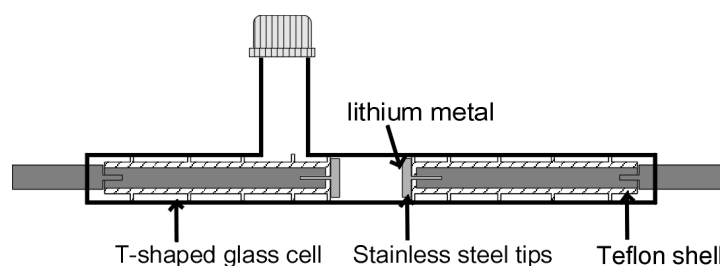


Figure 8.1: Schematic picture of used T-shaped cell.

The electrodes for all electrochemical measurements consist of fresh cut lithium foil pressed on stainless steel tips. Galvanostatic polarization experiments were carried out with current densities ranging from 0.04 to 0.18 mA cm⁻² and a polarization time of 400 s. Potentiostatic polarization experiments were done with an applied voltage of 10 mV for 1 h; impedances were measured in the frequency range of 0.1 to 10000 Hz. For electromotive force measurements two glass wool pieces are soaked with electrolyte of different concentrations and brought in contact by a non-aqueous salt bridge. One concentration was held constant (1 mol kg⁻¹ for LiPF₆ and LiDFOB in EC/DEC (3/7), respectively), whereas the second glass wool was soaked in several succeeding steps at the same electrolyte but at varying concentrations (for LiDFOB from 0.9 mol kg⁻¹ down to 0.01 mol kg⁻¹, and for LiPF₆ from 0.9 mol kg⁻¹ down to 0.02 mol kg⁻¹). As salt bridge a saturated tetraethyl ammonium tetrafluoroborate (TEABF₄) solution in EC/DEC (3/7) is used.

The NMR measurements were performed inside a standard 5 mm NMR tube in 0.5 mL non-deuterated solvent without field/frequency locking at 296.7 ± 0.2 K. Tiny amounts (0.35-0.45 percent by weight) of tetramethylsilane (TMS) were added to each sample as internal reference for the ^1H chemical shift and the diffusion coefficient of TMS was used to measure the viscosity of each sample. The spectra were recorded on a *Bruker Avance III* 400 MHz spectrometer equipped with a BBFO^{PLUS} room temperature probe with z-gradient (maximum gradient strength of 53.5 G cm^{-1}) and BVT 3200 temperature control unit.

The diffusion measurements were performed with a standard *Bruker* BPLED (*longitudinal eddy current delay with bipolar gradient pulses*) sequence in a pseudo 2D mode. For each experiment, 2 dummy scans and 16 scans were used with a relaxation delay of 2 s. The length of the gradient pulse δ was optimized for every nucleus in each sample and was 4.0-6.0 ms for ^1H -, 15.6-20.0 ms for ^7Li - and 5.6-9.4 ms for ^{19}F -DOSYs and a diffusion time Δ of 50 ms was used for all experiments. Sinusoidal shapes were used for the gradients and a linear gradient ramp with 12 increments for ^1H and 10 increments for ^7Li and ^{19}F between 5 and 95 % of the maximum gradient strength was applied for the diffusion relevant gradients. For the homospoil gradients, 9.165 and 7.046 G cm^{-1} were applied for HS1 and HS2. The spectra were processed with the *Bruker* program Topspin® and the diffusion coefficients were calculated with the *Bruker* software T1/T2 package. The measurements were repeated at least three times and all diffusion coefficients were within a standard deviation of ± 2 %.

Results

Potentiostatic polarization

Bruce and Vincent established a potentiostatic polarization method for ideal solid polymer electrolytes,^[25] which is also suitable for diluted solutions.^[26] Applying a small constant potential on an electrolyte between non-blocking lithium electrodes leads to a decrease of the initial current value until a steady-state value is reached. If no redox reaction occurs with the anions, the anion current will vanish in the steady-state and the total current will be caused by the cations.^[25] In this case, the cation transference number can be easily determined by dividing the steady-state cationic current by the initial current just after switching-on the polarizing voltage. Passivating layers at the electrodes usually impose an additional contact resistance. The corresponding additional voltage drop has to be subtracted from the applied potential difference. Because the resistances of the lithium electrode surfaces vary with time, the correction has to take this change into account. The contact resistance is determined by impedance measurements

shortly before and after the potentiostatic polarization.^[27] For small polarization potentials (≤ 0 mV), the transference number for the cation t_+ is given by^[27]:

$$t_+ = \frac{I_{ss}(\Delta V - I_0 R_0)}{I_0(\Delta V - I_{ss} R_{ss})} \quad (8.1)$$

where I_{ss} is the steady-state current, I_0 the initial current, ΔV the applied potential, R_e the electrolyte resistance, and R_{ss} and R_0 the electrode resistances after and before the polarization, respectively.

The method was verified by a measurement of LiPF₆ in an EC/PC/DMC (2/1/4) (m = 0.68 mol kg⁻¹) mixture and of LiBF₄ in PC, where the lithium ion transference numbers have been already published.^[28] Our experiments showed a transference number of 0.39 ± 0.024 for LiPF₆ and 0.35 ± 0.0062 for LiBF₄ in good accordance with the literature values, see Table 8.2.

Figure 8.2 and Figure 8.3 show the chronoamperometric and impedance measurement, respectively, for LiPF₆ in EC/DEC (3/7) with a concentration of 0.68 mol kg⁻¹. The determined lithium ion transference number is 0.34 ± 0.0053 . Other results received by this method are shown in Table 8.2. In this investigation and all following studies the uncertainty denoted by $\pm 0.x$ with respect to the given number value was calculated by the error propagation law.

The equivalent circuit to fit impedance data represents the electrolyte resistance R_e in series with the electrode resistances R_0 or R_{ss} . Because of electrode roughness and other surface phenomena the electrode resistances are combined with a constant phase element that leads to an equivalent circuit of the form $R_e(R_1CPE_1)(R_2CPE_2)$, with R_1+R_2 equal to R_0 or R_{ss} , respectively, seen in Figure 8.4. The finally determined lithium electrode resistances (R_0 and R_{ss}) and the initial and steady-state current are given in Table 8.1.

Table 8.1: Determined electrode resistances R_0 and R_{ss} before and after polarization, respectively, and initial current I_0 and steady current I_{ss} for 0.68 mol kg⁻¹ LiPF₆ in EC/DEC (3/7).

R_0 / Ω	R_{ss} / Ω	I_0 / A	I_{ss} / A
581.6	561.6	$1.0 \cdot 10^{-5}$	$6.99 \cdot 10^{-6}$

This method is very popular for measuring transference numbers of lithium electrolytes, because of its very simple and fast procedure and low costs. But it must be taken into account that the working equation (8.1) was developed for binary and ideal solid electrolytes.

Table 8.2: Transference numbers measured for different lithium electrolytes by different methods at 298 K.

System	Method	Concentration	Transference number	Literature value
LiPF ₆ in EC/PC/DMC	GP	0.68 mol kg ⁻¹	0.38 ± 0.025	0.38 ^[25]
	PP	0.68 mol kg ⁻¹	0.39 ± 0.024	0.2 ^[26]
LiPF ₆ in EC/DEC	PP	0.68 mol kg ⁻¹	0.34 ± 0.0053	this work
	GP	1.0 mol kg ⁻¹	0.24 ± 0.087	this work
	emf	1.0 mol kg ⁻¹	0.28 ± 0.003	this work
LiPF ₆ in PC	PP	1.5 mol L ⁻¹	0.370	Ref. ^[19]
		0.25 mol L ⁻¹	0.557	
	NMR	0.25 mol L ⁻¹	0.505	Ref. ^[19]
		1.5 mol L ⁻¹	0.330	
LiBF ₄ in PC	PP	0.68 mol kg ⁻¹	0.35 ± 0.0062	0.39 ^[27]
	GP	0.10 mol kg ⁻¹	0.38 ± 0.048	this work
LiDFOB in EC/DEC		1.0 mol kg ⁻¹	0.33 ± 0.05	
	PP	0.10 mol kg ⁻¹	0.38 ± 0.006	this work
	emf	1.0 mol kg ⁻¹	0.35 ± 0.041	this work
	NMR	0.05 mol kg ⁻¹	0.441 ± 0.0074	this work
		0.50 mol kg ⁻¹	0.448 ± 0.0074	
		0.70 mol kg ⁻¹	0.451 ± 0.0074	
		0.83 mol kg ⁻¹	0.456 ± 0.0074	
		0.93 mol kg ⁻¹	0.458 ± 0.0074	

GP galvanostatic polarization; PP potentiostatic polarization.

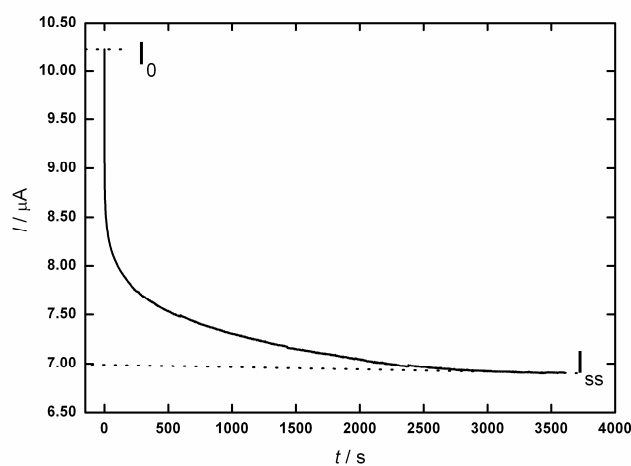


Figure 8.2: Chronoamperogram of 0.68 mol kg⁻¹ LiPF₆ in EC/DEC (3/7) with an applied voltage of 10 mV. I_0 indicates the initial current, I_{ss} the steady state current.

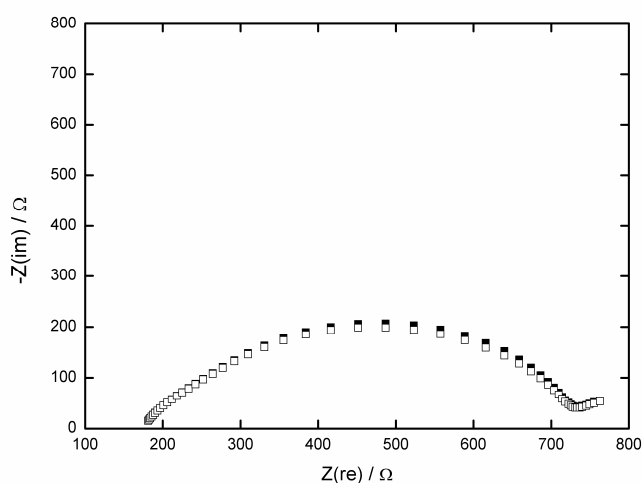


Figure 8.3: Nyquist plot of 0.68 mol kg⁻¹ LiPF₆ in EC/DEC (3/7). The filled squares show the impedance spectrum before the polarization experiment, the open squares after polarization.

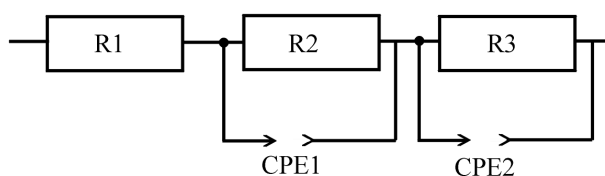


Figure 8.4: Equivalent circuit of electrode resistances.

Galvanostatic polarization

Ma et al. introduced a procedure for polymer electrolytes where a steady-state concentration gradient of the salt is established by a galvanostatic polarization.^[29] The concentration gradient is not measured directly, but the related cell potential difference during and after polarization is observed to determine the exact potential difference at the moment of current interruption. By combining the measurement of three different parameters, i.e., the measurement of the cell potential after galvanostatic polarization, the additional evaluation of the salt diffusion coefficient, and the determination of the concentration dependence of the potential difference, the cationic transference number can be calculated according to:^[30]

$$t_+ = 1 - \frac{mFc_\infty\sqrt{\pi D}}{4\left(\frac{d\Phi}{d\ln c}\right)} \quad (8.2)$$

where z_+ is the charge number of the cation, v_+ the stoichiometric number of cations per mole salt added to a solution, c_∞ the bulk concentration of the salt, F the Faraday constant, D the salt diffusion coefficient, $d\Phi/d\ln c$ the concentration dependence of the potential Φ and m is the slope of a plot of the cell potential at the time of current interruption obtained from $\Delta\Phi$ vs. $jt_i^{1/2}$ fits, where j is the current density and t_i the polarization time.

The method is restricted to binary electrolytes with the cation as the active species (anion current vanishes in the steady-state), no convection, semi-infinite diffusion and linear cell geometry.^[29] Nevertheless, it can be used for non-ideal, concentrated solutions^[30] making it a better choice for measuring transference numbers of electrolytes for lithium ion batteries.

The salt diffusion coefficient is determined by the restricted diffusion technique.^[31-32] The diffusion coefficient is evaluated from the slope of a plot of $\ln(\Delta\Phi)$ vs. time,^[33] which becomes linear for long times $t \gg L^2/D$. The corresponding slope m_D of the linear relation is given by:

$$m_D = -\frac{\pi^2 D}{L^2} \quad (8.3)$$

where L is the distance between the two electrodes.

The method was applied to an electrolyte consisting of 0.68 mol kg⁻¹ LiPF₆ in EC/PC/DMC (2/1/4) to verify this approach. The calculated value for the lithium ion transference number was 0.38 ± 0.025 , which is in good agreement with literature data,^[28] see Table 8.2. Figure 8.5 shows the plot of the cell potential $\Delta\Phi$ vs. $jt_i^{1/2}$ near the time of current interruption for an electrolyte of 1.0 mol kg⁻¹ LiPF₆ in EC/DEC (3/7)). One can see that the scattering of the data points is significant. The problem of large deviations is also known in the corresponding literature.^[28, 30, 34] Proposed explanations concern the very small potential range

(cf. Figure 8.5), so that normal disturbances become dominant, as well as convection flows or surface phenomena such as dendrite formation.

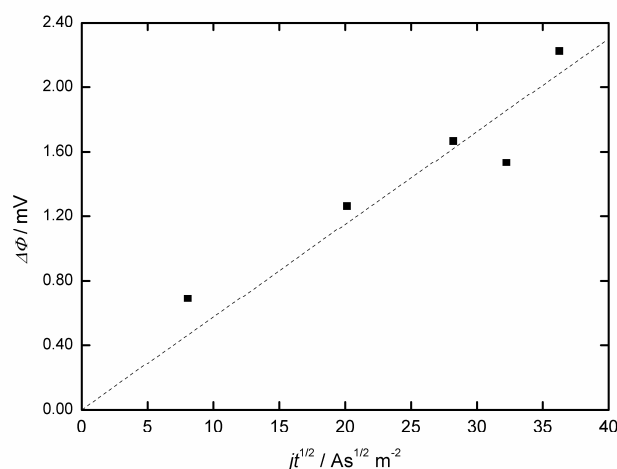


Figure 8.5: The determined potential $\Delta\Phi$ plotted vs. $j t_i^{1/2}$ for 1.0 mol kg⁻¹ LiPF₆ in EC/DEC (3/7).

The salt diffusion coefficient of the 1.0 mol kg⁻¹ electrolyte was calculated according to equation (8.3) from the slope of the plot $-\ln(\Delta\Phi)$ vs. t , seen in Figure 8.6, resulting in a value of $3.47 \cdot 10^{-10} \text{ m}^2 \text{ s}^{-1}$. The concentration dependence of the cell potential $\Delta\Phi/\text{d} \ln c$ is determined by concentration cell measurements without transference. As the final result, the lithium ion transference number of the 1.0 mol kg⁻¹ electrolyte is obtained as 0.24 ± 0.087 .

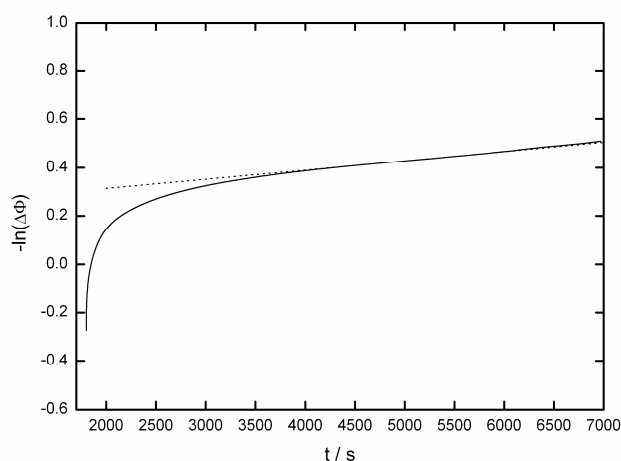


Figure 8.6: Plot of the negative logarithm of the open circuit potential $\Delta\Phi$ vs. time t after polarization of a 1.0 mol kg⁻¹ LiPF₆ solution in EC/DEC (3/7) in order to determine the diffusion coefficient.

To conclude, the chronopotentiometric method combines the results of three different measurements. Disadvantages are the time-consuming procedure and the fact that the errors of three measurements add up. An advantage, however, is that the calculation of transference numbers does not assume ideality or diluted solutions, making it interesting for lithium ion battery electrolytes under realistic working conditions.

Electromotive force method

Concentration cells with transference including different concentrations and liquid junction of the type $\text{Li} \mid \text{LiX} (m_1) \parallel \text{LiX} (m_2) \mid \text{Li}$, where $m_2 > m_1$ refer to molalities of the monovalent electrolyte LiX have a potential difference E_{trans} described by:^[35]

$$E = -\frac{2RT}{F} t_- \ln \left(\frac{m_2 \gamma_2}{m_1 \gamma_1} \right) \quad (8.4)$$

where γ is the mean activity coefficient of the cations, R the ideal-gas constant, T the thermodynamic temperature, other symbols were defined earlier.

If the activity coefficient is available, the transference number is determined by electromotive force (emf) measurements. The variation of the potential with concentration is given by the differential of equation (8.4), yielding:

$$dE = -\frac{2RT}{F} t_- d \ln \left(\frac{m_2 \gamma_2}{m_1 \gamma_1} \right) \quad (8.5)$$

If activity coefficients are not available, a measurement of a cell without liquid junction, i.e., with a salt bridge between half cells with different concentrations, is necessary. Its potential is given by:^[36]

$$E = -\frac{2RT}{F} \ln \left(\frac{m_2 \gamma_2}{m_1 \gamma_1} \right) \quad (8.6)$$

Equations (8.4) and (8.6) are used to calculate the transference number of the anion by the differential form:^[37]

$$t_- = \frac{dE_{\text{trans}}}{dE} \quad (8.7)$$

Of course, the method based on equation (8.7) includes the following restriction: The transference number is assumed to be constant in the measured concentration range.^[35] This assumption is generally not fulfilled. Figure 8.7 shows a plot of E_{trans} vs. E for LiDFOB in EC/DEC (3/7) at the fixed molality $m_2 = 1.0 \text{ mol kg}^{-1}$ and a varied molality m_1 .

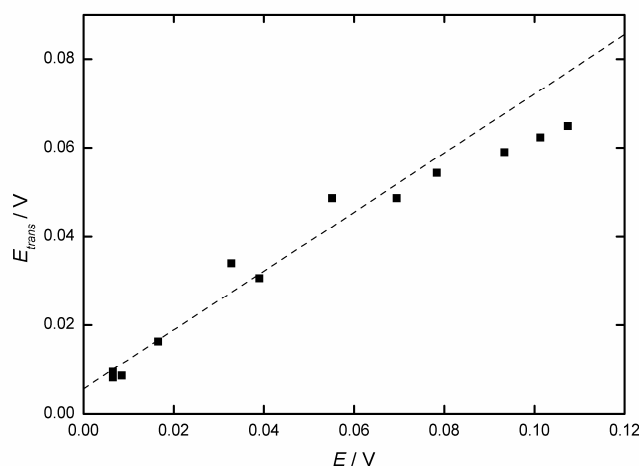


Figure 8.7: Plot of the emf with liquid junction vs. emf without liquid junction for. Values were measured at the same concentration of LiDFOB in EC/DEC (3/7) at 298 K.

The slope of the plot yields the anionic transference number; the cationic transference number for a binary electrolyte results from $t_+ = 1 - t_-$. The potentials E_{trans} and E are increasing with increasing concentration difference between the constant high concentration and the varied concentration of the salt. It can be seen, that the deviation from the ideal behavior increases with increasing concentration differences as the assumption of a constant transference number gets increasingly invalid. Surprisingly, a linear behavior between the potential of the concentration cell with transference E_{trans} and the concentration cell without transference E is observed up to rather high concentration differences up to 0.4 mol kg^{-1} . The lithium ion transference number for LiDFOB in EC/DEC (3/7) was determined by fitting the linear part of the plot (including concentrations up to 0.6 mol kg^{-1}) yielding 0.35 ± 0.0041 .

To check the reliability of this method we also measured the known transference number for LiPF_6 in EC/DEC (3/7), see Table 8.2, which is in good agreement with the results obtained by the galvanostatic polarization method.

Determination by NMR

The cation transference number may also be obtained from:

$$t_+ = \frac{D_+}{D_+ + D_-} \quad (8.8)$$

where D_+ is the self diffusion coefficient of the cation and D_- the self diffusion coefficient of the anion.

This equation is only valid in very dilute state, far from the salt concentrations in battery electrolytes, where association takes place. Deviating from equation (8.8), the diffusion coefficients obtained from NMR contain contributions from free ions as well as from ion pairs (and further clusters, if present), when the salt is not completely dissociated.

$$\begin{aligned} D_+^{\text{NMR}} &= \alpha D_+ + (1-\alpha) D_{\text{pair}} \\ D_-^{\text{NMR}} &= \alpha D_- + (1-\alpha) D_{\text{pair}} \end{aligned} \quad (8.9)$$

where D_{pair} denotes the diffusion coefficient of neutral ion pairs and α is the degree of salt dissociation.

This is well known from weakly dissociated polymer electrolytes, where the diffusion coefficients D_+^{NMR} and D_-^{NMR} are derived for e.g., lithium and fluorine containing anions by measuring the nuclei ^7Li and ^{19}F .^[38-39] Hence, D_+^{NMR} and D_-^{NMR} can be only used in equation (8.8) if the salt is completely dissociated. Otherwise, calculating the transference number with equation (8.8) with D_+^{NMR} and D_-^{NMR} instead of the diffusion coefficients D_+ and D_- will yield erroneous results.

The easiest way to determine D_+^{NMR} and D_-^{NMR} is the pulsed field gradient nuclear magnetic resonance (pfg-NMR) method.^[40-42] This technique was used for measuring diffusion in several electrolytes previously. In particular, the spin echo (SE)^[43-44] and stimulated echo (STE)^[19, 45-46] methodologies have been used so far. Annat et al. have shown that in highly viscous liquids the STE approach is superior to SE due to better suppression of internal gradients and reduced loss of magnetization due to T_2 relaxation.^[47] A further improvement of the STE approach is the use of bipolar gradient pulses and the incorporation of a longitudinal eddy current delay t_e before acquisition, which minimizes the effect of eddy currents caused by the gradients.^[48-49] The pulse sequence of this BPLED (*longitudinal eddy current delay with bipolar gradient pulses*) is shown in Figure 8.8.

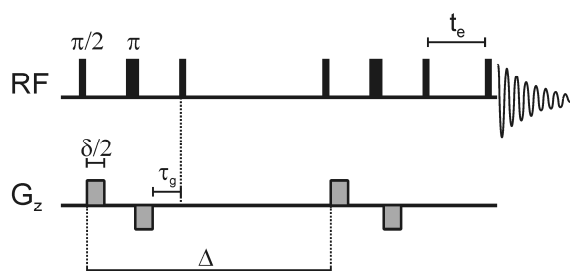


Figure 8.8: BPLED pulse sequence incorporating bipolar gradient pulses of duration δ , the diffusion time Δ , gradient refocusing delay τ_g and eddy current delay t_e .^[49] RF radio frequency pulses and G_z gradient pulses in z-direction.

Similar to the simple Stejskal and Tanner sequence,^[50] the diffusion coefficient D^{NMR} can be calculated for the BPLED experiment from a signal attenuation I/I_0 by equation (8.10).^[48-49]

$$I = I_0 \cdot \exp \left[-D \gamma^2 g^2 \delta^2 \left(\Delta - \frac{\delta}{3} - \frac{\tau_g}{2} \right) \right] \quad (8.10)$$

where γ is the gyromagnetic ratio, g the amplitude of the gradient pulses with duration δ , Δ the diffusion time and τ_g the gradient refocusing delay.

Table 8.3: Solution viscosity, experimental diffusion coefficients of the solvents EC (D_{EC}) and DEC (D_{DEC}), the reference substance TMS (D_{TMS}), the cation lithium (D_{Li^+}), the anion (D_{DFOB^-}), and the transference numbers (t_+) at 296.7 K.

Molality / mol kg ⁻¹	Viscosity / mPa s	$D / 10^{-10} \text{ m}^2 \text{ s}^{-1}$					t_+
		D_{EC}	D_{DEC}	D_{TMS}	D_+^{NMR}	D_-^{NMR}	
0.93	2.123	3.77	4.20	5.33	1.71	2.00	0.460
0.83	1.978	4.18	4.63	5.72	1.87	2.23	0.456
0.70	1.702	5.03	5.45	6.64	2.19	2.66	0.451
0.50	1.563	5.78	6.18	7.24	2.48	3.05	0.448
0.30	1.347	7.08	7.36	8.40	2.93	3.68	0.443
0.10	1.199	8.56	8.58	9.43	3.65	4.61	0.442
0.05	1.156	9.29	9.05	9.78	3.84	4.86	0.441

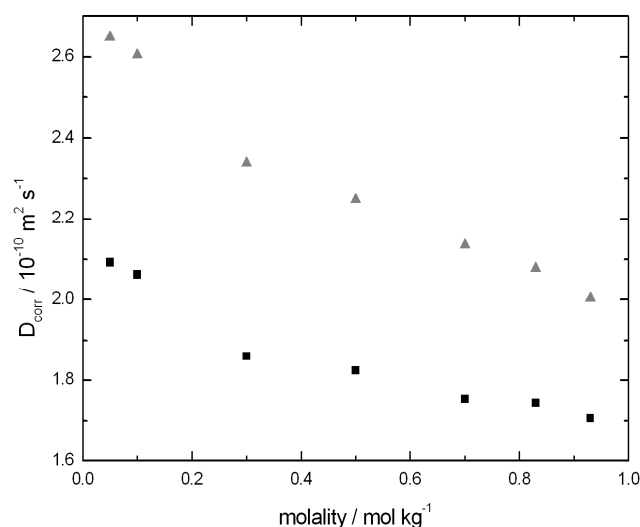


Figure 8.9: Concentration dependence of self diffusion coefficients of cation (■) and anion (▲) of LiDFOB in EC/DEC (3/7). Diffusion coefficients were corrected by viscosity.

In general, the diffusion coefficients of the ions are influenced mainly by the solvation of the ions, association, long range electrostatic interactions and the viscosity of the solution. As can be seen in Table 8.3, increasing salt concentration entails an increase of viscosity. To rule out the effect of viscosity, viscosity corrected diffusion coefficients D_{corr} were calculated with the help of the diffusion coefficient of TMS acting as viscosity reference.^[51] Figure 8.9 shows the concentration dependence of these diffusion coefficients of the cation and anion, D_+^{NMR} and D_-^{NMR} , respectively. As expected, viscosity corrected and experimental diffusion coefficients of all species decrease with increasing concentration. The diffusion coefficient of the anion shows a slightly stronger concentration dependence compared to those of the lithium cation. A similar concentration behavior was reported for LiPF₆/PC solutions by Zhao et al.^[22] Despite the smaller size of the lithium cation, the lithium cation always diffuses slower than the anion over the whole concentration range. This observation is in accordance with previous investigations of monovalent lithium salts in high dielectric solvents.^[52]

An explanation for this different concentration dependence can be attributed to different solvation behavior of cations and anions. This effect can be seen by checking the R parameter introduced by Hayamizu et al.^[52-53] From the Stokes-Einstein equation the individual diffusion coefficients can be related to individual diffusing radii (see equation (8.11)).

$$D_{solv} \sim \frac{1}{r_{solv}} \quad D_{ion} \sim \frac{1}{r_{ion}} \quad (8.11)$$

where D_{solv} is a diffusion coefficient of a given solvent (EC or DEC) and D_{ion} refers to the diffusion coefficient of a solvated ion.

A parameter R_{ion}^{solv} is defined by the ratios

$$R_{ion}^{solv} = \frac{D_{solv}}{D_{ion}} \sim \frac{r_{ion}}{r_{solv}} \quad (8.12)$$

where R_{ion}^{solv} reflects the ratio of the sizes of a diffusing ion relative to the solvent molecule, e.g.,

R_{Li}^{DEC} reflects the size ratio of the lithium ion relative to diethyl carbonate.

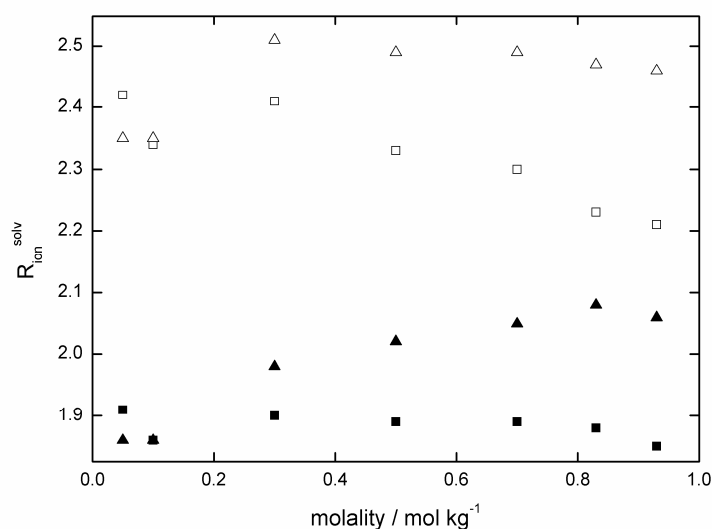


Figure 8.10: Concentration dependent R values of Li⁺ and DFOB⁻ in EC/DEC (3/7), for details see text.

R_{Li}^{DEC} (Δ), R_{Li}^{EC} (\square), R_{DFOB}^{DEC} (\blacktriangle) and R_{DFOB}^{EC} (\blacksquare).

The concentration dependent R values, shown in Figure 8.10 are in the range of 2.2-2.5 and 1.8-2.1 for the cation and the anion, respectively, similar to values obtained by Hayamizu et al.^[53] This observation reflects the larger volume of the solvated lithium cation when compared to the less solvated but larger anion.

Cazzanelli et al. have estimated for the lithium ion (LiClO₄ in EC/PC mixtures) a solvation number of 4 when the molar ratio $N = [Li^+]/[EC+PC] \leq 0.2$.^[54] In our very similar system the molar ratio N is maximum 0.1. In accordance with our results, a Li(EC)₂(DEC)₂⁺ cation and a less solvated DFOB⁻ anion can be assumed, at least at low concentrations.

Increasing the concentration leads to the formation of solvated ion pairs possessing a larger volume and therefore a decreased diffusion coefficient when compared to the separated ions. By forming an ion pair, the cation diffusion coefficient does not change much because the cation only exchanges a solvent molecule against the anion or adds the anion in the solvation sphere. In contrast, incorporating of the anion into an ion pair leads to a large increase of the volume and therefore a large decrease of the diffusion coefficient of the anion. Thus, the stronger concentration dependence of the diffusion coefficient of the anion compared to the lithium cation can be tentatively explained by different solvation strengths.

Cationic transference numbers t_+ were calculated according to equation (8.8) from D_+^{NMR} data. Figure 8.11 shows the observed concentration dependence of cationic transference numbers in LiDFOB in EC/DEC (3/7). Even at the lowest concentration with the lowest expected amount of ion pairing, transference numbers determined by NMR exceed the transference numbers obtained by electrochemical methods. E.g., a 0.1 molal LiDFOB in EC/DEC (3/7) has a transference number of 0.38 ± 0.05 , measured by galvanostatic polarization method, whereas the transference number measured by the NMR method has a value of 0.442 ± 0.0074 .

By increasing the concentration the transference number increases, which can be seen as a direct result of the stronger concentration dependence of the anion (see Figure 8.9). The calculation of the transference number with D_+^{NMR} instead of D_+ yields overestimated results due to the presence of ion pairs. This finding is in contradiction with results from electrochemical measurements, which are only detecting “free” ions yielding decreasing cationic transference numbers with increasing concentration, whereas the NMR method detects all nuclei in the solution and results in increasing cationic transference number with increasing concentration. These contradicting concentration dependencies from NMR and EC methods have also been detected from other groups, e.g., Zhao et al. investigated a LiPF₆/PC solution with NMR and polarization methods.^[22]

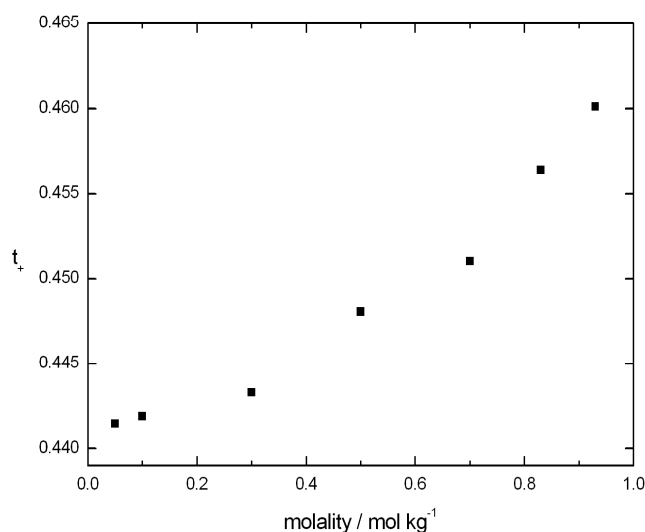


Figure 8.11: Concentration dependence of the lithium ion transference number for LiDFOB in EC/DEC (3/7), determined by the NMR method.

The NMR method offers the advantage that a binary electrolyte is not required and even multicomponent systems can be studied. A further interesting issue is that information from NMR can give a deep insight into the association equilibrium, if one does not treat the NMR technique as an independent method, but combines it with one of the electrochemical techniques. However, NMR requires expensive instrumentation, and is restricted to NMR-active nuclei.

Discussion

Comparison of methods

It is hard to say which method is the “best” one for an accurate and easy measurement of transference numbers. Every method has several assumptions or restrictions that have to be kept in mind. For a fast electrochemical estimation the potentiostatic polarization method would be the obvious choice, but it is restricted to binary, ideal electrolytes. The galvanostatic polarization method is more accurate for concentrated solutions but combines three different measurements, which are very time-consuming. The emf method requires an adequate non-aqueous salt bridge and reversible electrodes and - a serious restriction - it assumes ion transference numbers that are not varying with concentration. Obviously, for multicomponent systems the determination by NMR is the only useful method. However both ion pairs and free ions are detected.

Concentration dependence of transference numbers

Barthel et al. already showed for non-aqueous electrolytes that concentration dependence of transference numbers changes in a general way.^[55] Electrolytes with a transference number higher than 0.5 at infinite dilution increase with increasing concentration in contrast to those with transference numbers lower than 0.5 which decrease with concentration. For aqueous solution this dependence was already shown for higher concentrations.^[56] The basic theory for this prediction was developed by Fuoss-Onsager^[57] based on the work of Debye-Hückel.^[58]

To sum up, electrochemical methods and NMR measurements show contradicting results for cationic transference numbers in accordance with the work of Valoen and Reimers.^[28] Whereas electrochemical methods yield transference numbers decreasing with concentration in accordance with electrostatic theories, valid for low to intermediate concentrations of the electrolyte, NMR measurements show increasing transference numbers with increasing concentration. A probable reason for this observation is ion-ion interaction leading to ion pair formation (ion association). Whereas electrochemical methods detect only the transport of free lithium ions, NMR measurements also include ion pair transport. It is plausible to assume that association increases with increasing concentration of the electrolyte. As a direct consequence, transference numbers of cations with $t_+ < 0.5$ should decrease. Saito et al. measured the effective ion radii of LiTf in PC and recovered nearly equal ionic radii of solvated, single lithium ions and associated lithium ions.^[40] The ionic radii showed no strong concentration dependence, leading to the conclusion that the mobility of the lithium species, that is affected by the size of the moving species did not change much with concentration contrary to the anionic species. Our results confirm this suggestion. The diffusion coefficient of the fluoride components decreases stronger with increasing concentration when compared with diffusion coefficient of lithium components. As a result, the lithium ion transference number increases with increasing concentration.

Conclusion

Various methods for measurement of transference numbers in non-aqueous lithium ion electrolytes for batteries were investigated and exemplified at various electrolytes related to lithium batteries. The advantages and disadvantages of every method were discussed and their reliability for lithium electrolytes was proven. Different concentration dependences obtained by electrochemical methods and NMR measurements are tentatively explained by ion association and solvation effects.

8.3 Additional experimental findings

8.3.1 Background and aim of the project

For the determination of translational diffusion coefficients NMR-based DOSY experiments have become the method of choice, because they are fast, insensitive to impurities and allow for the investigation of several compounds simultaneously.^[49, 59] Therefore, DOSY spectra have been widely used in different areas of organic chemistry and biology^[60] for molecular size, aggregation and binding studies.^[59] Recently, electrochemists used spin echo (SE)^[43-44] and stimulated echo (STE)^[19, 45-46] type experiments for the determination of transference numbers of electrolytes in the rapid growing field of lithium ion battery research. From the historical point of view, electrochemists started their NMR diffusion measurements in solid polymer electrolytes^[61-63] and later on in ionic liquid materials.^[19, 64-68] Both of these media show very high viscosities^[66] compared to usual organic solvents. Therefore, potential convection effects in these solvents play only a secondary role. In order to improve the electrochemical transport properties, several less viscous solvents like carbonates^[22, 52-53, 69-70] have been investigated. But potential convection effects have still not been taken into account apart from first attempts of using sample spinning, reduced sample volume or special NMR tubes to reduce convection.^[71-72] But, to our knowledge, a convection compensating NMR pulse sequence has not been used in the field of electrochemistry. Furthermore, the influence of viscosity is often discussed and some effects are attributed to viscosity changes,^[66, 73] but the use of an internal viscosity standard like TMS was to our knowledge not considered before. Therefore, we considered this field as promising target for sophisticated investigations in diffusion measurements of currently discussed electrolytes for use in lithium ion batteries.^[74-77]

In general, these lithium ion electrolytes should simultaneously fulfill several properties like intrinsic thermal and electrochemical stability, good solubility in appropriate solvents, chemical stability of the anion against all cell components, high conductivity, low molecular weight, low cost and non-toxicity.^[6] However, optimization of one parameter often leads to the decline of another desirable property. LiPF₆ combines most of the required properties in a moderate manner and thus it is the most popular salt for electrolyte solutions employed today in secondary lithium ion batteries.^[6, 78-79] But LiPF₆ has a couple of drawbacks like hydrolysis of the anion by traces of water, moderate conductivity, low temperature stability and moderate performance at low temperature.^[6, 78-79] Therefore, the search for alternative salts with further improvements for the next generation of secondary lithium ion batteries is one of the main challenges for the future.^[6]

In cooperation with the research group of Prof. Gores, we investigated the two promising systems of LiDFOB in EC/DEC and LiAlCl₄ in liquid SO₂. The LiDFOB system has several advantages over the current standard LiPF₆-containing electrolyte: Higher electrochemical stability, better performance at low temperatures and lower tendency for decomposition at elevated temperatures,^[80] which are some of the key features for the application in hybrid or full electric vehicles. Furthermore, the electrolyte LiAlCl₄ in liquid SO₂ shows beside the non-flammability an extraordinary high conductivity of 70 mS cm⁻¹,^[74] by far outperforming the LiPF₆/carbonate electrolyte (LiPF₆ in EC/DMC 1/2: 10 mS cm⁻¹).^[78, 81]

Thus, NMR-based diffusion measurements for the calculation of the transference numbers of these electrolytes seemed very promising. Moreover, the comparison of the NMR-based method with electrochemical methods for the determination of the transference number should give us a deep insight into the hitherto not satisfactorily described concentration dependence of the transference numbers (see chapter 8.2).

8.3.2 Optimization of DOSY parameters

For the optimization of NMR spectroscopic parameters, 3,5-difluorophenylboronic acid was selected as a test system, since this compound offered the possibility to investigate the diffusion coefficients of several nuclei (¹⁹F, ¹¹B and non-exchangeable protons) in one single molecule. In addition, this non-charged test system excluded the potential influence of long range ion interactions.

For the reproducibility and subsequently an estimation of the achievable accuracy of the actual diffusion measurements, two different DOSY pulse sequences, both with bipolar gradient pulses, have been selected; the longitudinal eddy current delay (LED) and the double stimulated echo pulse sequence developed by Müller and Jerschow ("MJ"),^[82] whose inherent convection compensation results in a longer duration compared to the LED. The diffusion measurements were performed at a 400 MHz NMR spectrometer without its internal BVT temperature control unit, since first attempts for DOSY measurements failed due to the insufficient temperature stability of ±5 K produced by the BVT 3200 unit. Instead, the temperature was adjusted by the external air conditioning system, with T = 295±1 K. To take the residual temperature variability into account, a temperature correction was applied for the diffusion coefficients leading to the temperature corrected diffusion values D_{T-corr}. Additionally, a viscosity correction based on D_{TMS} was applied leading to temperature and viscosity corrected diffusion coefficients D_{corr}.

For 3,5-difluorophenylboronic acid in DMSO-d₆ constant $D_{T\text{-corr}}$ within an error range of 3 % could be obtained for ¹H- and ¹⁹F-LED and MJ experiments (see Table 8.4). Next, the minimum length of the gradient recovery delay d16 for complete reduction of eddy currents was investigated by variation of the d16 delay from 0.4 to 0.1 ms in ¹⁹F-MJ experiments.^[83] Since constant diffusion coefficients within the error range were observed (entry 11-15), a gradient recovery delay of 0.1 ms is sufficient for regaining homogenous field after gradient pulse.

Table 8.4: Diffusion coefficients of 3,5-difluorophenylboronic acid in DMSO-d₆ from ¹H- and ¹⁹F-LED and MJ-DOSYs at 295±1.1 K. Δ=50 ms, t_c=5 ms, gas flow=535 L h⁻¹ (if not otherwise stated), η calculated from D_{TMS}.

nuclei	pulse program	entry	d16 / ms	η / mPa s	D / 10 ⁻¹⁰ m ² s ⁻¹	
					D _{T-corr}	D _{corr}
¹ H	MJ	1	0.1	2.27	1.89	1.81
		2 ^[a]	0.1	2.38	1.78	1.80
		3 ^[a]	0.1	2.38	1.77	1.78
		4 ^[a]	0.1	2.36	1.78	1.77
		5	0.1	2.12	1.99	1.78
	LED	6 ^[a]	0.1	2.38	1.67	1.69
		7 ^[a]	0.1	2.35	1.68	1.67
		8 ^[a,b]	0.1	2.36	1.68	1.68
		9	0.1	2.28	1.74	1.68
		10	0.1	2.38	1.68	1.69
¹⁹ F	MJ	11	0.4	---	1.89	---
		12	0.4	---	1.86	---
		13	0.3	---	1.89	---
		14	0.2	---	1.77	---
		15	0.1	---	1.77	---
	LED	16	0.4	---	1.74	---

[a] gas flow 270 L h⁻¹, [b] with 20 Hz sample rotation.

After the test measurements with 3,5-difluorophenylboronic acid in DMSO, the electrolyte LiDFOB in EC/DEC was investigated with ¹⁹F-, ¹¹B- and ⁷Li-LED and MJ-DOSYs (see Table 8.5). The slow ¹¹B relaxation in LiDFOB ($T_1 = T_2 = 23$ ms) enabled a ¹¹B-LED-DOSY, which offered the same diffusion value within the error range as the ¹⁹F-LED experiments (see entry 5-6). Potential convection contributions were investigated with ⁷Li-MJ experiments with varying Δ (from 50 to 80 ms, see Table 8.5, entry 6-10), but constant $\delta^2\Delta$.^[52, 71-72, 84] Since a constant diffusion value within the experimental error was observed, convection contributions could be ruled out in this sample, as expected on account of the high viscosity of 2.11 mPa s (calculated from D_{TMS}).

Table 8.5: Diffusion coefficients of the cation and anion of 0.93 mol kg⁻¹ LiDFOB in EC/DEC from ¹⁹F-, ¹¹B- and ⁷Li-LED and MJ pulse sequences at 295±0.9 K.

nuclei	pulse program	entry	δ / ms	Δ / ms	D _{T-corr} / 10 ⁻¹⁰ m ² s ⁻¹
¹⁹ F	MJ	1	9.0	50	1.95
		2	9.0	50	2.04
		3	9.0	50	2.04
	LED	4	10.0	50	1.96
¹¹ B	LED	5	5.0	50	1.99
⁷ Li	MJ	6	20.4	50	1.71
		7	19.4	60	1.69
		8	18.4	70	1.70
		9	18.6	70	1.68
		10	18.0	80	1.73
	LED	11	20.0	70	1.65

The influence of TMS on the cation and anion diffusion values was investigated with a sample of 0.82 mol kg⁻¹ LiDFOB with increasing TMS content from 0.0 to 4.5 weight percent (see Table 8.6). The increase of the TMS content led to a decrease of the solution viscosity and thus to an increase of all experimental diffusion values. But even at the extraordinary high TMS content of 4.5 wt%, the reduction of the diffusion value was below 12 %. Thus, the TMS content had only a minor influence on the diffusion coefficients of the analytes. However, for all diffusion coefficients stated in the manuscript (chapter 8.2), a very small TMS weight percent of 0.035-0.045 wt% was used as a precaution, so the influence of TMS on these measurements could be neglected at this tiny amount.

Table 8.6: Diffusion coefficients of EC, DEC and TMS as function of the TMS weight percent, determined with a ¹H-MJ for 0.82 mol kg⁻¹ LiDFOB in EC/DEC at 297±0.1 K.

wt % TMS	η / mPa s	D _{exp} / 10 ⁻¹⁰ m ² s ⁻¹			D _{corr} / 10 ⁻¹⁰ m ² s ⁻¹	
		TMS	EC	DEC	EC	DEC
0.00	---	---	4.30	4.73	---	---
0.25	1.88	6.01	4.45	4.83	4.45	4.83
4.50	1.74	6.49	4.46	5.29	4.13	4.90

To summarize, several ¹H-, ¹⁹F-, ¹¹B- and ⁷Li-LED and MJ experiments for LiDFOB in EC/DEC and 3,5-difluorophenylboronic acid in DMSO-d₆ were performed. The typical error range of the different pulse sequences, the minimal gradient recovery delay, potential convection contributions and the influence of TMS was studied.

With this knowledge in hand, DOSY measurements of LiDFOB in EC/DEC with high accuracy have been enabled, which were used for a detailed comparative study about the differences of electrochemical and NMR based methods for the determination of transference numbers for lithium electrolytes (see chapter 8.2). This study was the starting point for our ongoing investigations on the concentration dependence of the transference number and of the amount of ion pairing (in combination with dielectric relaxation spectroscopy by Prof. R. Buchner), which will give us further insight into hitherto unknown transport processes for lithium electrolytes.

8.3.3 Investigations on the electrolyte system LiAlCl₄ in liquid SO₂

The second electrolyte system LiAlCl₄ in liquid SO₂ was investigated with NMR-based diffusion measurements due to several reasons, especially due to its extraordinary high conductivity of 70 mS cm⁻¹^[74] and remarkably low association constant,^[85] which are favorable for the use of LiAlCl₄/SO₂ in battery systems. Additionally, this low association constant offered a framework to validate the Haven ratio $\Lambda_{EC}/\Lambda_{NMR}$.^[86] This concept allows for an estimation of the association from the divergence from electrochemical and NMR-based ionic conductivities. Furthermore, the transference number of LiAlCl₄ in SO₂ at infinite diluted solution of $t_+=0.32$ ^[87] extremely differs from the value obtained by Hittorf measurements ($t_+=0.73$) in a 6.2 M solution.^[85] To fill the gap between diluted and concentrated solution and to correlate it with the electrochemical measurements, concentration-dependent DOSY measurements were performed to allow for an estimation of the association at high concentrations.

Starting from nearly saturated solution (6.2 M LiAlCl₄) a concentration series should be performed. But lowering of the salt-capacity led to an increase of the SO₂ vapor pressure (150 hPa in the 6.2 M solution), which was addressed with pressure stable NMR tubes (Wilmad 528-QPV-8). However, the application of these special tubes was connected with difficulties in the sample preparation. Therefore, so far only 6.2 and 4.7 M solutions could be investigated with NMR diffusion measurements.

For this electrolyte, ¹H-LED and MJ experiments were performed for TMS as viscosity reference, ⁷Li-LED and MJ pulse sequences were investigated for the diffusion coefficient of the Li⁺ cation and ²⁷Al-LED and MJ pulse sequences were investigated for the diffusion coefficient of the AlCl₄⁻ anion (see Table 8.7). For the anion no ²⁷Al diffusion experiments could be performed at 300 K due to the fast quadrupolar relaxation of the ²⁷Al nucleus with T_1 and T_2 relaxation times of 6 ms (see Table 8.7 for the diffusion values and Table 8.8 for the relaxation

times). However, by increasing the temperature and therefore deceleration of the quadrupolar relaxation, STE experiments (less time-demanding DOSY experiments without eddy current delay) could be accomplished, starting at 320 K. At 360 K, strong convection contributions were observed, which should at least partially be reduced by sample spinning. Thus, the obtained diffusion value at 360 K has to be handled with care. The alternative very long MJ sequence with convection compensation could not be applied at any temperature for the 6.2 M solution due to fast relaxation. By dilution of the sample the T_1 and T_2 relaxation times were also prolonged, so that the MJ sequence could be applied already at 320 K.

Table 8.7: Diffusion coefficients of the cation and anion of 6.2 and 4.7 M LiAlCl₄ in liquid SO₂ at 300-360 K, measured with varying pulse sequences. η calculated from D_{TMS} .

c / mol l ⁻¹	pulse program	entry	T / K	η / mPa s	$D_{\text{exp}} / 10^{-10} \text{ m}^2 \text{ s}^{-1}$		$D_{\text{corr}} / 10^{-10} \text{ m}^2 \text{ s}^{-1}$	
					D_{Li}	D_{Al}	D_{Li}	D_{Al}
6.2	MJ	1	300	8.23	2.45	---	2.45	---
		2	320	5.21	4.23	---	2.51	---
		3	340	2.53	6.40	---	1.74	---
	LED	4	300	---	2.39	---	---	---
		5	320	4.54	4.20	0.21 ^[a]	2.17	0.11
		6	340	2.50	6.82	4.20 ^[a]	1.83	1.12
		7	360	---	---	9.55 ^[b]	---	---
4.7	MJ	8	300	3.07	5.03	---	1.87	---
		9	320	1.82	7.12	5.10	1.48	1.06
	LED	10	300	3.10	4.86	3.11 ^[a]	1.83	1.17
		11	320	0.59	18.22	13.26 ^[a]	1.23	0.89

[a] STE, [b] with sample spinning for convection compensation.

Table 8.8: T_1 and T_2 relaxation times for LiAlCl₄ in liquid SO₂.

c / mol l ⁻¹	T / K	⁷ Li		²⁷ Al	
		T_2 / s	T_1 / s	T_2 / s	T_1 / s
6.2	300	0.177	5.4	0.006	0.006
	320	0.168	8.8	0.009	0.010
	340	0.100	11.2	0.010	0.015
	360	n.d.	n.d.	0.010	0.018
4.7	300	0.187	9.2	0.014	0.017
	320	0.114	12.0	0.014	0.020

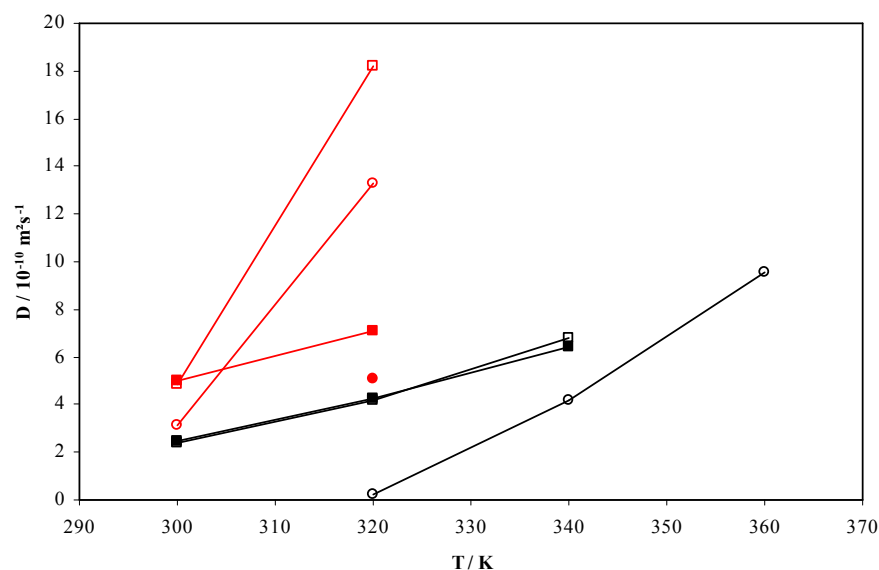


Figure 8.12: Temperature dependence of the experimental diffusion coefficients of cation and anion in 6.2 and 4.7 M LiAlCl₄ in SO₂. Black: 6.2 M, Red: 4.7 M; square: ⁷Li, circle: ²⁷Al; filled: MJ, open: LED.

The temperature and concentration dependencies of the diffusion coefficients of the cation and anion are shown in Figure 8.12. As the temperature was increased, the experimental diffusion values increased, which could be interpreted in view of a decrease of the viscosity. In contrast, the temperature and viscosity corrected diffusion values D_{corr} both for the cation and the anion (referenced to the 6.2 M solution at 300 K) showed a slight decrease with increasing temperature (see Table 8.7). As expected, dilution resulted also in a decrease of viscosity and thus an increase of the diffusion coefficients.

To summarize, multinuclear NMR measurements for 6.2 and 4.7 M LiAlCl₄ in liquid SO₂ were performed to study the individual behavior of Li⁺ by ⁷Li NMR, AlCl₄⁻ by ²⁷Al NMR. To allow for diffusion measurements of the ²⁷Al quadrupolar nucleus, various pulse sequences, dilution of the sample and increased temperatures up to 360 K were applied. Convection contributions, which get valid at $T \geq 320$ K, have been taken into account by using a MJ sequence whenever possible or should - at least partially - be reduced by sample spinning. The general trend of $D_{\text{Li}} > D_{\text{TMS}} > D_{\text{anion}}$ was quite different from the well-known behavior of monovalent lithium salts in high dielectric solvents showing $D_{\text{solvent}} > D_{\text{anion}} > D_{\text{Li}}$ (as it was also the case for LiDFOB in EC/DEC). Difficulties in sample preparation, due to the inevitable use of special pressure stable NMR tubes, impeded to pursue the concentration series and to correlate the NMR-based and electrochemical derived conductivities at low concentration.

8.3.4 Investigations of electrolyte systems with different pulse sequences

In the diffusion studies for the two electrolytes, the influence of potential convection effects should be investigated. Therefore, various pulse sequences, especially the MJ sequence due to its inherent convection compensation and normal STE/LED type experiments without convection compensation have been applied. In general, if convection is present, the LED sequence delivers diffusion values, which are extended about the convection contribution. Therefore, the obtained diffusion coefficient should always be as large as or larger than the values obtained from MJ experiments ($D_{\text{LED}} \geq D_{\text{MJ}}$).^[49] To our astonishment, this basic behavior was not observed for most MJ and LED diffusion values investigated for the electrolytes. In most cases, the MJ sequence delivered diffusion coefficients, which were 2-6 % larger than the STE/LED obtained ones (see Table 8.4 for 3,5-difluorophenylboronic acid in DMSO-d₆, Table 8.5 for LiDFOB in EC/DEC and Table 8.7 for LiAlCl₄ in SO₂). For instance, all STE/LED type experiments with and without bipolar gradients pulses delivered the same diffusion coefficient for 0.93 mol kg⁻¹ LiDFOB, while the MJ sequence delivered diffusion values significantly outside the standard deviation (< 1 %) of the STE/LED type experiments (see Table 8.9).

Table 8.9: Anion diffusion coefficients of 0.93 mol kg⁻¹ LiDFOB in EC/DEC determined with varying pulse sequences using the ¹⁹F nucleus. T=296.3±6 K.

pulse program	entry	t _e / ms	D1 / ms	D / 10 ⁻¹⁰ m ² s ⁻¹
MJ	1	5	2	2.086
	2	5	1	2.109
LED	3	5	1	2.040
	4	5	2	2.029
STE	5	---	2	2.028
STE ^[a]	6	---	2	2.020
LED ^[a]	7	5	2	2.003

[a] without bipolar gradient pulses

Several potential reasons could be considered to be responsible for this observation: Miss-calibration of pulses,^[88] phase distortions caused e.g. by an unsuited gradient recovery delay or convection contributions,^[89] not adequate gas flow combined with an unsuited temperature control,^[90] differential increase of the temperature during the experiment or the occurrence of internal gradients.^[47] The MJ sequence possesses a high number of rf pulses, so a miss-calibration of the $\pi/2$ and π pulse-flip-angle could have an influence on the actual diffusion value. Therefore, the $\pi/2$ pulse length was extended about +0.1 μ s (estimated error of the automated $\pi/2$ pulse length determination), but the corresponding ¹H-LED experiment resulted

in the same diffusion value as experiments with the correct pulses (data not shown). Phase distortions or an influence of an unsuited gradient recovery delay did not have been observed (see Table 8.4, entry 11-15). The influence of convection was investigated with sample spinning (see Table 8.4, entry 8) and with varying Δ (see Table 8.5, entry 7-11), but both experiments resulted in a constant diffusion value each, therefore potential convection contributions could be ruled out, as expected on account of the high viscosity. The influence of the gas flow used for temperature control was investigated with a variation of the gas flow from 270 up to 535 L h⁻¹ (and up to 1070 L h⁻¹ at a 600 MHz spectrometer, data not shown) for 3,5-difluorophenylboronic acid in DMSO, but did not affect the temperature and viscosity corrected diffusion coefficients, neither for ¹H-LED nor for ¹H-MJ experiments (see Table 8.4, entry 1-10).

During the investigations with out-of-action temperature control, the temperature increase in the course of the experiments was different for the LED and the MJ experiments. For the LED sequence a ΔT of +0.2 K and for the MJ sequence a ΔT of +0.4 K was observed, which can be attributed to the higher number of pulses for the MJ sequence compared to the LED sequence leading to elevated RF heating of the sample. But since this temperature increase was not observed at other spectrometers with internal temperature control unit, this effect could not be responsible for the unexpected behavior of MJ and LED sequences.

To further clarify, if this observation was real or just within the normal error range, the complete concentration series of LiDFOB was measured for all compounds with LED and MJ experiments (see Table 8.10). For all experiments, except for the cation diffusion coefficients at a concentration of 0.1 and 0.05 mol kg⁻¹, the MJ experiments delivered larger values compared to the LED experiments.

Table 8.10: Solution viscosity, experimental diffusion coefficients of the solvents EC and DEC, the reference substance TMS, the lithium cation, the anion and the transference number (t_+) of LiDFOB at 296.7 K, determined with the LED and MJ sequence.

LED ^[a]								MJ							
molality / mol kg ⁻¹	η / mPa s	D / 10 ⁻¹⁰ m ² s ⁻¹						molality / mol kg ⁻¹	η / mPa s	D / 10 ⁻¹⁰ m ² s ⁻¹					
		D _{EC}	D _{DEC}	D _{TMS}	D ₊ ^{NMR}	D ₋ ^{NMR}	t_+			D _{EC}	D _{DEC}	D _{TMS}	D ₊ ^{NMR}	D ₋ ^{NMR}	t_+
0.93	2.12	3.77	4.20	5.33	1.71	2.00	0.460	0.93	2.04	4.01	4.43	5.53	1.74	2.11	0.452
0.83	1.98	4.18	4.63	5.72	1.87	2.23	0.456	0.83	1.98	4.30	4.81	5.72	1.88	2.33	0.447
0.70	1.70	5.03	5.45	6.64	2.19	2.66	0.451	0.70	1.64	5.30	5.62	6.88	2.22	2.67	0.454
0.50	1.56	5.78	6.18	7.24	2.48	3.05	0.448	0.50	1.55	6.02	6.34	7.29	2.50	3.22	0.438
0.30	1.35	7.08	7.36	8.40	2.93	3.68	0.443	0.30	1.31	7.38	7.47	8.64	2.89	3.88	0.427
0.10	1.20	8.56	8.58	9.43	3.65	4.61	0.442	0.10	1.14	8.92	8.63	9.89	3.46	4.69	0.424
0.05	1.16	9.29	9.05	9.78	3.84	4.86	0.441	0.05	1.13	9.54	9.12	10.05	3.59	5.08	0.414

[a] reported in *Electrochimica Acta*, **2011**, 56, 11, 3926-3933.

Furthermore, for $\text{Al}(\text{O}^i\text{Pr})_3$ in the low viscous solvent CDCl_3 a $D_{\text{corr}}(\text{LED}) = 6.72 \cdot 10^{-10} \text{ m}^2 \text{ s}^{-1}$ and a $D_{\text{corr}}(\text{MJ}) = 6.67 \cdot 10^{-10} \text{ m}^2 \text{ s}^{-1}$ was observed. Based on the observation, that for the low viscous organic solvent CDCl_3 and partially in diluted and therefore less viscous EC/DEC solutions the normal expected behavior of $D_{\text{LED}} \geq D_{\text{MJ}}$ was observed, the high viscosity could potentially be involved in the inversion of the diffusion values. The influence of the high viscosity on the T_2 relaxation time and thus on the experimental diffusion coefficient was investigated by Annat et al.,^[47] who observed for highly viscous ionic liquids up to 20 % lower diffusion values with SE compared to STE in combination with line broadening and reduction of individual signal intensities in the SE compared to the ^1H spectrum. They explained these deviations with the existence of local internal gradients within the sample volume leading to differences in the T_2 relaxation for each signal. These differences were more significant for SE compared to STE.^[47] But, since for LED and MJ-DOSY experiments no line shape distortions or intensity variations compared to the normal spectra were observed for all nuclei, significant differences in the T_2 times could be excluded.

To summarize, an unexpected behavior of the MJ and LED-derived diffusion values ($D_{\text{LED}} \leq D_{\text{MJ}}$) in highly viscous solvents like DMSO, EC/DEC or SO_2 (liq.) was observed. Therefore, the influence of pulse lengths, phase distortions, gradient recovery delay and convection on the diffusion values for MJ and LED-DOSYs was studied. In addition, the influence of an unsuited temperature control combined with differential irradiation heat for LED and MJ was investigated with varying gas flow rates at different spectrometers.

All these observations direct to the assumption, that there is a systematic offset of 2-6 % of the MJ-derived diffusion values compared to STE or LED-derived values; but only noticeable in highly viscous solvents without convection contribution.

8.4 References

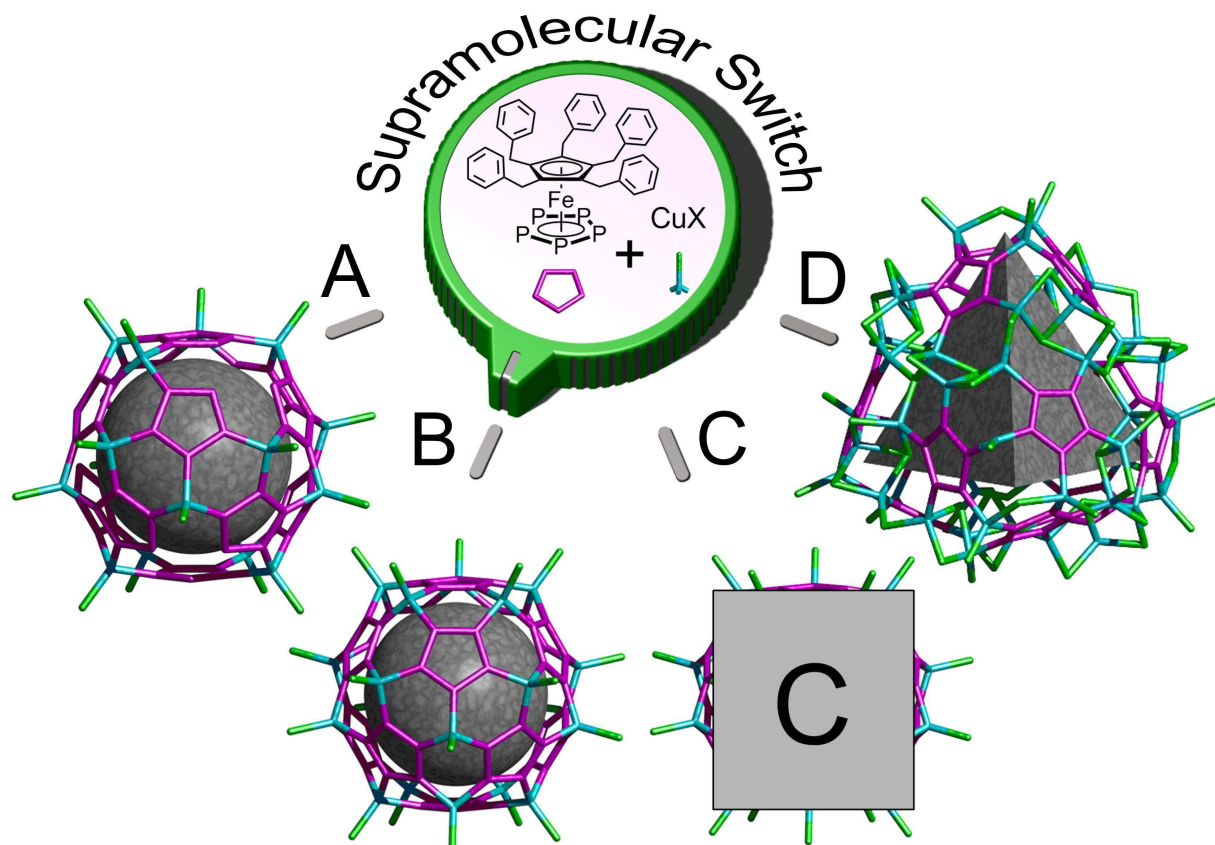
- [1] H. J. Gores, H. Schweiger, M. Multerer, in *Advanced Materials and Methods for Lithium Ion Batteries*, S. S. Zhang, **2007**.
- [2] A. Nyman, M. Behm, G. Lindbergh, *Electrochim. Acta* **2008**, *53*, 6356-6365.
- [3] M. Petrowsky, R. Frech, *J. Phys. Chem. B* **2008**, *112*, 8285-8290.
- [4] J. Newman, K. E. Tomas-Alyea, *Electrochemical Systems*, 3rd ed., John Wiley & Sons, **2004**.
- [5] K. E. Thomas, R. M. Darling, J. Newman, in *Advances in Lithium-Ion Batteries* (Eds.: W. A. van Schalkwijk, B. Scrosati), Kluwer Academic/Plenum Publishers, New York, **2002**, pp. 345-392.
- [6] H. J. Gores, J. Barthel, S. Zugmann, D. Moosbauer, M. Amereller, R. Hartl, A. Maurer, in *Handbook of Battery Materials*, 2. ed. (Ed.: C. Daniel), VCH, Weinheim, **2011**.
- [7] B. Scrosati, *The Chemical Record* **2005**, *5*, 286-297.
- [8] M. Ciosek, M. Marcinek, G. Zukowska, W. Wieczorek, *Electrochim. Acta* **2009**, *54*, 4487-4493.
- [9] A. Ghosh, C. Wang, P. Kofinas, *J. Electrochem. Soc.* **2010**, *157*, A846-A849.
- [10] L. Niedzicki, M. Kasprzyk, K. Kuziak, G. Zukowska, M. Armand, M. Bukowska, M. Marcinek, P. Szczecinski, W. Wieczorek, *J. Power Sources* **2009**, *192*, 612-617.
- [11] O. Söderman, W. S. Price, M. Schönhoff, D. Topgaard, *J. Mol. Liq.* **2010**, *156*, 38-44.
- [12] D. A. MacInnes, M. Dole, *J. Am. Chem. Soc.* **1931**, *53*, 1357-1364.
- [13] H. Harned, E. C. Dreby, *J. Am. Chem. Soc.* **1939**, *61*, 3113-3120.
- [14] L. G. Longworth, *J. Am. Chem. Soc.* **1932**, *54*, 2741-2758.
- [15] M. Bester-Rogac, R. Neueder, J. Barthel, *J. Solution Chem.* **1999**, *28*, 1071-1086.
- [16] R. A. Robinson, R. H. Stokes, *Electrolyte Solutions*, 2 ed., Butterworths, London, **1970**.
- [17] L. F. Li, H. S. Lee, H. Li, X. Q. Yang, K. W. Nam, W. S. Yoon, J. McBreen, X. J. Huang, *J. Power Sources* **2008**, *184*, 517-521.
- [18] H. F. Xiang, B. Yin, H. Wang, H. W. Lin, X. W. Ge, S. Xie, C. Chen, *Electrochim. Acta* **2010**, *55*, 5204-5209.
- [19] T. Froemling, M. Kunze, M. Schoenhoff, J. Sundermeyer, B. Roling, *J. Phys. Chem. B* **2008**, *112*, 12985-12990.
- [20] Y. Aihara, T. Bando, H. Nakagawa, H. Yoshida, K. Hayamizu, E. Akiba, W. S. Price, *J. Electrochem. Soc.* **2004**, *151*, A119-A122.
- [21] S. H. Chung, Y. Wang, L. Persi, F. Croce, S. G. Greenbaum, B. Scrosati, E. Plichta, *J. Power Sources* **2001**, *97-98*, 644-648.
- [22] J. Zhao, L. Wang, X. He, C. Wan, C. Jiang, *J. Electrochem. Soc.* **2008**, *155*, A292-A296.
- [23] C. Schreiner, M. Amereller, H. J. Gores, *Chemistry A European Journal* **2009**, *15*, 2270-2272.
- [24] S. Zugmann, D. Moosbauer, M. Amereller, C. Schreiner, F. Wudy, R. Schmitz, R. W. Schmitz, P. Isken, C. Dippel, I. M^u, R. A., M. Kunze, A. Lex-Balducci, M. Winter, H. J. Gores, *J. Power Sources* **2011**, *196*, 1417-1424.
- [25] P. G. Bruce, C. A. Vincent, *J. Electroanal. Chem. Interfacial Electrochem.* **1987**, *225*, 1-17.
- [26] V. Mauro, A. D'Aprano, F. Croce, M. Salomon, *J. Power Sources* **2005**, *141*, 167-170.
- [27] J. W. Evans, C. A. Vincent, P. G. Bruce, *Polymer* **1987**, *28*, 2324-2328.
- [28] L. O. Valoen, J. N. Reimers, *J. Electrochem. Soc.* **2005**, *152*, A882-A891.
- [29] Y. Ma, M. Doyle, T. F. Fuller, M. M. Doeff, L. C. de Jonghe, J. Newman, *J. Electrochem. Soc.* **1995**, *142*, 1859-1868.
- [30] H. Hafezi, J. Newman, *J. Electrochem. Soc.* **2000**, *147*, 3036-3042.
- [31] H. Harned, D. M. French, *Ann. N.Y. Acad. Sci.* **1945**, *46*, 267-284.
- [32] J. Newman, T. W. Chapman, *AIChE J.* **1973**, *19*, 343-348.
- [33] S. D. Thompson, J. Newman, *J. Electrochem. Soc.* **1989**, *136*, 3362-3369.
- [34] M. M. Doeff, P. Georen, J. Qiao, J. B. Kerr, L. C. de Jonghe, *J. Electrochem. Soc.* **1999**, *146*, 2024-2028.
- [35] D. A. MacInnes, J. Beattie, *J. Am. Chem. Soc.* **1920**, *42*, 1117-1128.
- [36] A. Basili, P. R. Mussini, T. Mussini, S. Rondinini, B. Sala, A. Vertova, *J. Chem. Eng. Data* **1999**, *44*, 1002-1008.
- [37] M. Spiro, in *Physical methods of chemistry: Electrochemical Methods, Vol. 1* (Eds.: A. Weissberger, B. Rossiter), Wiley-Interscience, **1971**, pp. 205-295.
- [38] M. Videa, W. Xu, B. Geil, R. Marzke, C. A. Angell, *J. Electrochem. Soc.* **2001**, *148*, A1352-A1356.
- [39] F. Kaneko, S. Wada, M. Nakayama, M. Wakihara, S. Kuroki, *ChemPhysChem* **2009**, *10*, 1911-1915.
- [40] Y. Saito, H. Yamamoto, O. Nakamura, H. Kageyama, H. Ishikawa, T. Miyoshi, M. Matsuoka, *J. Power Sources* **1999**, *81-82*, 772-776.
- [41] S. Bhattacharja, S. W. Smoot, D. H. Whitmore, *Solid State Ionics* **1986**, *18-19*, 306-314.

- [42] J. Saunier, W. Gorecki, F. Alloin, J. Y. Sanchez, *J. Phys. Chem. B* **2005**, *109*, 2487-2492.
- [43] K. Hayamizu, Y. Aihara, W. S. Price, *The Journal of Chemical Physics* **2000**, *113*, 4785-4793.
- [44] S. Duluard, J. Grondin, J.-L. Bruneel, I. Pianet, A. Grélard, G. Campet, M.-H. Delville, J.-C. Lassègues, *Journal of Raman Spectroscopy* **2008**, *39*, 627-632.
- [45] K. Hayamizu, E. Akiba, T. Bando, Y. Aihara, W. S. Price, *Macromolecules* **2003**, *36*, 2785-2792.
- [46] Y. Saito, T. Umecky, J. Niwa, T. Sakai, S. Maeda, *J. Phys. Chem. B* **2007**, *111*, 11794-11802.
- [47] G. Annat, D. R. MacFarlane, M. Forsyth, *J. Phys. Chem. B* **2007**, *111*, 9018-9024.
- [48] W. S. Price, *Concepts Magn. Reson.* **1998**, *10*, 197-237.
- [49] C. S. Johnson, *Prog. Nucl. Magn. Reson. Spectrosc.* **1999**, *34*, 203-256.
- [50] E. O. Stejskal, J. E. Tanner, *The Journal of Chemical Physics* **1965**, *42*, 288-292.
- [51] E. J. Cabrita, S. Berger, *Magn. Reson. Chem.* **2001**, *39*, S142-S148.
- [52] K. Hayamizu, A. Matsuo, J. Arai, *J. Electrochem. Soc.* **2009**, *156*, A744-A750.
- [53] K. Hayamizu, Y. Aihara, S. Arai, C. G. Martinez, *J. Phys. Chem. B* **1999**, *103*, 519-524.
- [54] E. Cazzanelli, F. Croce, G. B. Appetecchi, F. Benevelli, P. Mustarelli, *The Journal of Chemical Physics* **1997**, *107*, 5740-5747.
- [55] J. Barthel, d. Str^o, U., L. Iberl, H. Hammer, *Berichte der Bunsengesellschaft fuer physikalische Chemie* **1982**, *86*, 636-645.
- [56] M. Spiro, in *Physical Chemistry of Organic Solvent Systems* (Eds.: A. K. Convington, T. Dickinson, R. Fernandez-Prini), Plenum Press, London, **1973**, pp. 615-680.
- [57] R. M. Fuoss, *J. Am. Chem. Soc.* **1959**, *81*, 2659-2662.
- [58] P. Debye, c. H^u, E., *Physikalische Zeitschrift* **1923**, *24*, 185-206.
- [59] P. S. Pregosin, *Pure Appl. Chem.* **2009**, *81*, 615-633.
- [60] Y. Cohen, L. Avram, L. Frish, *Angew. Chem. Int. Ed.* **2005**, *44*, 520-554.
- [61] W. Gorecki, M. Jeannin, E. Belorizky, C. Roux, M. Armand, *J. Phys.: Condens. Matter* **1995**, *7*, 6823.
- [62] C. Capiglia, Y. Saito, H. Kataoka, T. Kodama, E. Quartarone, P. Mustarelli, *Solid State Ionics* **2000**, *131*, 291-299.
- [63] K. Hayamizu, Y. Aihara, S. Arai, W. S. Price, *Electrochim. Acta* **2000**, *45*, 1313-1319.
- [64] H. Shobukawa, H. Tokuda, S.-I. Tabata, M. Watanabe, *Electrochim. Acta* **2004**, *50*, 305-309.
- [65] K. Hayamizu, Y. Aihara, H. Nakagawa, T. Nukuda, W. S. Price, *J. Phys. Chem. B* **2004**, *108*, 19527-19532.
- [66] M. Galinski, A. Lewandowski, I. Stepniak, *Electrochim. Acta* **2006**, *51*, 5567-5580.
- [67] K. Hayamizu, S. Tsuzuki, S. Seki, Y. Ohno, H. Miyashiro, Y. Kobayashi, *J. Phys. Chem. B* **2008**, *112*, 1189-1197.
- [68] S. Tsuzuki, K. Hayamizu, S. Seki, Y. Ohno, Y. Kobayashi, H. Miyashiro, *J. Phys. Chem. B* **2008**, *112*, 9914-9920.
- [69] Y. Aihara, K. Sugimoto, W. S. Price, K. Hayamizu, *The Journal of Chemical Physics* **2000**, *113*, 1981-1991.
- [70] K. Hayamizu, Y. Aihara, *Electrochim. Acta* **2004**, *49*, 3397-3402.
- [71] K. Hayamizu, E. Akiba, T. Bando, Y. Aihara, *The Journal of Chemical Physics* **2002**, *117*, 5929-5939.
- [72] K. Hayamizu, W. S. Price, *J. Magn. Reson.* **2004**, *167*, 328-333.
- [73] H. D. B. Jenkins, Y. Marcus, *Chem. Rev.* **1995**, *95*, 2695-2724.
- [74] L. Zinck, M. Borck, C. Ripp, G. Hambitzer, *J. Appl. Electrochem.* **2006**, *36*, 1291-1295.
- [75] I. Stassen, G. Hambitzer, *J. Power Sources* **2002**, *105*, 145-150.
- [76] S. S. Zhang, *ECS Transactions* **2007**, *3*, 59-68.
- [77] S. S. Zhang, *J. Power Sources* **2007**, *163*, 713-718.
- [78] D. E. J. Linden, T. B. Reddy, *Handbook of Batteries*, 3. ed., McGraw-Hill, New York, **2002**.
- [79] A. Jossen, W. Weydanz, *Moderene Akkumulatoren richtig einsetzen*, 1. ed., Inge Reichardt Verlag, Untermeitingen, **2006**.
- [80] D. Moosbauer, S. Zugmann, M. Amereller, H. J. Gores, *J. Chem. Eng. Data* **2010**, *55*, 1794-1798.
- [81] K. Xu, *Chem. Rev.* **2004**, *104*, 4303-4418.
- [82] A. Jerschow, N. Müller, *J. Magn. Reson.* **1997**, *125*, 372-375.
- [83] H. Zhang, R. Kerssebaum, R. M. Gschwind, *Magn. Reson. Chem.* **2009**, *47*, 568-572.
- [84] K. Hayamizu, K. Sugimoto, E. Akiba, Y. Aihara, T. Bando, W. S. Price, *J. Phys. Chem. B* **2002**, *106*, 547-554.
- [85] R. Hartl, R. Neueder, H. J. Gores, *Acta Chim. Slov.* **2009**, *56*, 109-114.
- [86] M. Takeuchi, Y. Kameda, Y. Umebayashi, S. Ogawa, T. Sonoda, S.-i. Ishiguro, M. Fujita, M. Sano, *J. Mol. Liq.* **2009**, *148*, 99-108.
- [87] S. Takezawa, Y. Kondo, N. Tokura, *J. Phys. Chem.* **1973**, *77*, 2133-2137.
- [88] S. Augé, B. Amblard-Blondel, M.-A. Delsuc, *J. Chim. Phys.* **1999**, *96*, 1559-1565.

- [89] J. Lounila, K. Oikarinen, P. Ingman, J. Jokisaari, *Journal of Magnetic Resonance, Series A* **1996**, 118, 50-54.
- [90] N. M. Loening, J. Keeler, *J. Magn. Reson.* **1999**, 139, 334-341.

9 Self-assembled Switchable Supramolecular Container Molecules

“NMR detection and characterization of
soluble self-assembled pentaphosphaferrocene- Cu^{I} supramolecular switches,
study of their formation pathway and of the incorporation of guests”



Matthias Fleischmann, Fabian Dielmann,
M. Scheer, Ruth M. Gschwind

Science **2011**, Manuscript in Preparation.

The synthesis and X-ray characterization of the compounds
were performed by Fabian Dielmann.

9.1 Introduction

The design and synthesis of nanoscale molecular containers with defined sizes and inner cavities is attracting considerable interest in current chemistry. A wide array of molecular container compounds has been synthesized by covalent and noncovalent syntheses.^[1-6] Such hollow molecules provide confined nanospaces, which can regulate the reactivity and stability of molecules accommodated in their cavities.^[4-5] Otherwise labile species can be protected, substrates can be isolated from bulk media and if the size and shape of the cavity are rationally and precisely designed, chemical transformations can be directed by the cavity. For the bottom-up construction of discrete, well-defined nanoscale structures the self-assembly approach based on the reversible aggregation of smaller building blocks has received broad attention. Recently, Scheer et al. have shown that the combination of copper(I) halides with the *cyclo*-P₅ complex [Cp*Fe(η^5 -P₅)] (Cp* = η^5 -C₅Me₅) or the *cyclo*-P₄ complex [Cp''Ta(CO)₂(η^4 -P₄)] (Cp'' = η^5 -C₅H₃tBu₂) provide a powerful tool for the synthesis of inorganic shell structures with fullerene-type topology.^[7-13] These supramolecules can be used to encapsulate guest molecules like *o*-carboranes^[11] or C₆₀ fullerenes,^[10] whereby the shape of the inorganic host is controlled by the size of the respective template. Even without additional guest molecule the *cyclo*-P₅ complex [Cp*Fe(η^5 -P₅)] itself acts as template for the formation of spherical supramolecules^[8, 12-13] or nanosized capsules.^[9] However, all of the resulting host-guest compounds based on [Cp*Fe(η^5 -P₅)] have very low solubility and only by applying special reaction conditions the thermodynamically favored formation of 1D or 2D coordination polymeric products^[9, 14-15] can be avoided.

Herein, we report about the structure and formation process of soluble, nanometer-sized switchable container molecules, which are readily accessible by quantitative self-assembly of [Cp^{Bn}Fe(η^5 -P₅)] **1** (Cp^{Bn} = pentabenzylcyclopentadienyl) with CuX (X = Cl, Br). Their formation is not depending on template control and they even provide switchable hollow structures. Scheer et al. previously reported about the synthesis and properties of the pentaphosphaferrocene complex **1**.^[16] Its Cp^{Bn} ligand has a steric influence similar to that of Cp*, but contains flexible organic benzyl groups, which show the tendency to form intra- and intermolecular π -stacking interactions between the phenyl rings.^[17] It will be shown in the following that the Cp^{Bn} ligand is conducive to the stability of the supramolecules as well as responsible for their solubility, which for the first time allowed detailed NMR investigations on the self-assembly process of spherical molecules based on polyphosphorus ligand complexes and Cu(I) halides in solution. These solution state NMR investigations led to the discovery of - so far only for Cp* instead of Cp^{Bn}

reported - $[\{\text{Cp}^{\text{Bn}}\text{Fe}(\eta^5\text{-P}_5)\}_{12}\{\text{CuX}\}_{20}]$ **3a/3b** container molecules and to hitherto unknown $[\{\text{Cp}^{\text{Bn}}\text{Fe}(\eta^5\text{-P}_5)\}_{12}\{\text{CuX}\}_{16\pm x}]$ **2a/2b** clusters. In addition, a supramolecule with a completely new scaffold for such pentaphosphaferrocene-based complexes, $[\{\text{Cp}^{\text{Bn}}\text{Fe}(\eta^5\text{-P}_5)\}_{12}\{\text{CuX}\}_{48\pm x}]$ **4a/4b** (**a**: X = Cl, **b**: X = Br) was discovered and subsequently characterized by X-ray analysis. The solution characteristics of these supramolecules, their formation pathways, the incorporation of guests and their behavior as supramolecular switch will be described herein.

9.2 Results and Discussion

General formation of the supramolecules

For the formation of the supramolecules two different approaches have been developed based on the results of the NMR investigations. The approach, which provides the potential of a selective formation of supramolecules of **2a/2b** or **3a/3b** (**a**: X = Cl, **b**: X = Br) type is described first: By stirring a solution of **1** over solid CuX (X = Cl, Br) in CD_2Cl_2 at room temperature supramolecules of **3a/3b** type are formed in solution within few days (see Figure 9.1) and can be crystallized according to the reported procedure.^[17] In this setup, a heterogeneous suspension of CuX in CD_2Cl_2 is formed due to the very low solubility of CuX in pure CD_2Cl_2 . However, the coordination of CuX at **1** or secondary products derived therefrom provides sufficient solubility for CuX to form supramolecules of **2a/2b/3a/3b** (**a**: X = Cl, **b**: X = Br) type. The advantage of this setup is the directed formation of exclusively **2a/2b/3a/3b** without the formation of **4a/4b**, but this method needs relatively long reaction times.

A second approach for the simultaneous formation of all supramolecules in solution is the addition of low amounts of acetonitrile to the reaction mixture containing **1** and CuX in CD_2Cl_2 . Thereby, CuX-MeCN adducts are formed, which provide good solubility accompanied by the formation of a homogeneous CuX- $\text{CD}_3\text{CN}/\text{CD}_2\text{Cl}_2$ solution. This setup allows a very rapid formation of all supramolecules simultaneously. Therefore, the corresponding NMR solution state experiments for this preparation method are described first.

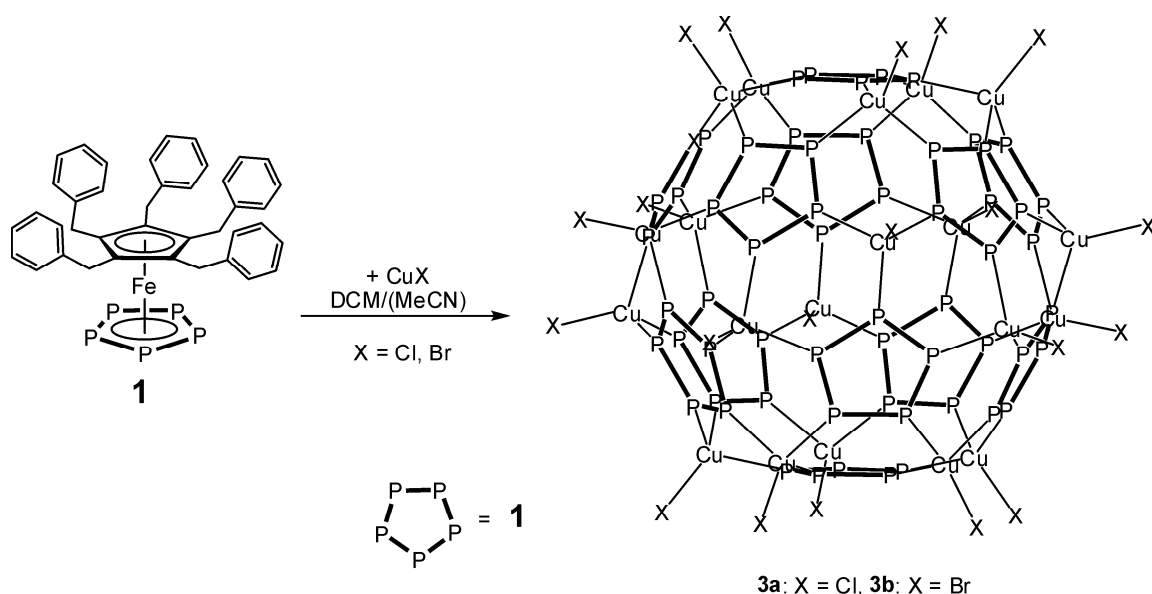


Figure 9.1: Formation of **3a/3b** supramolecules.

CuBr titration in CD_2Cl_2 with 9 vol% CD_3CN

The existence and spontaneous formation of $[\{\text{Cp}^{\text{Bn}}\text{Fe}(\eta^5\text{-P}_5)\}_{12}\{\text{CuX}\}_{16\pm x}]$ **2a/2b**, $[\{\text{Cp}^{\text{Bn}}\text{Fe}(\eta^5\text{-P}_5)\}_{12}\{\text{CuX}\}_{20}]$ **3a/3b** and $[\{\text{Cp}^{\text{Bn}}\text{Fe}(\eta^5\text{-P}_5)\}_{12}\{\text{CuX}\}_{48\pm x}]$ **4a/4b** in solution was investigated with samples containing the monomer $[\text{Cp}^{\text{Bn}}\text{Fe}(\eta^5\text{-P}_5)]$ **1** and increasing amounts of CuX (X = Cl, Br) from 0 to 8 equivalents of CuX relative to **1**. The different samples were prepared in analogy to the synthesis of **3a/3b** by stirring of **1** together with increasing amounts of CuX (X = Cl, Br) in CD_2Cl_2 with 9 vol% CD_3CN . After a reaction time of one hour each sample was filtrated and then characterized by means of ^1H and ^{31}P spectra. Due to the similarity of the spectra with CuCl (see Figure 9.20 in the SI) and CuBr (see Figure 9.2), only the experiments with CuBr are described in detail: As shown in Figure 9.2a, without CuBr only **1** was present in solution, which showed sharp signals in the ^1H spectrum for the para (6.88 ppm), meta (6.75 ppm), ortho (6.24 ppm) and methylene (3.64 ppm) protons. In the ^{31}P spectrum, a singlet at 161.29 ppm (and a signal at 157.89 ppm of the 2-5 % impurity of $[\text{Cp}^{\text{Bn}*}\text{Fe}(\eta^5\text{-P}_5)]$ ($\text{Cp}^{\text{Bn}*}$ = tetrabenzylcyclopentadienyl)) was observed. Very small line widths of 2.8-3.4 Hz in the ^1H spectrum and 4.4 Hz in the ^{31}P spectrum were observed, indicating **1** to be a monomeric species, which was confirmed by ^1H -DOSY^[18-21] measurements (see Table 9.1). Upon the addition of 0.5 eq. CuBr (see Figure 9.2b), beside the signals of **1**, several other broad and overlapping signals in the ^1H spectrum (6.80 ppm for H_{para} and 6.40-6.60 ppm for H_{ortho} and H_{meta} and at least three signals at 5.10, 4.84 and 4.67 ppm for the methylene protons (data not shown)) were detected, which all showed the same ^1H diffusion coefficient (see Table 9.1). In the ^{31}P spectrum, at least three very broad signals in the range of 65-125 ppm were observed,

indicating the formation of at least three very similar species or one species with several non-equivalent phosphorous atoms in P_5 -rings with varying CuBr coordination number. Therefore, these species are considered as one species A in the following. With one equivalent of CuBr (see Figure 9.2c), the amount of A was further increased at the expense of **1**. In addition, other species with separated 1H chemical shifts for the meta and ortho protons were observed under the 1H signals of A. In the ^{31}P spectrum additionally a sharp signal at 63.80 ppm and broader signals at 49.8-57.9 ppm appeared, which could be assigned to B and C. In the sample with 1.7 equivalents (see Figure 9.2d) the molar **1**:CuBr ratio was 12:20, the same ratio as in ideal **3b** crystals. Here, in the 1H spectrum the amount of **1** and A was drastically reduced and sharp signals with recognizable coupling fine structures at 6.75, 6.56, 6.44 and 5.09 ppm were detected. These signals of species B were overlapped with a considerable amount of signals of species C, which showed very similar 1H chemical shifts like A and B. This decrease of **1** and A and, at the same time, increase of B and C compared to the sample with one eq. CuBr was also observed in the ^{31}P spectrum with the sharp singlet at 63.80 ppm for B and a broader signal at 58.8 ppm for C. At a CuBr content of four eq. (see Figure 9.2e), the molar **1**:CuBr ratio was in the range of the **4b** supramolecule (12:48). In the 1H spectrum, the amount of B and C was reduced in support of a new species D (53 % B, 8 % C and 39 % D), whose aromatic signals (H_{para} 6.89 ppm, H_{meta} 6.78 ppm, H_{ortho} 6.63 ppm) were downfield shifted and the methylene signal (4.58 ppm) upfield shifted compared to A-C. In the ^{31}P spectrum, D showed a broad signal with a similar ^{31}P chemical shift like C, therefore, the increase of D and, at the same time, decrease of C, which was detected in the 1H spectrum, was hardly observable. The only slight reduction of the ^{31}P chemical shift from B to C and D indicated a complete coordination of all phosphorous atoms in the P_5 ring by CuBr for B-D, which is also found in the crystal structures of **3b** and **4b**. With eight eq. CuBr (see Figure 9.2f), a higher amount of D, a lower amount of B and only traces of C were observed (from the 1H integration: 40 % B, 4 % C and 56 % D).

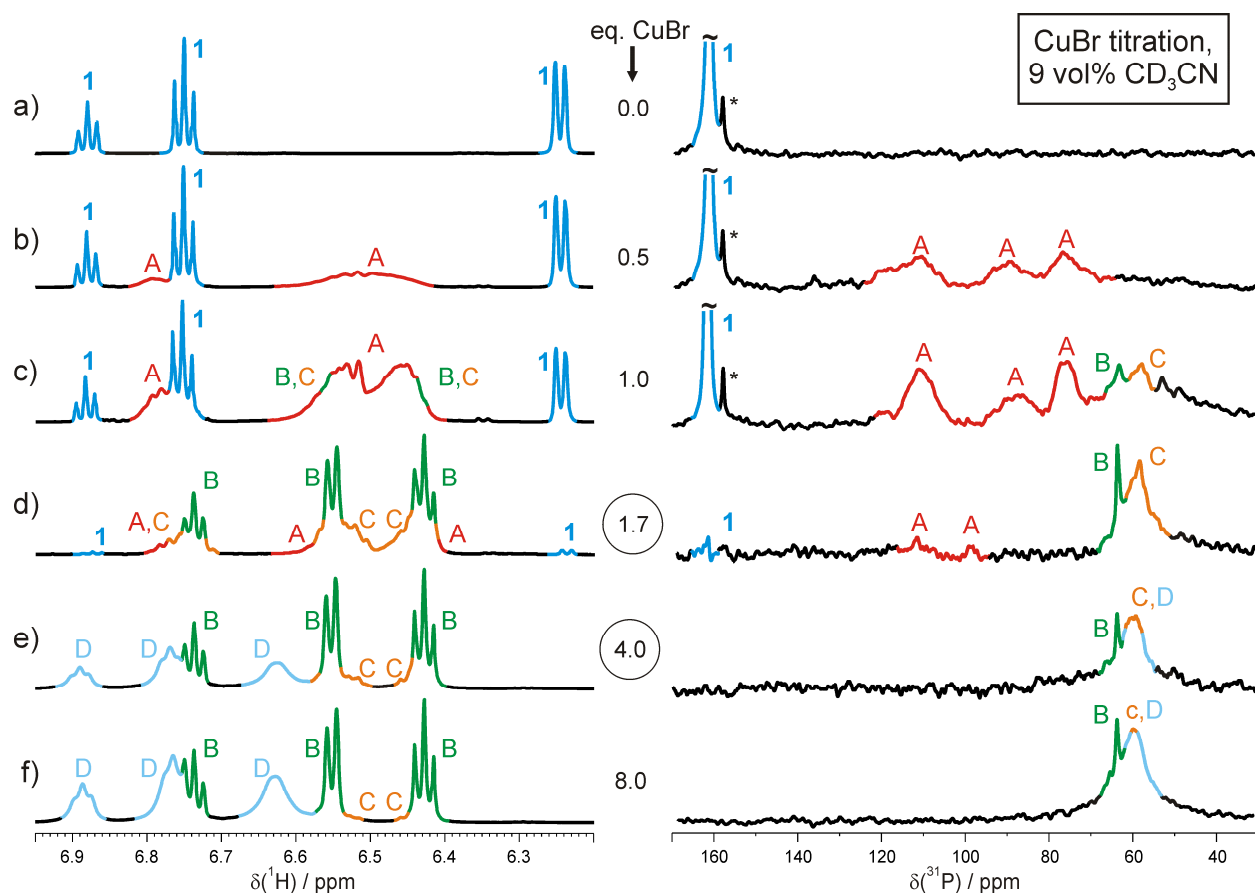


Figure 9.2: ^1H (left) and ^{31}P spectra (right) of samples containing **1** and increasing equivalents of CuBr: a) 0.0 eq., b) 0.5 eq., c) 1 eq., d) 1.7 eq., e) 4 eq., f) 8 eq., each in CD_2Cl_2 with 9 vol% CD_3CN . ^1H spectra at 298 K and 600 MHz, ^{31}P spectra at 300 K and 400 MHz.

Assignment of the different species

The different species A-D, detected by solution state NMR spectroscopy, were characterized with the help of their ^1H and ^{31}P line shapes and chemical shifts in combination with ^1H , ^1H -NOESY/ROESY and ^1H -DOSY experiments and were related to the different **2b/3b/4b** crystals: The species A was formed in the samples containing **1** and low amounts (0.5-1.7 eq.) of CuBr. The DOSY-derived hydrodynamic volume of A of $10.7 \pm 0.4 \cdot 10^3 \text{ \AA}^3$, averaged over all subspecies, was 15 times larger than of **1** ($0.7 \cdot 10^3 \text{ \AA}^3$) and $2.5 \cdot 10^3 \text{ \AA}^3$ smaller than the crystal-derived volume of $[\{\text{Cp}^{\text{Bn}}\text{Fe}(\eta^5\text{-P}_5)\}_{12}\{\text{CuBr}\}_{16 \pm x}]$ or $[\{\text{Cp}^{\text{Bn}}\text{Fe}(\eta^5\text{-P}_5)\}_{12}\{\text{CuBr}\}_{20}]$, $V_{\text{cryst}}(\textbf{2b/3b}) = 13.2 \cdot 10^3 \text{ \AA}^3$ (for details of the estimation of V_{cryst} see SI), which clearly indicated a supramolecular species (see Table 9.1). These results from the ^1H -DOSY experiments were verified by ^1H , ^1H -NOESY and ROESY experiments (for spectra see Figure 9.17 and Figure 9.18 in the SI). In the NOESY spectrum, the signals of **1** were in the extreme narrowing limit (negative sign of the cross peaks), indicating a fast reorientation typical for small molecules. In contrast, the signals of A were in the slow tumbling limit (positive cross peaks)

indicating a supramolecular assembly. Furthermore, exchange peaks between **1** and A were detected in the NOESY/ROESY spectra. These 2D NMR experiments revealed that all signals in the ^1H NMR spectra either correspond to monomeric **1** or to macromolecules with nearly the size of **2b/3b**, which demonstrated that the initial adducts of **1** and CuBr combined rapidly to spherical supramolecules. Due to the large deficit of CuBr compared to **1** and due to the line broadening of the ^1H and ^{31}P signals and due to the strong upfield shift of the ^{31}P chemical shifts induced by a CuBr coordination, the species A was assigned as supramolecule of **2b** type, in which the CuBr coordination sites are not fully occupied (the smaller volume of A compared to **2b/3b** might also hint at a missing of some of the $[\text{Cp}^{\text{Bn}}\text{Fe}(\eta^5\text{-P}_5)]$ units, too). Finally, the assignment of A as supramolecule of **2b** type was evidenced by the ^1H spectrum of dissolved **2b** crystals with approximately four CuBr disbondings (see Figure 9.4f), which shows the signals of A. This assembly was most probably stabilized by π -stacking interactions of the phenyl groups of neighboring $[\text{Cp}^{\text{Bn}}\text{Fe}(\eta^5\text{-P}_5)]$ units, which have been observed in the crystal structure of **3b**.^[17] In addition, the decreased diffusion coefficient of **1** in toluene- d_8 ($7.65 \pm 0.40 \cdot 10^{-10} \text{ m}^2 \text{ s}^{-1}$) compared to the one in CD_2Cl_2 ($10.69 \pm 0.13 \cdot 10^{-10} \text{ m}^2 \text{ s}^{-1}$) also indicated π -stacking interactions to the solvent toluene, which showed the high π -stacking ability of **1** in solution, too. These π - π interactions are supposed to have a significant contribution to the ball formation (with Cp^* instead of Cp^{Bn} , polymeric products are thermodynamically favored^[9, 14-15]) and could partially compensate the reduced stabilization of the structure by the incomplete CuBr scaffold.^[17]

The species B was present in all samples with one equivalent of CuBr or beyond. In contrast to A, B showed sharp proton signals with a distinct multiplet pattern in the ^1H spectra and just one very sharp singlet at 63.80 ppm in the ^{31}P spectra, which indicated the chemical equivalence of all phosphorous atoms in one single species. Furthermore, its DOSY-derived hydrodynamic volume of $12.1 \pm 0.4 \cdot 10^3 \text{ \AA}^3$ was very similar to the crystal-derived volume of **3b** ($V_{\text{cryst}}(\text{2b/3b}) = 13.2 \cdot 10^3 \text{ \AA}^3$, see Table 9.1). Therefore, B was assigned as complete “perfect” **3b** supramolecule without disbondings, in which all coordination sites are occupied by **1** and CuBr, respectively. Furthermore, the comparison of the ^1H chemical shifts of **1**, A and B confirms the assignment of A as **2b** cluster comprising a minimum amount of Cu^{I} halides in its scaffold and of B as complete **3b** container molecule: The CuBr coordination in A and B led to a downfield shift of the methylene and ortho protons and upfield shift of the meta and para protons of A and B compared to the monomer **1**, for instance, the chemical shift of the para proton was 6.88 ppm for **1**, 6.80 ppm for A and 6.75 ppm for B. This finding, that the chemical shifts of A were in between the fully CuBr-occupied B and the monomer, was observed for all protons of A and

confirmed the assignments of A and B. In addition, these assignments were also confirmed in the ^{31}P spectra, where a strong upfield shift of more than 40 ppm from **1** (161.29 ppm) to the different species of A (65-125 ppm) and to the sharp singlet of B at 63.80 ppm was observed. Finally, the assignment of B as supramolecule of **3b** type was evidenced by the ^1H spectrum of dissolved **3b** crystals (see Figure 9.4g), which shows mainly the signals of B beside low amounts of A and C.

Table 9.1: Diffusion coefficients and hydrodynamic volumes inclusive their standard deviations of the different species in CD_2Cl_2 at 298/300 K and 600 MHz.

Species	$D / 10^{-10} \text{ m}^2 \text{ s}^{-1}$	$V_H / 10^3 \text{ \AA}^3$
1	10.69 ± 0.13	0.7 ± 0.1
A ^[a]	3.98 ± 0.05	10.7 ± 0.4
B	3.81 ± 0.02	12.1 ± 0.2
C	4.20 ± 0.14	9.2 ± 0.6
D	3.49 ± 0.03	15.6 ± 0.4

[a] average of all subspecies. From crystallographic data the volumes of **1**, **2b/3b** and **4b** were estimated to be

$$V_{\text{cryst}}(\mathbf{1}) = 0.6 \cdot 10^3 \text{ \AA}^3, V_{\text{cryst}}(\mathbf{2b/3b}) = 13.2 \cdot 10^3 \text{ \AA}^3 \text{ and } V_{\text{cryst}}(\mathbf{4b}) = 17.5 \cdot 10^3 \text{ \AA}^3.$$

Within this series depicted in Figure 9.2 the species C was present in the samples with one eq. CuBr or higher with a maximum amount of C at 1.7 eq. CuBr. It showed ^1H chemical shifts, which were very similar to A and B and its ^{31}P chemical shift was further upfield shifted about 5.88 ppm compared to B, originating from a all-phosphorous coordination and/or a different structural scaffold. Its hydrodynamic volume of $9.2 \pm 0.6 \cdot 10^3 \text{ \AA}^3$ was smaller compared to B. Therefore, C could be assigned as a relatively large rudiment of the **3b** supramolecule, which most probably possesses less **1** and additional CuBr in the scaffold compared to B, which can be rationalized by the high amount of CuBr in solution. One possible very speculative hypothesis about the structure of this species might be a replacement of some of the $[\text{Cp}^{\text{Bn}}\text{Fe}(\eta^5\text{-P}_5)]$ units in the core scaffold by $(\text{CuBr})_n$ clusters, as found in the **4b** crystals. This arrangement might therefore be assigned as structural intermediate between the **3b** and **4b** supramolecules. Its most probably reduced thermodynamic stability might be responsible for the preferred crystallization of the **3b** and **4b** supramolecules. This hypothesis about the structure would be in agreement with the reduced hydrodynamic volume compared to B, the upfield shift of the ^{31}P chemical shift indicating a variation in the scaffold. Furthermore, the transformation of B into C might be also indicated by the major appearance of C at 1.7 eq. CuBr, which promoted the highest amount of B in this series and, thus, the highest amount of its rudiment C.

In the series depicted in Figure 9.2 the species D was formed in samples with a CuBr content of four equivalents or beyond, that means starting with a molar **1**:CuBr ratio of 12:48, which is in the range of the **4b** crystals. The hydrodynamic volume of D of $15.6 \cdot 10^3 \text{ \AA}^3$ was only slightly smaller than the crystal-derived volume of $[\{\text{Cp}^{\text{Bn}}\text{Fe}(\eta^5\text{-P}_5)\}_{12}\{\text{CuBr}\}_{48 \pm x}]$, $V_{\text{cryst}}(\mathbf{4b}) = 17.5 \cdot 10^3 \text{ \AA}^3$, which ruled out the small **3b** cluster and hinted at the large **4b** supramolecule (see Table 9.1). In addition, during some of the NMR experiments **3b** and **4b** crystals were formed inside the NMR tube in a similar ratio as found for B and D in solution. Furthermore, its ^{31}P chemical shift of 59.8 ppm was further upfield shifted compared to B, following the general trend observed for **1**, A, B and C of smaller ^{31}P chemical shifts at higher copper content. All aromatic protons of D are shifted downfield by 0.15-0.20 ppm compared to B, which is not in analogy to the trends observed for the protons of **1**, A and B and might indicate difference in the scaffolds of the **2b/3b** and the **4b** supramolecules. In addition, the broad lines of D in the ^1H and ^{31}P spectrum indicate exchange processes and/or overlay of signals with similar chemical shifts. These NMR findings of D strongly hinted at the **4b** cluster and this assignment was confirmed by X-ray analysis of the scaffold of **4b**: All phosphorous atoms are coordinated by CuBr, but the assembly between the P_5 rings can be either a single CuBr or a $(\text{CuBr})_n$ cluster (for the core scaffolds of the clusters see Figure 9.3). This leads to similar, but not identical coordinated phosphorous atoms and thus to similar ^1H and ^{31}P signals. The overlay and probably exchange of these signals leads to only one broad ^{31}P signal and broad ^1H signals observable for D. Thus, all experimental findings for D are in agreement with the assignment of D as a supramolecule of **4b** type.

For an overview of the species characterized by solution state NMR and X-ray analysis see Figure 9.3. There, the X-ray derived core scaffolds of the supramolecular structures of the different clusters are shown.

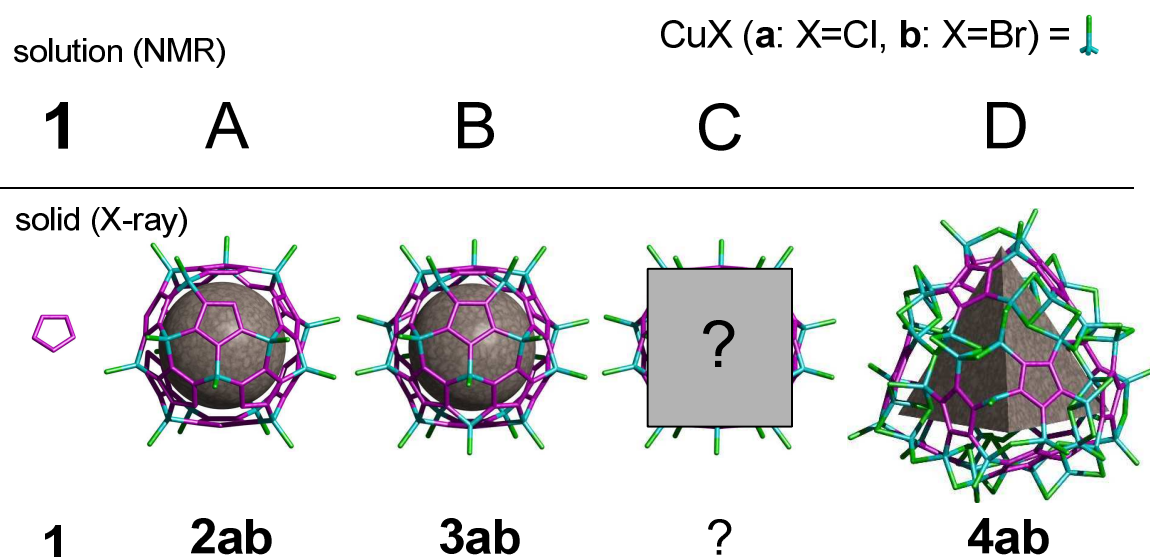


Figure 9.3: Overview of the species characterized by solution state NMR and X-ray analysis. The X-ray-derived core scaffolds of the supramolecular structures of the different clusters are shown.

Acetonitrile-free preparation

The assignment of the different species was further confirmed with experiments in pure CD_2Cl_2 with varying reaction time. In addition, the time-dependent appearance of the different species provides an insight into the formation pathway of the supramolecules. In order to decrease the formation and exchange rates, these experiments were conducted in pure CD_2Cl_2 , which drastically reduced the amount of CuX in solution. Despite the missing formation of CuX-MeCN adducts providing good solubility for CuX ($\text{X} = \text{Cl}, \text{Br}$) in CD_2Cl_2 , the presence of six eq. CuX would in principle allow for a potential formation of the species D, the supramolecule of **4b** type. The resulting ^1H and ^{31}P spectra were recorded after stirring a solution of **1** over solid CuBr over two hours and one, two, five and ten days and subsequent filtration, whereby the reaction was stopped due to removal of the CuBr source, are shown in Figure 9.4a-e. The corresponding spectra with CuCl can be found in Figure 9.19 in the SI, but due to the similarity of the spectra, only the experiments with CuBr are described in detail.

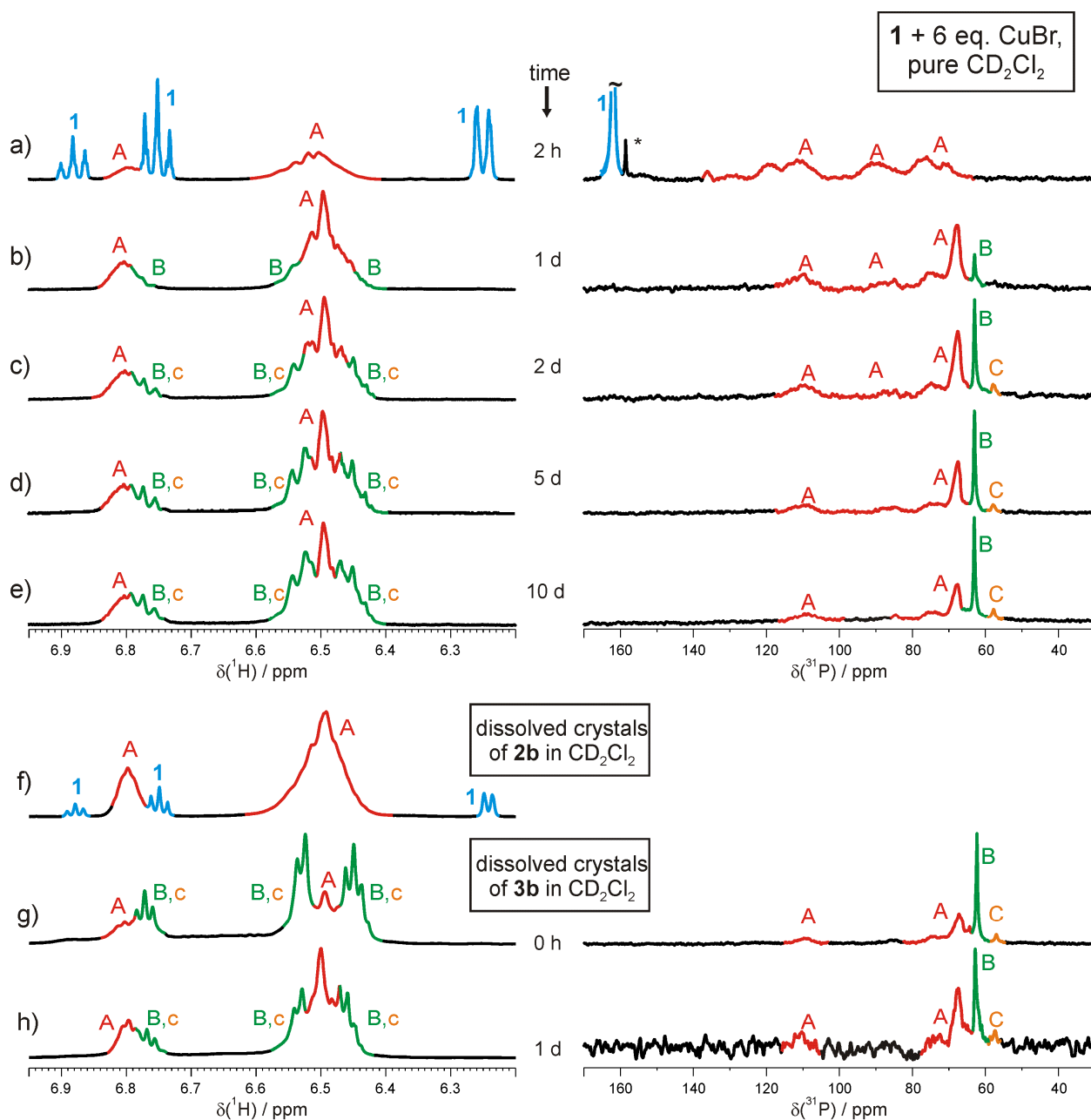


Figure 9.4: ^1H (left) and ^{31}P spectra (right) of samples containing **1** and six equivalents of CuBr in pure CD_2Cl_2 after a reaction time of a) 2 h, b) 1 d, c) 2 d, d) 5 d, e) 10 d, each at 300 K and 400 MHz and dissolved crystals of e) **2b** and g) **3b** and h) **3b** after 1 d in solution, each at 300 K and 600 MHz in pure CD_2Cl_2 .

After two hours (see Figure 9.4a), beside **1** exclusively A was detected with nearly equal population of the different sub species of A in the range of 65–125 ppm in the ^{31}P spectrum. No oligomeric building blocks were formed. After a stirring time of one day (see Figure 9.4b), **1** was complete consumed and the amount of A, especially the amount of the subspecies with the highest copper content increased (indicated by the high amount of the signal with the ^{31}P chemical shift of 67.8 ppm). In addition, a small sharp signal at 63.0 ppm was detected,

indicating the formation of small amounts of B (in CD_2Cl_2 with 9 vol% CD_3CN , this signal is at 63.8 ppm). After two days (see Figure 9.4c) the amount of B was further increased at the expense of A and small quantities of C were formed. These trends were further continued with longer reaction times (see Figure 9.4d and e), but the ^1H and ^{31}P spectra after ten days were very similar those after two days. The species D, which has the highest CuBr demand of all supramolecules, was not formed in pure CD_2Cl_2 , even after ten days.

These experiments indicated that the initially formed adducts rapidly assembly to supramolecule A. The further implementation of CuBr into A to form B is rather slow. This thermodynamically favored, but probably without CD_3CN kinetically/sterically hindered formation of B might be attributed to the extremely crowded organic shell of the A and B supramolecules due the Cp^{Bn} ligands, which provide an effective steric shielding of the core scaffold.^[17] These results are in agreement with the behavior of a sample of dissolved pure **3b** crystals in CD_2Cl_2 (the purity was tested by X-ray crystallography before dissolving and exclusively **3b** and no **2b** fractions due to disbondings in the scaffold were detected). Upon dissolving (see Figure 9.4g), beside B, small amounts of A and C are formed rapidly in solution, indicating that from some of the **3b** crystals CuBr is released to form A and the released CuBr might be incorporated in other molecule of B to form small amounts of C. After one day in solution (see Figure 9.4h), a further increase of the amount of A was detected. These experiments demonstrated, that it is possible to crystallize pure **3b** crystals without disbondings, but dissolving of the isolated **3b** crystals always leads to a partial disproportion of B into A and C in pure CD_2Cl_2 .

Acetonitrile titrations

The influence of acetonitrile on the formation of B-D and exchange between the supramolecules was investigated by means of ^1H and ^{31}P spectra with samples of dissolved **3b** crystals in CD_2Cl_2 and increasing amounts of CD_3CN from 0 to 25 vol% (see Figure 9.5). Without CD_3CN (see Figure 9.5a) distinct signals for B with a sharp signal at 63.8 ppm in the ^{31}P spectrum were detected, which is in analogy to the experiments above. Beside B, small amounts of A and C were detected. Upon the addition of four vol% CD_3CN (see Figure 9.5b), the relative amount of A decreased, while the relative amounts of B and C increased. In addition, small amounts of **1** and a line broadening of the signals in the ^{31}P spectrum was observed. A further increase of the CD_3CN content up to nine vol% and beyond (see Figure 9.5c-e) led to the vanishing of the sharp ^{31}P signals of B and C and instead only one very broad signal was observed for B and C in the ^{31}P spectrum. In the ^1H spectrum, the signals of A, B and C were

still observable. Furthermore, upon the increase of the CD_3CN content to nine vol% or beyond the amount of **1** further increased and the amount of A now slightly increased again, indicating a decomposition of the supramolecules at higher amounts of acetonitrile.

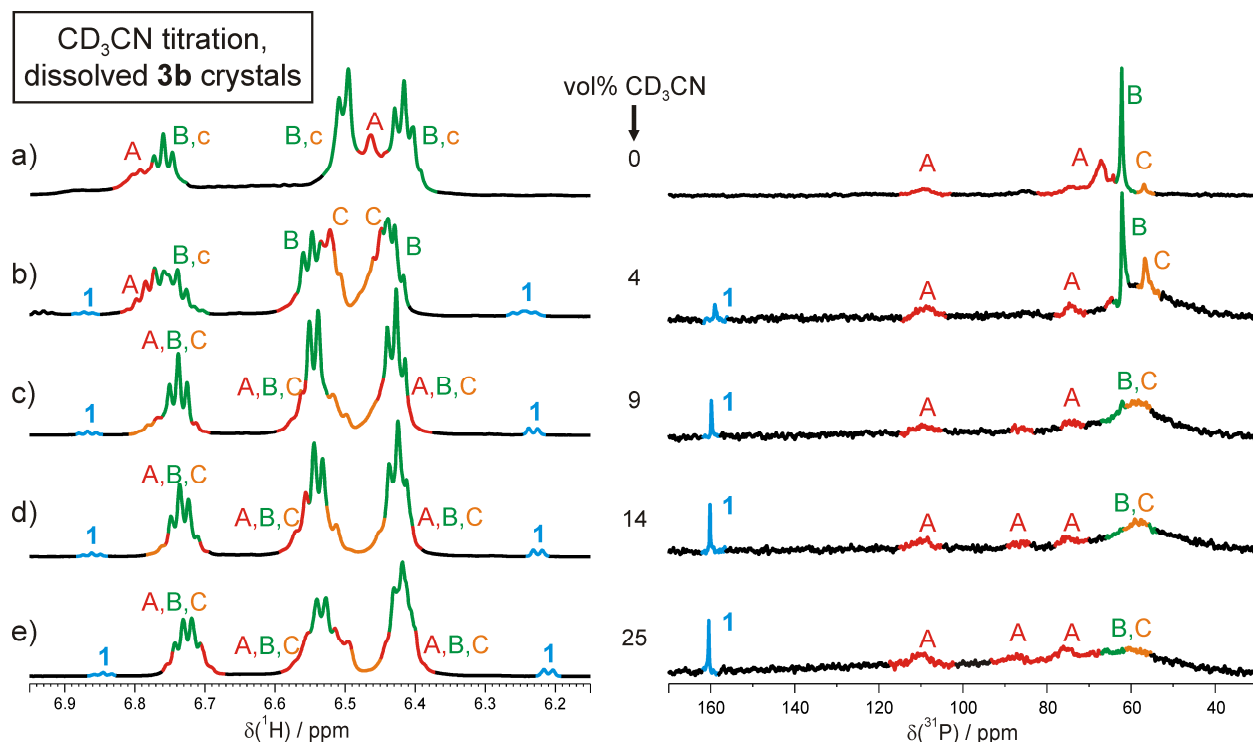


Figure 9.5: ^1H (left) and ^{31}P spectra (right) of samples containing **1** and 1.7 eq. CuBr in CD_2Cl_2 with increasing vol% of CD_3CN : a) 0 vol%, b) 4 vol%, c) 9 vol%, d) 14 vol%, e) 25 vol%, each at 298 K and 600 MHz.

These observations confirmed the assignment of the different species, allowed insight into the formation/decomposition and clarified the role of CD_3CN : Without CD_3CN , coexisting A, B and C showed sharp lines, indicating, that exchange between these species was mainly suppressed. The addition of CD_3CN leads to higher mobility of CuBr in solution and therefore most probably to pronounced exchange between B and C (due to the high structural similarity of A and B, an exchange of A and B is also supposed, but the overall large line widths of A impeded the detection of the supposed exchange broadening for A). Upon a further increase of CD_3CN on the one hand a release of CuBr from the scaffold of B is indicated, leading to an increase of A and also to a release of **1** and on the other hand the incorporation of CuBr into another fraction of B leads to C. Upon the decomposition process of B, no oligomeric buildings blocks were observed. As expected, species D, which possessed the highest CuBr demand, was not observed due to the low CuBr content of 1.7 equivalents.

Furthermore, the influence of CD_3CN was also investigated in a CuBr titration similar to the one depicted in Figure 9.2 but with 14 instead of 9 vol% CD_3CN in CD_2Cl_2 (see Figure 9.16 in the SI). There, the exchange broadening of the signals due to the presence of CD_3CN was also observed.

In addition, a CD_3CN titration with dissolved crystals of **4b** was also performed to further confirm the role of acetonitrile and to elucidate the appropriate conditions for the selective formation of the species D. There, similar observations have been made in the ^1H spectra (see Figure 9.6, no ^{31}P spectra have been measured here) as for the dissolved **3b** crystals:

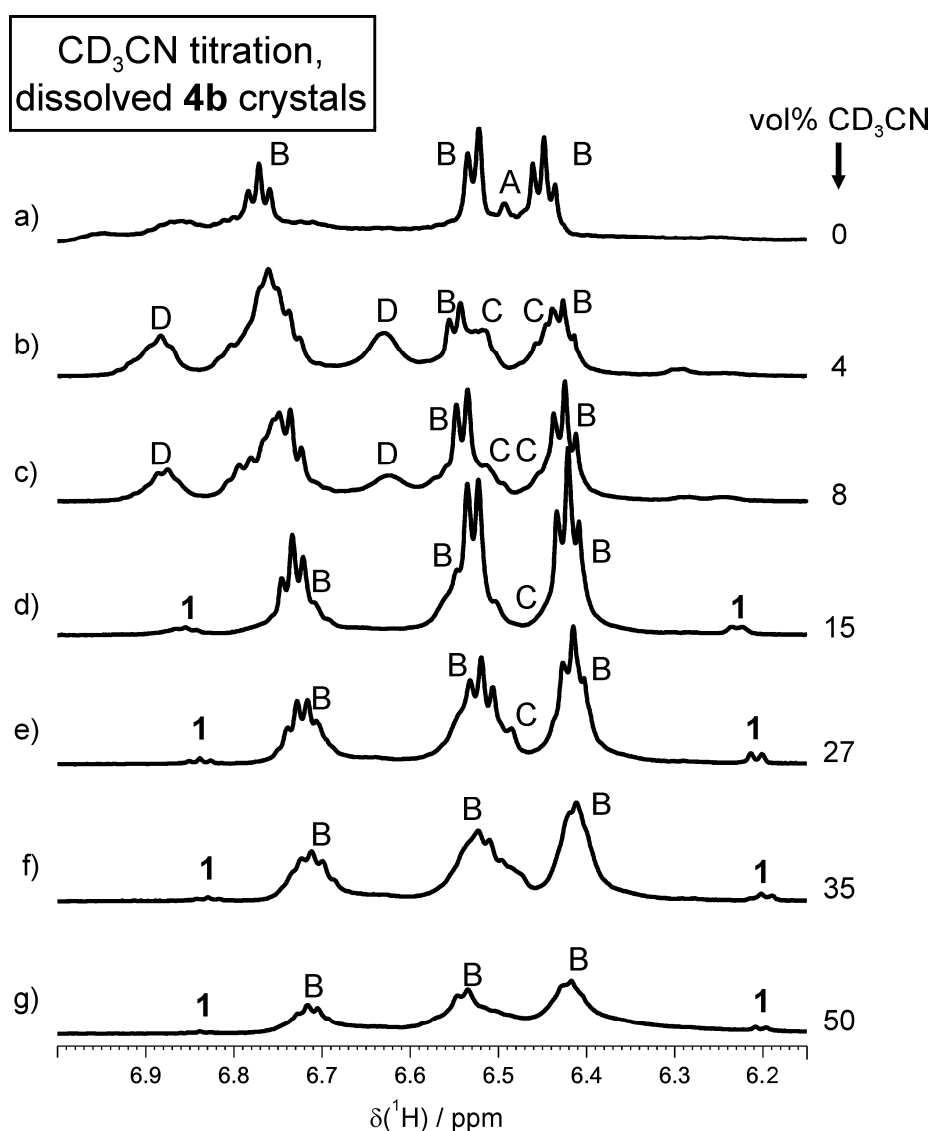


Figure 9.6: ^1H spectra of dissolved **4b** crystals in CD_2Cl_2 with increasing vol% of CD_3CN : a) 0 vol%, b) 4 vol%, c) 8 vol%, d) 15 vol%, e) 27 vol%, f) 35 vol%, g) 50 vol%, each at 298 K and 600 MHz.

Without CD₃CN, several signals in the aromatic region and a relative high amount of B were detected, indicating a fragmentation of D in pure CD₂Cl₂. Upon the addition of four vol% CD₃CN, high amounts of D (and C) were detected (29 % B, 27 % C, 44 % D), indicating the re-assembling of D. At higher contents of CD₃CN, the amount of D and C was reduced again in support of B (54 % B, 16 % C, 29 % D at eight vol% CD₃CN, see Figure 9.6c). In addition, low amounts of **1** were detected (e.g. its dublet at 6.2 ppm was clearly visible at 15-50 vol% CD₃CN). At 15 vol% CD₃CN, only traces of D were present. At 35 and 50 vol% of CD₃CN, the spectral quality was very poor. However, beside the signals of B and **1** also A and C might be indicated.

This CD₃CN titration with dissolved crystals of **4b** shows that low amounts (4-8 vol%) of acetonitrile are a absolute prerequisite to avoid fragmentation and to form the species D, which is in agreement with the acetonitrile-free experiments reported above. In contrast, at higher CD₃CN contents the CuBr is released from the scaffold, most probably due to the competing effect of MeCN-CuBr adducts, which leads to the decomposition of D accompanied with the formation of B. At further increased CD₃CN content B is disintegrated, too. This is in agreement with the decomposition of B in the CD₃CN titration of the dissolved **3b** crystals (see Figure 9.5).

To conclude, the appropriate solvent mixture is absolutely crucial for the directed formation of the supramolecules. Furthermore, the preferred formation of different supramolecules in different solvent mixtures provides the potential to purposefully switch between the different supramolecules. In addition, the knowledge about the different stabilizing/destabilizing effects of the distinct solvents in the applied concentration ranges provides the potential for a further improvement of the non-covalent synthesis of supramolecules in general.

Encapsulation of guest molecules

The design and synthesis of nanoscale self-assembling molecular containers with defined sizes and inner cavities is attracting considerable interest in current chemistry.^[1-6] In this context, the combination of copper (I) halides with the *cyclo*-P₅ complex [Cp*Fe(η^5 -P₅)] (Cp* = η^5 -C₅Me₅) or the *cyclo*-P₄ complex [Cp''Ta(CO)₂(η^4 -P₄)] (Cp'' = η^5 -C₅H₃tBu₂) provided a powerful tool for the synthesis of inorganic shell structures with fullerene-type topology.^[7-13] These container molecules were used to encapsulate guest molecules like *o*-carboranes^[11] or C₆₀ fullerenes,^[10] whereby the shape of the inorganic host was controlled by the size of the corresponding template. And even without additional guest molecule the *cyclo*-P₅ complex [Cp*Fe(η^5 -P₅)] itself acts as template for the formation of spherical supramolecules^[8, 12-13] or

nanosized capsules.^[9] However, all of these host-guest compounds based on $[\text{Cp}^*\text{Fe}(\eta^5\text{-P}_5)]$ showed very low solubility and their formation was depending on the encapsulated template. In contrast, **1** and CuX ($\text{X} = \text{Cl}, \text{Br}$) formed soluble, nanometer-sized supramolecules, which were readily accessible by quantitative self-assembly and their formation was not depending on template control. Therefore, these supramolecules seemed ideal for the use as nanometer-sized containers and, thus, the incorporation of several guests was studied.

To be incorporated, potential guests must have the appropriate size to fit into the inner cavity of **2b/3b** with an inner diameter of 0.82 nm or into the larger inner cavity of **4b** (X-ray analysis was not completed so far, thus, an exact inner diameter cannot be stated). In addition, to maximize the non-covalent interactions between host and guest, the shape of the compound should be similar to the shape of the inner cavity of the container molecules. For a good detectability of the guest signals beside the intense host signals (e.g. for B 120 protons contribute to the methylene signal), compounds possessing a singlet should be used to avoid intensity distribution due to multiplet splitting. For this purpose, P_4 (outer diameter: 0.47 nm^[22]) and ferrocene (outer diameter: 0.57 nm^[23]) were selected, which additionally have the advantage of a high number of magnetically equivalent protons or phosphorous atoms contributing to a singlet. In addition, the tetrahedral P_4 resembles the tetrahedral shape of the inner cavity of the **4b** supramolecule and the more globular ferrocene resembles the globular shape of the inner cavity of the **2b/3b** supramolecules (see Figure 9.3 or Figure 9.12 for the core scaffolds of the container molecules). These compounds were added under similar experimental conditions that had been successfully applied for the formation of B-D (**1** and two eq. CuBr in CD_2Cl_2 with 1-2 vol% CD_3CN). In addition, the behavior of A to act as host was also studied under similar experimental conditions that had been successfully applied for the formation of A (stirring of **1** over three equivalents of solid CuBr in CD_2Cl_2 without CD_3CN for one hour and then filtration to remove the residual solid CuBr).

Due to the strong shielding by the globular host, the incorporation of a guest should be indicated by an upfield shift of the signal of an encased molecule compared to the free compound, which was observed for the encapsulation of *o*-carborane (5 ppm in the $^{11}\text{B}\{^1\text{H}\}$ -MAS spectrum)^[24] and of C_{60} fullerene (3 ppm in the ^{13}C spectrum).^[25] In addition, host and guest must have the same diffusion coefficient and proton containing guests should show NOESY cross peaks to the host. In principle, TMS (added as internal viscosity standard), CD_3CN , CD_2Cl_2 , P_4 or ferrocene could be incorporated in the container molecules, but incorporated solvent or TMS molecules were not detected in previous control experiments, although an encapsulation of CD_2Cl_2 inside **3b** crystals was supposed from X-ray analysis. This

might be attributed to the expected low signal intensities of such incorporated solvents, since perdeuterated solvents with a high degree of deuteration (99.8 % or higher) were used. Furthermore, the ^1H signal intensities of the non-perdeuterated fraction of CHD_2CN and CHDCl_2 are distributed over their multiplet fine structure.

As expected, in both samples, which contained only **1**, A and P_4 or ferrocene, an incorporation of a guest was not detected, which was in agreement with the assignment of A as supramolecular species of **2b** type, in which some coordination sites are unoccupied and therefore impeded the permanent encapsulation of a guest.

In the two other samples, the addition of 1-2 vol% CD_3CN to the reaction mixture promoted the formation of B-D similar to the previous experiments (see Table 9.2). In the $\text{CD}_2\text{Cl}_2/\text{CD}_3\text{CN}$ sample with ferrocene, beside the singlet of free ferrocene at 4.15 ppm, a small singlet at 0.66 ppm could be detected in the ^1H spectrum (see Figure 9.7b), which possessed the same diffusion value of $3.76 \cdot 10^{-10} \text{ m}^2 \text{ s}^{-1}$ as B. (In addition, tiny signal at 0.31 and 0.13 ppm were detected, but their intensities were too small for further studies). Its upfield shift of 3.49 ppm compared to the free ferrocene was in the same range as observed for the encapsulation of *o*-carborane and C_{60} in similar pentaphosphaferrocene-derived capsules.^[24-25] The inclusion of ferrocene inside B was corroborated by a NOESY spectrum, in which a NOE cross peak from the singlet at 0.66 ppm to the methylene protons of B could be detected (see Figure 9.7c). Since no cross peak to the aromatic protons of B were observed, an attachment at the surface of B can be clearly excluded. No cross peaks from 0.66 ppm to the signals of C or D were observed. Furthermore, no exchange peak from the signal of encapsulated ferrocene to the signal of free ferrocene at 4.15 ppm was detected, confirming the permanent inclusion inside B. To conclude, the upfield shift of the signal, its diffusion value and its NOESY cross peak to the methylene protons of B showed clearly the enduring encapsulation of ferrocene inside B (from the ^1H integral ratio: $\text{Cp}_2\text{Fe}@B$ in 14 % of all B).

Table 9.2: Relative amounts of B, C and D in the sample containing **1** and two eq. CuBr in CD_2Cl_2 with 1-2 vol% CD_3CN .

Additive	Relative amounts / %		
	B	C	D
---	42	42	17
P_4	80	4	16
ferrocene	57	14	29

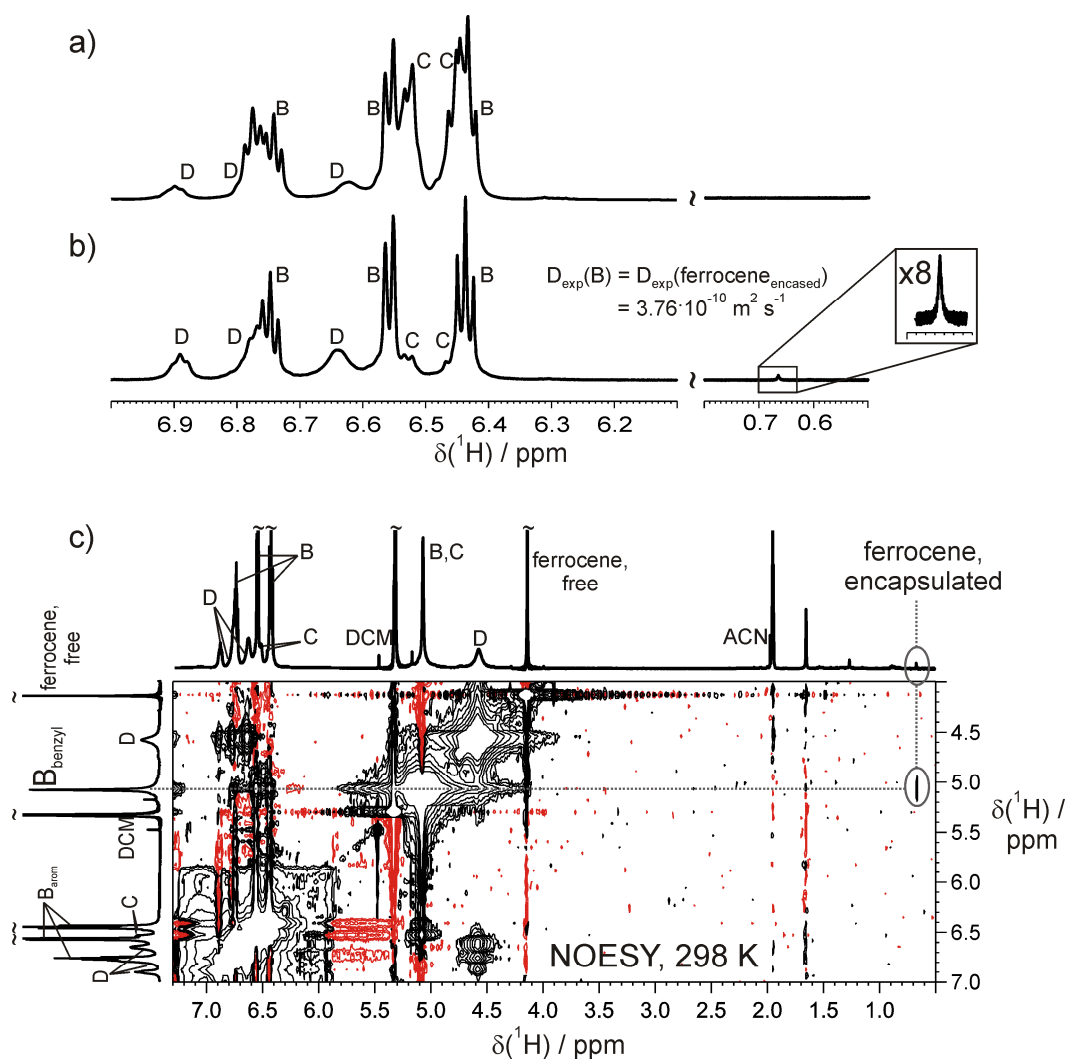


Figure 9.7: ^1H spectra of **1** + two eq. CuBr in $\text{CD}_2\text{Cl}_2/\text{CD}_3\text{CN}$ samples a) without and b) with ferrocene. c) NOESY spectrum (mixing time 350 ms) of **1** + two eq. CuBr in $\text{CD}_2\text{Cl}_2/\text{CD}_3\text{CN}$ sample with ferrocene, each at 298 K and 600 MHz. The complete NOESY spectrum is depicted in Figure 9.21 in the SI.

In contrast to ferrocene, no signals of an encapsulated P_4 were detected in the ^{31}P chemical shift range of +250 to -1300 ppm (free P_4 : -523.43 ppm). One possibility to explain the non-incorporation of P_4 (in contrast to ferrocene) inside **B** might be the reduced non-covalent interactions due to the different shapes of the tetrahedral P_4 and the globular inner cavity of the **3b** supramolecule, but also other aspects should be considered and further investigated.

Supramolecular switch

The rapid formation of the different species in the presence of low amounts of CD₃CN indicated that there is no kinetic hindrance for their transformation, but that the clusters represent different thermodynamic minima, which are separated by a relatively low energetic barrier. This thermodynamic equilibrium of the different supramolecules in solution was successfully manipulated by a variation of the CuBr content and of the solvent mixture (data not shown). In addition, a successful incorporation of ferrocene demonstrated the potential of these supramolecular assemblies to act as host-guest systems. Stimulated by these amazing results we investigated their potential to act as supramolecular switch. In addition, with ferrocene as guest, the potential in- and exclusion of guests was elucidated.

For this purpose, similar experimental conditions, which were successfully used for the incorporation of ferrocene (**1**, 2.0 eq. CuBr, 0.25 eq. ferrocene in CD₂Cl₂ with ca. 1 vol% CD₃CN stirred for several hours) were applied. In this setup, a potential crystallization of one of the supramolecules and, thus, potential shift of the thermodynamic equilibrium was avoided by the use of relatively low concentrations and could be finally excluded by the use of an external NMR standard. Therefore, all changes in the relative amounts of the supramolecules are clearly attributable to a transformation of the clusters into one another. In order to switch between the different container molecules (from C, D to B), the content of acetonitrile was increased up to 33 %, similar to the CD₃CN titration before. Then, in order to demonstrate the reversibility of this transformation, the CD₃CN/CD₂Cl₂ ratio was reduced again by the addition of CD₂Cl₂. Furthermore, in order to elucidate the reversibility of the whole system (including monomeric **1** and A) an excess of **1** was added to decompose the clusters and subsequently solid CuBr was added to elucidate the re-formation of the clusters. With these experiments the potential of the container molecules derived from **1** and CuX (X=Br, Cl) to act as supramolecular switches was investigated. The different states of the system were monitored by ¹H spectra (see Figure 9.8) and are described in the following:

With one vol% CD₃CN, the formation of the supramolecules B-D is favored and in the ¹H spectra as expected a very high amount of C was detected besides B and D (26 % B, 59 % C, 15 % D, derived from the ¹H spectrum.⁵ See Figure 9.9 for a graphical overview of the relative amounts of B and C in all samples). In addition, three small singlets at 0.66, 0.31 and 0.13 ppm

⁵ For a reliable integration of the partially overlapping ¹H signals, several different window functions were applied and the integration results were compared to each other. Thereby, the remaining error range of the integration could be estimated to be 10-20 % depending on the spectral quality. The obtained ¹H integral ratios are summarized for all samples of the switching experiment in Table 9.4. From these values, the relative amounts of B-D and Cp₂Fe@B and Cp₂Fe@C, depicted in Figure 9.9 - Figure 9.11, were calculated.

were detected. Outside this chemical shift range very intense signals are present in the ^1H spectrum originating from TMS and grease-like compounds, which might have impeded the detection of other small signals in this chemical shift range. The singlet at 0.66 ppm was again identified by its characteristic ^1H chemical shift, its diffusion coefficient (which was the same as for B) and by a NOESY spectrum to be an incorporated ferrocene inside 16 % of B, which is in excellent agreement with the host-guest experiments before (there: $\text{Cp}_2\text{Fe@B}$ in 14 % of B). The NOESY spectrum was measured at 18 vol% of CD_3CN , which provided a relatively high amount of $\text{Cp}_2\text{Fe@B}$ and allowed an easy detection of the NOE peak from the methylene protons of B to the signal at 0.66 ppm. But at this CD_3CN content both signals at 0.31 and 0.13 ppm were not present any more in the ^1H spectrum and therefore no information about these signals could be gained from the NOESY spectrum. However, the two other singlets at 0.31 and 0.13 ppm showed the same diffusion coefficient as C and slightly larger upfield shifts compared to free ferrocene as observed for $\text{Cp}_2\text{Fe@B}$ and were therefore identified as two different ferrocene molecules, which are encased by the supramolecule C (see Figure 9.10 for an graphical overview of the relative amounts of $\text{Cp}_2\text{Fe@B}$ and $\text{Cp}_2\text{Fe@C}$ in all samples). The small ^1H chemical shift difference of 0.18 ppm between these two host-guest compounds might indicate two different orientations of the ferrocene molecules inside C. Under the assumption, that C has less than 12 $[\text{Cp}^{\text{Bn}}\text{Fe}(\eta^5\text{-P}_5)]$ units in its scaffold, more than 42 % of C carry ferrocene. Upon the addition two vol% CD_3CN , the amount of C decreased and the amount of B increased, indicating that C was transformed into B. Simultaneously, the fraction of ferrocene incorporated in C was reduced in support of ferrocene incorporated in B. Upon the addition of CuBr , also a shift of the relative fractions from C to B and at the same time from $\text{Cp}_2\text{Fe@C}$ to $\text{Cp}_2\text{Fe@B}$ was observed. This was further continued up to a CD_3CN content of 17 %, where approximately no C and no $\text{Cp}_2\text{Fe@C}$ was detected. This was connected with a very high percentage of ferrocene carrying supramolecules B (36 % of all B). Upon a further increase of the CD_3CN content up to 33 vol%, a reduction of the intensity of the signal at 0.66 ppm was observed. This might indicate a partial release of some of the $\text{Cp}_2\text{Fe@B}$ from their hosts B due to the accelerated mobility of CuBr , which is in agreement with the observed partial decomposition of the supramolecules at high CD_3CN contents (see Figure 9.5 and Figure 9.6).

Upon a reduction of the CD_3CN content back to 18 vol%, the amount of $\text{Cp}_2\text{Fe@B}$ was increased again and nearly reached the previous value at 17 vol% CD_3CN (28 % vs. 36 %), indicating the re-formation of some of the supramolecules B. A further reduction of the CD_3CN content to three vol% by the addition of the fivefold amount of CD_2Cl_2 led to the formation of nearly pure B and to a further increase of $\text{Cp}_2\text{Fe@B}$ to 48 % of all B. However, the solely

formation of B (instead of a mixture of B, C and D as observed at the beginning of this series) might be attributed to the high dilution of the sample. Due to the high amount of nearly 50 % of ferrocene carrying B this sample was ideal to confirm the purposefully exclusion of the guest from the container molecules by the addition of **1**. Indeed, as expected from previous inclusion experiments, a complete release of ferrocene from all assemblies was observed, as indicated by the vanishing of the signal at 0.66 ppm. To “reload” the system and to test the hypothesis, that the high dilution was responsible for the solely formation of B at three vol% CD₃CN, CuBr was added to the sample. Now, similar amounts of B-D compared to the (concentrated) solution at three vol% CD₃CN at the beginning of the switching experiment were observed. This confirmed the hypothesis, that the low concentration was responsible for the solely formation of B before (this finding might be useful for the improvement of the directed synthesis of B). In addition, the two singlets at 0.31 and 0.13 ppm also re-appeared (with 17 and 13 %, respectively, of their signal intensities compared to the starting values) indicating the re-incorporation of ferrocene molecules in the supramolecule C.

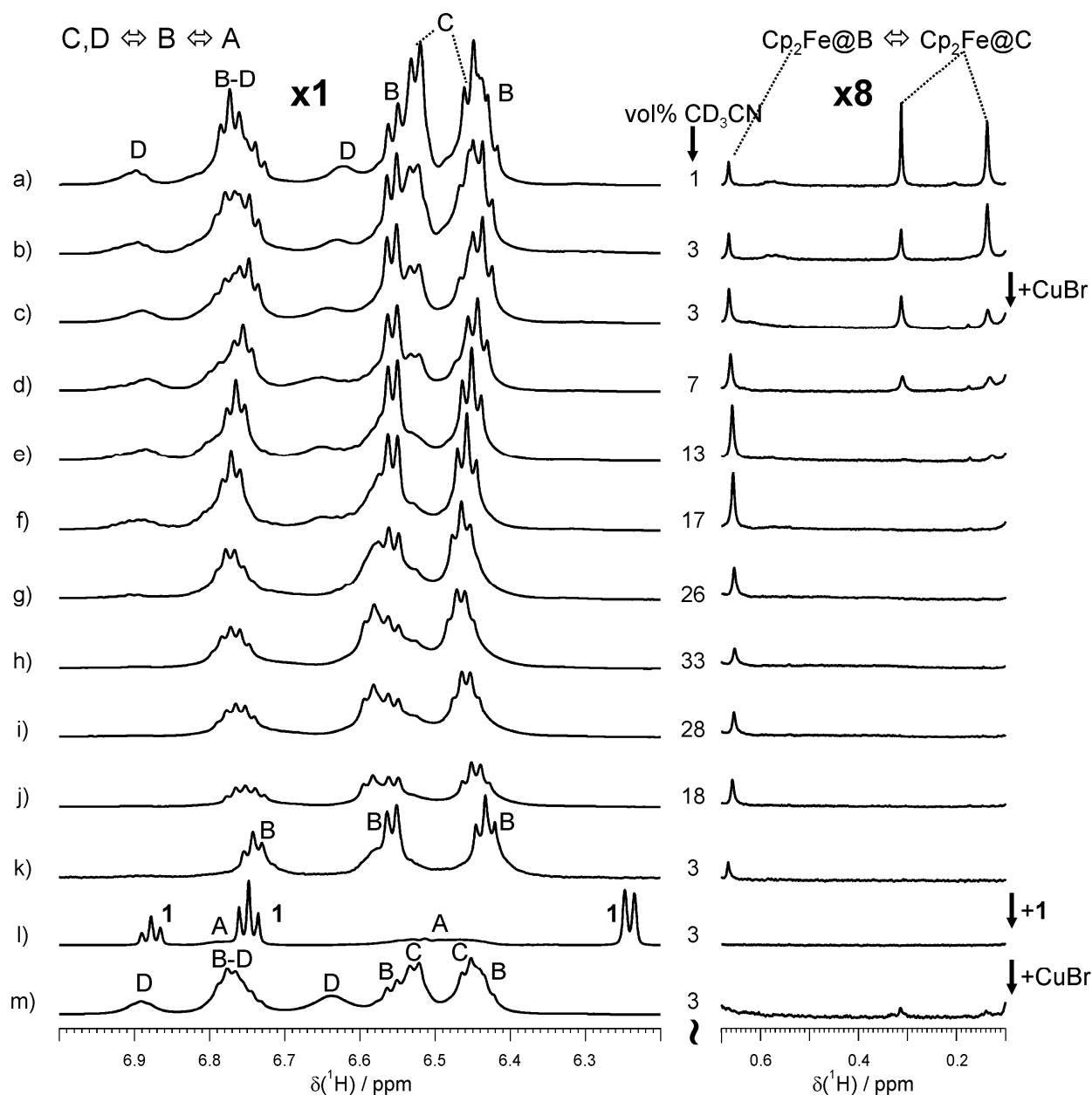
Self-assembling supramolecular switch with incorporated guests: **1** + 2 eq. CuBr + 0.25 eq. Cp₂Fe

Figure 9.8: ¹H spectra of the self-assembling supramolecular switch with incorporated guests composed of **1**, 2.0 eq. CuBr and 0.25 eq. ferrocene in CD₃CN/CD₂Cl₂ mixtures, each at 298 K and 600 MHz. The intensities of the ¹H sections on the right side are increased by a factor of eight.

The relative amounts of the container molecules B and C depending on the CD₃CN content are depicted in Figure 9.9 (in Figure 9.11, the relative amount of D is additionally taken into account). There, the switching from C to B with increasing CD₃CN content (filled symbols) and back from B to C with decreasing CD₃CN content (open symbols) is shown. In addition, in Figure 9.10 the corresponding acetonitrile depending switching from both Cp₂Fe@C to

$\text{Cp}_2\text{Fe@B}$ with increasing CD_3CN content (filled symbols) and back from $\text{Cp}_2\text{Fe@B}$ to both $\text{Cp}_2\text{Fe@C}$ with decreasing CD_3CN content (open symbols) is shown.

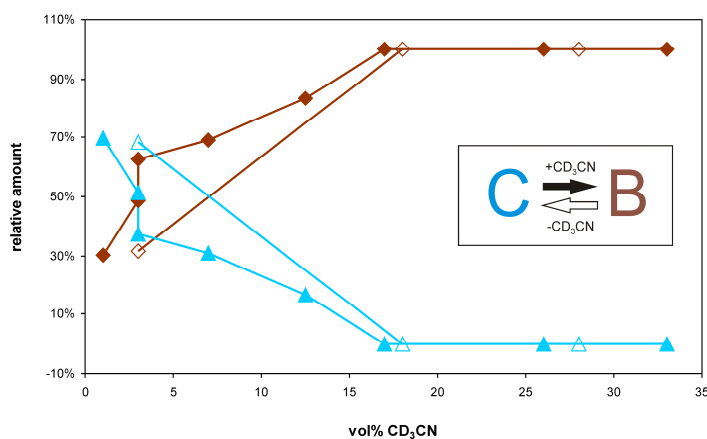


Figure 9.9: Acetonitrile depending switching from C to B with increasing CD_3CN content (filled symbols) and back from B to C with decreasing CD_3CN content (open symbols). B: Brown diamonds (\blacklozenge , \lozenge), C: Blue triangles (\blacktriangle , \triangle). Sum of B and C set to 100 %.

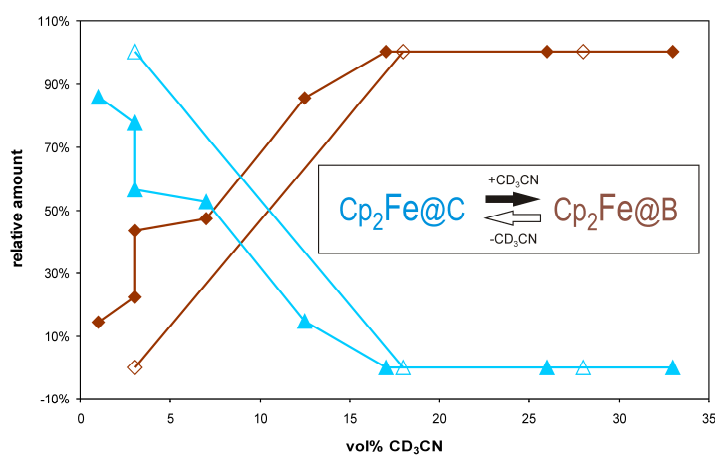


Figure 9.10: Acetonitrile depending switching from $\text{Cp}_2\text{Fe@C}$ to $\text{Cp}_2\text{Fe@B}$ with increasing CD_3CN content (filled symbols) and back from $\text{Cp}_2\text{Fe@B}$ to $\text{Cp}_2\text{Fe@C}$ with decreasing CD_3CN content (open symbols). $\text{Cp}_2\text{Fe@B}$: Brown diamonds (\blacklozenge , \lozenge), $\text{Cp}_2\text{Fe@C}$: Blue triangles (\blacktriangle , \triangle). Both $\text{Cp}_2\text{Fe@C}$ species are summarized.

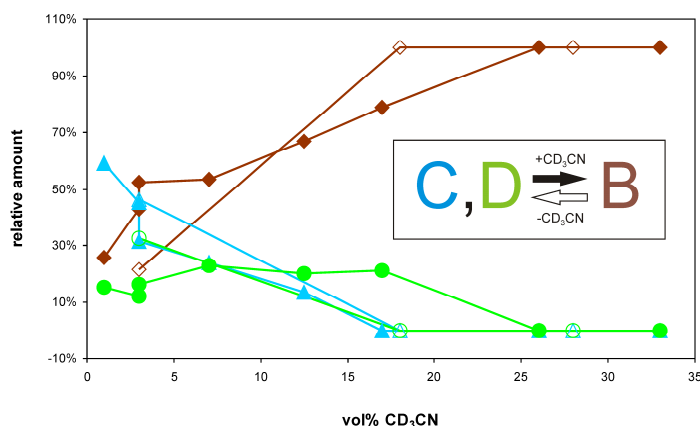


Figure 9.11: Acetonitrile depending switching from C, D to B with increasing CD₃CN content (filled symbols) and back from B to C with decreasing CD₃CN content (open symbols). B: Brown diamonds (◆, ◇), C: Blue triangles (▲, △), D: Green circles (●, ○).

Altogether, we demonstrated the potential of the supramolecules to act as supramolecular switch and additionally showed the in- and exclusion of the ferrocene guest. The switch from C, D to B was realized by an increase of the content of acetonitrile. The reversibility of the system and thus the reverse transformation from B to C, D was demonstrated by the subsequent reduction of the CD₃CN content. Furthermore, by the addition of an excess of **1** the included ferrocene was released from B, demonstrating the three states of the host-guest system (guest included in B, included in C or excluded). The re-formation of the clusters by the addition of **1** and CuBr again reconstitutes the supramolecular switch. With these experiments the potential of the self-assembling container molecules derived from **1** and CuBr to act as supramolecular switches was successfully investigated. A switch from B to C, D and back is possible by adjusting the appropriate solvent mixture. This switching seems to be independent of the presence of a guest (data for switching experiments without guest not shown). Furthermore, this self-assembling system composed of **1** and CuX (X=Cl, Br) might provide the potential to build up a four-state supramolecular switch with an exclusive formation of only one of the four different container molecules (A-D) in each state of the switch. Furthermore, the selective incorporation of several guests inside different container molecules seems possible.

Formation pathways

For such kind of self-assembly systems with several supramolecules different steps are involved in their formation pathways. First the formation of the initial adducts of **1** and CuX (X=Cl, Br) at the beginning of the reaction is described: For the formation of such kind of self-

assembly systems composed of two different building blocks (in this case **1** and CuX), in principle, two basic formation pathways could be considered: A simultaneous assembling, in which alternating **1** and CuX are incorporated step-by-step to form dimers, trimers, oligomeric building blocks and finally the supramolecular cluster or the formation of a predefined network of $[\text{Cp}^{\text{Bn}}\text{Fe}(\eta^5\text{-P}_5)]$ units with minimal CuX content and then subsequent incorporation of the missing CuX into the scaffold. (Of course, these two described pathways are absolutely borderline cases and the actual formation of such supramolecular assemblies will most probably contain contributions of both pathways. However, some tendencies might be indicated by our experiments).

The formation pathway of the different supramolecules composed of **1** and CuX might be rationalized with the experiments discussed above. By the variation of the reaction time, building blocks at different stages of the cluster formation should be detected. To allow for the formation of all types of supramolecules and to allow both a simultaneous or subsequent assembly of **1** and CuX, samples containing **1** and high amounts (six eq.) CuX were used. No CD_3CN was added in order to decelerate the formation process. The missing CD_3CN reduced the amount of dissolved CuX drastically, but a potential assembly in small intermediate building blocks should provide a sufficient solubility for CuX. In this setup (and likewise in all other experiments), however, no intermediate building blocks were detected. Instead, solely A was observed as initial adduct of **1** and CuX, which represents an assembly comprising a minimal amount of CuX in its scaffold. Beside the time-dependent observation of the formation of the supramolecules without CD_3CN , a direct NMR monitoring of their initial formation steps in the presence of CD_3CN was performed, which also hinted at A as initial (NMR detectable) adduct of **1** and CuX (for details see SI). This rapid formation of A clearly showed the thermodynamical preference for the formation of a predefined network of **2b** type with a minimal amount of CuX. This can be rationalized with the high π -stacking ability of the five phenyl groups of $[\text{Cp}^{\text{Bn}}\text{Fe}(\eta^5\text{-P}_5)]$.^[17] However, if CD_3CN and at the same time high amounts of CuX were present, e.g. in the CuX titration in CD_2Cl_2 with 9 or 14 vol% CD_3CN , the formation of A (and B) is so fast, that the formation pathway of A (and B) could not be elucidated in this case. Therefore, a simultaneous assembling of **1** and CuX to form A (and B) in the presence of CD_3CN and at the same time relatively high amounts of CuX cannot be completely excluded.

Furthermore, the subsequent formation pathways of the different clusters were elucidated by the interconversion of the supramolecules into one another by adjusting the appropriate reaction conditions (CuX content, CD_2Cl_2 - CD_3CN ratio). This switching from C, D to B and vice versa by the addition of either **1** or CuBr or variation of the $\text{CD}_3\text{CN}/\text{CD}_2\text{Cl}_2$ ratio is in agreement

with the postulated formation pathways depicted in Figure 9.12b and c. There, all crystallized supramolecules (A, B and D) are shown in brackets. In addition, Figure 9.12a shows the appropriate formation conditions and the X-ray derived core scaffolds of the molecular structures of the different container molecules.

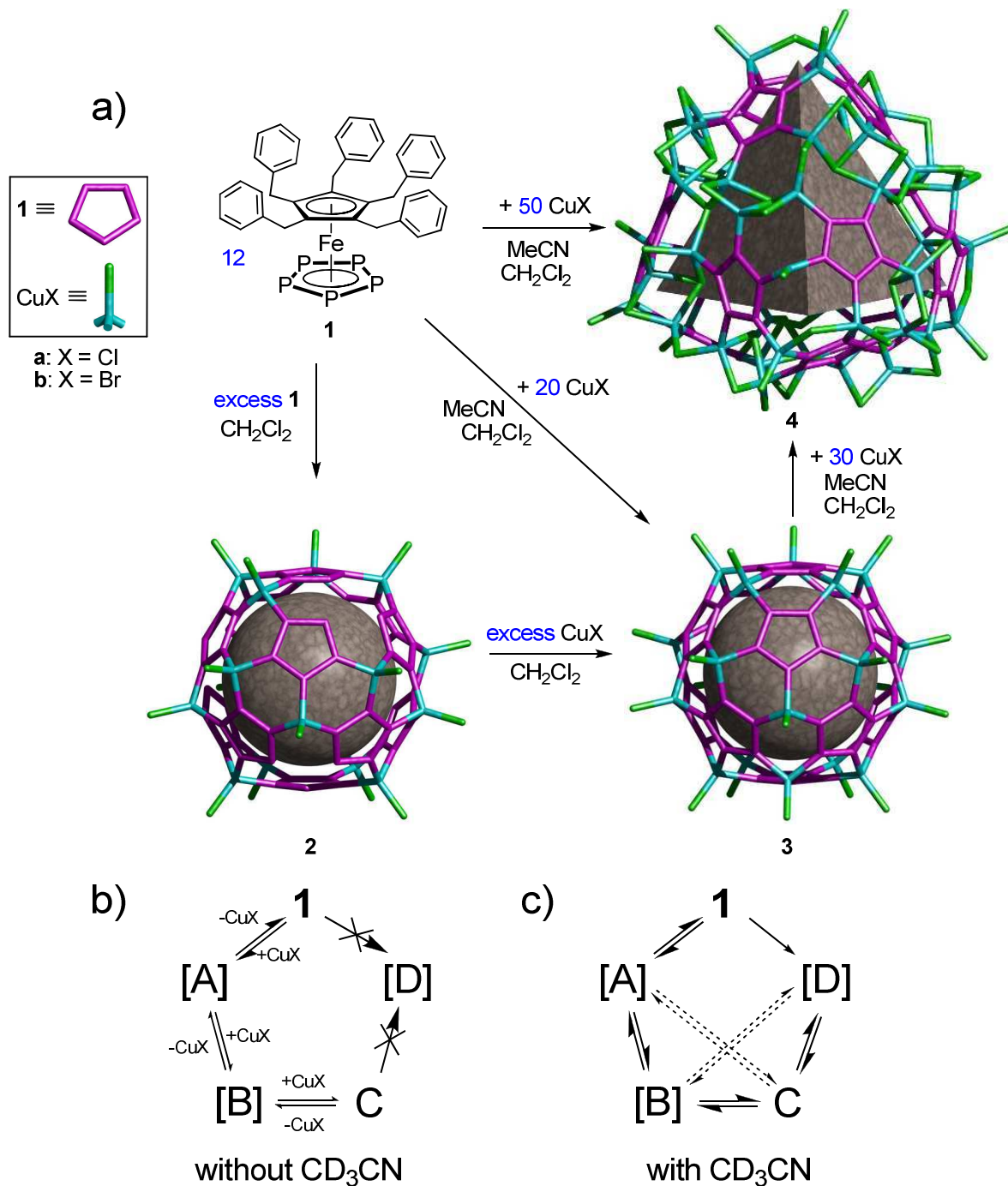


Figure 9.12: a) Scheme for the synthesis of **2a/2b**, **3a/3b** and **4a/4b** (a: X = Cl, b: X = Br) with the appropriate experimental conditions. The X-ray-derived core scaffolds of the molecular structures of the different supramolecules are shown. b,c) Proposed CuBr-dependent formation pathways c) with and b) without acetonitrile based on the discussed solution state NMR investigations. Crystallized supramolecules are shown in brackets.

CuI-derived supramolecules

With our NMR investigations, we could show the structure and formation process of soluble container molecules, which were readily accessible by quantitative self-assembly of **1** and CuX (X = Cl, Br). In addition, the incorporation of ferrocene inside the CuBr-derived container molecules B and C has been demonstrated. Thus, self-assembly systems composed of **1** and Cu^I halides provide the potential for the incorporation of suitable guests. Copper iodide together with **1** provides two different supramolecules of the same size as **3a/3b** and additional two larger assemblies, which are 1.6 times larger than **3a/3b** and 1.25 times larger than **4a/4b**. This large outer diameter is accompanied with a large inner cavity, which provides the potential to incorporate relatively large guests. Therefore, solution state NMR investigations for the CuI-derived systems seemed very promising. For this purpose, the CuI-derived supramolecules were investigated in preliminary experiments similar to the CuBr- and CuCl-derived systems.

The formation process was studied with a CuI sample, whose preparation was similar to the CuBr- and CuCl derived samples (stirring of **1** and six eq. CuI in CD₂Cl₂ for two hours and then subsequent filtration). The resulting ¹H spectrum and for comparison the corresponding spectra with CuBr and CuCl are shown in Figure 9.13. In the ¹H spectrum of **1**+CuI in CD₂Cl₂ (see Figure 9.13a), besides the signals of **1**, several very small overlapping signals at 6.3-6.7 ppm most probably for the meta and ortho protons and at least six signals at 3.8-4.6 ppm for the methylene protons could be detected. The intensities of these signals were significantly smaller compared to the corresponding signals in the CuBr- and CuCl-derived samples. The existence of several overlapping species was in analogy to the different subspecies of A in the CuBr- and CuCl-derived samples (see Figure 9.13b and c) and indicated the formation of several subspecies of type A. In addition, the averaged diffusion coefficient of the supramolecular assembly in the CuI sample revealed a hydrodynamic volume of 11.4·10³ Å³, which was very similar to the volume of A in the CuBr samples (10.7·10³ Å³). These findings indicate the presence of a supramolecule of type A in the CuI sample, too. However, the relatively large chemical shift differences for the methylene protons of the supramolecular assemblies in the CuI and the CuBr and CuCl samples might indicate structural differences of the scaffolds or more CuI in the scaffolds. However, these chemical shift differences could also be attributed to the different Cu^I halides.

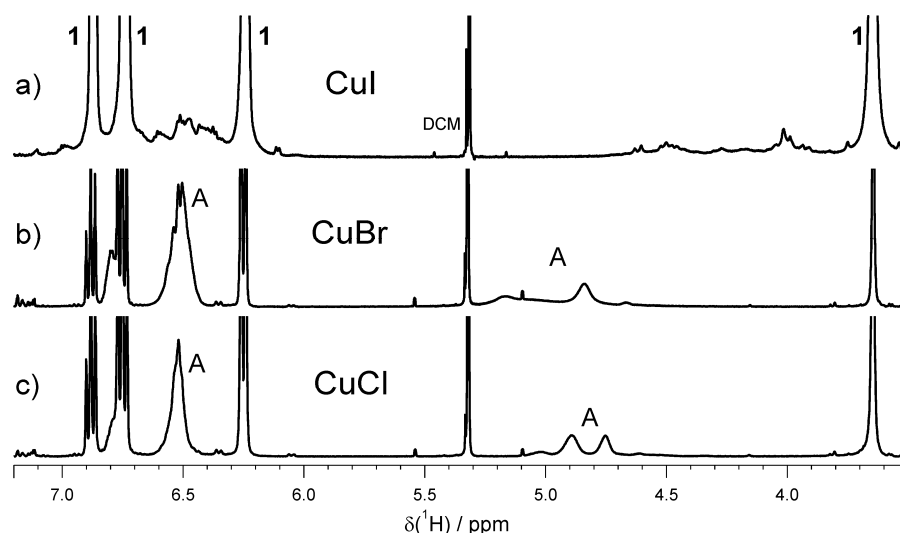


Figure 9.13: ^1H spectra of samples containing **1** and six eq. of a) CuI, b) CuBr and c) CuCl after a reaction time of 2 h in CD_2Cl_2 at 300 K, a) at 600 MHz, b) and c) at 400 MHz.

In addition, the coexistence and formation of the different CuI containing supramolecules were investigated with a mixed crystal composed of all four types of CuI-derived supramolecules. This mixed crystal was isolated from the reaction mixture and subsequently dissolved in CD_2Cl_2 . To decelerate exchange between the different macromolecules, no CD_3CN was added. The ^1H spectrum of this sample was compared to the one of a sample of dissolved CuBr-derived crystals of **4b** type (see Figure 9.14a and b).

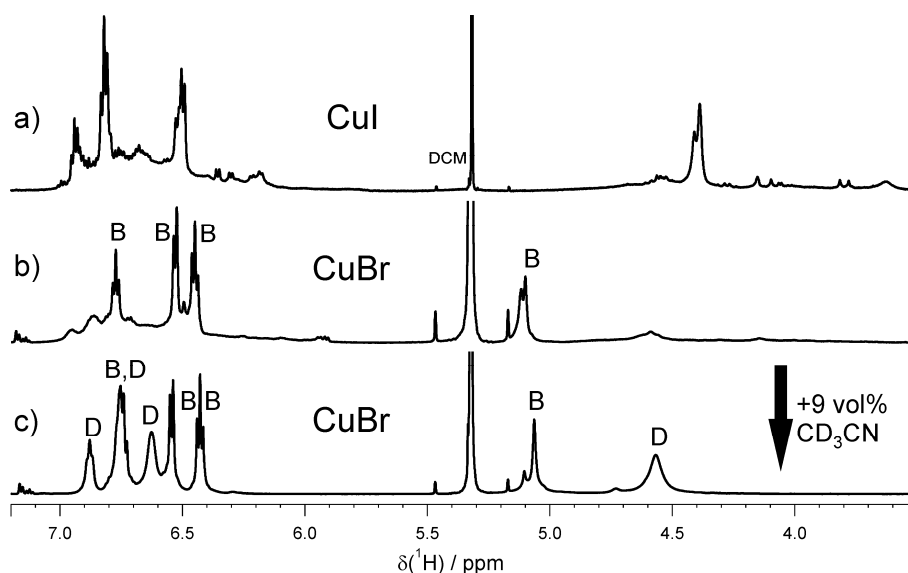


Figure 9.14: ^1H spectra of samples containing a) dissolved CuI-derived mixed crystals in CD_2Cl_2 and b) dissolved CuBr-derived **4b** crystals in CD_2Cl_2 and c) in CD_2Cl_2 with 9 vol% CD_3CN , each at 300 K and 600 MHz.

As expected, several species were detected in the ^1H spectrum of the dissolved CuI-derived mixed crystals (see Figure 9.14a) with one dominating species with signals at 6.94, 6.82, 6.50 and 4.40 ppm in the ratio 1:2:2:2. This overlay of signals showed the coexistence of several species and subspecies due to potential fragmentation, as expected with regard to the mixture of crystals dissolved. The identification of the different supramolecules from this sample seems to be impeded due to the high number of fragments present in the sample. However, the spectrum might be simplified by the addition of CD_3CN , which could accelerate exchange between some of the fragments. This was successfully demonstrated for the exchange acceleration for the different fragments of D upon the addition of CD_3CN , leading to simplified identification of D for the dissolved **4b** crystals (see Figure 9.14b and c). To conclude, by the use of appropriate solvent mixtures and by the preferential use of crystals composed of only one type of the supramolecules, a further characterization of the CuI-derived supramolecules in solution seems possible.

9.3 Conclusion

In summary, we have presented a combined solution state NMR and X-ray study about soluble, self-assembling supramolecular four-state switches with the ability to incorporate guests, composed of $[\text{Cp}^{\text{Bn}}\text{Fe}(\eta^5\text{-P}_5)]$ **1** and CuX ($\text{X} = \text{Cl}, \text{Br}$) in solution. Four different supramolecules (A-D) were characterized in solution and related to the newly discovered crystals of $[\{\text{Cp}^{\text{Bn}}\text{Fe}(\eta^5\text{-P}_5)\}_{12}\{\text{CuX}\}_{16\pm x}]$ **2a/2b**, $[\{\text{Cp}^{\text{Bn}}\text{Fe}(\eta^5\text{-P}_5)\}_{12}\{\text{CuX}\}_{20}]$ **3a/3b** and $[\{\text{Cp}^{\text{Bn}}\text{Fe}(\eta^5\text{-P}_5)\}_{12}\{\text{CuX}\}_{48\pm x}]$ **4a/4b** (**a**: $\text{X} = \text{Cl}$, **b**: $\text{X} = \text{Br}$), the latter possessing a completely new scaffold for such pentaphosphaferrocene-based complexes. Due to the high π -stacking ability of the Cp^{Bn} ligands of **1**, the initial adduct of **1** and CuBr is A, which represents a **2b** supramolecule comprising a predefined network of **1** with a minimal amount of CuX in the scaffold. Successive incorporation of CuX in the scaffolds can lead to the formation of the other container molecules. Their template-independent formation was found to be dependent on the CuX content, the overall concentration and the $\text{CD}_3\text{CN}/\text{CD}_2\text{Cl}_2$ mixture. Especially the formation of good soluble CuX-MeCN adducts plays a particular role for the selective synthesis and the thermodynamic equilibrium between the different clusters. The manipulation of the solvent mixture delivers a self-assembling reversible supramolecular four-state switch, which even allows the selective incorporation of guests. Ferrocene was incorporated in nearly 50 % of B during the switching between C, D and B. This guest can be easily removed and again incorporated from the host by addition of an excess of **1** or CuBr , respectively.

First attempts with **1** and CuI indicated a similar behavior compared to the CuBr- and CuCl-derived systems. Due to the large inner cavities of the CuI-derived supramolecules, this system might provide the potential to incorporate very large guests.

The results of this study, e.g. the knowledge about the role of the applied solvents, especially strong coordinating solvents like acetonitrile, will considerably contribute to the improvement of the directed synthesis of such pentaphosphaferrocene-derived molecules. In addition, these results will help to improve the purposefully design of supramolecular switches and will contribute to the further progress in the field of supramolecular chemistry.

9.4 Supporting Information

9.4.1 Experimental Section

NMR spectra were recorded on a Bruker Avance 400 MHz spectrometer equipped with a BBO probe with z-gradient and BVT 2000 temperature control unit at 300 K, a Bruker Avance III 600 MHz spectrometer equipped with a TBI $^1\text{H}/^{31}\text{P}$ -BB z-gradient probe and BVT 3000 unit at 300 K and an Avance III 600 MHz spectrometer equipped with a 5 mm TCI z-gradient cryo probe and BVT 3000 unit at 298 K. The spectra were processed with the Bruker program Topspin® and the diffusion coefficients were calculated with the Bruker software *T1/T2* package. All experimental diffusion coefficients were within a standard deviation of $\pm 3\%$ and are stated as temperature- and viscosity-corrected diffusion coefficients in the manuscript.

For the calibration of the ^{31}P chemical shifts, the Ξ value corresponding to TMS was applied. For the calibration of the ^1H and ^{13}C chemical shifts and for the temperature- and viscosity-correction of the diffusion coefficients, TMS (tetramethylsilane) was added to each sample. All ^1H -diffusion measurements were performed with the convection suppressing DSTE (double stimulated echo) pulse sequence, developed by Mueller and Jerschow^[20] in a pseudo 2D mode. For each experiment, 2 dummy scans and 16 scans were used with a relaxation delay of 2 s. Sinusoidal shapes were used for the gradients and a linear gradient ramp with either 12 or 16 increments between 5 and 95 % of the maximum gradient strength was applied for the diffusion relevant gradients. For the homospoil gradients, 7.046, 10.700, and 9.165 G cm^{-1} were applied for HS₁, HS₂, and HS₃. The length of the gradient pulse δ was adjusted for every species in the sample to achieve appropriate signal attenuation curves. As a result, a δ of 1.5 ms for TMS, 2.2 ms for the monomer and 3.2 ms for the supramolecules was used in most cases. A diffusion time Δ of 50 ms was used for all experiments.

Sample concentrations of 33 mM of **1** (15 mg in 0.6 mL solvent) in CD_2Cl_2 or toluene- d_8 were typically applied for the NMR measurements. Assignments of proton, carbon and phosphorous resonances of the species were obtained by one- and two-dimensional NMR spectra (^1H , ^{31}P , $^1\text{H},^{13}\text{C}$ -HSQC, $^1\text{H},^{13}\text{C}$ -HMBC, $^1\text{H},^1\text{H}$ -ROESY and $^1\text{H},^1\text{H}$ -NOESY (mixing times of 600, 350 and 100 ms) spectra.

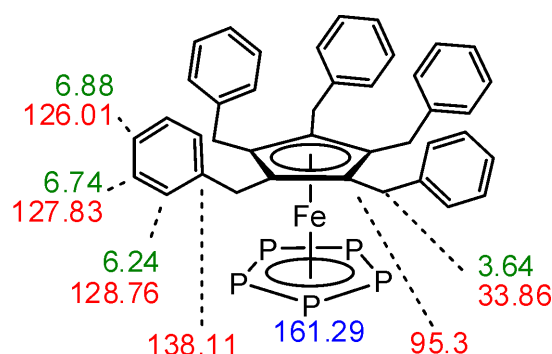


Figure 9.15: ^1H , ^{13}C and ^{31}P chemical shifts of **1** in CD_2Cl_2 at 298 K.

9.4.2 Size estimation from DOSY and X-ray data

From diffusion-ordered spectroscopy (DOSY) experiments^[18, 26] the translational self-diffusion coefficients D of molecules in solution can be calculated according to the Stejskal-Tanner equation.^[18, 20, 26-27] With the diffusion coefficients D of the analyte and of TMS (acting as viscosity reference), the hydrodynamic radius r_{H} (and thereof the hydrodynamic volume V_{H}) of the analyte can be estimated following the Stokes-Einstein equation.^[28]

From crystallographic data the volume of the monomer was estimated to be $V_{\text{cryst}}(\mathbf{1})=589 \text{ \AA}^3$. In addition, the volume of the **2b/3b** clusters was estimated to be $V_{\text{cryst}}(\mathbf{2b/3b})=13.2 \cdot 10^3 \text{ \AA}^3$ from the maximum C-C distance plus the length of a C-H bond (0.12 \AA) and the Van-der-Waals radius of a proton (0.109 \AA ^[11]). For the **4b** cluster, from crystallographic data so far only a upper size limit of $V_{\text{cryst}}(\mathbf{4b})=17.5 \cdot 10^3 \text{ \AA}^3$ could be obtained, see Table 9.3.

Table 9.3: Estimation of the volumes of the ball from crystallographic data.

Ball	$V_{\text{cryst}} / 10^3 \text{ \AA}^3$
1	0.6
2b/3b	13.2
4b	17.5 ^[a]
Larger CuI-derived clusters	22.0

[a] upper size limit estimated from the unit cell.

9.4.3 Experimental spectra

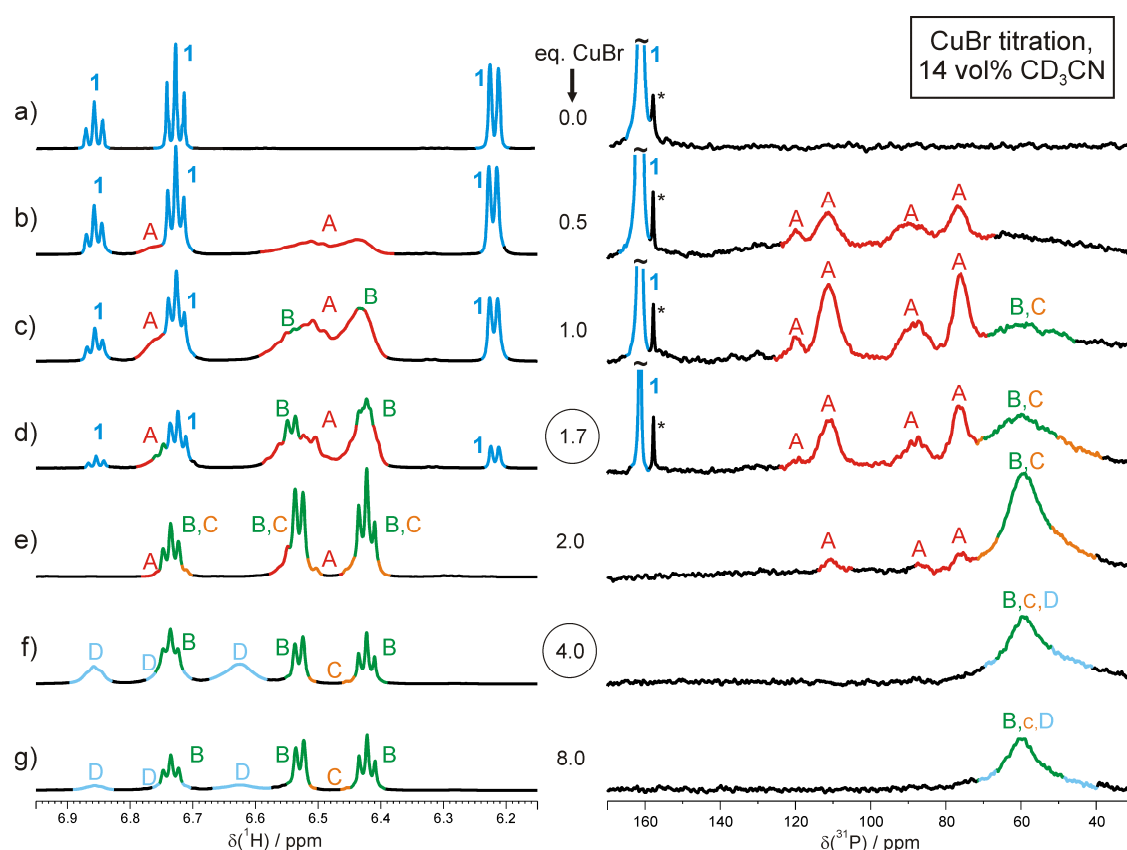


Figure 9.16: ^1H (left) and ^{31}P spectra (right) of samples containing **1** and increasing equivalents of CuBr: a) 0.0 eq., b) 0.5 eq., c) 1 eq., d) 1.7 eq., e) 2 eq., f) 4 eq., g) 8 eq., each in CD_2Cl_2 with 14 vol% CD_3CN at 298 K and 600 MHz.

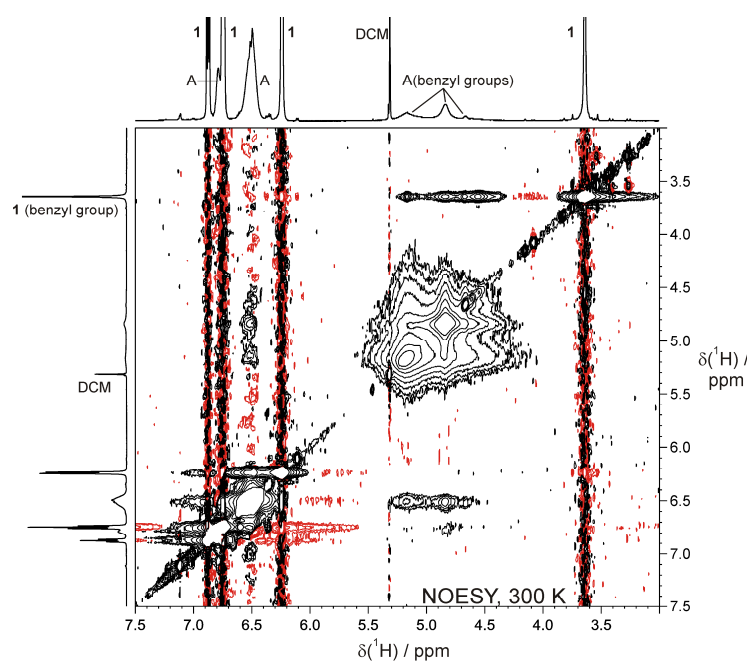


Figure 9.17: NOESY spectrum (mixing time 350 ms) of **1**+CuBr in CD_2Cl_2 at 300 K and 600 MHz.

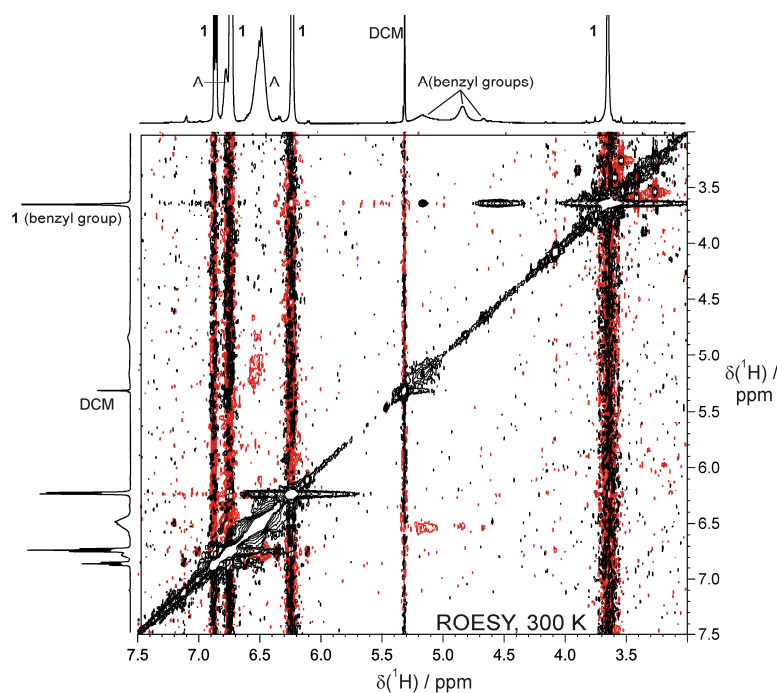


Figure 9.18: ROESY spectrum of **1**+CuBr in CD₂Cl₂ at 300 K and 600 MHz.

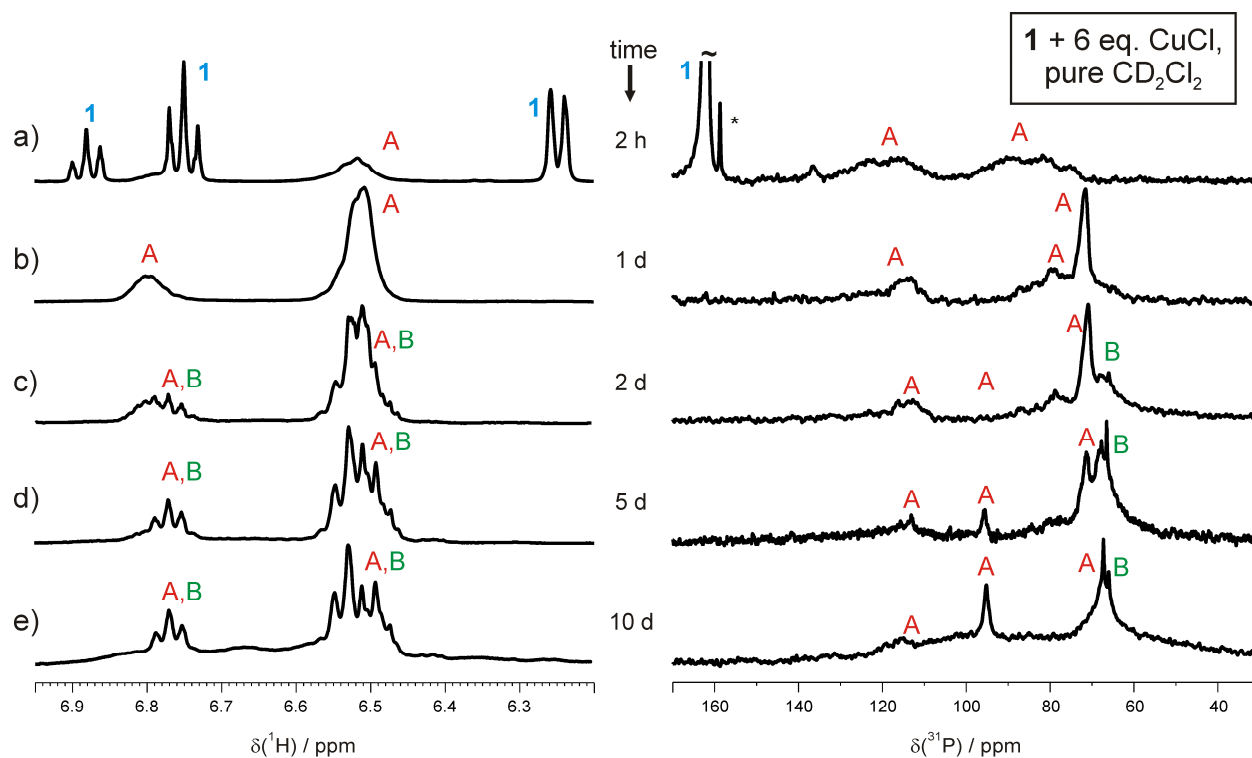


Figure 9.19: ¹H (left) and ³¹P spectra (right) of samples containing **1** and six equivalents of CuCl in pure CD₂Cl₂ after a reaction time of a) 2 h, b) 1 d, c) 2 d, d) 5 d, e) 10 d, each at 300 K and 400 MHz.

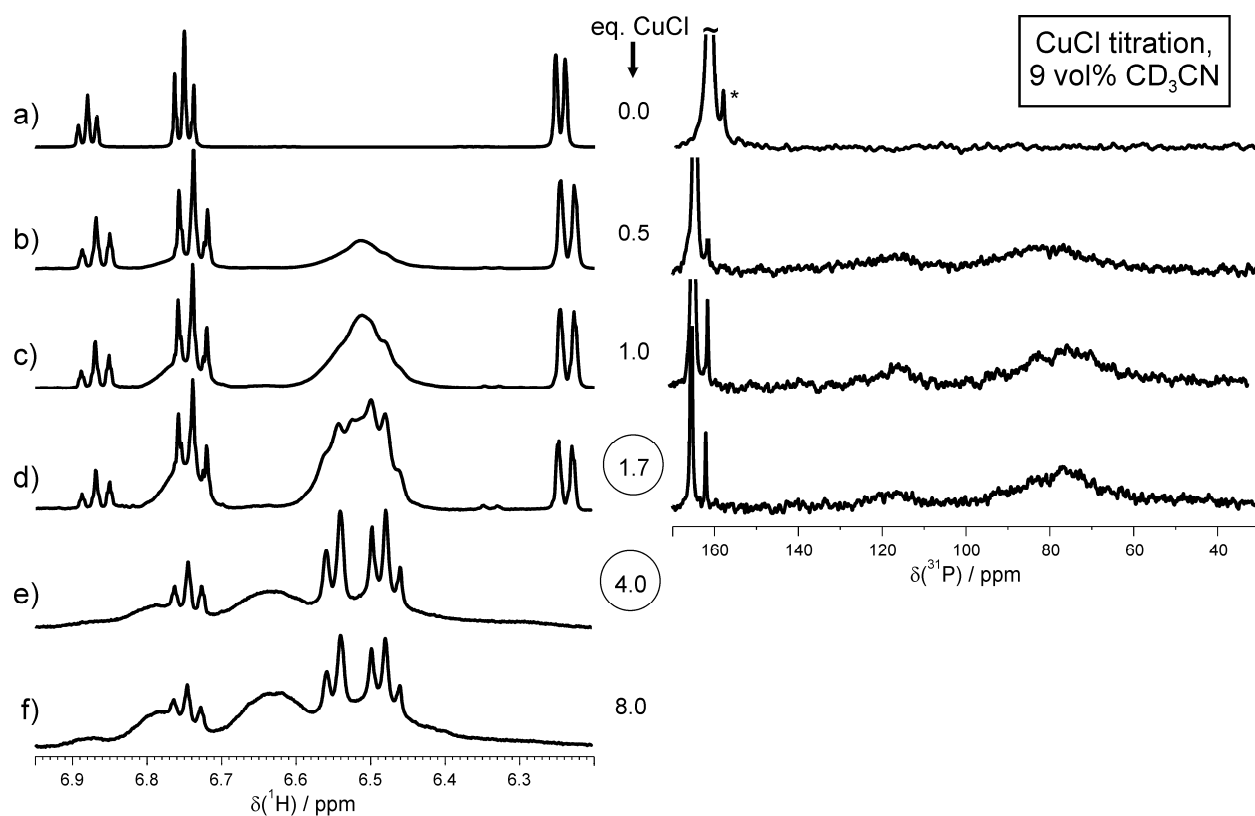


Figure 9.20: ^1H (left) and ^{31}P spectra (right) of samples containing **1** and increasing equivalents of CuCl: a) 0.0 eq., b) 0.5 eq., c) 1 eq., d) 1.7 eq., e) 4 eq., f) 8 eq., each in CD_2Cl_2 with 9 vol% CD_3CN at 300 K and 400 MHz.

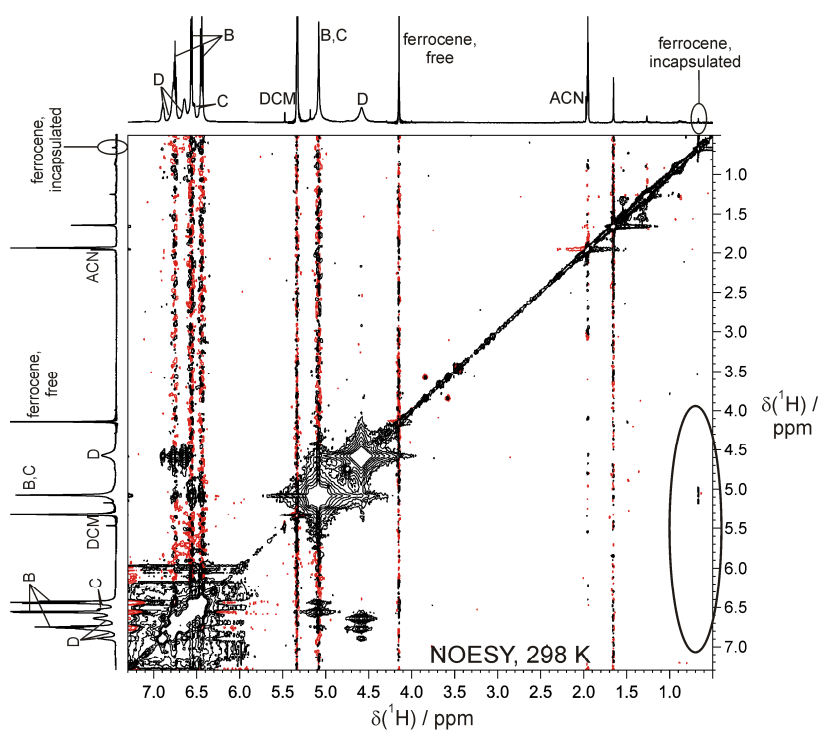


Figure 9.21: NOESY spectrum of **1**+six eq. CuBr+ferrocene in CD_2Cl_2 with 1-2 vol% CD_3CN at 298 K and 600 MHz. A cross peak from a encapsulated ferrocene guest to the methylene protons of B could be detected.

Table 9.4: ^1H integrals from the switching experiment depicted in Figure 9.8, from which the relative amounts of B-D and $\text{Cp}_2\text{Fe@B}$ and $\text{Cp}_2\text{Fe@C}$, depicted in Figure 9.9 - Figure 9.11, were calculated.

Vol% CD_3CN	^1H integrals					
	B	C	D	0.66 ppm	0.31 ppm	0.13 ppm
1	100	230	59	1.34	3.79	4.32
3	100	105	28	1.10	1.17	2.63
3	100	60	31	1.94	1.36	1.17
7	100	45	43	2.13	1.04	1.32
13	100	20	30	2.62	0.08	0.37
17	100	0	27	3.00	0.00	0.00
26	100	0	0	1.80	0.00	0.00
33	100	0	0	1.22	0.00	0.00
28	100	0	0	1.10	0.00	0.00
18	100	0	0	2.34	0.00	0.00
3 ^[a]	100	0	0	4.00	0.00	0.00
3 ^[b]	0	0	0	0.00	0.00	0.00
3	100	216	152	0.00	0.65	0.56

[a] High dilution, [b] Due to the large excess of **1**, only **1** and A was detected.**NMR online monitoring of the initial adducts of **1** and CuBr**

A direct NMR monitoring of the initial steps of the fast reaction of **1** and CuBr in the presence of CD_3CN was performed. Therefore, inside the NMR tube a sample with two layers was prepared, one layer with **1** in CD_2Cl_2 and the other layer with CuBr in CD_3CN . This setup with two layers was similar to the original synthesis procedure of the supramolecules. The low contact surface of the two solutions inside the NMR tube reduced the reaction rate. Upon spinning of the sample a mixing of the two solutions was performed and the reaction was monitored with ^1H spectra. Due to the inhomogeneous composition of the sample only a poor spectral quality was obtained. However, also in this setup, only **1** and A and no oligomeric building blocks were observed (data not shown), indicating A to be the exclusive initial adduct of **1** and CuBr.

NMR investigations in toluene- d_8

Since **1** was good soluble in toluene- d_8 , the use of this solvent for the further investigation of the supramolecules was tested by means of dissolved crystals of $[\{\text{Cp}^{\text{Bn}}\text{Fe}(\eta^5\text{-P}_5)\}_{12}\{\text{CuCl}\}_{20}]$ **3a**. But the transparency of the sample already hinted at a very low solubility of **3a** in toluene, which was also confirmed by the ^1H spectrum, in which no signals of **1** or any other species were detected. Therefore, no further attempts for the use of toluene as solvent have been made.

9.5 References

- [1] Z. Laughrey, B. C. Gibb, *Chem. Soc. Rev.* **2011**, 40, 363–386.
- [2] S. J. Dalgarno, N. P. Power, J. L. Atwood, *Coord. Chem. Rev.* **2008**, 252, 825–841.
- [3] C. Schmuck, *Angew. Chem. Int. Ed.* **2007**, 46, 5830–5833.
- [4] B. Breiner, J. K. Clegg, J. R. Nitschke, *Chem. Sci.* **2011**, 2, 51.
- [5] T. S. Koblenz, J. Wassenaar, J. N. H. Reek, *Chem. Soc. Rev.* **2008**, 37, 247–262.
- [6] D. M. Rudkevich, *Bul. Chem. Soc. Jap.* **2002**, 75, 393–413.
- [7] B. P. Johnson, F. Dielmann, G. Balazs, M. Sierka, M. Scheer, *Angew. Chem. Int. Ed. Engl.* **2006**, 45, 2473–2475.
- [8] J. Bai, A. V. Virovets, M. Scheer, *Science* **2003**, 300, 781–783.
- [9] S. Welsch, C. Gröger, M. Sierka, M. Scheer, *Angew. Chem. Int. Ed.* **2011**, 50, 1435–1438.
- [10] M. Scheer, A. Schindler, R. Merkle, B. P. Johnson, M. Linseis, R. Winter, C. E. Anson, A. V. Virovets, *J. Am. Chem. Soc.* **2007**, 129, 13386–13387.
- [11] M. Scheer, A. Schindler, C. Groeger, A. V. Virovets, E. V. Peresypkina, *Angew. Chem., Int. Ed.* **2009**, 48, 5046–5049.
- [12] M. Scheer, A. Schindler, J. Bai, B. P. Johnson, R. Merkle, R. Winter, A. V. Virovets, E. V. Peresypkina, V. A. Blatov, M. Sierka, H. Eckert, *Chem. Eur. J.* **2010**, 16, 2092 – 2107.
- [13] M. Scheer, J. Bai, B. P. Johnson, R. Merkle, A. V. Virovets, C. E. Anson, *Eur. J. Inorg. Chem.* **2005**, 4023–4026.
- [14] J. Bai, A. V. Virovets, M. Scheer, *Angew. Chem.* **2002**, 114, 1808–1811.
- [15] J. Bai, A. V. Virovets, M. Scheer, *Angew. Chem. Int. Ed.* **2002**, 41, 1737–1740.
- [16] F. Dielmann, R. Merkle, S. Heint, M. Scheer, *Z. Naturforsch., B: J. Chem. Sci.* **2009**, 64, 3–10.
- [17] F. Dielmann, PhD thesis, University of Regensburg (Regensburg (Germany)), **2011**.
- [18] C. S. Johnson, *Prog. Nucl. Magn. Reson. Spectrosc.* **1999**, 34, 203–256.
- [19] Y. Cohen, L. Avram, L. Frish, *Angew. Chem. Int. Ed.* **2005**, 44, 520–554.
- [20] A. Jerschow, N. Müller, *J. Magn. Reson.* **1997**, 125, 372–375.
- [21] W. S. Price, *Concepts Magn. Reson.* **1997**, 9, 299–336.
- [22] A. F. Holleman, N. Wiberg, *Lehrbuch der Anorganischen Chemie*, 102. ed., de Gruyter, Berlin, **2007**.
- [23] C. Elschenbroich, *Organometallchemie*, 5. ed., Teubner, Wiesbaden, **2005**.
- [24] M. Scheer, A. Schindler, C. Gröger, Alexander V. Virovets, Eugenia V. Peresypkina, *Angew. Chem. Int. Ed.* **2009**, 48, 5046–5049.
- [25] M. Scheer, A. Schindler, R. Merkle, B. P. Johnson, M. Linseis, R. Winter, C. E. Anson, A. V. Virovets, *J. Am. Chem. Soc.* **2007**, 129, 13386–13387.
- [26] W. S. Price, *Concepts Magn. Reson.* **1998**, 10, 197–237.
- [27] E. O. Stejskal, J. E. Tanner, *The Journal of Chemical Physics* **1965**, 42, 288–292.
- [28] A. Macchioni, G. Ciancaleoni, C. Zuccaccia, D. Zuccaccia, *Chem. Soc. Rev.* **2008**, 37, 479–489.

10 Summary and Outlook

Over the last decade the field of organocatalysis, *i.e.* the use of small organic molecules as catalysts, has grown to a prospering area of general concepts and widely useful reactions connected with a vast increase of the research activities. Various generic activation modes, such as H-bond, counterion, enamine, iminium, SOMO or photoredox catalysis, have been identified and successfully applied for a broad variety of asymmetric reactions. Despite the great number of synthetic applications of organo- and photocatalysis, conformational and mechanistic studies for a better understanding of the underlying origin of stereoselectivity, activation modes and mechanisms are rather scarce. But for a further development and improvement of catalysis in general, this knowledge is highly desirable, since it may allow the optimization of existing methodologies as well as the design of new catalytic systems and activation modes for organo- and photocatalysis. The goal of this thesis was therefore the elucidation of several conformational and mechanistic issues of organo- and photocatalysis by means of modern NMR spectroscopic methodologies. In addition, these NMR techniques were also applied for investigations on the field of supramolecular chemistry and electrochemical research.

In the first part of this thesis, conformational studies of three tripeptidic foldamers were performed in a combined NMR/MD study in the field of peptidic organocatalysts. Thereby, especially the influence of the configuration of (\pm)-*cis*- β -ACC was investigated, since the configuration of β -ACC was found to be decisive for the selectivities in their organocatalytic and pharmaceutical applications. Residual dipolar couplings were applied for the validation of structure coordinates for molecular dynamics simulations and the peptide backbone and sidechain conformations were revealed by NOE and/or RDC-based MD simulations. All three peptides showed independent of the β -ACC configuration an unexpected high stability of the backbone conformation, induced by a bifurcated H-bond network together with allylic strain in the β -ACC-Pro3 sub unit. The orientation of the cyclopropane ring and its methoxy substituent could therefore be manipulated by the inversion of the configuration of β -ACC without changing the peptide conformation. This may explain the different selectivities found in the applications of β -ACC in organocatalysis and medicinal chemistry and should allow an improvement of these β -ACC involving applications.

In a mechanistic study in the field of organocatalysis, NMR spectroscopy was used successfully to distinguish between the activation modes of hydrogen bonding and ion pairing in Brønsted acid catalysis. Before this study, it was assumed that full protonation of the imine by the phosphate catalyst resulted in the formation of an ion pair, which would subsequently react with a nucleophile. However, our experiments clearly showed that hydrogen bonded and ion pair complexes (and also a free protonated iminium species) co-exist. The ratio between hydrogen bonding and ion pairing could be manipulated readily by simply introducing substituents with different electronic properties. Contrary to previous assumptions, the hydrogen bond strength and the amount of the hydrogen bonded species present were found to be decisive for the catalytic reaction. These results provided for the first time insight into the different activation modes in Brønsted acid catalysis and are expected to guide the development of more efficient catalytic systems.

Beside organocatalysis, also mechanistic issues in the field of photocatalysis have been addressed in this thesis:

For the photocatalytic water reduction by intramolecular Ru/Pt catalysts, the formation and relevance of Pt-colloids and the supposed cleavage of a chloride from the photocatalyst $[(\text{tbbpy})_2\text{Ru}(\text{tpphz})\text{PtCl}_2](\text{PF}_6)_2$ under irradiation with visible light was investigated by NMR spectroscopy. The detection methods for the $^3J_{1\text{H},195\text{Pt}}$ coupling acting as a sensor for a potential Pt-cleavage were optimized by means of a model compound and subsequently applied for the photocatalyst. It could be successfully shown that without the sacrificial electron donor triethylamine TEA no cleavage of the $\text{Cl}^-/\text{PtCl}_2$ unit from the photocatalyst or a Cl^-/OH^- exchange upon irradiation with blue light (470 nm) in $\text{CD}_3\text{CN}/\text{D}_2\text{O}$ takes place. First irradiation experiments in the presence of TEA showed a decomposition of the photocatalyst upon the photocatalytic reaction. These results offer several starting points for the further detailed elucidation of mechanistic issues of the photocatalytic water reduction.

To allow for online-monitoring of this and other photocatalytic reactions, a glass fiber-based NMR-illumination unit was constructed, which allows simultaneous illumination inside the NMR spectrometer. First measurements for the photooxidation of MBA with RFT were successfully performed with this setup. Upon illumination the decrease of the MBA signals and simultaneous increase of the aldehyde signals could be observed. This NMR-illumination unit opens up the door to further investigations of flavin photocatalysis, the photocatalytic water reduction with Ru/Pt catalysts and other photocatalytic reactions and is expected to elucidate these and other issues in photocatalysis in even more detail.

The flavin photocatalysis was also investigated by means of DOSY experiments dealing with the self aggregation of riboflavin tetraacetate RFT and a potential association with paramethoxybenzyl alcohol MBA. In pure acetonitrile RFT is a dimer, whereas in water it is a monomer. These aggregation tendencies could be successfully correlated with the solvent dependency of the quantum yield of the photooxidation of MBA with RFT and are used for the design of sterically hindered (chiral) flavin derivatives with potentially higher quantum yields. No hints for an association of RFT and MBA are observed by NMR spectroscopy.

In cooperation with the research group of Prof. H. J. Gores, for the first time four different methods for the measurement of cationic transference numbers of several non-aqueous lithium ion electrolytes were compared to each other, especially regarding their concentration dependence. The transference number, which is one of the most important properties of lithium ion electrolytes, was determined by galvanostatic polarization, potentiostatic polarization, electromotive force method and NMR DOSY for the recently developed lithium difluoromono(oxalato)borate (LiDFOB) in EC/DEC and other promising Li^+ electrolytes. Whereas the three electrochemical methods yielded transference numbers decreasing with concentration, NMR DOSY measurements showed increasing transference numbers with increasing concentration. The different concentration dependences obtained by electrochemical methods and NMR measurements could be explained by ion association and solvation effects.

In cooperation with the research group of Prof. M. Scheer, the soluble, self-assembling supramolecular system composed of the monomer $[\text{Cp}^{\text{Bn}}\text{Fe}(\eta^5\text{-P}_5)]$ and CuX ($\text{X} = \text{Cl}, \text{Br}$) was investigated. The Cp^{Bn} ligand is conducive to the stability of the supramolecules as well as responsible for their solubility, which for the first time allowed detailed NMR investigations on the self-assembly process of spherical molecules based on polyphosphorus ligand complexes and Cu(I) halides in solution. Four different supramolecules were discovered and characterized by solution state NMR and related to the newly discovered crystals of $[\{\text{Cp}^{\text{Bn}}\text{Fe}(\eta^5\text{-P}_5)\}_{12}\{\text{CuX}\}_{16\pm x}]$, $[\{\text{Cp}^{\text{Bn}}\text{Fe}(\eta^5\text{-P}_5)\}_{12}\{\text{CuX}\}_{20}]$ and $[\{\text{Cp}^{\text{Bn}}\text{Fe}(\eta^5\text{-P}_5)\}_{12}\{\text{CuX}\}_{48\pm x}]$, the latter possessing a completely new scaffold for such pentaphosphaferrocene-based complexes. Their solution characteristics, formation pathways, optimal formation conditions and their ability to incorporate guests were investigated. Their template-independent formation was found to be dependent on the CuX content, the overall concentration and the $\text{CD}_3\text{CN}/\text{CD}_2\text{Cl}_2$ mixture. The manipulation of the solvent mixture delivers a self-assembling reversible supramolecular four-state switch. The switching process was found to be independent of the presence of a ferrocene

guest inside two of the capsules. Furthermore, first preliminary investigations with CuI indicated a similar behavior compared to the CuBr- and CuCl-derived systems. Altogether, these detailed NMR investigations in the field of supramolecular chemistry on the hitherto unknown self-assembly process of spherical molecules based on polyphosphorus ligand complexes and Cu(I) halides in solution will considerably contribute to the improvement of synthesis strategies of such supramolecules and to the further progress of supramolecular chemistry in general.

11 Appendix

11.1 Curriculum Vitae

Matthias Fleischmann

Geboren am 17.05.1982 in Roding



Dissertation:

11/2007 – 07/2011 Universität Regensburg, AK Prof. Ruth M. Gschwind
“NMR investigations on catalysts and conformations in organo- and photocatalytic reactions, and characterization of electrolytes and supramolecular switchable container molecules”
ab 05/2010: Vorarbeiten für den Graduiertenkolleg GRK 1626 Chemische Photokatalyse
11/2007 - 01/2010: Stipendium des Graduiertenkollegs GRK 760 Medizinische Chemie

Studium und Schulbildung:

10/2002 - 10/2007 Studium Diplomchemie, Universität Regensburg
Abschluss als Dipl. Chem. (univ.)
01/2007 – 10/2007 Diplomarbeit in organischer Chemie bei Prof. Ruth M. Gschwind:
“NMR-Strukturuntersuchungen an Peptiden und Synthese anisotroper Gele“
09/2001 –06/2002 Grundwehrdienst
09/1992 – 07/2001 Regental-Gynasium Nittenau
Allgemeine Hochschulreife

11.2 Publikationen

- (8) **Self-assembled supramolecular switchable container molecules**
F. Dielmann, M. Fleischmann, R. M. Gschwind, M. Scheer
Science **2011**, Manuscript in Preparation.
- (7) **Characterization of the platinum catalytic centre of a supramolecular photocatalyst**
M. Fleischmann, M. Pfeffer, S. Rau, R. M. Gschwind
Dalton Transactions **2011**, to be submitted.
- (6) **Tripeptides with (\pm)- β -ACC: Foldamers with tunable orientation of the steric shielding.**
M. Fleischmann, M. B. Schmid, V. D'Elia, O. Reiser, R. M. Gschwind
ChemBioChem **2011**, to be submitted.
- (5) **Brønsted Acid Catalysis: Hydrogen bonding vs. ion pairing in Imine Activation.**
M. Fleischmann, D. Drettwan, E. Sugiono, M. Rueping, R. M. Gschwind
Angew. Chem. Int. Ed. **2011**, *50*, 6364-6369. *
Angew. Chem. **2011**, *123*, 6488-6493. *
- (4) **Measurement of transference numbers for lithium ion electrolytes via four different methods, a comparative study.**
S. Zugmann, M. Fleischmann, M. Amereller, Ruth M. Gschwind, H.-D. Wiemhöfer, H. J. Gores
Electrochimica Acta **2011**, *56*, 3926-3933. *
- (3) **Residual dipolar couplings in short peptidic foldamers: combined analyses of backbone and side-chain conformations and evaluation of structure coordinates of rigid unnatural amino acids.**
M. B. Schmid, M. Fleischmann, V. D'Elia, O. Reiser, W. Gronwald, R. M. Gschwind
ChemBioChem **2009**, *10*, 440-444. *
- (2) **Temperature Dependence of the Non-Stokesian Charge Transport in Binary Blends of Ionic Liquids.**
P. Wachter, M. Zistler, C. Schreiner, M. Fleischmann, D. Gerhard, P. Wasserscheid, J. Barthel, H.J. Gores
J. Chem. Eng. Data **2009**, *54*, 491-497.
- (1) **Temperature Dependent Impedance Analysis of Binary Ionic Liquid Electrolytes for Dye-Sensitized Solar Cells.**
M. Zistler, P. Wachter, C. Schreiner, M. Fleischmann, D. Gerhard, P. Wasserscheid, A. Hinsch, H.J. Gores
J. Electrochem. Soc. **2007**, *154*, B925-B930.

* Permission for partial or full reuse of these articles in this PhD thesis is granted by Rightslink.

11.3 Vorträge und Posterpräsentationen

Vorträge auf internationalen Konferenzen:

- (1) **EUROMAR 2009**
European Magnetic Resonance conference
5.-9. Juli 2009 in Göteborg, Schweden
M. Fleischmann
Conformational Studies on β -ACC containing Tripeptides in Solution by NMR and MD

Posterpräsentationen auf nationalen und internationalen Konferenzen:

- (10) **3. EuCheMS 08/2010**
29.8.-02.09.2010 in Nürnberg
M. Fleischmann, M. Schmid, V. D'Elia, O. Reiser, W. Gronwald, R. M. Gschwind
Conformational Studies on Tripeptides Containing the Unnatural Amino Acid β -ACC in Solution by NMR and MD
- (9) **ISO μ , International Symposium on Organokatalyses 07/2010**
14.-17. Juli 2010 in Mülheim an der Ruhr
M. Fleischmann, M. Schmid, V. D'Elia, O. Reiser, W. Gronwald, R. M. Gschwind
Conformational Studies on Tripeptides Containing the Unnatural Amino Acid β -ACC in Solution by NMR and MD
- (8) **Joint EUROMAR and 17. ISMAR 07/2010**
4.-9. Juli 2010 in Florenz, Italien
M. Fleischmann, M. Schmid, V. D'Elia, O. Reiser, W. Gronwald, R. M. Gschwind
Conformational Studies on β -ACC containing Tripeptides in Solution by NMR and MD
- (7) **EUROMAR 07/2009**
5.-9. Juli 2009 in Göteborg, Schweden
M. Fleischmann (Posterupgrade zu Vortrag)
Conformational Studies on β -ACC containing Tripeptides in Solution by NMR and MD
- (6) **4. Summer School Medicinal Chemistry 09/2008**
29. September – 1. Oktober 2008 in Regensburg
M. Fleischmann, M. Schmid, V. D'Elia, O. Reiser, W. Gronwald, R. M. Gschwind
Stable Tripeptide Conformation in Solution Stabilized by the Unnatural Amino Acid β -ACC

(5) **30. GDCh Fachgruppentagung Magnetische Resonanzspektroskopie der GDCh, GÖCh und SCG 09/2008**

22. - 25. September 2008 in Regensburg

M. Fleischmann, M. Schmid, V. D'Elia, O. Reiser, W. Gronwald, R. M. Gschwind

Stable Tripeptide Conformation in Solution Stabilized by the Unnatural Amino Acid β -ACC

(4) **EUROMAR 07/2008**

6. – 11. Juli 2008 in St. Petersburg, Russland

M. Fleischmann, M. Schmid, V. D'Elia, O. Reiser, W. Gronwald, R. M. Gschwind

Comparison of two Tripeptide Conformations in Solution Stabilized by the Unnatural Amino Acid β -ACC

(3) **5. Nuclear Magnetic Resonance in Condensed Matter 07/2009**

NMRCM Summer School

4.-5. Juli 2008 in Peterhof, St. Petersburg, Russland

M. Fleischmann, M. Schmid, V. D'Elia, O. Reiser, W. Gronwald, R. M. Gschwind

Comparison of two Tripeptide Conformations in Solution Stabilized by the Unnatural Amino Acid β -ACC

(2) **Frontiers in Medicinal Chemistry 03/2008**

2.-5. März 2008 in Regensburg

M. Fleischmann, M. Schmid, V. D'Elia, O. Reiser, W. Gronwald, R. M. Gschwind

Conformational Studies on Tripeptides Containing the Amino Acid β -ACC Using NMR Spectroscopy and MD Simulations

(1) **29. Fachgruppentagung Magnetische Resonanzspektroskopie der GDCh 09/2007**

26-29. Sept. 2007 in Göttingen

M. Fleischmann, M. Schmid, V. D'Elia, O. Reiser, W. Gronwald, R. M. Gschwind

Stabilization of Tripeptide Conformations in Solution Induced by the Unnatural Amino Acid β -ACC

Kooperationen:

- | | |
|--|---|
| ➤ Prof. O. Reiser (Universität Regensburg) | Peptidische Organokatalysatoren |
| ➤ Prof. W. Gronwald (Universität Regensburg) | MD-Simulation kleiner Peptide |
| ➤ Prof. M. Rueping (RWTH Aachen) | Bronstedsäure-Katalyse |
| ➤ Prof. S. Rau (Universität Ulm) | Photokatalytische Wasserspaltung |
| ➤ Prof. B. König (Universität Regensburg) | Flavin-Photokatalyse |
| ➤ Prof. H. J. Gores (Universität Regensburg) | Überföhrungszahlbestimmung von Lithium-Ionen-Elektrolyten |
| ➤ Prof. M. Scheer (Universität Regensburg) | Supramolekulare Containermoleküle |